MODELLING CARDIAC ELECTRODYNAMICS IN LARVAL ZEBRAFISH

By SHUANG QIAN

A thesis submitted to
The University of Birmingham
for the degree of
DOCTOR OF PHILOSOPHY

School of Engineering
College of Engineering and Physical Sciences
The University of Birmingham
September 2019

Abstract

Models of cardiac electrodynamics are useful tools in understanding electrical activities in heart. Currently, whole heart models often used a continuum approach, where the heart is treated as a syncytium. Models which incorporate the detailed cellular structure, have only been applied for sections of cardiac tissue. To date, no whole vertebrate heart models incorporating cellular details such as gap junctions have been developed, because of the computational power required. Therefore how detailed cellular arrangements and intercellular connectivity affect cardiac conduction at a whole heart level remains unclear. This thesis described such cell based models of larval zebrafish hearts. The model scales range from one cell, to cardiac tissue and then to the whole heart which were modelled with finite element modelling software. These models are able to reproduce published electrophysiological results including, the electrocardiogram, action potentials and conduction velocities in different regions. By varying in intercellular electrical connectivity, a cardiac condition: atrioventricular block was simulated which is comparable to experimental results qualitatively. As the models are able to estimate the gap junction resistances, they can be used in investigating the role of gap junctions in cardiac propagation. These models can be improved by adding more histological details in the future.

Acknowledgements

First, I would like to express my sincere gratitude to my supervisor Dr Edward Tarte for guiding me into this interesting research topic. Thank you for your continued guidance and support throughout the research. Without your constant and insightful feedback, this thesis would not have been possible.

I also would like to thank Dr Daniel Espino for providing constant guidance and kind supervision during the absence of my supervisor. Thanks for your inspiring professional suggestions which makes this project more valuable and guides it into a new direction in the future.

I am also grateful to Dr James Churm, for proofing reading this thesis and helpful discussions on this project. To Dr James Crowcombe, for providing measurement data and useful advice. To School of Engineering for providing financial support. To Dr Alexandros Feresidis and Dr Raya Al-Dadah for offering technical supports on the use of software.

Last but not the least, I would like to thank my husband, Xingchi Liu, for being with me in the past eight years, for the support, encouragement and accompany he gave in the hard times during my PhD. In addition, I would like to thank my parents, Hui Ma and Jiuyang Qian, for your unconditional support and encouragements throughout my life.

Contents

Abstract..I

Acknowledgements II

Contents III

List of illustrations... VIII

List of tables...XXIII

Glossary of terms XXVII

1. INTRODUCTION 1

1.1 Motivation 1

1.2 Overview 6

2. CARDIAC ELECTROPHYSIOLOGY AND THE HEART...................10

2.1 Cardiac electrophysiology 10

2.1.1 Cellular electrophysiology 11

2.2.2 Cable equations for an axon..20

2.2 Heart anatomy and function 22

2.2.1 Cellular structure of cardiac tissue 24

2.2.2 Development of the larval zebrafish heart 27

2.3 Electrocardiogram..29

2.3.1 Depolarization and repolarization waves...29

2.3.2 Human and larval zebrafish ECGs 30

2.3.3 ECG diagnosis 33

3. CARDIAC MODELLING 36

3.1 The torso model 36

3.2 Cardiac tissue model 38

3.2.1 Continuum approach 39

3.2.2 Discrete approach 41

3.2.3 Ionic current model 43

3.3 Modelling tools 46

3.3.1 Finite element method 46

3.3.2 Introduction of COMSOL 47

4. SINGLE CARDIAC MYOCYTE MODEL 49

4.1 Single zebrafish myocyte model 50

4.1.1 Model geometry 50

4.1.2 Electrical model 51

4.1.3 Ionic current model 53

4.1.4 Stimulation method investigation 55

4.1.5 Time step investigation 59

4.1.6 Measurement of the AP 60

4.1.7 AP comparison 61

4.1.8 Adjustments of the FHN parameters 63

4.2 Single human myocyte model 73

4.2.1 Model geometry and electrical model 73

4.2.2 Ionic current models 74

4.2.3 Applying finite element analysis 83

4.3 Summary.. 84

5. CARDIAC FIBRE MODELS 89

5.1 Model geometry.. 90

5.2 Electrical model 91

5.3 AP propagation 95

5.4 Gap junction investigation... 100

5.5 Convergence analysis... 102

5.6 Investigation of stimulation current 105

5.7 Investigation of the extracellular space size 107

5.8 Discussion... 112

5.9 Summary.. 117

6. CARDIAC TISSUE MODELS 119

6.1 Modelling cardiac propagation in 2 dimensions.................................. 120

6.1.1 Model geometry... 120

6.1.2 Cubic cell array model... 121

6.1.3 Investigation of factors that affected the conduction velocity 125

6.1.4 Polygonal cell array model 127

6.1.5 Cubic cell array to polygonal cell array..................................... 129

6.1.6 Varying the gap junction conductance.. 131

6.2 Modelling the cardiac propagation in 3 dimensions 133

6.2.1 Model geometry... 134

6.2.2 AP propagation.. 135

6.2.3 Varying the gap junction conductance.. 138

6.2.4 Mesh convergence analysis.. 139

6.3 Summary.. 140

7. WHOLE HEART MODEL... 143

7.1 Model geometry.. 144

7.2 Model settings... 148

7.3 AP comparison.. 152

7.4 AP propagation 155

7.5 ECG comparison.. 160

7.5.1 Filtered ECGs.. 164

7.6 Gap junction resistivity 167

7.7 Mesh convergence analysis 168

7.8 Bulbus arteriosus... 170

7.9 Summary.. 171

8. APPLICATION AND EXTENSION OF THE HEART MODEL 173

8.1 Gap junction remodelling.. 173

8.1.1 Varying atrial gap junction resistivities.. 175

8.1.2 Varying AV band gap junction resistivities 178

8.1.3 Varying ventricular gap junction resistivities 181

8.2 52 hours post fertilisation zebrafish model 184

8.2.1 Model settings 184

8.2.2 Modelling results 187

8.2.3 Modified 52 hpf zebrafish heart model 195

8.3 Summary 201

9. CONCLUSION AND FUTURE WORK 203

9.1 Future work 205

9.1.1 Geometrical refinement 206

9.1.2 Ionic current model 208

9.1.3 Electromechanical model 208

10. APPENDIX 210

11. BIBLIOGRAPHY 211

List of illustrations

Figure 2.1: (A) Potassium conductance and (B) Sodium conductance versus time in a voltage clamp experiment. The clamp voltage is expressed as a change from the resting potential. 14

Figure 2.2: The transmembrane potential, the sodium and potassium conductance (GK and GNa) and their sum during an AP produced by the Hodgkin-Huxley model from [37]. 17

Figure 2.3: A typical AP of cardiac cell. The AP amplitude is shown in green and different APD are shown in blue. 19

Figure 2.4: The equivalent circuit model of an axon according to the cable theory. 20

Figure 2.5: (A) Schematic anatomy of human heart including the conduction pathways [50]; (B) anatomy of a 3 dpf zebrafish heart [51] 23

Figure 2.6: (A) Histology of human cardiac tissue in [65]; (B) Schematic diagram of gap junction [66]; (C) Wild-type zebrafish hearts at 24, 48, and 100 hpf immunostaining with anti-Cx40 or anti-Cx43 antibodies (red) [67]; (D) Confocal image of a wild-type zebrafish heart at 72 hpf stained with anti-Cx43. The arrowhead points to outflow tract cardiomyocytes with slightly elevated Cx43 concentrations. Scale bar: 10 μm. [57] 26

Figure 2.7: Recording signals produced by (A-B) the depolarization wave and (C-D) the repolarization wave from a cardiac muscle fibre from the electrodes placing at the outside of the fibre [83]. 30

Figure 2.8: (A) 12 lead ECG system showing the electrodes' placements from [84]. (B) The electrodes' placements of larval zebrafish ECG from [36]. 31

Figure 2.9: APs of for each region in the human heart and resultant ECG [85] 32

Figure 2.10: (A) Human ECG labelling with ECG intervals [84]; (B) A typical 72 hpf zebrafish measured ECG at a position near ventricle [36] 33

Figure 2.11: ECGs during the AV blocks from [37] 35

Figure 3.1: The transmembrane potential u in solid line and the recovery variable v in dashed line are plotted against dimensionless time produced by Rogers model [42] 45

Figure 4.1: (A) Confocal section of ventricle in 72 hpf zebrafish heart stained with anti-β-catenin found in [57]; scale bar, $10\ \mu m$. (B) ventricular myocytes in a 48 hpf zebrafish heart found in [39]. Nucleus express red fluorescent protein and membrane of myocytes is labelled with Zn5 antibody (green). (C) Single larval zebrafish myocyte model geometry. The stimulation current is applied to the myocyte membrane in blue. The ground boundary condition is applied to the extracellular space boundary in red. (D) Cross-sectional view of the single larval zebrafish myocyte model geometry. Membrane are marked in green. The inside of the membrane is the intracellular space and the outside is the extracellular space. 51

Figure 4.2: mesh of the zebrafish single cell.. 55

Figure 4.3: Strength- duration curve from [37]. The units are relative......................... 56

Figure 4.4: (A) Stimulation currents using in the single larval zebrafish myocyte model with the maximum value $Istimmax$ at $50, 100, 150\ and\ 200\ \mu A/cm2$. (B) Transmembrane potential versus time in the single larval zebrafish myocyte model using different stimulation currents. (C) The first 4 ms of the transmembrane potentials in (B). (D) The time derivatives of transmembrane potential versus time in the first 4 ms...... 57

Figure 4.5: (A) Transmembrane potential versus time in the single larval zebrafish myocyte model by setting the intracellular potential to different values above the resting potential. (B) The first $4\ ms$ of the transmembrane potentials in (A). (C) The

corresponding time derivative of transmembrane potential versus time. (D) The first 4 ms of the time derivative of transmembrane potential in (D) during the upstroke period. .. 58

Figure 4.6: The first 2 ms of the time derivative of transmembrane potential during upstroke period with time step as (A) 1 ms and (B) 0.01 ms using two stimulation methods. The blue line is for applying a stimulation current with the maximum magnitude at 150 $\mu A/cm2$. The green line is for setting the initial intracellular potential to $-40\ mV$. 60

Figure 4.7: The MUV of the whole membrane of the single larval zebrafish myocyte produced by (A) the model using a stimulation current with the maximum magnitude at 150 $\mu A/cm2$; and (B) the model using an initial intracellular potential at $-40\ mV$. The colour bar is from 0 V/s in blue to 1000 V/s in red........ 61

Figure 4.8: (A) APs of the single larval zebrafish myocyte model with varying “c1” parameter in the FHN model. (B) The APs during the upstroke period in (A). (C) The time derivatives of transmembrane potential versus time with varying “c1” parameter in the FHN model. (D) The time derivatives of transmembrane potential versus time in (D) during upstroke period. 65

Figure 4.9: The MUV and the APD of the APs produced by the single larval zebrafish myocyte model versus the parameter “c1”........ 65

Figure 4.10: (A) APs of the single larval zebrafish myocyte model with varying “e” parameter in the FHN model. (B) The APs during the upstroke period in (A). (C) The time derivatives of transmembrane potential versus time with varying “c1” parameter in the FHN model. (D) The time derivatives of transmembrane potential versus time in (D) during upstroke period. 67

Figure 4.11: The MUVs and the APDs produced by the single larval zebrafish myocyte model versus the parameter “e” 67

Figure 4.12: (A) APs of the single larval zebrafish myocyte model with varying stimulation currents. (B) (B) The time derivatives of transmembrane potential versus time with varying stimulation currents. 68

Figure 4.13: (A) APs of the single larval zebrafish myocyte model with varying parameter “A” and “B” in the FHN model. (B) The time derivative of transmembrane potential versus time with varying parameter “A” and “B” in the FHN model. 69

Figure 4.14: (A) APs of the single larval zebrafish myocyte model with varying initial intracellular potentials. (B) The time derivative of transmembrane potential versus time with varying initial intracellular potentials. 70

Figure 4.15: (A) APs of the single larval zebrafish myocyte model of 48 hpf zebrafish and 72 hpf zebrafish. (B) The time derivatives of transmembrane potential versus time produced by the single larval zebrafish myocyte model of 48 hpf zebrafish and 72 hpf zebrafish. 72

Figure 4.16: (A) The micrograph of a typical human ventricular myocyte from [127]. Scale bar: $50\ \mu m$; (B) Geometry of single human ventricular myocyte model. Scale bar: $50\ \mu m$. The stimulation current is applied to the myocyte membrane in blue. The ground boundary condition is applied to the extracellular space boundary in red. 73

Figure 4.17: (A) APs of the single human myocyte model using the FHN model with various stimulation currents. (B) The time derivatives of transmembrane potential versus time of the single human myocyte model using the FHN model with various stimulation currents. 75

Figure 4.18: (A) APs of the single human myocyte model using the LR model with various stimulation currents. (B) The time derivative of transmembrane potential versus time of the single human myocyte model using LR model with various stimulation currents. 81

Figure 4.19: APs produced by the single human myocyte model using the FHN model and the LR model and the original AP produced by the LR model [43]. The original AP produced by the LR model were redrawn from [43] using the standard settings (extracellular potassium concentration $Ko = 5.4\ mM$). 82

Figure 4.20: Meshes of the human cell 83

Figure 5.1: (A) Geometry of the LZVF model and a close-up view of a few myocytes; (B) cross-sectional view of the LZVF model; (C) Geometry of the HVF model and a close-up view of a few myocytes; (D) cross-sectional view of the HVF model. The red dots represent the points at which transmembrane potential was measured. 90

Figure 5.2: Overview of physical equations in the LZVF and the HVF models 92

Figure 5.3: Oblique views of the meshes in (A) the LZVF model and (B) the HVF model. Note that only the elements which meet the surface can be seen. Each cell in the LZVF model contains an average of 1875 elements whilst each cell in the HVF model contains an average of 67 elements. 94

Figure 5.4: (A) Mean mesh element volumes of different regions in the LZVF model. (B) Mean mesh element areas of different regions in the LZVF model. (C) Mean mesh element volumes of different regions in the HVF model. (D) Mean mesh element areas of different regions in the HVF model. The error bars are the standard deviations of mesh element volume/area. 94

Figure 5.5: APs of 6 equally spaced points of which the distances from the stimulated membrane is $Dstim$ for (A) LZVF1 model, (B) LZVF2 model and (C) HVF model. .. 96

Figure 5.6: Distances from the stimulated membrane vs activation time for: (A) LZVF1 model (blue) and LZVF2 model (green); (B) HVF model.. 96

Figure 5.7: the time derivative of transmembrane potential vs time produced by (A) the LZVF1 model, (B) the LZVF2 model and (C) the HVF model. (D) close-up view of the first $20\ ms$ of (C)... 97

Figure 5.8: The maximum upstroke velocities of the whole fibre in (A) the LZVF1, (B) the LZVF2 and (C) the HVF models. The black boxes show the maximum upstroke velocities of both ends of the model human ventricular fibre. 99

Figure 5.9: Transmembrane potential Vm in the (a) LZVF1 model, (b) LZVF2 model at time $60\ ms$ during the upstroke period with corresponding transmembrane potential plotted against the distance from the stimulated membrane below; (c) Transmembrane potential Vm in the HVF model at time $7\ ms$ during the upstroke period and a close-up view of 10 myocytes during the upstroke period with the corresponding Vm plotted against the distance from the stimulated membrane. Colour bar: from $-80\ mV$ (blue) to $50\ mV$ (red). 100

Figure 5.10: Convergence analysis: Distance of 6 equally spaced points, from the stimulated membrane plotted against time when the transmembrane potential reaches $0\ mV$ in (A) LZVF1 model, (B) LZVF2 model, and (C) HVF model; the proportional differences of CV between the finest mesh results and each mesh results versus different mesh levels in (D) LZVF1 (blue) and LZVF2 (red) models, (E) HVF model. 104

Figure 5.11: Stimulation current $Istim$ in the LZVF model (blue) and the HVF model (green). 105

Figure 5.12: Stimulation current investigation: Distance of 6 equally spaced points from the stimulated membrane vs time when the transmembrane potential reaches 0 mV with a variation of the maximum stimulation current $Istimmax$ at: 50 (blue), 100 (green), 150 (red), and 200 (black). 107

Figure 5.13: The MUVs of the whole fibre in LZVF1 model with a variation of the maximum stimulation current $Istimmax$: (A) 100, (B) 150, and (C) 200. Scale bar: 0 V/s (blue) to 20 V/s (red). 107

Figure 5.14: Extracellular potential Ve of the 6 equally spaced points versus time for the HVF model with various side lengths of cross-section area of extracellular spaces Dex equal to: (A) 18.17 μm; (B) 19 μm; (C) 20 μm; (D) 40 μm. 109

Figure 5.15: Distances of 6 equally spaced points, from the stimulated membrane versus time when the transmembrane potential reaches 0 mV in the HVF model with various side lengths of cross-section area of extracellular space: 18.17 μm (blue), 19μm (black), 20 μm (green) and 40 μm (red). 110

Figure 5.16: Extracellular potential Ve of the 6 equally spaced points versus time by the LZVF1 model with various side lengths of the cross-section area of extracellular spaces Dex: (A) 10.1 μm; (B) 10.2 μm; (C) 11 μm; (D) 40 μm........ 111

Figure 5.17: Distances of 6 equally spaced points from the stimulated membrane vs the time when the transmembrane potential reaches 0V in the LZVF1 model with various side lengths of cross-section area of extracellular space:18.17 μm (blue), 19 μm (green), 20 μm (red) and 40 μm (black)........ 112

Figure 6.1: (A) Histological human cardiac tissue from [148]; (B) Cubic cells in black outlines and polygonal cells filled in grey; (C) Cubic cell array model geometry; (D) polygonal cell array model geometry; The stimulation currents were applied to the left

boundary of cell at left bottom corner marked in the blue and the ground conditions were applied to a boundary on the extracellular block at the opposite side of the stimulated cell marked in red. 121

Figure 6.2: (A) APs measured at the point marked in black in (B) produced by the cubic cell array model using various stimulation currents of 200, 400 and $800\ \mu A/cm2$; MUVs produced by the cubic cell array model using various stimulation currents of (B) 200, (C) 400 and (D) $800\ \mu A/cm2$. 122

Figure 6.3: (A) Activation time map of the cubic cell array model and (B) Distances from the stimulated membrane along the black diagonal line shown in (A) versus activation time labelled with CVs for section 1 (green points), section 2 (blue points) and section 3 (red points).. 124

Figure 6.4: Distances from the stimulated membrane versus activation time labelled with CVs for sections in different colours (each section includes 5 cell points) with a larger cell array model having: (A) 25*25 cells and (B) 45*45 cells. 125

Figure 6.5: CVs of three sections in the cubic cell array model shown in Figure 6.3 (B) versus: (A) the magnitude of the stimulation current, (B) extracellular spaces dimensions, (C) effective GJ conductance. 126

Figure 6.6: (A) Activation time map and (B) Distances from the stimulated membrane along the diagonal line versus activation times of cells on the line labelled with the CVs for section 1 (green points), section 2 (blue points) and section 3 (red points) similar to Figure 6.3 (B). 129

Figure 6.7: Activation time maps of (A) polygonal cell array 1 ($L12$), (B) polygonal cell array 2 ($L8$), (C) polygonal cell array 3 ($L6$); (D) CVs of the section 2 in the cubic and

polygonal cell array models versus the internal extracellular volume percentages as shown in Table 6.2. 131

Figure 6.8: CVs of section 2 in the polygonal cell array models versus various effective GJ conductance. 133

Figure 6.9: (A) Image of 24 hpf zebrafish heart from [56]; Model geometry for (B) cubic cell cylinder and (C) polygonal cell cylinder; (D) a cell ring in the polygonal cell cylinder including 15 cells; The stimulation current is applied to a surface boundary of a cell at the bottom cell ring marked in the blue circle and the ground condition is applied to a boundary on the extracellular block at the opposite side of the stimulated cell marked in red. 135

Figure 6.10: Activation time maps of (A) cubic cell cylinder model and (B) polygonal cell cylinder model. The cells on red arrow lines were used to plot Figure 6.10 for the cardiac propagation in longitudinal and transverse directions 136

Figure 6.11: Distances from the stimulated membrane along the longitudinal line vs activation times of cells on the line labelled with CVs for section 1 (green points), section 2 (blue points) and section 3 (red points) for (A) cubic cell cylinder model and (C) polygonal cell cylinder model. Distances from the stimulated membrane along the transverse line vs activation times of cells on the line labelled with CVs for section 1 (green points), section 2 (black circle) and section 3 (red points) for (B) cubic cell cylinder model and (D) polygonal cell cylinder model 137

Figure 6.12: CVs versus the mesh levels in (A) cubic cell array model, (C) polygonal cell array model and in (E) cubic and (G) polygonal cell cylinder models; Proportional difference of CV versus the mesh levels in (B) cubic cell array model, (D) polygonal cell array model and in (F) cubic and (H) polygonal cell cylinder models 140

Figure 7.1: Geometry of the 72 hpf zebrafish heart model at: (A) front view, (B) side view, (C) vertical view; (D), (E), and (F) are transparent graphs of (A), (B) and (C) respectively. 144

Figure 7.2: Microscopy images of zebrafish heart with myocytes' shapes: (A) 48 hpf zebrafish heart with nucleus stained in red and cell membranes stained in green. IC: inner curvature. OC: outer curvature. [39]; (B) 72 hpf zebrafish ventricle with cell membranes stained with anti-β-catenin [57]; (C) 72 hpf zebrafish ventricle with the membrane stained in green and red. BA: Bulbus arteriosus. V: ventricle [81]. (D) 48 hpf zebrafish heart with cell membranes stained in green. The yellow box shows the AV cardiomyocytes [56]. 145

Figure 7.3: Cellular information of different regions in the model larval zebrafish heart (black) comparing with the literature for larval zebrafish heart in different developing stages (coloured) including (A) myocyte number, (B) average surface area per myocyte, (C) average circularity per myocyte. 147

Figure 7.4: Microphotographs of a 72 hpf zebrafish body in (A) dorsal view and (C) left-side view[157]. Model geometry of the whole 72 hpf zebrafish body with heart in (B) left-side view and (D) dorsal view. Scale bar is $200\ \mu m$ for all images. The ground condition is applied to the boundary in the blue circle. 148

Figure 7.5: Electrical equations applied to different regions in the zebrafish heart model including the intracellular space consisting of the sinoatrial region (red) and the other non-self-excitatory regions (blue), the extracellular space (white), membrane (black) and the gap junctions' area (yellow). 149

Figure 7.6: (A) Meshes of the model larval zebrafish heart; (B) close-up view of mesh elements in the model heart. 152

Figure 7.7: Model APs measured at the points shown in (D) in (A) atrium; (B) AV band and (C) ventricle. The lines of the model APs in (A), (B) and (C) are measured at the points that have the same colours. The recorded APs are from [56]. 153

Figure 7.8: Average model AP characteristics comparing with the recorded AP characteristics including (A) action potential amplitude, (B) APD, (C) MUV and (D) maximum downstroke velocity. (n=5) student's t test: Error bars: s.e.m. 154

Figure 7.9: Maximum upstroke velocity of the 72 hpf zebrafish heart model 155

Figure 7.10: Temporal sequences of the transmembrane potential Vm at different stages. Time 0 ms: the start of atrial depolarisation. (A)activation started at sinoatrial region; (B) atrium depolarisation; (C) atrium repolarisation and ventricle depolarisation; (D) the end of atrium repolarisation and plateau stage of ventricle; (E)-(H) ventricle depolarisation. 156

Figure 7.11: (A) Transmembrane potential Vm at time $62\ ms$ during depolarisation vs the distance along the line starting from the sinoatrial region on heart surface as shown in blue in (B). (B) The approximate centreline on the heart with several points marked in black with distances. 156

Figure 7.12: Activation time maps of the model heart (A) and the real heart [57] (B). In (A), the AV band (yellow box) is enlarged in the right. Several myocytes are labelled with their activation times. In (B), isochronal lines represent the activation times at $5\ ms$ interval from [57]. These isochronal lines are labelled from “A” near the sinoatrial region where the activation starts to “P” at the end of ventricle where the latest activation happens. 157

Figure 7.13: Activation time versus the distance along the line starting from the sinoatrial region on heart surface as shown in Figure 7.11 (B). 158

Figure 7.14: Model ECGs measured near (A) atrium, (B) AV band and (C) ventricle comparing with the recorded ECGs from [36]. Model 1 has an APD same to the reference [56] (Figure 7.8). Model 2 has a reduced APD (Figure 7.16) to fit with the QT length in the recorded ECGs. 160

Figure 7.15: ECGs produced by the model 1 measured on the surface of the fish body near: (A) the atrium at point “a”, (B) the AV band at point “b” and (C) the ventricle at point “c” along with the APs measured from the points at the start and end of atrial and ventricular activations shown in (D). The lines of the model APs in (A), (B) and (C) are measured at the points that have the same colours. 162

Figure 7.16: APs comparison between the model 1 and the model 2 in (A) atrium, (B) AV band and (C) ventricle. The measured points of the APs are the middle points (green) in the regions in Figure 7.7 (D). 164

Figure 7.17: (A) Magnitude and phase responses and (B) of the band pass filter used in recording procedure and in the model.. 166

Figure 7.18: Filtered Model 2 ECGs measured near (A) atrium, (B) AV band and (C) ventricle comparing with the original model ECGs and recorded ECGs from [36]..... 166

Figure 7.19: Mesh convergence analysis of the zebrafish heart model: (A) Four activation time intervals vs the mesh levels of the models. (B) The proportional difference of the same four activation time intervals between each result with the result produced by the model with the finer mesh level vs the mesh levels of the models............................. 169

Figure 7.20: Activation time map of zebrafish heart model with bulbus arteriosus..... 170

Figure 8.1: Activation time maps of models with the atrial gap junction resistivities at (A) $0.35\ \Omega \cdot m2$, (B) $0.7\ \Omega \cdot m2$ and (C) $1.05\ \Omega \cdot m2$. The ECGs for these three models measured at (D) atrium, (E) AV band and (F) ventricle were plotted. 177

Figure 8.2: Activation time maps of models with the AV band gap junction resistivities at (A) $0.23\ \Omega \cdot m2$, (B) $0.46\ \Omega \cdot m2$and (C) $0.8\ \Omega \cdot m2$. The ECGs for these three models measured at (D) atrium, (E) AV band and (F) ventricle were plotted. 180

Figure 8.3: Activation time maps of (A) the model 1 with inner ventricular gap junction resistivity at $0.13\ \Omega \cdot m2$ and outer ventricular gap junction resistivity at $0.2\ \Omega \cdot m2$ and the larger $Rven$ models with both inner and outer ventricular gap junction resistivities at (B) $0.8\ \Omega \cdot m2$ and (C) $2\ \Omega \cdot m2$. The ECGs for these three models measured at (D) atrium, (E) AV band and (F) ventricle were plotted. 183

Figure 8.4: (A) heart geometry of 52 hpf zebrafish heart model; (B) Images of 52 hpf zebrafish heart with fluorescent markers expressed in myocardial cells report calcium transient activity and cell positions in [46]. 184

Figure 8.5: (A) Activation time of the boundaries on the approximated centreline versus the distance along the line from the sinoatrial region in the 52 hpf zebrafish heart model. (B) Boundaries on the approximated centreline in the 52 hpf zebrafish heart model are shown in blue. (C) The distribution of activation times along the centerline in the real 36, 44, and 52 hpf zebrafish hearts in [46]. Dots indicate activation time of each cell and the smooth regression profiles are solid lines. (D) The centreline of the 52 hpf zebrafish heart in [46]. 189

Figure 8.6: (A) Activation time map of the 52 hpf zebrafish heart model. The activation time is defined as the time when the transmembrane potential reaches 0 mV during the rising phase of its AP. (B) measured activation time of calcium transient in 52 hpf zebrafish heart [46]. The activation time $tact$ is based on the time-point of 10% calcium transient amplitude in every individual cell. Colour bar in (A) was generated based on the RGB values in order to resemble (B). 190

Figure 8.7: (A) CV map based on the visualized 3D networks of the 52 hpf zebrafish heart in [46]. (B) Descriptive statistics of CVs of the 52 hpf zebrafish heart in [46] in regions corresponding to atrium (blue), AC band (grey), and ventricle (orange). (The number “8” was added manually) (C) CV map of the 52 hpf zebrafish heart model based on the 8 neighbours’ method. (D) Box plot of CVs produced by model in regions corresponding to atrium (blue), AC band (grey), and ventricle (orange). 192

Figure 8.8: A typical example of 8 neighbour cells in blue of the cell in green in 52 hpf zebrafish heart model. 192

Figure 8.9: Boxplot and the corresponding probability density function of a normal $N(0,1\sigma 2)$ population from [164]. 195

Figure 8.10: (A) Boundaries in the sinoatrial region in 52 hpf zebrafish heart model in blue where stimulation current was applied. (B) Stimulation current versus time....... 196

Figure 8.11: Activation time map of the modified 52 hpf zebrafish heart model 198

Figure 8.12: (A) CV map of the modified 52 hpf zebrafish heart model based on 8 neighbours’ method. (B) Box plot of CVs produced by model in regions corresponding to atrium (blue), AC band (grey), and ventricle (orange). (C) CV map based on the visualized 3D networks of the 52 hpf zebrafish heart in [46]. (D) Descriptive statistics of CVs in [46] in regions corresponding to atrium (blue), AC band (grey), and ventricle (orange). (The number “8” was added manually) 198

Figure 8.13: (A) 8 neighbours (blue) of the target cell (green) in 52 hpf zebrafish heart model found by the 8 neighbours’ method; (B) the actual 8 neighbours (blue) of the target cell (green). 199

Figure 8.14:A typical example of 4 neighbours (blue) of the target cell (green) in the 52 hpf zebrafish heart model. 200

Figure 8.15: (A) CV map of the modified 52 hpf zebrafish heart model based on the 4 neighbours' method. (B) Box plot of CVs produced by model in regions corresponding to atrium (blue), AC band (grey), and ventricle (orange). (C) CV map based on the visualized 3D networks of the 52 hpf zebrafish heart in [46]. (D) Descriptive statistics of CVs in [46] in regions corresponding to atrium (blue), AC band (grey), and ventricle (orange). (The number "8" was added manually) 201

Figure 9.1: (A) cross-sectional view of the larval zebrafish heart at 3-5 dpf from [80] (B) heart in developing larval zebrafish heart from [79] with the endocardial and myocardial membranes labelled in red and green, respectively. Arrowheads show the trabecular cardiomyocytes. 207

Figure 9.2: (A) Computational set-up of modelling the mechanical and hydrodynamics in a 48 hpf zebrafish heart for a given time point: red points, source points; black points, collocation points (wall points); vectors, velocity boundary conditions. (B–D) Computed instantaneous velocity field (vectors) and wall shear stress (colour coded) at three different time points during the atrial contraction.[167] 209

List of tables

Table 2.1: Constants in the Hodgkin-Huxley model 16

Table 2.2: Meanings of symbols in the equivalent circuit model of an axon according to the cable theory in Figure 2.4 20

Table 3.1: Parameters used in the Rogers-McCulloch version of Fitzhugh-Nagumo equations from [42] 44

Table 4.1: Parameters of the FHN model used in the previous larval zebrafish heart model for ventricle [36] 54

Table 4.2: The key AP parameters produced by the single larval zebrafish ventricular myocyte model using the same FHN parameters as the previous larval zebrafish heart model [36] comparing with the results of the previous larval zebrafish heart model and experimental results of 48 hpf and 72 hpf zebrafish found in literature. 63

Table 4.3: Comparison of parameters of the FHN model used in the single myocyte model and the previous larval zebrafish heart model for ventricle [36]. 71

Table 4.4: The key AP parameters produced by the single myocyte model of 48 hpf zebrafish and 72 hpf zebrafish comparing with experimental results of 48 hpf and 72 hpf zebrafish found in the literature. 72

Table 4.5: Parameters of the FHN model used in the single human ventricular myocyte 75

Table 4.6: Initial values of the gate variables used in the LR model in the single human myocyte model from [115] 80

Table 4.7: The key AP parameters produced by the single human myocyte model using the FHN model and the LR model using the same stimulation current at $80\ \mu A/cm2$ in

maximum comparing with the model AP produced by the LR model in standard settings (extracellular potassium concentration $Ko = 5.4\ mM$) and the measured human results. 82

Table 4.8: Mesh and computation information of the single human ventricular myocyte models using the FHN model and the LR model 84

Table 5.1: Comparison of the model geometry of the LZVF and the HVF models with the literature (z for the LZVF model and h for the HVF model) 91

Table 5.2: Electrical parameters used in the LZVF and the HVF models (z for zebrafish, h for human and [a] is for the fitted values). 92

Table 5.3: Parameters of the FHN model used in the LZVF1, the LZVF2 and the HVF models 93

Table 5.4: Initial conditions in the LZVF and the HVF models 93

Table 5.5: Mesh and computation information using COMSOL 94

Table 5.6: The key AP parameters produced by the LZVF and the HVF models compared with the measured APs in literature. In addition, the targeted experimental CV values are shown to compare to those achieved in the models 98

Table 5.7: Gap junction information in the LZVF and HVF models (z for zebrafish, h for human and h* are derived values from the literature by applying the same method as the model values) 101

Table 5.8: Investigation of the effect of extracellular space size on CV and maximum absolute extracellular potential in the HVF model. 110

Table 5.9: Investigation of effects of extracellular space size on CV and maximum absolute extracellular potential in the LZVF1 model. 112

Table 6.1: Varying gap junction resistivities in the cubic cell array model 127

Table 6.2: Varying the internal extracellular spaces in the polygonal cell array model compared with the cubic cell array model 130

Table 6.3: GJ information and CVs of section 2 in cubic and polygonal cell array models 133

Table 6.4: Gap junction information and CVs of section 2 in longitudinal line in cubic and polygonal cell cylinder models 138

Table 7.1: Electrical parameters used in the 72 hpf zebrafish heart models................ 150

Table 7.2: Parameters of the ionic current model used for the different regions of the larval zebrafish heart compared with the parameters used in the LZVF1 model......... 151

Table 7.3: Initial conditions in the zebrafish heart model.. 151

Table 7.4: Comparison of activation time intervals and conduction velocities in different regions of heart between the model and values obtained from Figure 7.12 (B). 159

Table 7.5: Comparison of the ECG characteristics between the model and recorded results. 164

Table 7.6: Comparison of the ECG characteristics between the original model 2, the filtered model 2 and the recorded results. 167

Table 7.7: Gap junction resistance investigation in 72 hpf zebrafish heart model....... 168

Table 8.1: ECG characteristics comparison between the model 1 and two models using larger atrial gap junction resistivities Ra as shown in Figure 8.1(D-F)....................... 178

Table 8.2: Gap junction information of the larger Ra models comparing with the model 178

Table 8.3: ECG characteristics comparison between the model 1 and two models using larger AV gap junction resistivities Rav as shown in Figure 8.2 (D-F)..................... 180

Table 8.4: Gap junction information of the larger Rav models comparing with the model 1 180

Table 8.5: ECG characteristics comparison between the model 1 and two models using larger ventricular gap junction resistivities $Rven$ as shown in Figure 8.3 (D-F). 183

Table 8.6: Gap junction information of the larger $Rven$ models comparing with the model 1 184

Table 8.7: Geometrical comparison of the 72 hpf and 52 hpf zebrafish heart model with the literature (some of them were estimated from images). 186

Table 8.8: Gap junction information of the 52 hpf zebrafish model comparing with the 72 hpf zebrafish heart model 187

Table 8.9: Gap junction information of the modified 52 hpf zebrafish heart model comparing with the previous 52 hpf zebrafish heart model and 72 hpf zebrafish heart model 197

Table 9.1: Gap junction information comparison between different models in Chapter 5-8 205

Glossary of terms

Symbol/Abbreviation and units	Description
$\alpha_d, \alpha_f, \alpha_j, \alpha_h, \alpha_m, \alpha_n$	Transfer rate coefficients (Hodgkin-Huxley Model or Luo and Rudy model)
$\beta_d, \beta_f, \beta_j, \beta_h, \beta_m, \beta_n$	Transfer rate coefficients (Hodgkin-Huxley Model or Luo and Rudy model)
Θ	Conduction velocity [m/s]
σ	Conductivity [S/m or mS/cm]
σ_e, σ_i	Extracellular and intracellular conductivities[mS/cm]
τ_y	Time constant of gate y in Luo and Rudy model
AP	Action potential
APD	Action potential duration
AV	Atrioventricular
c_i, c_o	Intracellular and extracellular ion concentrations [mol/m^3]
c_m	Membrane capacitance per unit length of axon [$\mu\text{F}/cm$]
C_m	Membrane capacitance per unit area [$\mu\text{F}/cm^2$]
CV	Conduction velocity
dpf	Days post fertilisation
E_{Na}, E_K	The reversal potential of sodium and potassium
ECG	Electrocardiography, Electrocardiogram.

F	Faraday's constant $[9.649 \times 10^4\ C/mol]$
FHN	Fitzhugh-Nagumo equations
G_κ	Membrane conductance per unit area for κ ion $[mS/cm^2]$
G_{gap}	Gap junction conductance per unit area $[S/m^2]$
GJ	Gap junction
hpf	Hours post fertilisation
HVF	Human ventricular fibre
I_i	Total longitudinal intracellular current [μA]
I_o	Total longitudinal extracellular current [μA]
i_m	Total transmembrane current per unit length of axon [μA/cm] (in radial direction)
I_{stim}	Stimulation current [μA$/cm^2$]
$I_{stimmax}$	Maximum stimulation current [μA$/cm^2$]
I_m	transmembrane current per unit membrane area
I_{ion}	Ionic current
I_v	Current source per unit volume
in vivo/in situ/in vitro	Whole biological systems/in situation where phenomenon occurs/cell cultures
LR model	Luo and Rudy model (ionic current model)
LZVF	Larval zebrafish ventricular fibre
MUV	Maximum upstroke velocity $[V/s]$
$\boldsymbol{n}$	Normal vector

r_i	Intracellular axial resistance of the intracellular space per unit length of axon $[k\Omega/cm]$
r_o	Extracellular axial resistance of the extracellular space per unit length of axon $[k\Omega/cm]$
r_m	Membrane resistance times unit length of axon $[k\Omega \cdot cm]$ (not that this is in the radial direction which accounts for its dimensions)
T	Temperature
R	Universal gas constant $[8.314\, J/(mol \cdot K)]$
T_{stim}	Stimulation current duration $[ms]$
∇	Spatial Derivative
T	Temperature
U	Recovery variable in FHN model
V_i	Intracellular electric potential
V_e	Extracellular electric potential
V_m	Transmembrane potential, the potential difference between the inside and outside of the cell membrane $(V_i - V_e)$
V_R	Reversal voltage
V_r	Resting potential
V'	Deviation of the membrane voltage from the resting state [mV](= $V_m - V_r$)
P_k, P_{Na}, P_{Cl}, P_{Ca}	the permeability of potassium, sodium, chloride and calcium ions

z_k	Valence of k ion
$[K]_i$, $[K]_o$	Intracellular and extracellular potassium concentration in Luo and Rudy model [mM]
$[Ca]_i$	Initial intracellular calcium concentration
$\overline{G_{Na}}$, $\overline{G_K}$	Maximum conductance of the sodium and potassium channels in Luo and Rudy model $[mS/cm^2]$
$\mathrm{k}, \mathrm{c}_1, c_2, A, B, a, b, d, e$	Parameters in the FHN model

1.INTRODUCTION

The thesis introduces the development of a novel larval zebrafish heart model to simulate the action potential (AP) propagation based on the cellular nature of cardiac tissue. This model also simulates the electrocardiogram (ECG) and is compared with measured ECGs in the larval zebrafish heart. This chapter starts with the motivation of this project followed by a brief overview of each chapter.

1.1 Motivation

Cardiovascular disease is currently the largest cause of death globally and results in 17.3 million deaths per year, this number is expected to grow to more than 23.6 million by 2030 [1]. In order to investigate these cardiovascular diseases, such as arrhythmia and cardiomyopathy, the zebrafish, a tropical teleost fish, has been recently used to develop a vertebrate model organism with which to study human cardiac electrophysiology and heart development [2].

Although zebrafish have a simple two-chamber heart, many electrophysiological characteristics of zebrafish are similar to humans. Unlike the other animal models with high heart rate, such as rats at 330 to 480 beats/min [3], the heart rate of zebrafish is about 110–130 beats/min [4, 5] which is close to the human heart rate (60–100 beats/min at rest). The AP morphologies of zebrafish also resemble a human's better in both shape and duration when compared with the mouse [6]. Similar to human APs, the zebrafish ventricular APs have a long plateau phase and atrial APs have a relatively shorter plateau phase [7, 8].

The propagation of APs in the zebrafish heart is also similar to a human's, and gives a similar ECG recording, with a distinct P-wave, QRS-complex, and T-wave [9]. Especially due to the zebrafish AP having a long plateau phase, the QT interval of zebrafish is distinct at about

$200 - 290\ ms$ [9] which is close to $300 - 450\ ms$ in human ECG, comparing with the mouse QT interval at about $83 - 96\ ms$ [10].

The ionic current function and molecular composition of ion channels in zebrafish are also similar to humans in many aspects. The fundamental ionic currents in human atrial and ventricular myocytes such as the sodium current I_{Na}, the calcium current I_{Ca} and potassium current I_K also exist in zebrafish myocytes [11]. In addition, the major repolarizing currents I_{K1} and I_{Kr} are presented in both hearts. At a genetic level, orthologs of all major ion channels in the human are also present in zebrafish, such as the Ca^{2+} channel Cav1.2 [12] and the K^+ channels ERG[13].

Behind all the similar cardiac physiological properties, the zebrafish is a vertebrate which implies similarities to humans in genetic aspects. Comparison between the human reference genome with the zebrafish genome shows that there are about 70% of human genes having at least one zebrafish orthologue [14]. Since the gene is amendable, zebrafish is widely used as a vertebrate genetic model system to identify factors regulating organogenesis, complex disease, and other vertebrate processes [15]. It also paves a way to link the functional information with specific genes by applying various gene manipulation methods such as the forward genetic screens, and transient gene knockdowns using Morpholino (MO) antisense oligonucleotides [16]. A large number of zebrafish models are created to model various human diseases especially the cardiovascular diseases such as arrhythmia and cardiomyopathy [17]. For example, a zebrafish model has been developed using the ENU mutagenesis method to recapitulate type 2 long QT syndrome. The mutant fish with gene defects in the KCNH2 gene, called *breakdance*, exhibits symptoms similar to humans, in that ventricular action potential duration (APD) is prolonged, resulting in longer QT interval and 2:1 AV block is discovered [13]. Subsequently this mutant fish *breakdance* can be effectively treated by two compounds;

flurandrenolide and the novel compound *2-MMB*, which act by shortening the ventricular APD [18]. Another zebrafish mutation discovered in a large-scale genetic screen exhibits poorly contractile [19]. It has been shown that this mutation attributed to an alternatively spliced exon of the gene ttn which causes blockage of the sarcomere assembly and results in disorders resembling human idiopathic dilated cardiomyopathy [20]. These zebrafish models enable the study of human diseases in-depth, and potentially aid in identifying new compounds with therapeutic potential [17, 21].

As a freshwater teleost, many technical advantages of zebrafish are established. Given the transparency of zebrafish during the early development stage, internals of the fish can be observed directly, making it easy to monitor the functional heart and assess the heart rate [22]. Zebrafish embryos and hearts do not require an intact blood circulation for proper functioning, as long as sufficient nutrients are provided. Hence both *in vivo* or *ex vivo* studies can be conducted easily [23]. Zebrafish are also cost-efficient in terms of developing into a genetic, pharmacological and toxicological high throughput system because of the small size, ease of maintenance and housing, large offspring size, rapid maturation and less stringent bioethical limitations [21, 24, 25].

ECG is one of the most useful tools to study cardiac electrical activities of the heart and assess cardiac dysfunction and diseases. It is measured by attaching a sensor to the surface of the body to record the electrical signals generated by the beating heart. This technique has been widely used in humans and is well developed and understood. Recently it is developed for zebrafish and has been applied to adult zebrafish and larval zebrafish at different developmental stages[2, 26, 27]. As the effects of various drugs on zebrafish are comparable to those of humans, larval zebrafish have been used in screening for various chemical agents [28]. Because zebrafish ECGs are similar to the humans, with other technical advantages stated, larval zebrafish is found to be a suitable model for developing a high throughput screening system which has a potential to accelerate the drug discovery process [29]. Currently, there are several high-throughput screening systems of larval zebrafish that have been developed which can measure heart rates [30, 31].

Computational models of the electrical activity in the larval zebrafish heart have the potential to aid understanding of experimental observations and allow cardiac defects to be modelled in order to investigate their effects on the ECGs. Previous models have mainly focused on the human heart. Simulations of the heart range in scale from a single cell [32], a piece of cardiac tissue [33], a region of heart [34] to the whole heart [35]. For comparison, there are very limited models for zebrafish heart. However, recently a larval zebrafish heart model has been developed to simulate ECGs [36]. The bidomain model [37] was applied to this model which describes the cardiac tissues using a continuum approach, where the tissue parameters were captured and intracellular and extracellular conductivities defined for the whole domain of the cardiac tissue. Intracellular and extracellular potentials were also defined over the whole domain of cardiac tissue with ionic membrane currents relating them at each point. The conductivities used in the bidomain model are the mean values, calculated by fitting the conduction velocity in the model with the measured values, and these conductivities include both the cellular conductivity and the conductance of the gap junctions. Although this model was able to simulate zebrafish cardiac activity which was consistent with experimental observations, in order to achieve the realistic measured CVs in the larval zebrafish heart, the fitted conductivities values are about one hundred thousand times smaller than the measured conductivities of the human heart [36]. This difference is significant when compared with bidomain models of human cardiac tissue, where the measured conductivities are within a factor of 10 of the model conductivities [38]. It shows that this continuum approach is applicable to the human cardiac tissue, where the cardiomyocytes are much smaller than the size of the heart. However, for the zebrafish embryo heart which consists of around three hundred cells [39], it is less appropriate as it ignores the role of gap junctions and the cellular structure of cardiac tissue in cardiac electrodynamics.

In reality, the propagation of APs in the heart is discontinuous due to the cellular nature of cardiac tissue which is firstly proved by Spach [40] in 1952. The conduction between cardiac cells is modulated by gap junctions, which are a collection of channels allowing the exchange of ions within the intracellular space. The gap junctions are low-resistance pathways because their resistances are lower than the resistance of two membranes butted together, but it is much higher than the intracellular resistance [41]. In this thesis, a hypothesis has been made which is the large difference of CVs between human and zebrafish heart is because of the large differences of gap junctions between them. Therefore, instead of using the bidomain model, a more realistic model of larval zebrafish heart is developed which simulates the discontinuous AP propagation because of the effect of gap junctions at the cellular level. The ECGs produced by this model has also been compared to recorded ECGs. In order to study the mechanism of some cardiovascular diseases, this model was modified to simulate some cardiac conditions such as the atrioventricular (AV) block. The model introduced here is the first cell-based whole heart model for larval zebrafish which incorporates the cellular features of cardiac tissue into modelling cardiac electrodynamics. In order to validate the models described in this thesis, careful comparisons have been made against the measured/ recorded parameters such as APs, CVs, and ECGs when available. It is expected that most of results produced by the model should resemble the measured values as close as possible achieving a resemblance of 90%, such as, AP parameters and CVs. For the model ECGs, as shown in the previous zebrafish heart model [36], it has poor resemblance to the recorded ECGs due to experiments conditions etc. Therefore, in this thesis, a lower resemblance is also acceptable but the overall shapes of model ECGs (upward/downward peaks) should match the recorded ECGs.

1.2 Overview

In order to understand the electrical activities that modulate and maintain the normal functionalities in the larval zebrafish and human heart, in Chapter 2, the basis of cardiac electrophysiology is described including the origins of electrical signals at the cell membrane which results in APs and the AP propagation between cells. The classical cable theory is then described using a simple example of AP propagation in a straight axon. It follows with a comparison of the anatomy of the larval zebrafish heart and human heart. It includes an introduction of cellular structure of cardiac tissue and how it affects the AP propagation in the heart. Then the anatomical and functional differences of larval zebrafish heart at different development stages are described. At last, the ECG is introduced starting from its generation following with how it is measured in the larval zebrafish and human, and a brief introduction of typical human and larval zebrafish ECGs. After that, the ECGs measured in a common cardiac disorder: AV block are described.

In Chapter 3, it introduces the common modelling methods used for simulating the electrical activities at tissue level or in the whole heart. It starts with the torso model which describes the electrical potential distribution in the area around the heart. Then, the cardiac tissue models are introduced which simulate the cardiac propagation and the cellular electrical activities (AP). At last, a brief introduction of the finite element method (FEM) is given following by how the software COMSOL Multiphysics, based on the FEM, is used in the implementation of the models described in this thesis.

Chapter 4 is the first results chapter. It described the initial stage of the development of a larval zebrafish heart which is the development of a single myocyte model. A ventricular myocyte in the 48-72 hours post fertilisation (hpf) larval zebrafish was chosen to simulate. In this model, the intracellular and extracellular spaces are treated separately with the ionic current model applying to the membrane boundaries. No boundary condition of gap junctions was used in this model. A single human ventricular myocyte model was developed for the validity of the ionic current model used in the larval zebrafish model. Two different types of ionic current models were applied to this human myocyte model. One is a FitzHugh Nagumo (FHN) type model [42], the same as the zebrafish myocyte model. The other ionic current model is the Luo and Rudy (LR) model [43] which is a more realistic model, based on the currents of different ions on the cell membrane. At last, the APs produced by both models are compared with the measured results in the literature.

In Chapter 5, the single myocyte models described in Chapter 4 are expanded to cardiac fibre models which simulate the AP propagation in a unidirectional direction. Two larval zebrafish ventricular fibre (LZVF) models are implemented for the zebrafish in two different development stages. Then a human ventricular fibre (HVF) model is implemented for the validity of the LZVF models. The FitzHugh Nagumo (FHN) type model is chosen to use in both zebrafish and human models. Similar electrical models as the single myocyte models were used with adding the boundary conditions of gap junctions between the neighbouring myocytes. The LZVF models simulate discontinuous cardiac propagation and reproduce the measured CVs in the 48 hpf and 72 hpf zebrafish heart by adjusting the gap junction resistivity. Whist the HVF model reproduces the measured CVs in the human heart with all of the parameters determined by the published electrophysiological properties of human cardiac tissue. In order to compare the gap junction resistivity used in the LZVF model to the HVF model, the total resistance of gap junctions per myocyte is determined by the gap junction resistivity and the total gap junction area per myocyte and compared with measured results found in literature.

In Chapter 6, the LZVF models described in Chapter 5 are expanded to larval zebrafish cardiac tissue models which simulate the more complex multidirectional cardiac propagation. The effects of factors such as cell morphology, extracellular spaces, and the number of gap junctions and their spatial distribution on the conduction velocity are investigated using two model geometries: a cell array and a cell cylinder. The cell array models simulate the cardiac propagation on a flat pad in 2 dimensions and the cell cylinder models simulated the propagation in 3 dimensions. This chapter describes the preparatory works for the development of the whole larval zebrafish heart model.

In Chapter 7, the development of a larval zebrafish whole heart model is described. A 72 hpf zebrafish is chosen to simulate here because of the availability of measured ECGs. The model geometry is developed based on the microscopy images of larval zebrafish and a previous larval zebrafish heart model [36]. The electrical model used is similar to the models in Chapter 5 and 6. Different gap junction resistivities are used for different regions of the heart in this model to reproduced the measured CVs found in the literature. This model successfully reproduces the cardiac propagation in the real larval zebrafish heart and simulate the ECGs resembling the recorded ECGs. It has been found that after filtering the model ECGs using the same low pass filter used in the recordings, the model ECGs resemble the recorded ECG much better than the unfiltered ones.

In Chapter 8, an application and an extension of the larval zebrafish heart model in Chapter 7are described. First, the larval zebrafish heart model was modified to apply to simulate a common cardiac disorder: gap junction remodelling which has been found in some cardiac conditions such as cardiac ischaemia [44] and the congestive heart failure [45]. Second, the original heart model was modified to be a 52 hpf zebrafish heart model which reproduced the measured results including the activation time and CVs reported in [46].

Chapter 9 is the final chapter which summarised the major achievements of this thesis. It follows with the limitations of this work and possible improvements and extensions that could be done in the future.

Note that the results chapters in this thesis were described by following a logical order which starts from single myocyte models, then the ventricular fibre models, cardiac tissue models and finally the heart model. However in the process of the research, the development of the single myocyte models failed at the beginning because the wrong physical interfaces in COMSOL have been used. With the help of the technical support team of COMSOL, the ventricular fibre models have been implemented successfully at first. Therefore, the researches actually start with the ventricular fibre models described in Chapter 5. Then the whole heart models in Chapter 7 and 8 have been implemented and investigated. After that, the single myocyte models and the cardiac tissue models described in Chapter 3 and 6 were developed and investigated.

2. CARDIAC ELECTROPHYSIOLOGY AND THE HEART

This chapter has three sections. The first section is the basic cardiac electrophysiology which is concerned with the electrical activity of cardiac cells. The cardiac cell is a type of muscle cell which is similar to the nerve cell. They are excitable cells which means they are able to produce electrical impulses if a suitable stimulus is applied. The origin of this electrical activity in an excitable cell is described here, including both resting state and active state. The chapter follows with the cable equations which are used to describe the propagation of the electrical impulses in an axon (nerve cell). In the second section, the electrical activity in the whole heart is described with a brief review of the anatomical and physiological basis of both human and larval zebrafish heart. In the third section, the ECG is introduced starting with the basic mechanism of its generation. A simple example of the depolarisation and repolarisation in a cardiac fibre is then explained. Both human and zebrafish ECGs are introduced along with the measurement methods used. Finally, how ECGs are applied for diagnosis is described following with the ECGs measured in a common cardiac disorder: atrioventricular block (AV block). The AV block is chosen to introduce because this disorder has been simulated using the larval zebrafish heart model introduced in Chapter 8.

2.1 Cardiac electrophysiology

All cells in the body exhibit a potential difference across the cell membrane. But only the excitable cells are able to manipulate this potential difference to produce an electrical impulse in order to communicate with other cells. The electrical impulse is called an AP which is generated because of the exchanges of free charge ions such as sodium (Na^+), potassium (K^+), chloride (Cl^-) and calcium (Ca^{2+}) through the membrane via ion channels. In the heart, the APs can propagate to other neighbouring cells which initiate and maintain the rhythmic contraction of the heart. First, the cellular electrophysiology for general excitable cells is described. Most of the contents are adapted from [37] unless specified.

2.1.1 Cellular electrophysiology

The potential difference shown between the membranes of an excitable cell is the transmembrane potential and is defined as

$$V_m = V_i - V_e \tag{2.1}$$

where V_i is the intracellular potential and V_e is the extracellular potential. The membrane plays an important role in establishing the resting or active states of the excitable cells by regulating the movements of ions between the extracellular and intracellular spaces through specialized ion channels. The membrane permeability quantifies the ease of an ion to cross the membrane. Different ion species have different membrane permeability. The permeability of different ions varies during the activation which regulates the concentration of ions between the membranes and then reflects on the variation of transmembrane potential. The changes in transmembrane potential can be triggered by applying a stimulus. If the stimulus is high enough, resulting the transmembrane potential reaching the threshold potential, then the cell will be activated exhibiting an AP. If the stimulus is insufficient, then the membrane will not activate. With no stimulation, the cell will be in its resting state and its transmembrane potential will remain in a constant value.

2.2.1.1 Resting state

The transmembrane potential stays the same in the resting state which is because the cell membrane regulates the movement of ions between the intracellular and extracellular spaces. It is found that concentrations of each ion on either side of the membrane have a large difference. This is because of the differing membrane permeability to different ions. This generates a concentration gradient for all permeable ions between the membranes. As a result, the ions tend to move from the region of high concentration to the region of low concentration via diffusion. An electric field is established across the cell membrane because of this. This field exerts forces on the ions which carry the charges crossing the membrane. An equilibrium is achieved when the diffusion forces balance the force of the electrical field.

The equilibrium voltage is the transmembrane potential achieved at equilibrium which is derived by Nernst [37] known as the Nernst equation. It describes the equilibrium voltage V_k across the membrane for the k^{th} ion as

$$V_k = V_i - V_e = -\frac{RT}{z_k F} ln \frac{c_{i,k}}{c_{o,k}} \tag{2.2}$$

where R is gas constant, T is absolute temperature, z_k is the valence of the k^{th} ion, and F is Faraday's constant. $c_{i,k}$ and $c_{o,k}$ are the intracellular and extracellular concentration of the k^{th} ion respectively.

However in reality, the cell membrane is not only permeable to one type of ions. There are several permeable ions and the flux of each is independent of the others. The transmembrane potential is based on multiple ions and is described by the Goldman-Hodgkin-Katz equations which is:

$$V_m = \frac{RT}{F} ln \frac{P_k c_{i,k} + P_{Na} c_{i,Na} + P_{Cl} c_{i,Cl} + P_{Ca} c_{i,Ca}}{P_k c_{o,k} + P_{Na} c_{o,Na} + P_{Cl} c_{o,Cl} + P_{Ca} c_{o,Ca}} \tag{2.3}$$

where P_k, P_{Na}, P_{Cl}, P_{Ca} are the permeability of potassium, sodium, chloride and calcium ions respectively. $c_{i,k}$, $c_{i,Na}$, $c_{i,Cl}$ and $c_{i,Ca}$ are the concentrations of potassium, sodium, chlorine and calcium ions in intracellular spaces respectively while $c_{o,k}$, $c_{o,Na}$, $c_{o,Cl}$ and $c_{o,Ca}$ are the concentrations of potassium, sodium, chlorine and calcium ions in extracellular spaces. Based on the experimental results of the cell at the resting state, the transmembrane potential can be calculated which is known as the resting potential.

2.2.1.2 Active state

An excitable cell at the resting state can turn to an active state by the application of a strong enough stimulus which results in the transmembrane potential increase to a value higher than the threshold potential. In the activation process, the membrane permeability of different ions changes because of the higher transmembrane potential. At the same transmembrane potential, the variations of the permeabilities for different ions are different which are modulated by the voltage sensitive proteins in the ion channels. Therefore different amount of ions move differently across the membrane which results in further changes of transmembrane potential which exhibits as an AP. Note that if the stimulus is not strong enough, the cell won't be activated.

A mathematical model to describe the AP of the giant squid axon was introduced by Hodgkin and Huxley in 1952 [47]. This is the first model which incorporates the properties of multiple ionic channels on the excitable cell membranes. The model was developed based on an experimental method called the voltage clamp which measures the ion currents through the membranes of excitable cells while holding the transmembrane potential at prescribed values. In the Hodgkin and Huxley model, the electric current flowing across the cell membrane during the activation, the transmembrane current, consists of four current components which are the sodium current, potassium current, the current carried by other ions (leakage current) and capacitive current. It writes as

$$I_m = G_{Na}(V_m - V_{Na}) + G_K(V_m - V_K) + G_L(V_m - V_L) + C_m \frac{dV_m}{dt} \tag{2.4}$$

where I_m is the transmembrane current per unit area $[mA/cm^2]$, G_{Na}, G_K and G_L are the sodium, potassium and leakage conductance per unit area $[S/cm^2]$, V_{Na}, V_K and V_L are Nernst voltage for sodium, potassium and leakage ions $[mV]$, C_m is the membrane capacitance per unit area $[\mu F/cm^2]$.

As measured by the voltage clamp method, the potassium and sodium conductances vary in time using different clamp voltages as shown in Figure 2.1.

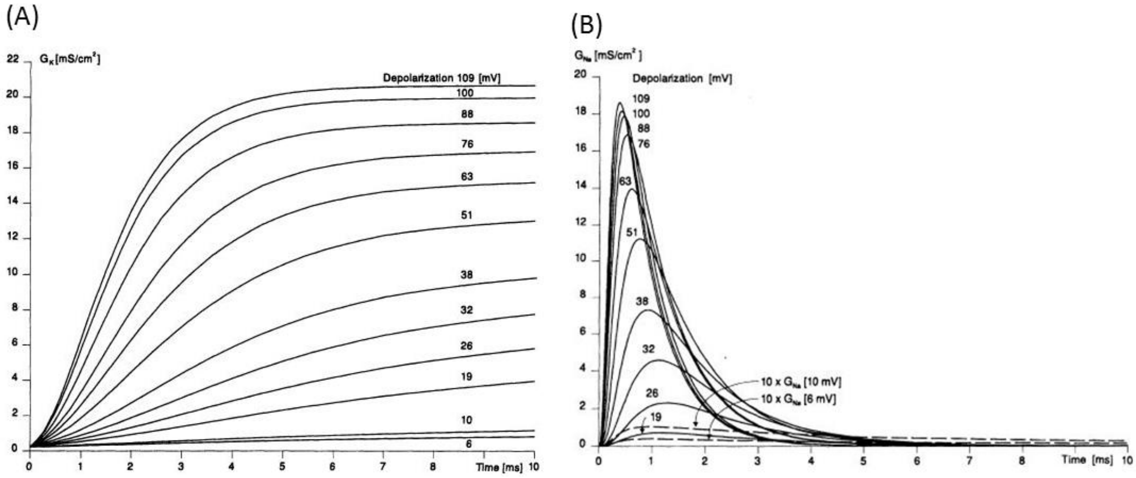

Figure 2.1: (A) Potassium conductance and (B) Sodium conductance versus time in a voltage clamp experiment. The clamp voltage is expressed as a change from the resting potential.

Taking the potassium conductance as an example, as the potassium ions can only cross the membrane through potassium ion channels, it supposes that the opening and closing of the specific ion current channels are controlled by electrically charged particles called n-particles. The n-particles could be in an open position, or in a closed position and in moving from one state to another. If the probability of an n-particle in the open position is n, the probability in the close position is $1 - n$, where $0 \leq n \leq 1$. The voltage- and time-dependent transitions of the n-particles between the open and the closed positions are described by the changes in the parameter n with the voltage-dependent transfer rate coefficients α_n and β_n. A first-order reaction is described as

$$n \underset{\beta_n}{\overset{\alpha_n}{\leftrightarrows}} (1 - n) \tag{2.5}$$

where α_n is the transfer rate coefficient for n-particles from the closed to open state, β_n is the transfer rate coefficient for n-particles from the open to the closed state, n is the fraction of n-particles in the open state and $1 - n$ is the fraction of n-particles in the closed state.

The probability n can be calculated by solving:

$$\frac{dn}{dt} = \alpha_n(1-n) - \beta_n n \tag{2.6}$$

If the initial value of the probability n is known. Then it is assumed that the potassium channel will be open only if four n-particles exist in the open position within a certain region. In addition, the probability of any one of the four n-particles being in the open position does not depend on the positions of the other three. Therefore, the probability of the channel being open is proportional to n^4. The potassium conductance per unit area is given by the conductance of a single channel multiply the number of open channels. If the conductance $G_{k_{max}}$ is the maximum conductance when all channels are open. Therefore, the potassium conductance is

$$G_K = G_{K_{max}} n^4 \tag{2.7}$$

where $G_{K_{max}}$ is the maximum value of potassium conductance $[mS/cm^2]$, and n is derived by equation (2.6).

Similarly, the sodium conductance is derived based on two particles: the m-particle and the h-particle which is finally given by:

$$G_{Na} = G_{Na_{max}} m^3 h \tag{2.8}$$

The transfer rate coefficients are:

$$\alpha_n = \frac{0.01 \cdot (10 - V')}{e^{(10-V')/10} - 1} \tag{2.9}$$

$$\beta_n = \frac{0.125}{e^{V'/80}} \tag{2.10}$$

$$\alpha_m = \frac{0.1 \cdot (25 - V')}{e^{(25-V')/10} - 1} \tag{2.11}$$

$$\beta_m = \frac{4}{e^{V'/80}} \tag{2.12}$$

$$\alpha_h = \frac{0.07}{e^{V')/20}} \tag{2.13}$$

$$\beta_h = \frac{1}{e^{(30-V')/10} + 1} \tag{2.14}$$

$$V' = V_m - V_r \tag{2.15}$$

where V_r is the resting potential.

Constants in the Hodgkin-Huxley model are shown in Table 2.1.

Table 2.1: Constants in the Hodgkin-Huxley model

Constants in Hodgkin-Huxley model	Values
Membrane capacitance per unit area C_m	$1\ \mu F/cm^2$
Maximum value of potassium conductance $G_{K_{max}}$	$36\ mS/cm^2$
Maximum value of sodium conductance $G_{Na_{max}}$	$120\ mS/cm^2$
Conductance of leakage current G_L	$0.3\ mS/cm^2$
$V_r - V_{Na}$	$-115\ mV$
$V_r - V_K$	$12\ mV$
$V_r - V_{Na}$	$-10.61\ mV$

The AP produced by the Hodgkin-Huxley model is shown in Figure 2.2 along with the variation of sodium and potassium conductance during the AP. The AP can be classified into five phases: the rising phase, the peak phase, the falling phase, the undershoot phase and the refractory period. The membrane starts to depolarize during the rising phase. The transmembrane potential reaches the maximum value at the peak phase. After that, the transmembrane potential decreases towards the resting potential during the falling phase. Then it follows with the undershoot (afterhyperpolarisation) phase which the transmembrane potential decreases to a more negative value than the resting potential. Finally the transmembrane potential returns to the resting potential during the refractory period. In this period, another AP is impossible or hard to be triggered.

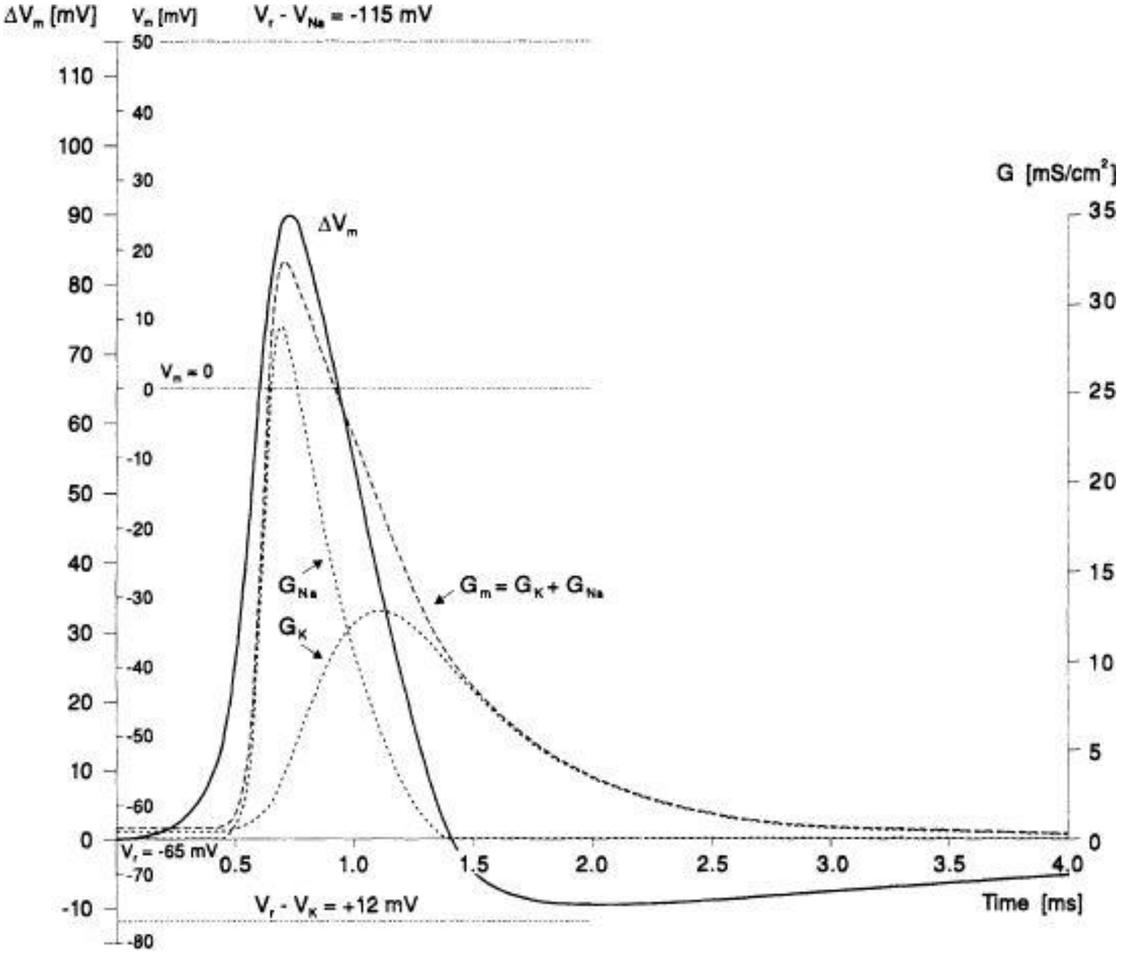

Figure 2.2: The transmembrane potential, the sodium and potassium conductance (G_K and G_{Na}) and their sum during an AP produced by the Hodgkin-Huxley model from [37].

The cardiac AP is different from the neuron AP mainly because it has a long plateau phase as shown in Figure 2.3. Similarly to the neuron AP, the APs of regular non-pacemaker cardiac cells has five phases:

Phase 0 is the depolarisation phase also known as the upstroke period of the AP. In this phase, a rapid and positive change in transmembrane potential V_m happens which is mainly because of the sodium ion channels. The sodium ion channels are activated (opened) because the injection of the stimulation rises the V_m reaching its threshold potential (Usually the threshold potential is $20\ mV$ higher than the resting potential). Therefore, the Na^+ ions move into the cell which rapidly increases the V_m further towards its maximum. However if the stimulation is not strong enough to make the V_m reach the threshold potential, the Na^+ channels will not be activated (opened) thus no AP will be produced. The maximum upstroke velocity, at which the voltage changes the fastest during phase 0, is an important parameter of AP which is found to be proportional to conduction velocity [48].

Phase 1 is the notch after the peak of the AP [49]. In this phase, the Na^+ channels are deactivated (closed) which slows up the movement of Na^+ ions into the cell. Meantime, K^+ channels open allowing a small flow of K^+ ions out of the cell which results in the V_m deceasing by a small amount.

Phase 2 is the plateau phase of the AP as the V_m almost remains constant. This is because the charges moving in and out of the cell are nearly balanced in this phase. Both K^+ channels and L-type Ca^{2+} channels are opened during this phase. The K^+ ions leave the cell through the K^+ channels while the Ca^{2+} ions move in the cell through Ca^{2+} channels. Meantime, the Cl^- channels open which allow Cl^- ions moving in the cell. The Ca^{2+} ions move into the cells which causes the calcium-induced calcium release from the sarcoplasmic reticulum, resulting in contraction.

Phase 3 is the repolarisation phase. During this phase, the Ca^{2+} channels close while the K^+ channels are still open. The K^+ ions continue moving out of the cell which leads to the reduction of V_m. Finally the V_m returns to the resting potential and the K^+ channels close.

Phase 4 is the period when the cell returns to the resting state known as diastolic. After an AP, for a short period of time, the channels cannot be opened regardless of the strength of the excitatory stimulus which is called the refractory period.

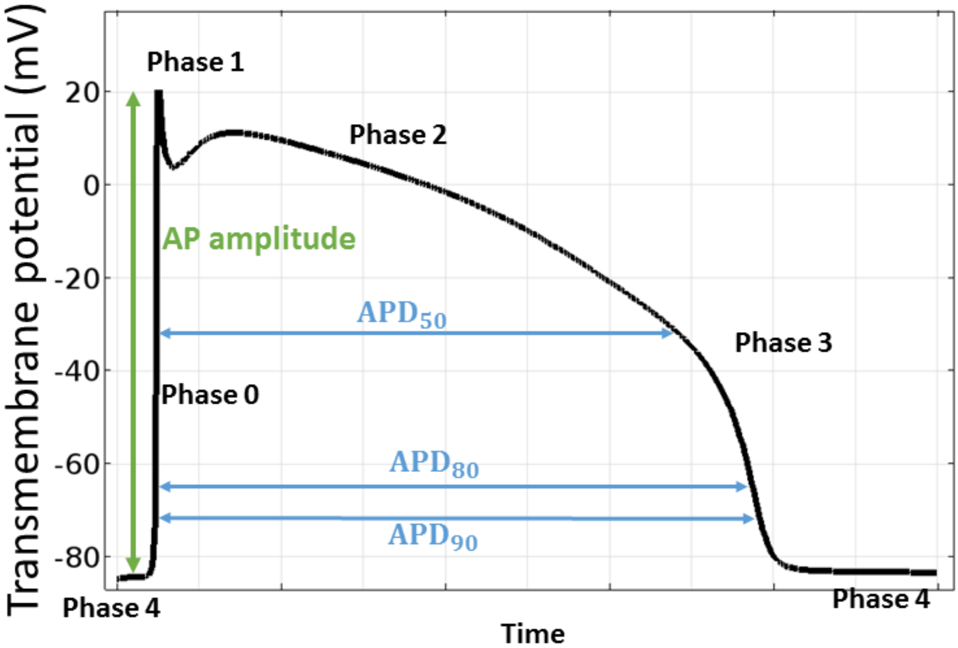

Figure 2.3: A typical AP of cardiac cell. The AP amplitude is shown in green and different APD are shown in blue.

The stimulation in the heart is started from a group of specialised cells which are known as the pacemaker cells. These cells are located in the sinoatrial region of the heart which can automatically generate APs. The AP produced by the pacemaker cell is different from the other cardiac cells described above. The pacemaker cell is never at rest. In phase 4, the V_m gradually increase until it reaches the threshold potential. Then it starts to activate. In addition, there is no plateau phase in the pacemaker APs.

The APs can be studied quantitatively by measuring serval key parameters including the resting potential, the maximum upstroke velocity, the peak of AP, the AP amplitude and the AP duration (APD) etc. As is shown in Figure 2.3, the AP amplitude is measured as the voltage difference between the resting potential and the peak. The APD is referred to the time difference between the repolarisation percentage of the AP. For example, APD_{90} is the time at 90% repolarization minus the time at 10% depolarisation. The percentage of depolarization/repolarization is calculated from the AP amplitude. The cardiac cells in both human and zebrafish heart exhibit different APs in different regions but all operate under the same basis as described above. This diversity of APs in the heart is because of the diverse cell types which are crucial to modulate and maintain the normal functionality of the heart.

2.2.2 Cable equations for an axon

Classical cable theory is an important mathematical model which describes the voltage and current flow in the neuronal structure. According to the cable theory, the electric activities in an axon can be described by the equivalent circuit shown in Figure 2.4. In the cable theory, the extracellular and intracellular spaces of the axon are assumed to be resistances. The cell membrane is assumed to be a resistance in parallel with capacitance. The meanings of the symbols used in the cable theory shown in Figure 2.4 are listed in Table 2.2.

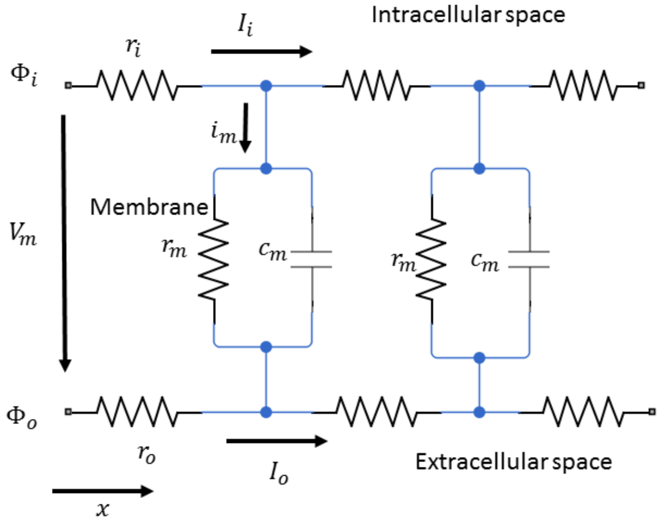

Figure 2.4: The equivalent circuit model of an axon according to the cable theory.

Table 2.2: Meanings of symbols in the equivalent circuit model of an axon according to the cable theory in Figure 2.4

r_i	Intracellular axial resistance of the intracellular space per unit length of axon $[k\Omega/cm]$
r_o	Extracellular axial resistance of the extracellular space per unit length of axon $[k\Omega/cm]$
r_m	Membrane resistance times unit length of axon $[k\Omega \cdot cm]$ (note that this is in the radial direction which accounts for its dimensions)
c_m	Membrane capacitance per unit length of axon $[\mu\mathrm{F}/cm]$
I_i	Total longitudinal intracellular current $[\mu\mathrm{A}]$
I_o	Total longitudinal extracellular current $[\mu\mathrm{A}]$
i_m	Total transmembrane current per unit length of axon $[\mu\mathrm{A}/\mathrm{cm}]$ (in the radial direction)

From Ohm's law, the relationships of currents and voltages in the circuit shown in Figure 2.4 are given by

$$\frac{\partial V_i}{\partial x} = -I_i r_i \tag{2.16}$$

$$\frac{\partial V_e}{\partial x} = -I_o r_o \tag{2.17}$$

According to the current conservation laws, the transmembrane current i_m is related to the loss of I_i or to the gain of I_o:

$$i_m = -\frac{\partial I_i}{\partial x} = -\frac{\partial I_o}{\partial x} \tag{2.18}$$

From the definition of the transmembrane potential:

$$\frac{\partial \mathrm{V}_m}{\partial x} = \frac{\partial V_i}{\partial x} - \frac{\partial V_e}{\partial x} = -I_i r_i + I_o r_o \tag{2.19}$$

By differentiating the above equation with respect to x:

$$\frac{\partial^2 \mathrm{V}_m}{\partial x^2} = -r_i \frac{\partial I_i}{\partial x} + r_o \frac{\partial I_o}{\partial x} \tag{2.20}$$

Substituting equation (2.18) into (2.20) gives:

$$\frac{\partial^2 \mathrm{V}_m}{\partial x^2} = (r_i + r_o) i_m \tag{2.21}$$

which is known as the general cable equation.

In an ideal axon with radius a, the membrane current per unit length is

$$i_m = 2\pi a I_m \tag{2.22}$$

where I_m is the membrane current per unit area in $\mu\mathrm{A}/cm^2$.

The intracellular resistance per unit length is

$$r_i = \frac{\rho_i}{\pi a^2} \tag{2.23}$$

where ρ_i is the intracellular resistivity in $k\Omega/cm$.

The resistance of the extracellular space per unit length, r_o, is usually omitted because it is so small when the extracellular space is extensive. Therefore,

$$I_m = \frac{i_m}{2\pi a} = \frac{1}{2\pi a (r_i + r_o)} \frac{\partial^2 \mathrm{V}_m}{\partial x^2} \cong \frac{1}{2\pi a r_i} \frac{\partial^2 \mathrm{V}_m}{\partial x^2} = \frac{\pi a^2}{2\pi a \rho_i} \frac{\partial^2 \mathrm{V}_m}{\partial x^2} = \frac{a}{2\rho_i} \frac{\partial^2 \mathrm{V}_m}{\partial x^2} \tag{2.24}$$

According to the Hodgkin-Huxley equation in equation (2.4), the transmembrane current can be written as:

$$\frac{a}{2\rho_i}\frac{\partial^2 \mathrm{V}_m}{\partial x^2} = G_{Na}(V_m - V_{Na}) + G_K(V_m - V_K) + G_L(V_m - V_L) + C_m\frac{dV_m}{dt} \tag{2.25}$$

Under the steady-state condition, the AP propagation is in a constant velocity. Thus it can be described by the wave equation:

$$\frac{\partial^2 \mathrm{V}_m}{\partial x^2} = \frac{1}{\Theta^2}\frac{\partial^2 \mathrm{V}_m}{\partial t^2} \tag{2.26}$$

where Θ is the conduction velocity in m/s.

Substituting equation (2.26) in equation (2.25) gives:

$$\frac{a}{2\rho_i\Theta^2}\frac{\partial^2 \mathrm{V}_m}{\partial t^2} = G_{Na}(V_m - V_{Na}) + G_K(V_m - V_K) + G_L(V_m - V_L) + C_m\frac{dV_m}{dt} \tag{2.27}$$

This is an ordinary differential equation which is feasible to solve. The conduction velocity can be written in the form:

$$\Theta = \sqrt{\frac{Ka}{2\rho_i}} \tag{2.28}$$

where K is a constant in $1/s$. It shows the conduction velocity is directly proportional to the square root of axon radius a which is supported by experimental results.

2.2 Heart anatomy and function

The heart is an important organ in the circulatory system which pumps blood through the blood vessels to distribute nutrients, oxygen, etc. to the body. Firstly, the human heart is introduced.

A schematic diagram of a human heart is shown in Figure 2.5 (A). The human heart consists of four chambers: the right atrium, the left atrium, the right ventricle and the left ventricle. The deoxygenated blood from the systemic circulation goes into the right atrium and then goes to right ventricle. Then the deoxygenated blood is ejected to the lungs. Oxygenated blood goes from the lungs to the left atrium first and then to the left ventricle. The movement of blood is controlled by the rhythmic contraction of these chambers. The contractions are regulated by cardiac conduction.

The electrical signals in the human heart originate in the sinus node (SA node) as shown in Figure 2.5 (A) because of the specialized muscle cells: pacemaker cells. As introduced before, these cells are self-excitatory and can automatically generate APs. The APs from the SA node propagate throughout the right atrium first and then to the left atrium. In a normal heart, the APs cannot propagate from the atriums directly to the ventricles but have to go through the AV node as shown in Figure 2.5 (A). From the AV node, the AP propagation goes through a network of specialized cells called the His-Purkinje fibre system. This network has a common bundle called the bundle of His. This bundle then separates into two bundle branches: the right and left bundle branches. More distally the bundles diverge to Purkinje fibres which are in the inner sides of the ventricular walls. Then the APs propagate through the ventricle from many activation sites in the inner sides of the ventricular walls. Note that the propagation is much slower in SA node and AV node than in the His-Purkinje fibre system and in the chambers.

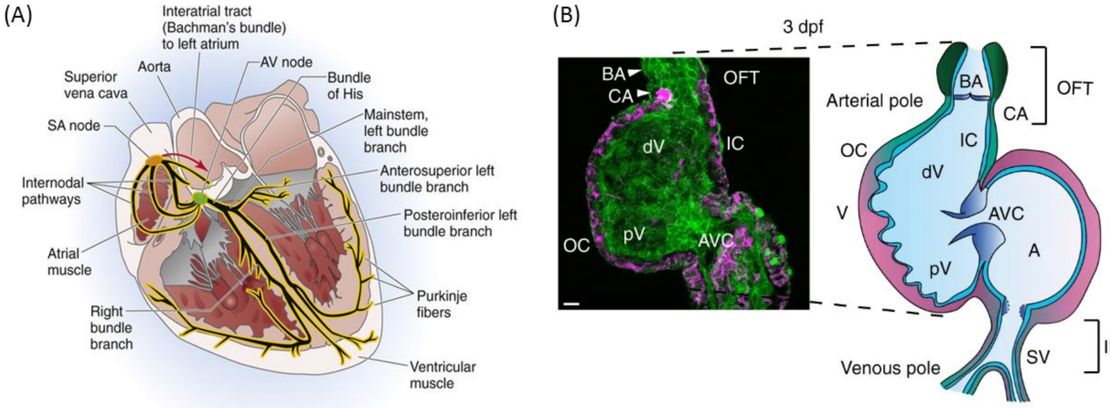

Figure 2.5: (A) Schematic anatomy of human heart including the conduction pathways [50]; (B) anatomy of a 3 dpf zebrafish heart [51]

A 3 days post fertilisation (dpf) zebrafish heart is shown in Figure 2.5 (B). Unlike the human heart, there are only two chambers in the larval zebrafish heart, atrium (A) and ventricle (V). Atrioventricular canal (AVC) is located between the atrium and the ventricle and in this region, the AP propagation is much slower than in the chambers which is similar to the AV node in the human heart.

The circulatory system of zebrafish is simpler than the humans. The blood first goes into the atrium from the inflow tract (IFT) as shown in Figure 2.5 (B). Then it goes through the ventricle and goes out through the outflow tracts (OFT). Just like the human heart, the blood movement is controlled by the contraction of chambers which is regulated by cardiac conduction.

The cardiac conduction system of larval zebrafish heart is also simpler than the humans. The initial APs start at the SA node located at the sinus venous (SV) near atrium and then propagate across the atrium. The propagation is delayed at the AVC and then propagate rapidly across the ventricle. Note that in the larval zebrafish stage before 4 weeks post-fertilization, the bulbus arteriosus (BA) has same characteristics as the cardiac muscle cell which is excitable and then it gradually transformed to smooth muscle [52]. Therefore, in the 3 dpf zebrafish heart, eventually the APs propagate from the ventricle to the BA.

2.2.1 Cellular structure of cardiac tissue

The wall of the heart is made up of cardiac muscle called myocardium. A typical histological picture of cardiac muscle is shown in Figure 2.6 (A). Just like the skeletal muscle, the cardiac muscle is striated. The dark areas crossing the cardiac muscle fibres in Figure 2.6 (A) are intercalated discs. Cardiac myocytes are connected by these, both mechanically and electrically. The electrical connections between cells are via the gap junctions, which are low-resistance channels allowing the exchange of ions within intracellular space. Note that gap junctions are characterized as low-resistance pathways because the gap junction resistance is lower than the resistance of two membranes butted together but it is much higher than the intracellular resistance [41].

Due to the existence of gap junctions, the propagation of AP in the heart is discontinuous which was not proven until 1952 by Spach [40]. After then, characteristics of gap junctions has been studied in details in genetics and at a biological level [53, 54]. As shown in Figure 2.6 (B), each gap junction channel are made up of two connexons (or hemichannels). Each connexon consists of six symmetrical integral membrane protein units called connexions. Connexin40 (Cx40), connexin43 (Cx43), and connexin45 (Cx45) are 3 main connexins regulating the functionality of myocytes in the mammalian heart[55]. Two connexins, Cx40 and Cx43 have been detected in the zebrafish larva heart [56, 57]. Previous research has also shown that the zebrafish genome contains orthologues to vertebrate connexins such as the mammalian Cx40 (zfCx45.6)[58], and Cx45 in chicken and mammals (Cx43.4) [59].

In human cardiac muscle, gap junctions are distributed in intercalated discs of the cardiomyocytes as shown in Figure 2.6 (A). They are mainly located on the surface perpendicular to the muscle fibre direction and only a few are located at the lateral surface of the muscle fibre [60]. Because of the cellular structure and the distribution of gap junctions in human cardiac tissue, the cardiac propagation is anisotropic. The conduction velocities (CVs) of the cardiac tissue depends on the fibre orientation. The CVs in the longitudinal direction along the fibre CV_L are usually larger than the CVs in the transverse direction of the fibre CV_T. The anisotropy ratio (AR) is defined as CV_L divide CV_T varying in different regions of the heart [61]. For example, the AR is about 2 in the ventricle [62] and it ranges from 1.2 to 3.2 in right and left atria [63].

There is limited literature about the distribution of gap junctions in the zebrafish heart. According to the confocal images of connexins in the larval zebrafish heart at 24-72 hpf shown in Figure 2.6 (C) and (D), gap junctions are distributed all over the cell membranes. There is also a literature reported that, in zebrafish heart, gap junctions are not only in the intercalated discs, but also in other regions like the lateral walls of the fibres [64]. It is not clear whether the cardiac propagation in the zebrafish heart is anisotropic or not. Therefore, in the models introduced later, it is assumed that the gap junctions are distributed uniformly in all cell membrane connected with their neighbouring cells.

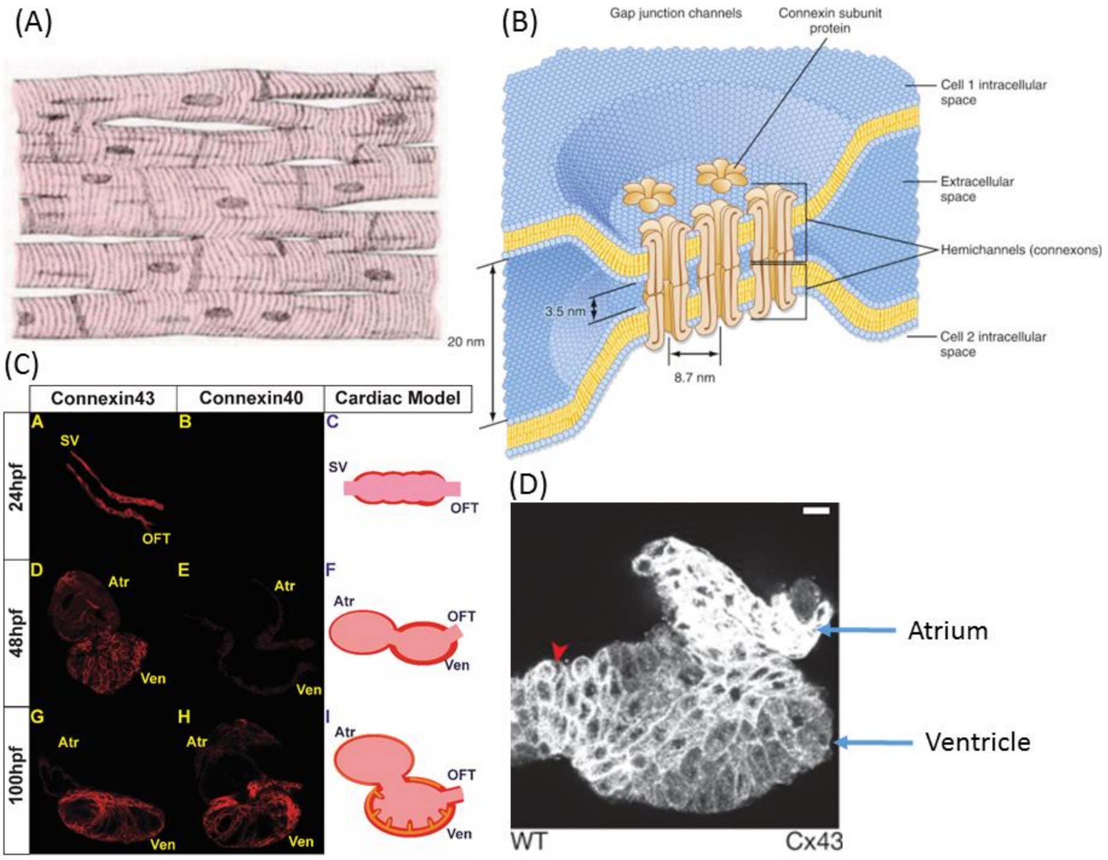

Figure 2.6: (A) Histology of human cardiac tissue in [65]; (B) Schematic diagram of gap junction [66]; (C) Wild-type zebrafish hearts at 24, 48, and 100 hpf immunostaining with anti-Cx40 or anti-Cx43 antibodies (red) [67]; (D) Confocal image of a wild-type zebrafish heart at 72 hpf stained with anti-Cx43. The arrowhead points to outflow tract cardiomyocytes with slightly elevated Cx43 concentrations. Scale bar: 10 μm. [57]

Gap junctions play a vital role to maintain normal electrical propagation, and coordinate the contraction of the heart in both mammalian and zebrafish heart. Knockout of connexin43 (Cx43) in mice heart resulted in slowing ventricular conduction velocity up to about 50% and dramatically increasing susceptibility to inducible ventricular arrhythmias, even sudden arrhythmic death [68-70]. Connexin 40 is important to modulate the contraction of cardiac muscle and Cx40 knock-out mice exhibited a delay in atrioventricular and intraventricular conduction and atrium-derived abnormalities in cardiac rhythm implying that the possibilities of causing cardiac arrhythmogenesis [71]. Besides losing one type of gap junctions in heart, other reasons have been found to be responsible for cardiomyopathies such as disturbances in the distribution of gap junctions and changes in the number or type of connexin(s) expressed [72-74]. However, it is still unknown how gap junction remodelling is related to the likelihood of arrhythmogenesis. It is uncertain whether the connexins' dislocation far away from the intercalated discs or the reduction of gap junctions or both may be the important reasons causing myocardial diseases.

2.2.2 Development of the larval zebrafish heart

Unlike the other model animals such as mouse, the development of a larval zebrafish is very fast, with the heart beating at 24 hours post fertilisation (hpf) [75]. It makes the larval zebrafish an excellent vertebrate model organism to study the development of the cardiac conduction system. As larval zebrafish hearts, at different development stages, are modelled in the later sections, a review of the development of the larval zebrafish heart from the early stage is described here.

In 20-24 hpf zebrafish as shown in Figure 2.6 (C), the heart appears as a tube and conduction of AP travels linearly and unidirectionally across the heart from sinus venous where the pacemaker activity at the SA node started the conduction [56]. By 24 hpf, regular contraction and circulation in this tube heart begins [76]. During 24-48 hpf this tube-like heart develops the AV canal, separating two bean-shaped chambers, the atrium and ventricle, and each chamber shows distinct the outer curvature (OC) and inner curvature (IC) [77]. Electrophysiological properties vary significantly in this stage compared with 20-24 hpf such that APD decreases, the ventricular conduction velocity increases and a conduction delay presents at the sinoatrial, AV and ventriculo-aortic boundaries [56, 57, 78]. At 48 hpf, the myocardium in most area has only one cell layer except for the ventricle which has two to three layers. The formation of trabeculae starts at about 60 hpf and become clearly visible by 72 hpf

[79]. Trabeculae are muscular ridges lined by endocardial cell inside the ventricle chamber. The formation of trabeculae increases the myocardial surface area for blood oxygenation [80]. Meantime, the pericardial cells develop and gradually attach to the surface of myocardium. At 72 hpf, the zebrafish ventricle shows a clear three-layered structure as endocardial, myocardial and epicardial layers [81]. Between 72 hpf and 120 hpf, the zebrafish heart becomes relatively stable in terms of APD and conduction velocities [78]. In this stage, the trabeculae network is rapidly developed within the zebrafish ventricle. In 96 hpf zebrafish ventricle, the trabeculae extends from apex to base and finally increases throughout the whole ventricle at 120 hpf. Optical mapping of 100 hpf zebrafish hearts demonstrated that rather than linear propagating from the AV canal to the ventricle outflow tracts at 48 hpf, the conduction in ventricle becomes much more complex that it is propagated from the OC to the IC [67]. The measurement of conduction velocity in the zebrafish ventricle at 72 hpf reveals that the conduction velocity within the OC is three times faster than it in the IC [57].

During the development of the embryonic zebrafish heart, growth of the heart is not only associated with increasing cardiomyocytes number, such as between 48 and 72 hpf a 50% increase is found in total cardiomyocytes number [39], but also with varying the cardiomyocytes morphology. Comparing with the cardiomyocyte in 25 hpf zebrafish heart, the atrial cardiomyocytes in 48-58 hpf zebrafish heart retain their squamous cell morphology and the inner curvature ventricular cardiomyocytes remain cubical, while the outer curvature (OC) ventricular cardiomyocytes change significantly to become flattened and elongated [56, 77]. These variations on myocyte morphology can be verified by the measurements of circularity index and the myocyte surface area. It is reported that the circularity index of ventricular myocytes varies from 0.86 in 27 hpf to 0.85 in IC myocytes and 0.73 in OC myocyte in 52 hpf zebrafish heart, while the average surface area of ventricular myocytes varies from 90 μm^2 to

$100\ \mu m^2$ in IC myocytes and $115\ \mu m^2$ in OC myocytes in 52 hpf zebrafish ventricle [77]. More experimental data of the variations of circularity index and myocyte surface area in the 30 and 54 hpf zebrafish heart are available in [82] mainly concerning the endocardial myocytes in different regions (atria or ventricle, OC or IC). Moreover, cardiomyocytes at the AV boundary become extremely elongated and form a ring around the AV canal [56].

2.3 Electrocardiogram

The electrical activity in the heart can be measured by placing electrodes on the skin. In a cardiac cycle, the AP propagation through the heart generates electric field spreading from the heart into the surrounding tissues. It developed electrical potential on the surface of the body which can be recorded by the electrodes.

2.3.1 Depolarization and repolarization waves

As explained before, an AP includes two major stages: the depolarization and repolarisation. The generation of ECG is because of the propagation of both the depolarization and repolarisation waves in the heart. As the ECG generated from the heart is complicated, therefore as a start, a simple example of a cardiac muscle fibre is given in here.

In Figure 2.7 (A), the depolarisation is started from the left end where in the left half of the fibre, the normal negative potential inside the fibre, becomes positive and the potential outside of the fibre becomes negative. It leads to a positive signal measured at the recording meter because the right (positive) electrode is now in positive polarity and the left (negative) electrode is now in negative polarity. It becomes the maximum positive value when the depolarization reaches halfway.

In Figure 2.7 (B), the depolarization spreads over the entire cardiac fibre. The recording signals by the electrodes returns to zero because both electrodes have the same potential.

In Figure 2.7 (C), the repolarization spreads across half of the fibre. It leads to a negative signal recorded by the meter as the right (positive) electrode is now in negative polarity and the left (negative) electrode is now in positive polarity.

In Figure 2.7 (D), the whole fibre is repolarized. Therefore both electrodes have the same potential which causes the measured electric signal becoming zero.

In summary, when the depolarisation wave moves towards the positive electrode or the repolarisation wave moves away from the positive electrode, it measured as a positive signal. In turn, when the repolarisation wave moves away from the positive electrode or the repolarisation wave moves towards the positive electrode, it measured as a negative signal.

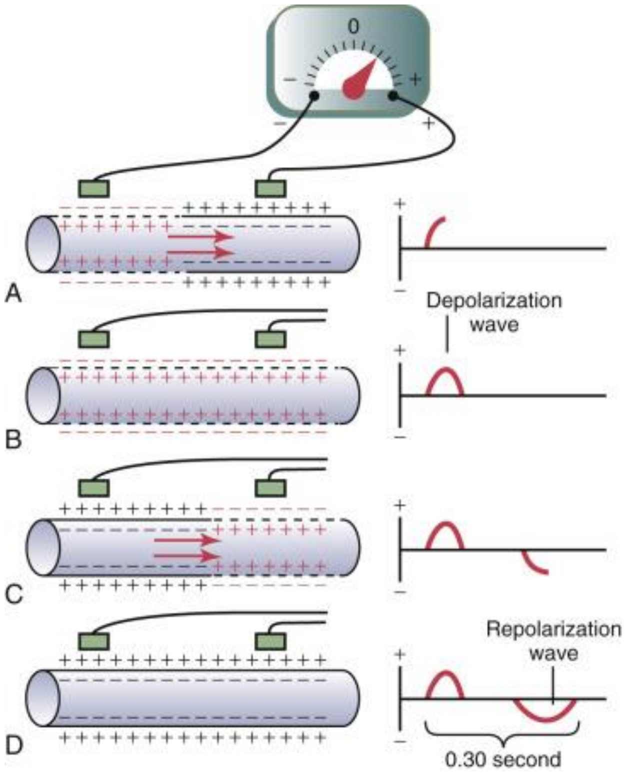

Figure 2.7: Recording signals produced by (A-B) the depolarization wave and (C-D) the repolarization wave from a cardiac muscle fibre from the electrodes placing at the outside of the fibre [83].

2.3.2 Human and larval zebrafish ECGs

The depolarisation and repolarisation of different regions in the heart contributes to different waves in the ECG. The polarity of the recorded signals depends on the manner in which the electrodes are applied to the surface of the body and how close the electrodes are to the heart. A standard ECG measurement system, a 12 Lead ECG system, is well-developed for use with human. This system sets standards of the electrode positions on the body, therefore the resultant ECGs are measured in the same positions and any changes in the normal ECG can be distinguished which is caused by cardiac abnormalities. In the 12 Lead ECG measurements, the electrodes are positioned as shown in Figure 2.8 (A) to obtain recordings made from the six precordial electrodes near the heart and six recordings from the limb electrodes (left arm, right arm and left leg). The right leg electrode is used as a reference. For larval zebrafish, there are no available standard ECG measurement system. The electrodes positions of the recorded larval zebrafish ECGs used later for model comparison are shown in Figure 2.8 (B) [36].

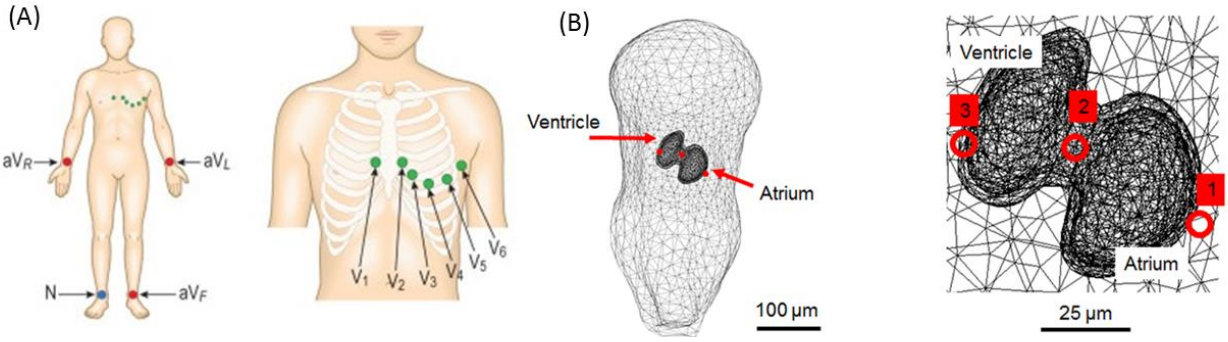

Figure 2.8: (A) 12 lead ECG system showing the electrodes' placements from [84]. (B) The electrodes' placements of larval zebrafish ECG from [36].

A normal human ECG is composed of a P wave, a QRS complex, and a T wave as shown in Figure 2.9. The QRS complex includes three waves: the Q wave, the R wave, and the S wave. The P wave is caused by electrical potentials generated when the atria depolarize. The QRS complex is caused by potentials generated when the ventricles depolarize. The T wave is caused by potentials generated as the ventricles repolarize which is known as a repolarization wave. The Q wave is because of the depolarization of the septum. The S wave is because of the depolarisation in the Purkinje fibres. The opposite direction of S wave from the R wave is because the Purkinje fibres spread throughout the ventricles from the top to bottom and then go back to the walls of the ventricles.

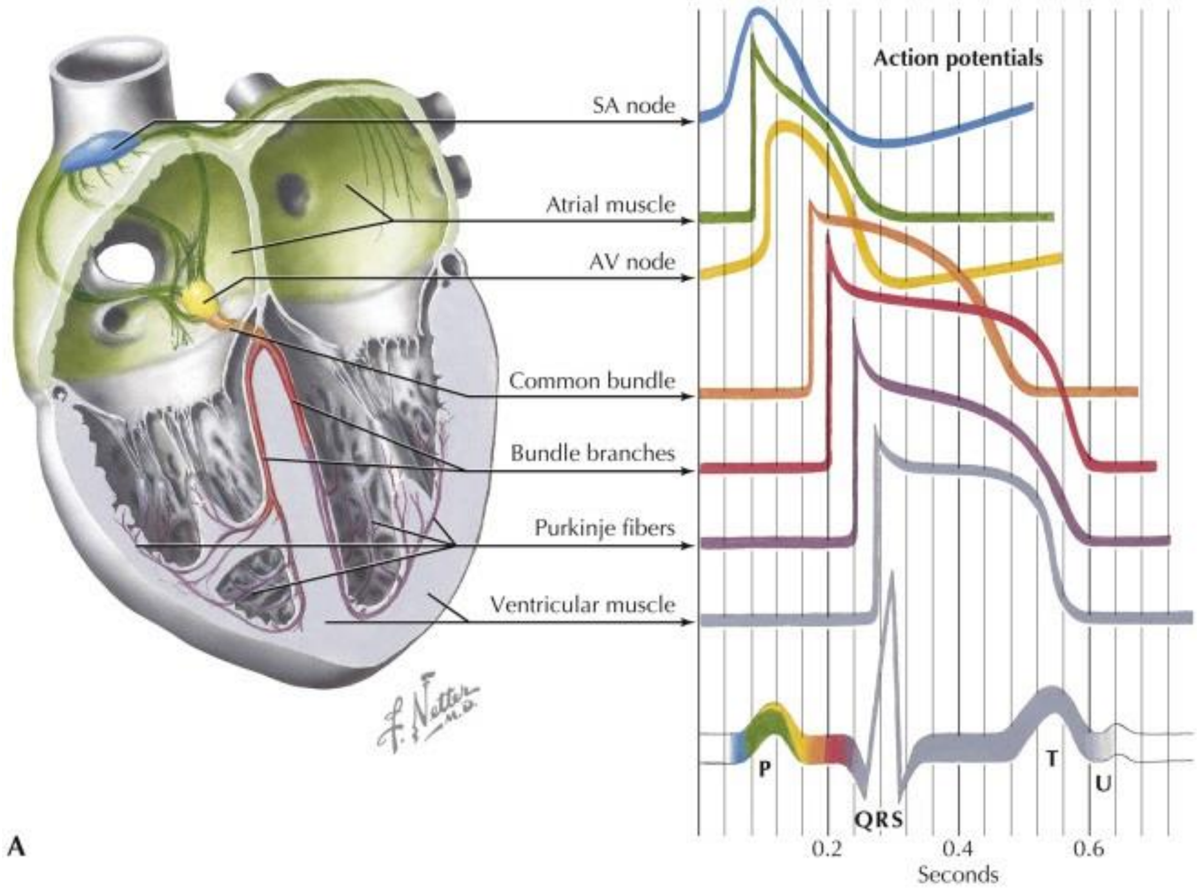

Figure 2.9: APs of for each region in the human heart and resultant ECG [85]

The definitions of intervals in the human ECG are labelled in Figure 2.10 (A). The PR interval is the time between the start of the P wave and the start of the QRS complex. It represents the delay between atrial depolarisation and ventricular depolarisation. The QT interval is the time from the start of the Q wave to the end of the T wave which is about the time delay between ventricular depolarisation and ventricular repolarisation. ST segment is the time between the end of the S wave and the start of the T wave which represents the time when the ventricular APs are in the plateau phase.

A typical ECG of a 72 hpf larval zebrafish measured at a position near ventricle is shown in Figure 2.10 (B). As is introduced in the last section, the depolarisation in the larval zebrafish heart is initiated in the SA region and then spreads into the atrium which fully depolarises. After that, the depolarisation wave enters the AV band and propagates in a slower speed than in the atrium. Finally, it enters the ventricle. The repolarisation in the atrium happens about the same time as the ventricular depolarisation. By measuring at a position near the ventricle, the ECG shows a positive P wave and R wave as the depolarisation wave propagates towards the electrode. Then it shows a negative T wave as the repolarisation wave propagates towards the electrode as well. The time intervals of the larval zebrafish ECG are labelled in Figure 2.10 (B).

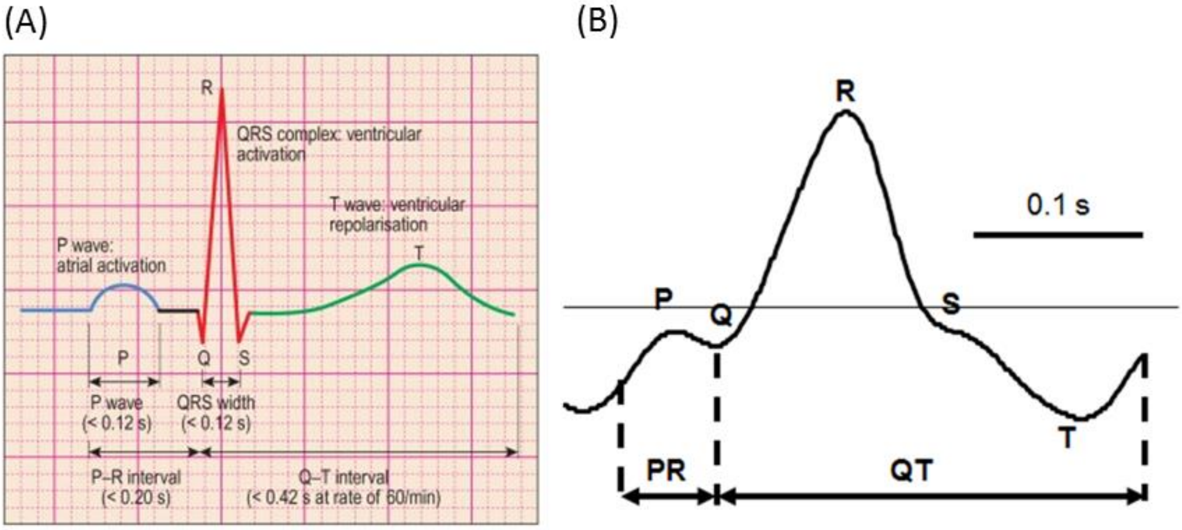

Figure 2.10: (A) Human ECG labelling with ECG intervals [84]; (B) A typical 72 hpf zebrafish measured ECG at a position near ventricle [36]

2.3.3 ECG diagnosis

By comparing the measured ECGs with the normal ECGs, cardiac abnormities and conditions can be diagnosed including abnormal cardiac rhythms and conduction, ischemia or infarction, and effects of abnormal electrolyte levels and drugs [85].

AV block is one of common cardiac disorders which could be caused by various conditions such as ischaemia, infarction, fibrosis and drugs. In the AV block, the normal conduction pathways between the atria and ventricles in the heart are disrupted which results in abnormal ECGs. There are three types of AV blocks: first-degree AV block, second-degree AV block, and third-degree AV block as shown in Figure 2.11. In a normal human ECG, the P wave occurs before the QRS complex and the PR interval ranges from 0.12 s to 0.2 s which represents the normal conduction in the AV node. The first-degree AV block is caused by a lengthened conduction in the AV node which illustrates in the ECG as a prolonged PR interval (> 0.2 s) as shown in Figure 2.11. If the PR interval becomes much longer, in the ECG, some P waves are not followed by a QRS complex. It means in some cardiac cycles, the ventricles are not depolarized while the atria are depolarized as usual. As a result, the ventricles contract less frequently than the atria. This is the second-degree AV block which is also called as a Wenkebach phenomenon. When the depolarisation wave is not conducted from atria to ventricle completely, it is the third-degree AV block. On the resultant ECG, the P-P intervals and R-R intervals are regular but the P waves are not followed by the QRS complexes synchronously. In other words, the atria and ventricles depolarize independently and the QRS complexes occur less frequently than the P waves. In this case, the contraction of the ventricle is controlled by the intrinsic frequency of ventricle at 20-55 beats/min which is smaller than the normal heart rate at 60-100 beats/min.

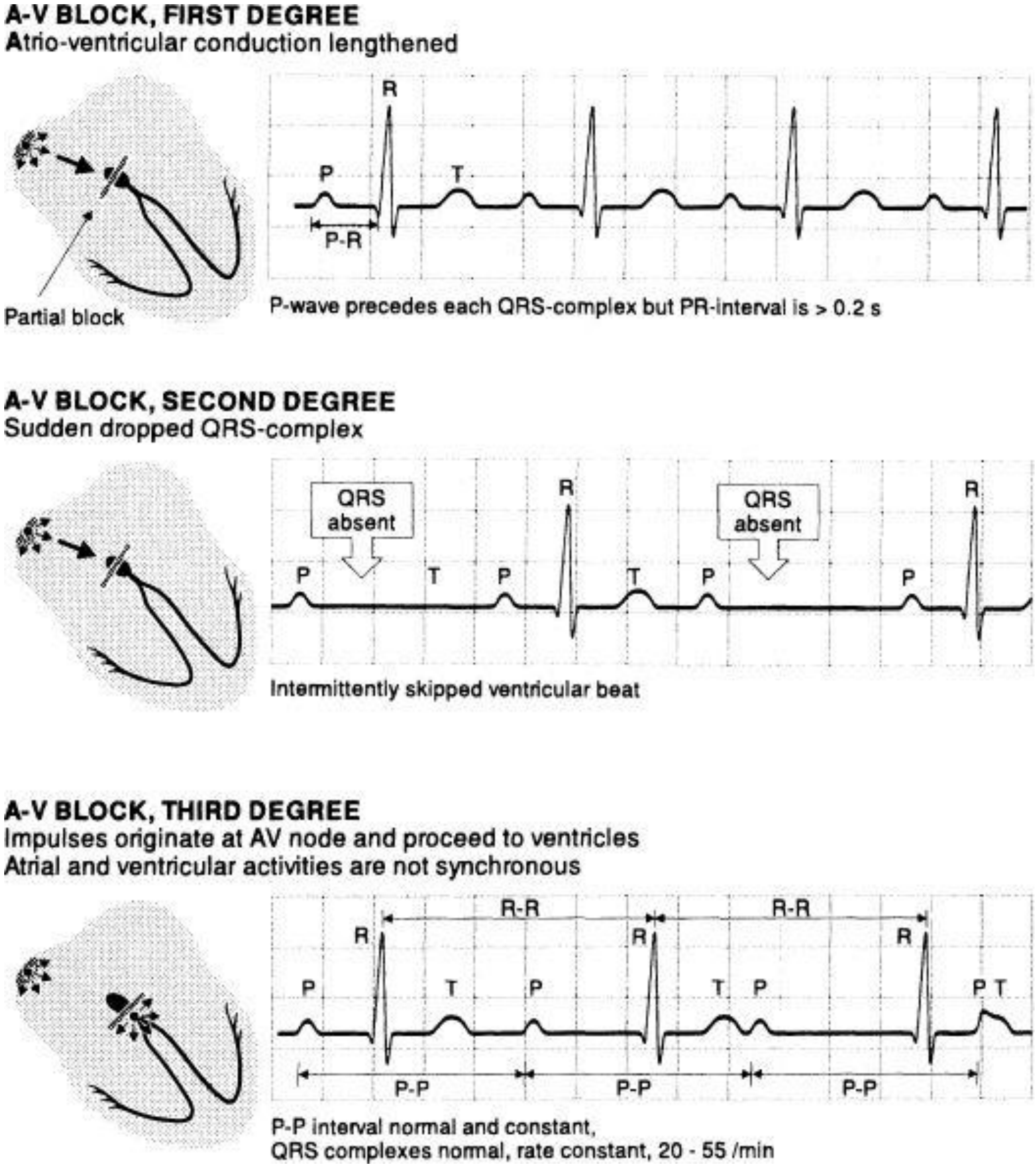

Figure 2.11: ECGs during the AV blocks from [37]

3. CARDIAC MODELLING

In the last five decades with high development of computer science, many computational models simulating the physiological electrical activities have been developed which are difficult to study within living organisms. By carefully comparing with measured data, these models become realistic and provide informative data to give insights into the mechanism of heart diseases, for example cardiac arrhythmias, and subsequently help with developing new therapies or drug screening. In this chapter, various modelling methods used for modelling the electrical activities at tissue level or the whole heart are introduced starting with the torso model for describing the electrical potential distribution in the area around the heart. It follows with the cardiac tissue models for describing the cardiac propagation and the cellular electrical activities (AP). It ends with a brief introduction of the finite element method (FEM) and how the software COMSOL Multiphysics, based on the FEM, is used in the implementation of the models introduced in this thesis.

3.1 The torso model

In the heart, cardiac cells activate and produce APs which generate currents inside the cell and also in the surrounding area (the torso). The surrounding area is a passive conducting medium which can be considered as a volume conductor. A volume conductor can be defined as a volume which has conductivity and permittivity in which a current source resides. The current source can be cardiac tissue or the heart in this case.

The volume conductors can be classified into two types: homogeneous or inhomogeneous based on the conductivity distribution. A homogeneous volume conductor has a constant conductivity in the region while an inhomogeneous volume conductor has varied conductivities. In the human body, conductivities for different tissue shows distinct differences for example the lung at $0.09\,S/m$ comparing with the bones at $0.006\,S/m$ [37]. An inhomogeneous volume conductor replicates the real physical situation more than the homogeneous volume conductor. However due to the limitation of measured conductivities in the larval zebrafish, homogenous volume conductors are applied to all models in this thesis.

The current source (the heart) in the volume conductor (the torso) results in field quantities which can be described by the Maxwell equations [86]. A quasi-static approximation [87] can be used for a macroscopic volume. Therefore, the distribution of electrical potential V in a homogeneous volume conductor with conductivity σ can be written as a Poisson's equation:

$$\nabla \cdot \sigma \nabla \mathrm{V} = -I_v \tag{3.1}$$

where σ is the electrical conductivity of the volume conductor, I_v is the current source per unit volume. Assuming the current source is included in the volume conductor, then a Laplace's equation can be applied as

$$\nabla \cdot \sigma \nabla \mathrm{V} = 0 \tag{3.2}$$

Appropriate boundary conditions are needed in this case to determine the distribution of electrical potential in this volume conductor. As the heart is enclosed in the zebrafish body in all models described in this thesis, equation (3.2) is applied and the boundary conditions are added to resemble the current source (heart).

The heart can be considered as a biological volume source (conductor) which is placed inside of a volume conductor in torso shape. This biological volume source generates electrical potential on the surface of the volume conductor which can be measured as the ECGs. The purpose of cardiac modelling is to investigate the function of the heart or cardiac tissue by replicating the realistic mechanism of the heart as accurately as possible and then comparing the model performance to the experimental results. In order to understand the basis of the volume source, the cardiac source has been simplified and simulated as a simple equivalent current source such as the dipole model [37]. In the dipole model, the depolarisation and repolarisation waves in the heart are approximated as a double layer source including a positive and a negative charge in parallel. There are also other more realistic models based on the equivalent current sources such as the moving dipole, the multiple dipoles and multipole model. These model may replicate the electrical potential distribution on the body produced by the electrical activity of the heart. However they do not account for the realistic cardiac activities in the heart or cardiac tissue such as the APs and their propagation. Therefore in next section, more realistic models are described which incorporate such electrophysiological properties.

3.2 Cardiac tissue model

In order to replicate the electrical activities in cardiac tissue, there are two major biophysical processes required for the model. The first is the electrical behaviour on the cardiac cell membrane which can be simulated by different types of ionic current models similar to the Hodgkin-Huxley model as described in section 2.2.1.2. The second is the cardiac propagation in the cardiac tissue.

In this section, the models to simulate cardiac propagation in the cardiac tissue are introduced firstly. There are two modelling approaches developed for this task: the continuum approach and the discrete approach. As described in section 2.2.1, the heart wall is made of cardiac tissues based on cardiac muscle cells which produce electrical activities. Therefore, a realistic model of cardiac tissue should reproduce the electrical behaviour of each individual cell and the gap junctions connected between them. The discrete approach is implemented in this way. However this is not a good option when it has to deal with a large section of cardiac tissues or the whole heart as this approach increases the computational load massively. Even with the current advanced computational power, it is still not feasible to model the whole human heart using the discrete approach as there are two to three billion cardiac muscle cells in a human heart [88]. The other approach, the continuum approach, is an alternative way to deal with a large section of cardiac tissues or the whole heart.

3.2.1 Continuum approach

The continuum approach may be adopted with a condition that the length scale of the cardiac tissue or heart is greater than that of a single cell. In this approach, the heart is treated as a functional syncytium where the electrical properties of cells and the gap junctions are averaged out. Continuum approach is implemented by the bidomain model. In the bidomain model framework, a model cardiac tissue has two interpenetrating domains, the intracellular space and the extracellular space which coexist in the same coordinate system and can be derived as below [86, 89]. The intracellular and extracellular spaces have electrical potential fields as V_i and V_e with conductivity tensors σ_i and σ_e. The conductivity tensors σ_i and σ_e are constants as the averaged values over the whole cardiac tissue. It is assumed that currents only flow between the extracellular and intracellular spaces, therefore according to the current conservation, the intracellular current density J_i and the extracellular current density J_e can be described by:

$$-\nabla \cdot J_i = \nabla \cdot J_e = A_m I_m \tag{3.3}$$

where I_m is the transmembrane current per unit area and A_m is the area.

Based on the Ohm's law and using the quasistatic approximation [87], both intracellular and extracellular current densities can be given by:

$$J_i = -\sigma_i \nabla V_i \tag{3.4}$$

$$J_e = -\sigma_e \nabla V_e \tag{3.5}$$

Substitute equation (3.4) and (3.5) in equation (3.3):

$$\nabla \cdot (-\sigma_i \nabla V_i) = \nabla \cdot (\sigma_e \nabla V_e) \tag{3.6}$$

The transmembrane current can be derived from equation (2.2) where the sum of the ionic currents based on different channels can be replaced as I_{ion}:

$$I_m = I_{ion} + C_m \frac{dV_m}{dt} \tag{3.7}$$

The current density can be rewritten from equation (3.6) and (3.7) as

$$\nabla \cdot (-\sigma_i \nabla (V_i - V_e)) + \nabla \cdot (-\sigma_i \nabla V_e) = A_m (I_{ion} + C_m \frac{dV_m}{dt}) \tag{3.8}$$

Then the equation (3.8) can be expressed as

$$\nabla \cdot (-\sigma_i \nabla V_m) + \nabla \cdot (-\sigma_i \nabla V_e) = A_m (I_{ion} + C_m \frac{dV_m}{dt}) \tag{3.9}$$

This equation is the second of the bidomain equations and can be used to calculate the transmembrane potential. The cardiac tissue model can be simulated by the bidomain equations with a proper ionic current model used to describe the I_{ion} which will be described in detail in the next section.

Due to the efficiency and simplicity of the bidomain method, it is widely applied to cardiac models ranging from cardiac tissue [90, 91] to the whole heart [92], from the human heart to the zebrafish heart [36]. However, the conductivities used in bidomain model are the mean values by fitting the conduction velocity in the model with the measured values, and also these conductivities include both cellular conductivity and the conductance of the gap junctions. If these conductivities applied to a large-scale cardiac tissue model are then applied to a cardiac tissue model with a small number of cells, it would result in the same conduction velocity as in the large-scale cardiac tissue model. However this result disagrees with measurements. As from experiment conducted on real tissue, measured conduction velocity decreases when the size of tissue decreases (cell number decreases) because of the effect of gap junctions [93]. Therefore, the bidomain model is limited because it doesn’t take account of the microscopic structure and it is not suitable for modelling the larval zebrafish heart containing only 300 cardiac muscle cells [39].

3.2.2 Discrete approach

As mentioned in Chapter, the cardiac propagation in cardiac tissue is discontinuous due to its cellular nature. In cardiac tissue, cells are not only connected with adjacent cells via gap junctions, but also surrounded by extracellular spaces. The extracellular space occupies 20-25% of the total volume in human heart [94]. Both factors are of importance to modulate cardiac propagation. Thus, the most realistic model of heart is a discrete approach which means, each cell should be treated individually, connected via gap junctions and both extracellular and intracellular spaces should be treated as distinct volumes, electrically coupling with applying boundary conditions of ionic currents on the membrane. The disadvantage of this approach is that it increases the numerical complexity and is inefficient and not feasible for modelling a large number cells. However this discrete approach has been applied to multiple cardiac models with a relatively small number of cells starting from the 1970s. The first evidence of discontinuous propagation was presented by Spach and his colleagues [40]. They found that the shape of the AP time course depends on the direction of propagation. It means that in the direction of the long cell axis, slower upstrokes were associated with high propagation velocities while in the direction transverse to the long cell axis, fast upstrokes were associated with low propagation velocities. There are many discrete models after this model to study various aspects of cardiac propagation. For example, a cardiac muscle fibre model of about 50 cells with intercalated disk between adjacent cells is developed in 1983 and found that increasing the disk resistance results in decreasing conduction velocity but increasing the upstroke velocity [95]. There were more models developed for studying the shape of AP in cardiac cells [96], the lateral coupling on both planar and curved wavefront propagation [97] and so on. Most recent works can be found in [98-101]. Over the last ten years with the advancement of computer science, it becomes possible to model cardiac tissue using a discrete approach for a large sheet of cardiac tissues and it has been applied to model human cardiac tissue such as a bundle of ventricular myocardium with 132 cells [98], a cardiac fibre with 50 cells in a simplified shape [99], and up to 16,000 human cardiac cells [100]. Therefore, it is a feasible approach to model the larval zebrafish heart which only contains about 300 cells and is applied to the larval zebrafish heart model in the following sections. The mathematical representation of this approach can be found in Chapter 5 and 6.

Another class of the discrete models is aiming to create a stylized representation cardiac activation called the cellular automata model [86]. The concept of this model is firstly proposed back to 1964 by Moe, Reheinboldt and Abildskov [102]. Rather than modelling the biophysical process of each cell using ionic current models, this approach only models the network of the cells in the cardiac tissue. In this approach, the cardiac tissue is divided into regular grids. Each grid represents a cell connected with neighbour cells. In a simple cellular automata model, only two states, which is resting and excited (on and off), plus a set of internal rules are used to describe the transition from one state to the other and back again. In order to capture more details of AP, more states are designed for one cell for example three states: resting (relaxed and excitable), refractory 1 (excited, able to excite neighbouring cells), and refractory 2 (excited, but not able to excite neighbouring cells) [103]. The advantage of this model is that it demonstrates the main properties of cardiac propagation and can be applied to model large scale cardiac tissue efficiently. A series of cellular automata models are developed in the last 60 years aiming to study the anisotropic propagation in tissue level or a region of heart for example the ventricle by altering the rules of interaction among cells [104, 105]. This method has also been successfully implemented to model the whole heart to simulate ECG [106, 107]. Lately, models called hybrid automata have been developed which enable to incorporate the temporal morphology of AP [108, 109]. Overall, these models allow efficient analysis of large scale of tissue or even the whole human heart, however it cannot incorporate the biophysical process in each cell which is not a realistic approach to modelling the larval zebrafish heart in this project.

3.2.3 Ionic current model

Apart from the cardiac propagation, the other important biophysical process in the heart, the electrical activity of excitable cells on their membrane, is simulated by the ionic current models. The flow of ions across the cell membrane are controlled by different ionic channels, pumps and exchangers located on the cell membrane. Inspired by the Hodgkin and Huxley model [47] which was introduced in Chapter 2, many ionic current models have been developed to model this process based on the contribution of different ion currents across the cell membrane to the total ion current [110]. In order to model the behaviour of each ion channel, gate variables are introduced to describe the variation of the conductance of each ion channel upon time. Then different ion currents are summed up as the total ionic current. With the development of ionic current models in the past few decades, the level of ion current details in these models are increasing. There are 4 ordinary differential equations (ODEs) in the Hodgkin and Huxley model [47] comparing with 8 ODEs in the Luo and Rudy model for ventricular cells in 1991 [43], 22 ODEs in the Noble model for ventricular cells in 1998[111] and 39 ODEs in the Grandi model in 2010 [112]. Considering its complexity, these models can be computationally intensive. Note that most of them are created for human or other common mammalian model animals such as rat, guinea pig and rabbit. Until the time of writing, no ionic current models has been designed for zebrafish based on the biophysical processes of ionic channels.

An alternative way of modelling the ionic currents is the phenomenological model. This model can be used in the cases that the details of ionic currents are not necessary. Rather than based on the details of each ionic current, this model is aiming to reproduce the shape of an AP at a minimal computational cost. The two-variable FitzHugh Nagumo (FHN) model [113] is a typical phenomenological model. The advantage of the FHN model that it captures the main macroscopic characteristics of the AP and it is relatively simple to manipulate the model parameters to quantitatively reproduce certain overall characteristics of the APs such as the APD. The original FHN model was designed to model the nerve AP. Later on, a modified version was developed known as the Rogers-McCulloch version of Fitzhugh-Nagumo equations [42] to model the cardiac AP and its propagation. The mathematic equations are written as:

$$\frac{du}{dt} = \nabla \cdot D\nabla \mathrm{u} + c_1 u(u-a)(1-u) - c_2 uv \tag{3.10}$$

$$\frac{dv}{dt} = b(u - dv) \tag{3.11}$$

where u is equivalent to the transmembrane potential and v is a recovery variable. The a, b, c_1, c_2 and d are constant parameters which define the shape of the AP. The diffusion term $\nabla \cdot D\nabla \mathrm{u}$ is added here in order to model the AP propagation through the space where D is the diffusion tensor. The values of the parameters are generated by trial and error as shown in Table 3.1. As a result, the u and v are plotted as a function of dimensionless time in Figure 3.1.

Table 3.1: Parameters used in the Rogers-McCulloch version of Fitzhugh-Nagumo equations from [42]

Parameters	Values
a	0.13
b	0.013
c_1	0.26
c_2	0.1
d	1
D	1 to 4

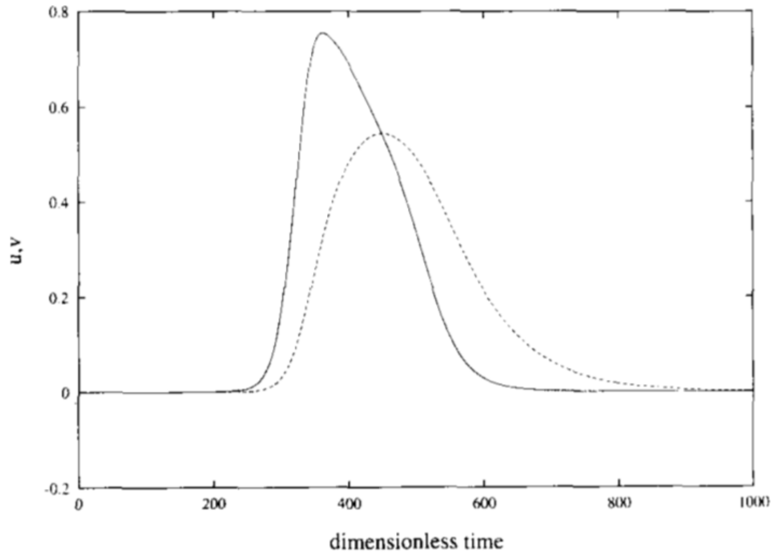

Figure 3.1: The transmembrane potential u in solid line and the recovery variable v in dashed line are plotted against dimensionless time produced by Rogers model [42]

In the Rogers model, the arbitrary units used in the original FHN equations are converted to real units by comparison to measured results. Specifically, one time unit equivalent to $0.63\ ms$ and one space unit is equivalent to $0.99\ mm$. However this is difficult to apply these converted units to 3D models in the real time and space scales. Therefore, modified equations are developed by Dokos [114] who scaled the equations so that one time unit corresponded to one second and one voltage unit corresponded to one volt. The new modified equations are written as:

$$\frac{du}{dt} = kc_1(V_m - B)\left[a - \frac{(u-B)}{A}\right]\left[1 - \frac{(u-B)}{A}\right] + kc_2 v(u-B) \tag{3.12}$$

$$\frac{\mathrm{dv}}{\mathrm{dt}} = ke\left[\frac{(u-B)}{A} - dv - b\right] \tag{3.13}$$

where the k scales the time, A scales the potential and B offset the potential. These equations have been applied to model the larval zebrafish AP in the previous larval zebrafish heart model [36] and are chosen to use in the models introduced in the later chapters. No diffusion term is included in this case as the cardiac propagation is described by the discrete approach as introduced in section 3.2.2. Although this FHN type model cannot reproduce the details of each individual ionic currents, by carefully choosing the parameters used in the FHN model, it can still resemble all the main features of AP.

3.3 Modelling tools

3.3.1 Finite element method

The electrical potential contribution in the cardiac tissue can be solved from the ODEs described above. Previously they have been solved analytically but only limited to simple model geometry, for example an axon in a cylinder shape with a constant radius as introduced in section 2.2.2. In order to deal with more complex biological systems, various numerical methods have been developed including the finite difference method (FDM), finite element method (FEM) and finite volume method (FVM). In general, these numerical methods are based on discretization which is to divide the complex domain into smaller and simple sections (elements). Then the physical equations in each section are solved and finally integrated into the complex domain for study and analysis. All these numerical methods have been applied to solving the ODEs for electrical activity in the heart [115]. The FEM method is chosen to use here because it is able to deal with complex model geometry and has been a widely-used, efficient method, since the 20th century [116, 117]. Moreover, the previous larval zebrafish heart model based on the bidomain model [36] has been implemented using a commercial modelling software based on the FEM which gives confidence of implementing the discrete larval zebrafish heart model using the FEM.

FEM is a popular numerical method used to solve field problems like the electrical activity in the heart which is also known as finite element analysis (FEA). In order to obtain an approximate solution of the PDEs, in FEM, a complex model structure is divided into pieces called elements. The types of elements vary from 1 dimensional (1D) to three-dimensional (3D) for example a tetrahedron for a 3D element, a triangular for a 2D element and an edge for a 1D element. Neighbouring elements are connected at the edges by nodes. In each element, the equations are solved by assuming basis functions of the unknown variables at the nodes. The approximate solution in the element is computed from a combination of nodal values of the variables and the basis functions. Then based on the initial conditions and boundary conditions applied to the elements, the solution of all elements can be solved by assembling each individual elements together [118]. Depending on the sizes of the elements, errors can be introduced and all solutions obtained by FEM are approximate results. As these elements are made smaller and smaller, as the mesh is refined, the computed solution will approach the true solution. However reducing the element size results in increasing the total element number which would require more solution time and computational memory. The solution time and computational memory are related to the number of degrees of freedom (DOFs) in the model. The DOFs can be calculated by the number of nodes multiple the number of dependent variables. The approximate relation between the number of nodes and the number of elements depends on the order of the elements and differs between 2D and 3D. For example, in 2D, the number of nodes based on linear triangular elements is half of the number of elements while in 3D, the number of nodes based on the linear tetrahedral elements is 0.2 times the number of elements. Larger DOFs means that it requires longer solution time and large componential memory which is limited by the processing power of the computer used. A mesh convergence analysis is often conducted to judge whether the element size is small enough which results in reliable modelling results.

3.3.2 Introduction of COMSOL

All models introduced in this thesis were implemented using COMSOL Multiphysics 5.2. The software is a finite element analysis simulation software which is able to solve various types of problems including the electrical field problem. There are predefined physical interfaces which allow boundary conditions to be imposed and set up initial values. In addition, there are also mathematical interfaces which allow the input of self-defined equations. A key feature of this software is that it can combine multiple physical models together for example the mechanics, the fluid flow and the electrics, and solve them simultaneously via shared physical constraints.

In the models introduced later, the geometries of the single myocyte model and cardiac tissue models and the model heart are generated in COMSOL using various geometrical tools. The zebrafish body geometry is imported using the previous larval zebrafish body geometry generated by Crowcombe found in [36] and then adjusted in COMSOL.

The electric currents interface under the AC/DC module within COMSOL is used to model the electrical potential distribution in all models introduced here. The membrane behaviour described by ionic current model such as the FHN model is implemented with boundary ODEs and DAEs under the mathematics module. This model benefits from the multi-physics nature of COMSOL which allows the coupling of the two interfaces of the body and the heart together. The equations of ionic current models are applied only to the cell membrane of the heart which is then connected with the body and heart interfaces using boundary conditions. Models are solved in time-dependent solver and the results can be analysed using the pre-set post processing tools in COMSOL or exported as data for further processing using other numerical software such as MATLAB (MATLAB 2016b, The MathWorks, Inc., Natick, Massachusetts, United States).

4. SINGLE CARDIAC MYOCYTE MODEL

The aim of this project is to simulate the electrical activity in the larval zebrafish heart incorporating the cellular nature and the myocyte interconnectivity compared with the human cases. A previous zebrafish heart model has been developed using the bidomain model [36]. However this model only captures the essential electrical properties in two parameters, the intracellular conductivity and the extracellular conductivity [37]. It fails to take account of the cellular structures of cardiac tissue. As it considers that the intracellular and extracellular spaces coexist in the same area and the effects of gap junctions are averaged out and included in the parameter, intracellular conductivity. But in reality, the cardiomyocytes are surrounded by extracellular spaces and connected to adjacent myocytes via gap junctions. A most realistic model would be a discrete model where each myocyte is treated individually with gap junctions connected to one another. In addition, both extracellular and intracellular spaces should be treated as distinct volumes, electrically coupling while applying boundary conditions of ionic currents on the membrane.

This chapter describes the development of a single ventricular myocyte model for the larval zebrafish and human using a similar approach as the discrete approach. Briefly the intracellular and extracellular spaces are treated separately in this single myocyte model with ionic current model applying to the membrane boundaries. No boundary condition of gap junctions was used in this model. This chapter begins with the single ventricular myocyte model for larval zebrafish. A ventricular myocyte in the 48-72 hpf larval zebrafish was chosen to simulate. The model geometry of the myocyte was developed to replicate the realistic size of the larval zebrafish ventricular myocyte. It follows with a description of the electrical model. The ionic current model using in the single larval zebrafish myocyte model was chosen to be a FitzHugh Nagumo (FHN) type model which was applied to the previous larval zebrafish heart model [36]. The parameters of the FHN model applied to the ventricle in the previous model [36] were used in this single myocyte model at the beginning. Then several aspects of the simulation such as activation, time step and measurement point that can possibly affect the action potential (AP) of the single myocyte model were investigated. Next the parameters of the FHN model were adjusted to give APs which matched the APs of 72 and 48 hpf zebrafish.

This chapter follows with the single human ventricular myocyte model. The model myocyte is in the similar size of a typical human ventricular myocyte. The electrical model of the human myocyte model is similar to those used in the single larval zebrafish myocyte model. Two different ionic current models were applied to this human myocyte model. One is the FHN model, the same as the zebrafish myocyte model. The parameters of the FHN model and stimulation methods were adjusted in a similar process as in the zebrafish myocyte model to replicate the measured human ventricular APs in the literature. The other ionic current model is the Luo and Rudy (LR) model [43] which is a more realistic model of human ventricular AP, based on the currents of different ions on the myocyte membrane. Finally, the APs produced by the model using optimal parameters of the FHN model were compared with the model AP produced by the LR model, in standard settings, and the measured human results in the literature.

4.1 Single zebrafish myocyte model

4.1.1 Model geometry

The shape of the ventricular larval zebrafish myocyte varies from myocyte to myocyte as shown in Figure 4.1 (A) and (B). According to the scale bar in Figure 4.1 (A), the average surface area of the myocyte is about $100\ \mu m^2$. Based on Figure 4.1 (A) and (B) and also the other images of ventricular myocytes in the larval zebrafish heart at 48-72 hpf [57, 119, 120], the model myocyte was simplified into a cube with $10\ \mu m$ length surrounding by a bigger block representing the extracellular space in $20\ \mu m$ length as shown in Figure 4.1 (C) and (D).

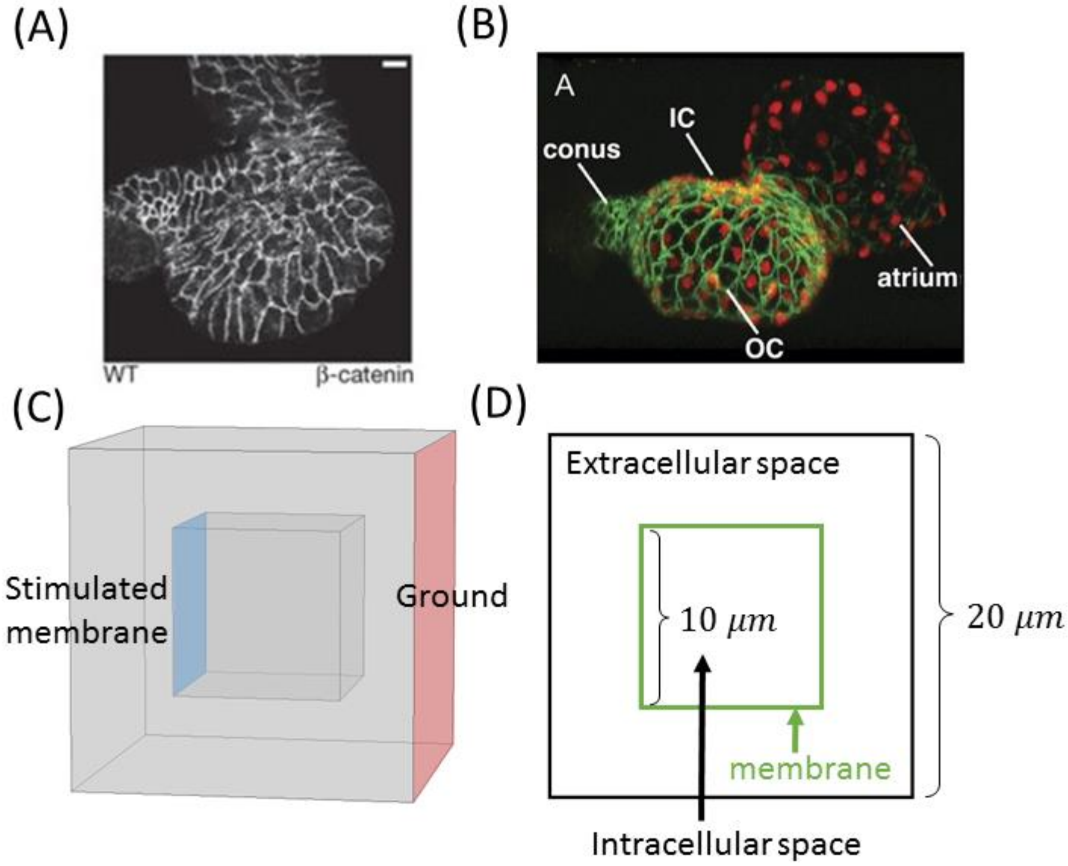

Figure 4.1: (A) Confocal section of ventricle in 72 hpf zebrafish heart stained with anti-β-catenin found in [57]; scale bar, $10\ \mu m$. (B) ventricular myocytes in a 48 hpf zebrafish heart found in [39]. Nucleus express red fluorescent protein and membrane of myocytes is labelled with Zn5 antibody (green). (C) Single larval zebrafish myocyte model geometry. The stimulation current is applied to the myocyte membrane in blue. The ground boundary condition is applied to the extracellular space boundary in red. (D) Cross-sectional view of the single larval zebrafish myocyte model geometry. Membrane are marked in green. The inside of the membrane is the intracellular space and the outside is the extracellular space.

4.1.2 Electrical model

The extracellular space and intracellular space of the single myocyte model were treated as distinct homogenous, isotropic volume conductors with no electrical sources. The electrical activities in both regions were described by the Laplace’s equations as

$$\nabla \cdot \sigma_\mathrm{i} \nabla \mathrm{V}_\mathrm{i} = 0 \tag{4.1}$$

$$\nabla \cdot \sigma_\mathrm{e} \nabla \mathrm{V}_\mathrm{e} = 0 \tag{4.2}$$

where σ_i and σ_e are conductivities of the intracellular space and the extracellular space, V_i and V_e are the intracellular and extracellular potential respectively.

The transmembrane current density I_m flowing from the intracellular space into the extracellular space was determined by

$$\mathrm{I}_\mathrm{m} = \sigma_\mathrm{i} \nabla \mathrm{V}_\mathrm{i} \cdot \boldsymbol{n} \tag{4.3}$$

where $\boldsymbol{n}$ is the normal vector at the boundary between the intracellular and extracellular spaces. A similar equation was used to determine the transmembrane current density from extracellular space as

$$\mathrm{I}_\mathrm{m} = -\sigma_\mathrm{e} \nabla \mathrm{V}_\mathrm{e} \cdot \boldsymbol{n} \tag{4.4}$$

According to the conservation of current, all current leaving the intracellular space must enter the extracellular space. Therefore the boundary condition of the interfaces between intracellular spaces and extracellular space (membrane) was:

$$\mathrm{I}_\mathrm{m} = \sigma_\mathrm{e} \nabla \mathrm{V}_\mathrm{e} \cdot \boldsymbol{n} = -\sigma_\mathrm{i} \nabla \mathrm{V}_\mathrm{i} \cdot \boldsymbol{n} \tag{4.5}$$

The transmembrane current density between extracellular and intracellular spaces was related to the displacement, ionic and stimulation current densities using

$$\mathrm{I}_\mathrm{m} = C_m \frac{\partial V_m}{\partial t} + I_{ion} + I_{stim} \tag{4.6}$$

where C_m is the membrane capacitance, I_{ion} is the ionic current density, I_{stim} is the stimulation current density and V_m is the transmembrane potential given by

$$V_m = V_i - V_e \tag{4.7}$$

The outer boundaries of the extracellular space were assumed to be electrically insulated with a no-flux boundary condition given by

$$\sigma_e \nabla V_e \cdot \vec{n} = 0 \tag{4.8}$$

A ground boundary condition was applied to the boundary at the right end of the extracellular space as shown in Figure 4.1 (C) such that

$$V_e = 0 \tag{4.9}$$

The extracellular and intracellular conductivities are $20\ mS/cm$ and $4\ mS/cm$ based on the measured extracellular and intracellular conductivities for the human heart [121] [122], as no measured passive electrical data can be found for the zebrafish heart. The membrane capacitance is also based on measured data for the human heart as $1\ \mu F/cm^2$[123].

4.1.3 Ionic current model

A phenomenological ionic current model, the Rogers-McCulloch version of Fitzhugh-Nagumo (FHN) equations [114] was used in the single larval zebrafish myocyte model. The equations are written as:

$$\mathrm{i_{ion}} = kc_1(V_m - B)\left[a - \frac{(V_m - B)}{A}\right]\left[1 - \frac{(V_m - B)}{A}\right] + kc_2u(V_m - B) \tag{4.10}$$

$$\frac{\mathrm{du}}{\mathrm{dt}} = ke\left[\frac{V_m - B}{A} - du - b\right] \tag{4.11}$$

where u is the recovery variable and $\mathrm{k}, \mathrm{c}_1, c_2, A, B, a, b, d$ and e are parameters used to adjust the shape of the AP.

There is a previous study [124] to investigate the effects of different FHN parameters on the AP shape. It has been found that ‘k’ affects the time scale/duration, ‘A’ affects the AP magnitude, ‘B’ offsets the voltage to set the resting potential, ‘c1’ and ‘c2’ affect the upstroke/downstroke and both ‘a’ and ‘e’ affect the APD. This study also provided a set of FHN parameters for different regions in larval zebrafish heart such as the ventricle. Therefore the FHN parameters used for the previous model ventricle as shown in Table 4.1 were applied to this single larval zebrafish ventricular myocyte model.

Table 4.1: Parameters of the FHN model used in the previous larval zebrafish heart model for ventricle [36]

FHN parameters	Zebrafish
a	0.13
b	0
c1	0.572
c2	0.5
d	1
e	0.0011
A	0.1205
B	-0.075
k	1000

Initial conditions for intracellular potential $\mathrm{V_i}$, extracellular potential $\mathrm{V_e}$, and recovery variable u were $-75\ mV$, $0\ mV$ and 0. The initial value of intracellular potential was chosen to be the same as in the previous zebrafish heart model [36].

The finite element method was used to solve this single larval zebrafish myocyte model with COMSOL. The model was solved from $0\ s$ to $400\ ms$ at $0.1\ ms$ time step to simulate one cardiac cycle. The preset physical-controlled mesh at the fine level was used. The final mesh contains 31159 tetrahedral elements with 55836 number of degrees of freedom. The mesh of the cell is shown in Figure 4.2. There are 3979 elements in the cell mesh and its average element size is $0.25\ \mu m^3$. The time-dependent solver used is a direct solver with absolute tolerance for all scaled unknowns as 0.001. In order to compute all parameters from two different physics interfaces for intracellular and extracellular spaces, the ‘fully coupled’ approach is chosen rather than using the segregated approach. The ‘fully coupled’ approach solves all the unknowns and includes the couplings between the unknowns at once within a single iteration. This solver is applied to all models described later. Each simulation takes about 10 mins on a computer with an Intel Core i5-4590 CPU @3.3GHz and 16 GB of RAM.

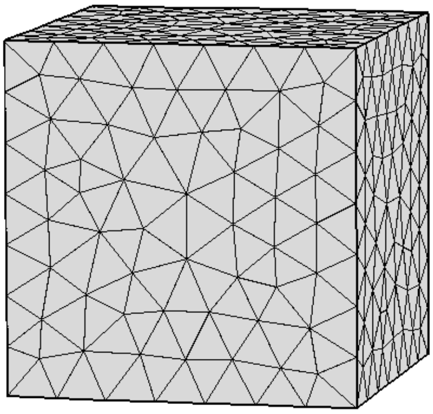

Figure 4.2: mesh of the zebrafish single cell

4.1.4 Stimulation method investigation

As is introduced in Chapter 2, the excitable myocyte can be activated to generate an AP when the transmembrane potential rises about $20\ mV$ and reaches the threshold. For example for a human nerve myocyte with the resting potential of $-70\ mV$, when the membrane voltage changes from -70 mV to about $-50\ mV$, the myocyte activated to generate an AP.

The rise of the transmembrane potential could be triggered by two methods in the model. The first method is the injection of stimulation current. If the stimulation current is big enough, the transmembrane potential of the membrane rises up reaching the threshold and generates an AP. If the stimulation current is insufficient to cause the transmembrane potential to reach the threshold, then the transmembrane potential may rise up a little but the membrane will not be activated. The amount of stimulation current required by the membrane for an AP can be described by the strength-duration curve [37] as shown in Figure 4.3. The stimulation current is normalized so that the rheobasic stimulation current has the strength of unity. The smallest current required for an AP is called the rheobasic current. With this rheobasic current, infinite stimulation time duration is required. The current strength and the time duration is inversely related. As the current strength increases, the time required to stimulate the membrane decreases to maintain a constant effect on starting an AP [125].

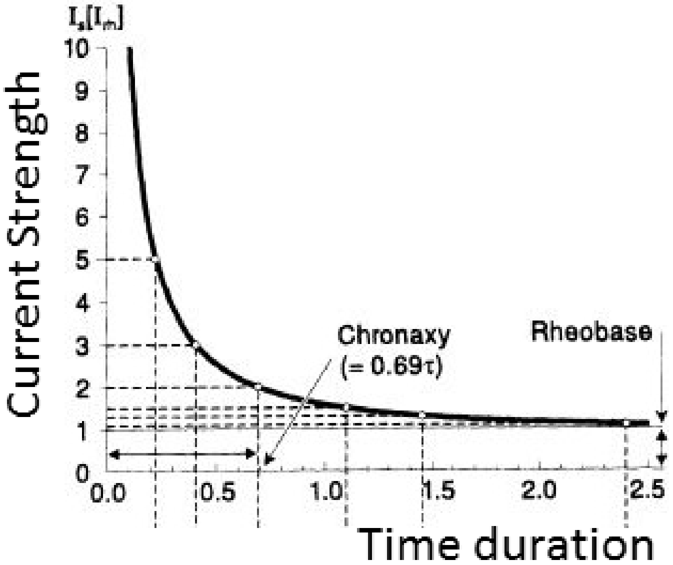

Figure 4.3: Strength- duration curve from [37]. The units are relative.

To begin with, an external stimulation current I_{stim} was applied to the stimulated membrane as shown in Figure 4.1 (C). For simplicity, the stimulation time duration T_{stim} was set to a constant value as $2\ ms$ and only the stimulation current strength were varied to find the suitable value to start an AP. The stimulation current applied can be described by a piecewise function with smoothing between the maximum value and zero to avoid sudden changes as shown in Figure 4.4 (A). The maximum current strengths $I_{stimmax}$ were set to $50, 100, 150\ and\ 200\ \mu A/cm^2$ to see the effect of stimulation current on the depolarisation of this single myocyte. The resulting transmembrane potentials of a point on the membrane of the myocyte were plotted against time as shown in Figure 4.4 (B) and (C). The point on the membrane was chosen to be at the opposite side of the stimulated membrane to avoid possible distortions caused by the stimulation currents (explained later in section 4.1.6). As shown in Figure 4.4 (B), the transmembrane potential did not rise up to become an AP with a smaller stimulation current $I_{stimmax}$ at $50\ \mu A/cm^2$ while with the other three stimulation currents, the myocytes were all activated to generate an AP. The shapes of the AP are in general the same but the upstroke periods are different as shown in Figure 4.4 (C). The higher stimulation current resulted in a faster upstroke of the AP. The upstroke velocities produced by different stimulation currents were plotted against time in Figure 4.4 (D). It shows that higher stimulation current results in higher maximum upstroke velocities (MUVs).

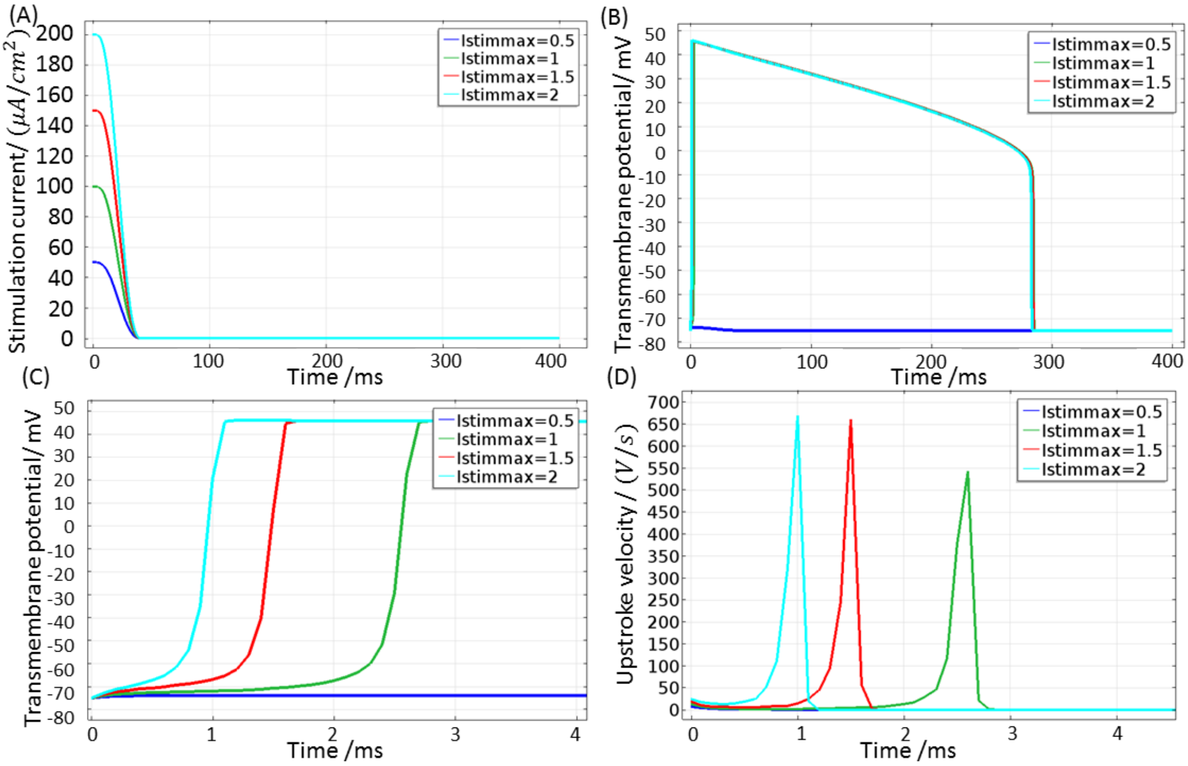

Figure 4.4: (A) Stimulation currents using in the single larval zebrafish myocyte model with the maximum value $I_{stimmax}$ at $50, 100, 150\ and\ 200\ \mu A/cm^2$. (B) Transmembrane potential versus time in the single larval zebrafish myocyte model using different stimulation currents. (C) The first 4 ms of the transmembrane potentials in (B). (D) The time derivatives of transmembrane potential versus time in the first 4 ms.

Secondly, the single myocyte model was activated by setting the initial intracellular potential of the whole myocyte to a value above the resting potential at $-60, -40\ and -20\ mV$. The resulting transmembrane potentials and their time derivatives of transmembrane potential measured at the same point on the membrane as in Figure 4.4 were plotted against time as shown in Figure 4.5 (A) and (C). The first 1 ms during the upstroke period of both plots were shown in Figure 4.5 (B) and (D). It shows that setting the intracellular potential to $-60\ mV$ would not activate the myocyte. Similar to results shown in Figure 4.4, the shapes of the APs of setting intracellular potential at $-40\ and - 20\ mV$ are in general the same but the upstroke of the action potential are different. As shown in Figure 4.5 (D), setting intracellular potential to a higher value as $-20\ mV$ resulted in a higher upstroke velocity at time equal to $0\ ms$ ($560\ V/s$) comparing with $240\ V/s$ of setting to $-40\ mV$. However the upstroke velocity droped after the start time in the $-20\ mV$ case while it increased to $800\ V/s$ in the $-40\ mV$ case. As shown in Figure 4.5 (B), the higher initial intracellular potential at $-20\ mV$ caused a faster upstroke than the $-40\ mV$ case. It implies that although the higher initial intracellular potential resulted in a faster upstroke, the MUV could be smaller. The MUV as a key AP parameter of evaluating the upstroke of the APs could be misunderstood if the myocyte is stimulated by setting the initial intracellular potential to a higher value. However as shown in Figure 4.5 (B) and (D), there are only two data points during the upstroke as the time step used in here is $0.1\ ms$. A smaller time step may be able to provide a better result. Therefore, the time steps of the simulation were varied in next section.

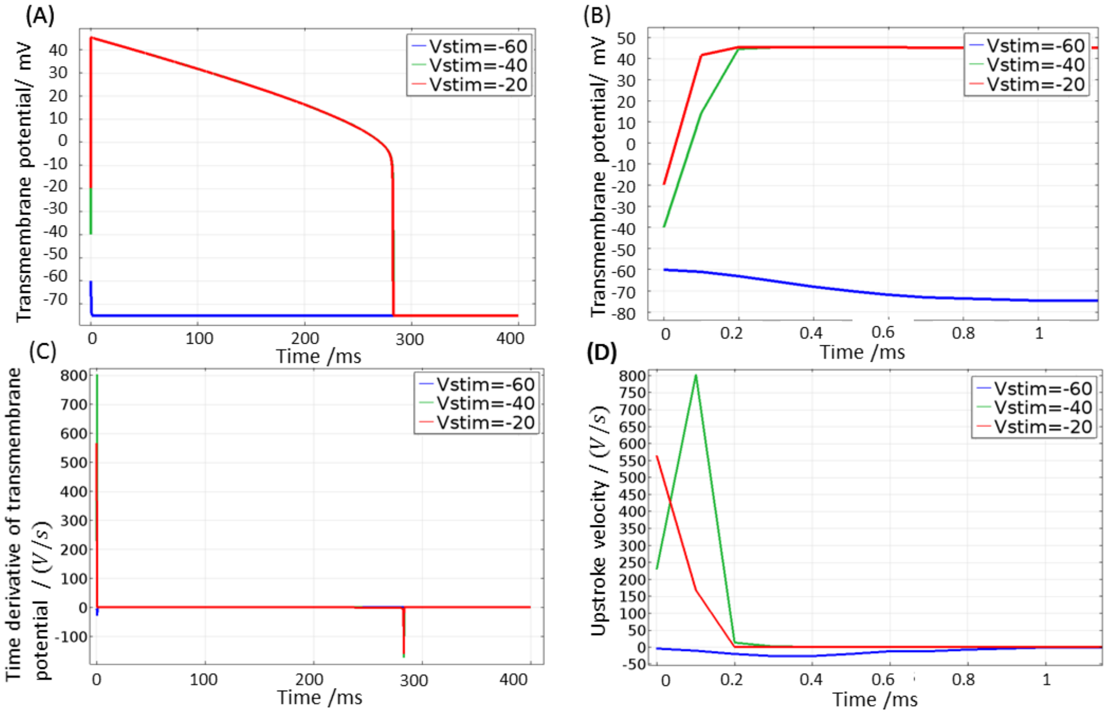

Figure 4.5: (A) Transmembrane potential versus time in the single larval zebrafish myocyte model by setting the intracellular potential to different values above the resting potential. (B) The first 4 ms of the transmembrane potentials in (A). (C) The corresponding time derivative of transmembrane potential versus time. (D) The first 4 ms of the time derivative of transmembrane potential in (D) during the upstroke period.

4.1.5 Time step investigation

As found in the last section, it usually takes about $0.2\ ms$ for the single larval zebrafish myocyte model to reach its maximum voltage using setting a higher initial intracellular potential than the resting potential. The time step used in this case is $0.1\ ms$ which means there are only two data points during the upstroke period. In order to investigate whether the time step of the simulation would affect the modelling results, the time steps were varied to a much longer value as $1\ ms$ and also to a much shorter value as $0.1\ ms$. Two stimulation methods were tested. The first is by applying a stimulation current with the maximum magnitude at $150\ \mu A/cm^2$ to the stimulated membrane as shown in Figure 4.1 (C) same to the results in red line in Figure 4.4. The second is by setting the initial intracellular potential to $-40\ mV$ same to the results in green line in Figure 4.5. The upstroke velocities using both stimulation methods were plotted against time in Figure 4.6. The time steps of the simulation are $1\ ms$ in Figure 4.6 (A) and $0.01\ ms$ in Figure 4.6 (B). It is shown in Figure 4.6 (A) that the time step of $1\ ms$ fails to capture the variation of the upstroke velocities during the upstroke period. Using this $1\ ms$ time step would give a wrong maximum upstroke velocity at $230\ V/s$ for stimulation current method and $20\ V/s$ for the higher initial intracellular potential method. As shown in Figure 4.6 (B), the whole upstroke period was illustrated at a better resolution with the smaller time step as $0.01\ ms$. Surprisingly the maximum upstroke velocities produced by the model using the $0.01\ ms$ time step are similar to the results produced by the model using the $0.1\ ms$ time step. For model using the stimulation current, the MUV with the time step at $0.01\ ms$ is $650\ V/s$ which is same to $650\ V/s$ produced by the model with the time step at $0.1\ ms$ as shown in Figure 4.4 (D). For model using the initial intracellular potential method, the MUV with the time step at $0.01\ ms$ is $800\ V/s$ which is also same to $800\ V/s$ produced by the model with the time step at $0.1\ ms$ as shown in Figure 4.5 (D).

In summary, the time step of the simulation affects the MUV when the time step is much longer than the upstroke period. But increasing the time step of the stimulation would not affect the MUV when there are up to two data points during the upstroke period. Therefore, the time step used in the previous section at 0.1 ms is a reasonable value and will be applied to all models introduced later unless otherwise specified.

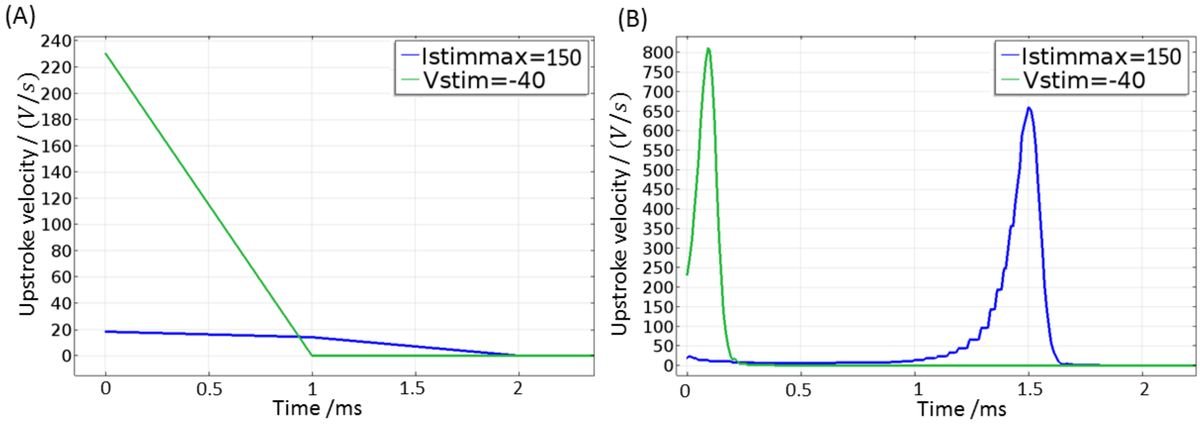

Figure 4.6: The first 2 ms of the time derivative of transmembrane potential during upstroke period with time step as (A) 1 ms and (B) 0.01 ms using two stimulation methods. The blue line is for applying a stimulation current with the maximum magnitude at 150 $\mu A/cm^2$. The green line is for setting the initial intracellular potential to $-40\ mV$.

4.1.6 Measurement of the AP

As the MUV is a sensitive parameter of the AP which could be affected by the stimulation method applied to the model, in this section, the MUV was plotted on the whole membrane of the single myocyte to find the best measurement point of the AP. As shown in Figure 4.7 (A), the model was stimulated by a current with the maximum magnitude at 150 $\mu A/cm^2$. The MUVs produced by this model near the stimulated membrane varied from 600 V/s to up to 1000 V/s while the other side of the myocyte has uniform MUVs at about 600 V/s. This implies that the modelling results could be affected and distorted because of the injection of the stimulation current. This is because the stimulated membrane was applied with a large number of charges which cause sudden and fast changes of the transmembrane potential resulting in a disordered pattern of the MUVs. Therefore the measurement point should be chosen at a point which is far from the stimulated membrane. As shown in Figure 4.7 (B), the model was stimulated by setting the initial intracellular potential of the whole intracellular space to $-40\ mV$ and the resulting MUVs were uniform on the whole membrane at about $800\ V/s$. By setting the initial intracellular potential of the whole myocyte, the transmembrane potentials on all membranes were changed spontaneously, thus a uniform pattern of the MUVs was shown. Therefore in this case, the measurement point can be chosen at any place.

Note that all models shown before are using the measurement point marked in black in Figure 4.7 to plot the results. This measurement point is an optimal point that avoids the distortions caused by the stimulation methods.

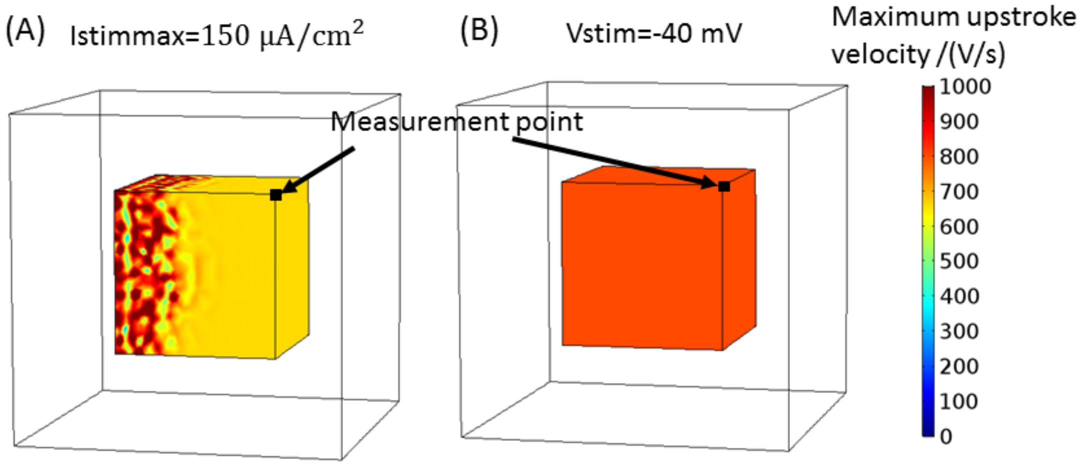

Figure 4.7: The MUV of the whole membrane of the single larval zebrafish myocyte produced by (A) the model using a stimulation current with the maximum magnitude at $150\ \mu A/cm^2$; and (B) the model using an initial intracellular potential at $-40\ mV$. The colour bar is from $0\ V/s$ in blue to $1000\ V/s$ in red.

4.1.7 AP comparison

The key AP parameters for the single larval zebrafish ventricular myocyte model are compared with the previous ventricular AP produced in the previous zebrafish heart model [36] in Table 4.2 together with the experimental results of larval zebrafish in different development stages found in the literature. Initially only the myocyte in the 72 hpf zebrafish heart was aimed to simulate, however the AP parameters of 72 hpf zebrafish in the literature were very limited and some of them had not been found. Therefore the 48 hpf zebrafish was also included for reference. Note that all APDs described later are APD80 as in Chapter 2 which is calculated by the time at 80% repolarization minus the time at 20% depolarization.

From Table 4.2, it is found that the resting potential and AP amplitude produced by the single larval zebrafish myocyte model were very close to the results produced by the previous zebrafish heart model [36]. From the previous study of the FHN model [36], it is known that the resting potential is controlled by the parameter “B” and the AP amplitude are controlled by the parameter “A”. Thus it shows that same “A” and “B” of the FHN model resulted in the same effects of AP in the single myocyte model and the previous zebrafish heart model.

However the MUVs and maximum downstroke velocities produced by the single myocyte model ($540\ to\ 800\ V/s$ and $-144\ to - 150\ V/s$) were hundreds of times bigger than those produced by the previous heart model ($4.16\ V/s$ and $-1.7\ V/s$). The MUVs and maximum downstroke velocities produced by the single myocyte model has a range because of different stimulation methods used. However the effect of the stimulation method would not contribute to the difference as large as hundreds of times. This large difference of MUVs and maximum downstroke velocities could have various explanations. From the aspects of the electrical model used, two different approaches are taken. Specifically, the previous heart model uses the bidomain model where the ion currents are defined everywhere and act as sources for coupled diffusion equations describing the propagation of changes in the intracellular and extracellular potential. In the single myocyte model, the ion currents were only defined on the membrane boundaries and the Laplace’s equations were defined everywhere in the domains. In addition, the previous heart model is computed at a time step at $1\ ms$ which is too long to produce a reliable result of MUV as explained in section 4.1.5.

Given the MUVs in the myocyte model are much larger than the measured values, in order to replicate the real measured APs in the larval zebrafish, the parameters of the FHN model in the myocyte model were adjusted next. As shown in Table 4.2, some AP parameters produced by the previous heart model do not resemble the experimental results to a very good extent. For example the MUV produced by the previous heart model is $4.16\ V/s$ comparing with $6-7.15\ V/s$. Therefore, the adjustments made to the FHN parameters in the myocyte model aimed to resemble the experimental results found in the literature as close as possible rather than resemble the modelling results of the previous zebrafish heart model.

Table 4.2: The key AP parameters produced by the single larval zebrafish ventricular myocyte model using the same FHN parameters as the previous larval zebrafish heart model [36] comparing with the results of the previous larval zebrafish heart model and experimental results of 48 hpf and 72 hpf zebrafish found in literature.

	Resting potential/ mV	MUV/(V/s)	Maximum down stroke velocity/(V/s)	AP amplitude/mV	APD /ms
Single myocyte model	-75	540-800	-144-150	121	280
Previous heart model [36]	-75	4.16	-1.7	116	329
Experimental results of 48 hpf zebrafish	-66[11], -70[5], -78.5[56]	6[5],7.15[56]	-1.69[56]	91.9[11],104[5], 117[56]	231[11], 272[5], 350[56]
Experimental results of 72 hpf zebrafish	No data	7.5-9[57]	No data	No data	220[57]

4.1.8 Adjustments of the FHN parameters

The parameters used in the single larval zebrafish myocyte model were adjusted in this section to replicate the measured AP of the 48 hpf zebrafish shown in Table 4.2. The stimulation current with the maximum magnitude at $150\ \mu A/cm^2$ applied to a boundary of the myocyte were chosen to be the stimulation method for the following models and later will be compared with initial voltage stimulation method. The AP of the myocyte was measured at the measurement point as shown in Figure 4.7.

4.1.8.1 Varying “c1” in the FHN model

First, parameters in the FHN model were adjusted to achieve the measured MUV of the 48 hpf zebrafish AP. From the previous study of the FHN model in [36], it is found that the parameters “c1” and “c2” control the upstroke and downstroke of the AP. In this myocyte model, the parameter “c1” was varied with all other parameters fixed. The APs and the time derivatives of the transmembrane potential produced by the models with the various parameters “c1” were plotted in Figure 4.8 (A) and (C) and these plots for the upstroke period were plotted in Figure 4.8 (B) and (D). As shown in Figure 4.8 (B), with reducing the parameter “c1”, the upstroke period of the AP became longer and also the MUVs reduced. For example, the MUV reduced from $660\ V/s$ with “c1” equal to 0.572 to $30\ V/s$ with “c1” equal to 0.007. From Figure 4.8 (A) it is found that the reduction of “c1” not only reduced the MUV, but also reduced the APD. The APD produced by the model using the smaller “c1” of 0.007 is $19\ ms$ which is 15 times smaller than $280\ ms$ produced by the model using the original “c1” of 0.572. The MUVs and the APDs were plotted against the parameter “c1” in Figure 4.9. It is shown that the MUVs and the APDs increased with the increase of parameter “c1”. By reducing “c1” to 0.007, the MUV reduced to $30\ V/s$ which is much closer to the real MUV of 48 hpf zebrafish AP as shown in Table 4.2. However the resulting APD is too short as $19\ ms$. Therefore, other parameters in the FHN model need to be adjusted to increase the model APD.

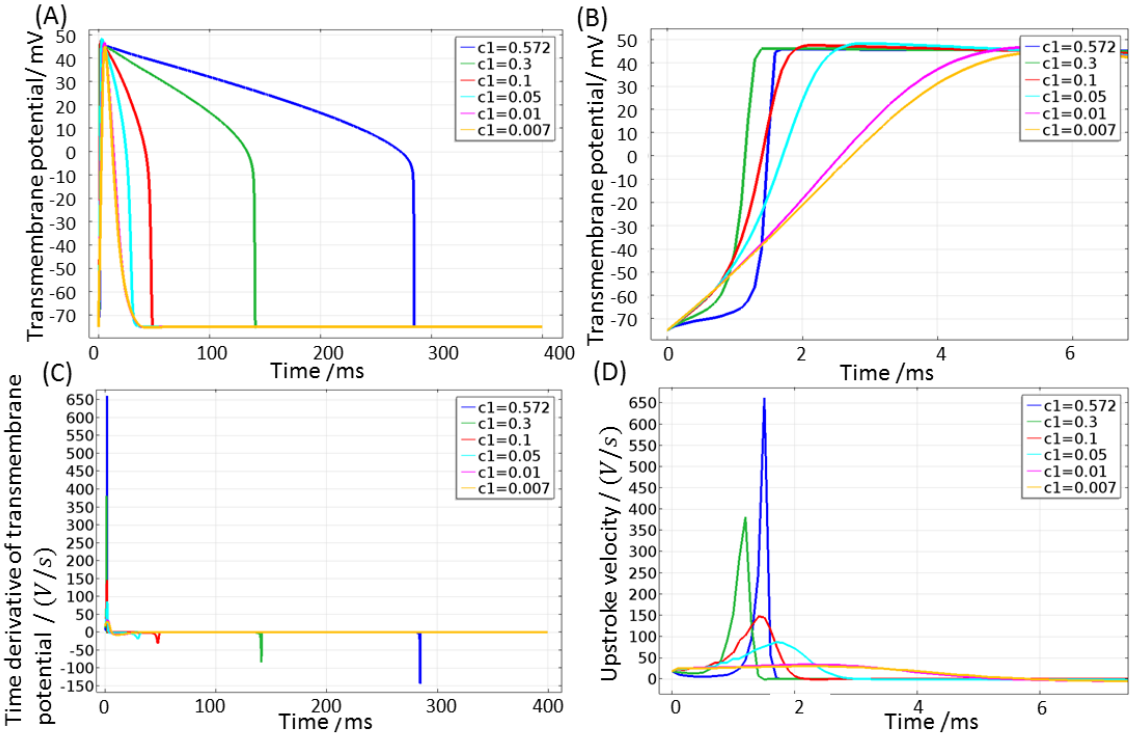

Figure 4.8: (A) APs of the single larval zebrafish myocyte model with varying “c1” parameter in the FHN model. (B) The APs during the upstroke period in (A). (C) The time derivatives of transmembrane potential versus time with varying “c1” parameter in the FHN model. (D) The time derivatives of transmembrane potential versus time in (D) during upstroke period.

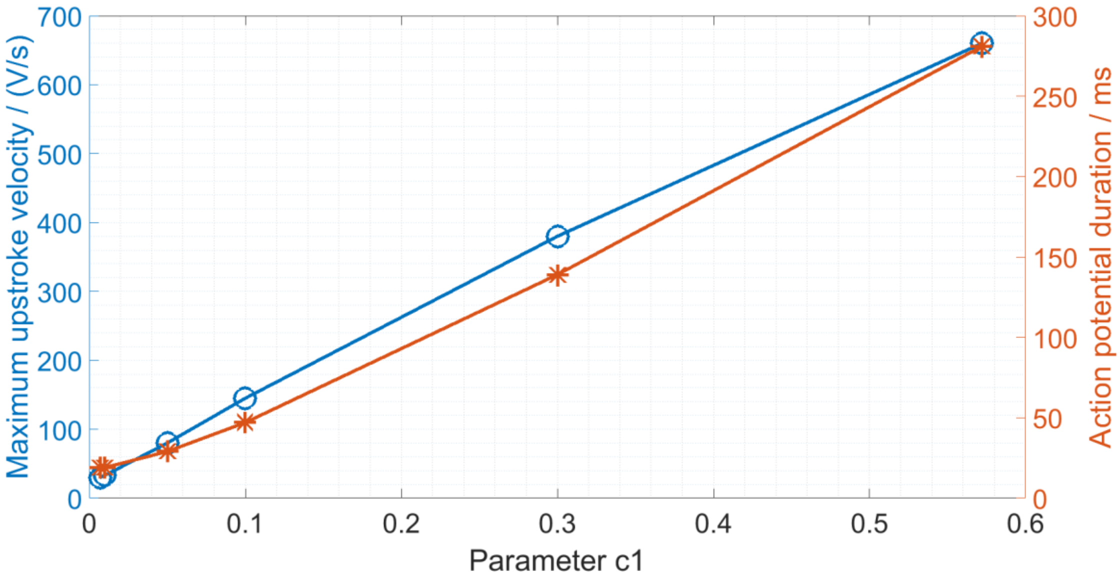

Figure 4.9: The MUV and the APD of the APs produced by the single larval zebrafish myocyte model versus the parameter “c1”

4.1.8.2 Varying "e" in the FHN model

From the previous study of FHN model in [36], the parameter "e" affects the APD. Therefore, the parameter "e" in the single myocyte model was varied with the parameter "c1" fixed at 0.007. The resulting APs with various parameters "e" were plotted in Figure 4.10 (A) and the corresponding time derivatives of transmembrane potential were plotted against time in Figure 4.10 (C). Both plots were plotted for the upstroke period in Figure 4.10 (B) and (D). In addition, the MUVs and the APDs were plotted against the parameter "e" in Figure 4.11. It is shown in Figure 4.10 (A) and (D) that with the decrease of the parameter "e", the APDs increased while the MUVs did not change much. As shown in Figure 4.10 (A), the APD produced by the model with the parameter "e" equal to 0.000013 is $289\ ms$ which is in the range of the measured APD ($231\ ms$ to $350\ ms$) of the 48 hpf zebrafish as shown in Table 4.2. However the AP shows a hump as high as $70\ mV$ comparing with the 40 mV of the original model. This hump of AP resulted in a bigger AP amplitude at $145\ mV$ which is much larger than the reference ranging from $90\ mV$ to $117\ mV$ as shown in Table 4.2. This hump during the upstroke period of the AP could be caused by the injection of a large stimulation current. Therefore, the stimulation current was reduced in the next step.

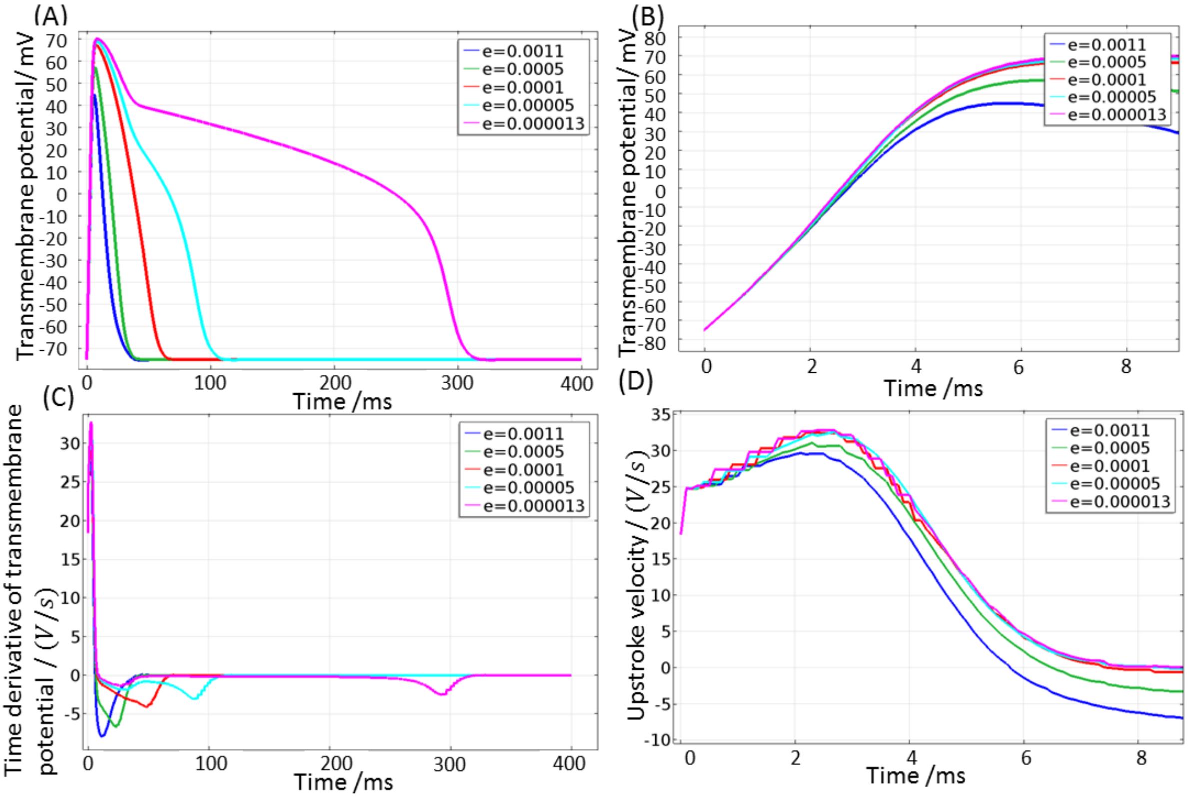

Figure 4.10: (A) APs of the single larval zebrafish myocyte model with varying “e” parameter in the FHN model. (B) The APs during the upstroke period in (A). (C) The time derivatives of transmembrane potential versus time with varying “c1” parameter in the FHN model. (D) The time derivatives of transmembrane potential versus time in (D) during upstroke period.

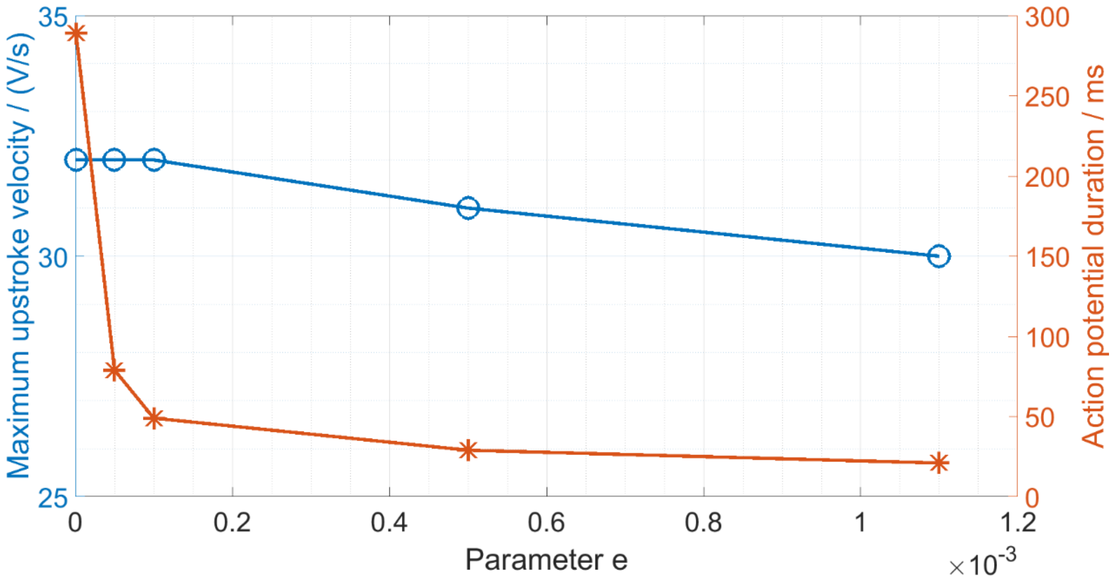

Figure 4.11: The MUVs and the APDs produced by the single larval zebrafish myocyte model versus the parameter “e”

4.1.8.3 Varying the stimulation current

The maximum magnitude of the stimulation current is reduced gradually from 150 $\mu A/cm^2$ with the parameter “e” fixed to 0.000013. The resulting APs and time derivatives of transmembrane potential were plotted in Figure 4.12 (A) and (B). It is shown that with the decrease of the stimulation current, the AP amplitudes and the MUVs both reduced. As shown in Figure 4.12 (A), there is no hump during the upstroke period produced by the model using a smaller stimulation current of $50\ \mu A/cm^2$ in maximum. The AP amplitude produced by this model was 120 mV which is a little bigger than the reference ranging from 92 mV to 117 mV and the MUV was 7.6 V/s which is very close to the reference ranging from 6 V/s to 7.15 V/s as shown in Table 4.2. Therefore the stimulation current with the maximum magnitude of 50 $\mu A/cm^2$ were chosen.

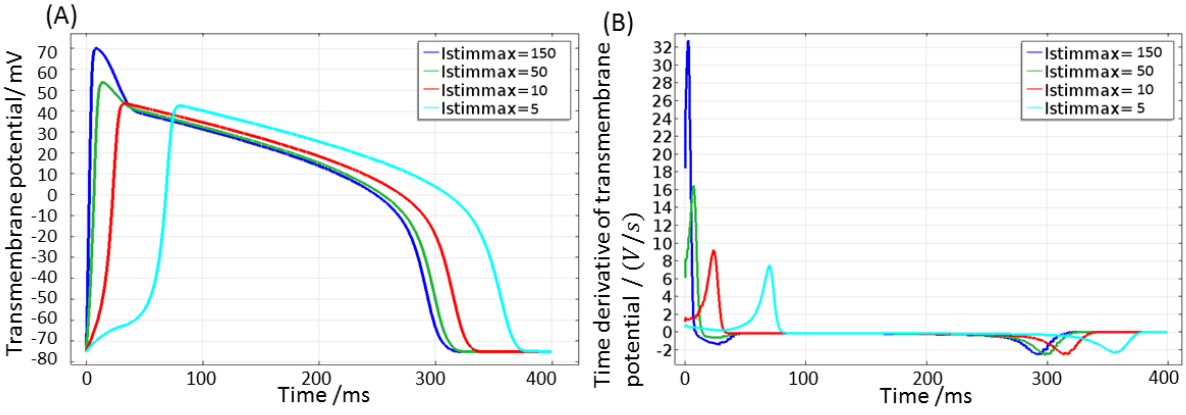

Figure 4.12: (A) APs of the single larval zebrafish myocyte model with varying stimulation currents. (B) (B) The time derivatives of transmembrane potential versus time with varying stimulation currents.

4.1.8.4 Varying “A” and “B” in the FHN model

Based on the previous study of the FHN model [36], the parameter “A” controls the AP amplitude and parameter “B” controls the resting potential. Therefore, with the stimulation current fixed to $50\ \mu A/cm^2$, the parameter “A” were varied to reduce the AP amplitude. Meantime, in order to investigate the effect of parameter “B” on the AP, it was changed from $-75\ mV$ to $-70\ mV$ which is still in the range of the reference resting potential as shown

Table 4.2. The initial intracellular potential was also changed to $-70\ mV$. The resulting APs and time derivatives of transmembrane potential were plotted in Figure 4.13 (A) and (B). As shown in Figure 4.13 (A), the parameter "B" changed from $-75\ mV$ to $-70\ mV$, thus the resting potential changed from $-75\ mV$ to $-70\ mV$. The AP amplitude reduces to $106\ mV$ produced by the model with "A" equal to 0.108 from $120\ mV$ produced by the model with "A" equal to 0.1205. The new resting potential and AP amplitude are still in the range of the measured results as shown in Table 4.2. As shown in Figure 4.13 (B), the MUV reduces a little to 7.1 V/s produced by the model with new "A" and "B" from 7.6 V/s which is more close to the measured result ranging from 6 V/s to 7.15 V/s.

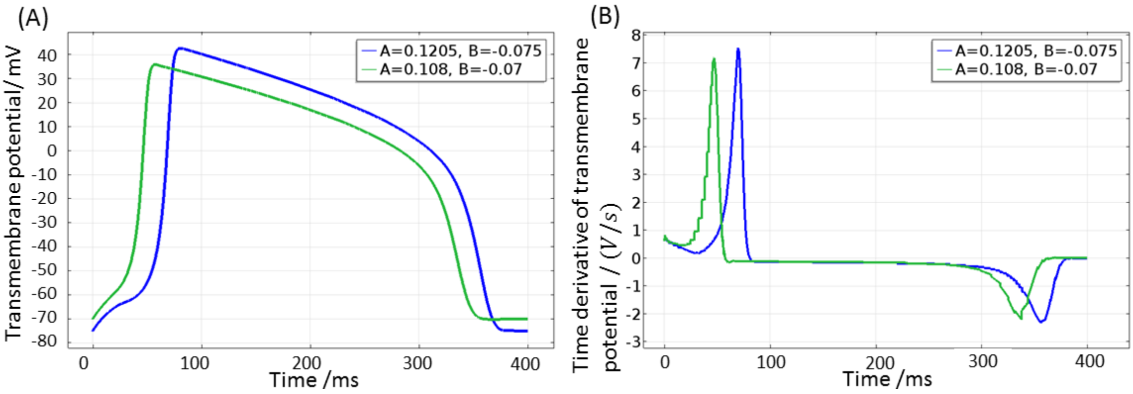

Figure 4.13: (A) APs of the single larval zebrafish myocyte model with varying parameter "A" and "B" in the FHN model. (B) The time derivative of transmembrane potential versus time with varying parameter "A" and "B" in the FHN model.

4.1.8.5 Comparison with the voltage stimulation method

The stimulation method in the myocyte model for 48 hpf zebrafish was changed to set initial intracellular potential to a value higher than the resting potential using the final settings of parameters in the FHN model. The initial intracellular potentials were varied to -50, -40 and -20 mV and the resulting transmembrane potentials and their time derivatives were plotted against time in Figure 4.14. As shown in Figure 4.14 (A), the depolarisations of the myocyte started earlier than using the stimulation current shown in Figure 4.13. The MUVs are about 9 V/s which are larger than 7.15 V/s using the stimulation current shown in Figure 4.13. As is shown in the previous section that larger stimulation currents lead to larger MUVs, if the stimulation current used in Figure 4.13 increases, the resulting MUV would increase as well which is similar to the 9 V/s produced by the model using voltage stimulation method. Therefore, it can be concluded that both stimulation methods are able to start an AP with the same effects on the AP parameters such as the MUV. The stimulation current method was chosen to use in the models introduced later because of the ease of adjustment. The stimulation voltage method is also an applicable approach to start an AP and will be used in the larval zebrafish heart model in Chapter 7.

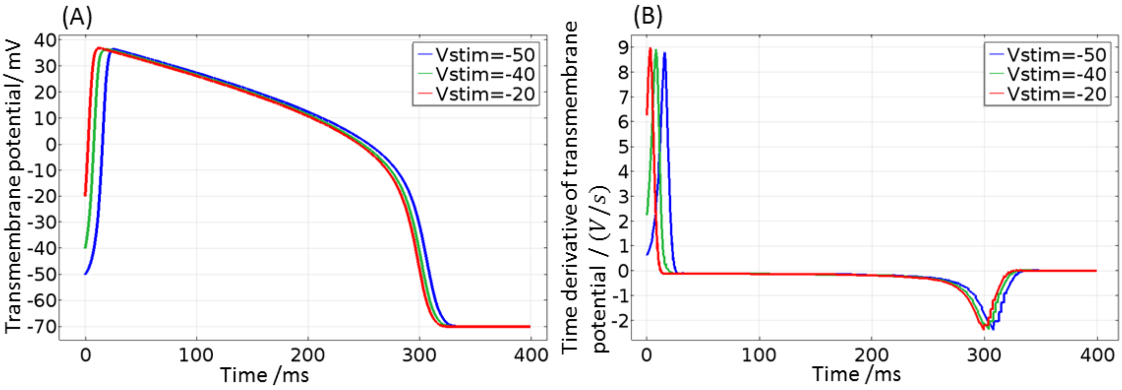

Figure 4.14: (A) APs of the single larval zebrafish myocyte model with varying initial intracellular potentials. (B) The time derivative of transmembrane potential versus time with varying initial intracellular potentials.

4.1.8.6 Final parameters used in the single larval zebrafish myocyte models

For the 72 hpf case, it is found that direct electrophysiological AP measurements were not available as a fluorescence technique was used. Although this technique reported the shape of the AP, several key AP parameters such as the resting potential and the AP amplitude were not shown. Therefore, these unknown values were assumed to be same as the 48 hpf zebrafish case. In addition, the MUV is inferred by assuming an AP amplitude of 100 mV and scaling the data appropriately which gave a comparable value to the 48 hpf zebrafish case. The single myocyte model of the 72 hpf zebrafish was developed using a similar optimisation process of the model parameters which is not specified here. The final parameters of the FHN model for both models are shown in Table 4.3 comparing with the parameters in [36] which are used at the start of the single myocyte model. Briefly, the parameter “c1” was reduced to reduce the MUV. As a consequence, the APD reduced. Then the parameter “e” was reduced to bring back the APD. After that, it is found there is a hump of the transmembrane potential as high as $70\ \mathrm{mV}$ which gives a large AP amplitude with the smaller “e”. It is assumed to be blamed for a large stimulation current. Therefore the stimulation current was reduced and found there is no hump of the transmembrane potential with a smaller stimulation current. However the AP amplitude was a little larger than the measured result. Thus, the parameter “A” and “B” were reduced to reduce AP amplitude and offset the resting potential. Note that the stimulation method used in both models are the same which is to apply a stimulation current with its maximum magnitude at $50\ \mu A/cm^2$ to the stimulated membrane. Note that in both cases where a range of values for a parameter is reported in the literature, midrange values were taken, otherwise the modelled parameters were adjusted to be as close as possible to measured values with the maximum tolerance of up to 25% being allowed for down stroke velocity, which does not determine CV values. This selection criteria of parameters in the FHN model also applied for all models described later.

Table 4.3: Comparison of parameters of the FHN model used in the single myocyte model and the previous larval zebrafish heart model for ventricle [36].

FHN model parameters	Reported parameters[36]	48 hpf zebrafish single myocyte	72 hpf zebrafish single myocyte
a	0.13	0.13	0.13
b	0	0	0
c1	0.572	0.007	0.0085
c2	0.5	0.5	0.5
d	1	1	1
e	0.0011	0.000013	0.0000225
A	0.1205	0.108	0.108
B	-0.075	-0.07	-0.07
k	1000	1000	1000

The resulting APs of the single myocyte model for 48 hpf and 72 hpf zebrafish are shown in Figure 4.15 (A) and the time derivatives of transmembrane potential for both models were plotted against time in Figure 4.15 (B). The key AP parameters of both models were compared to the experimental results in the literature in Table 4.4. It is shown that the modelling key AP parameters show good agreements to the experimental results.

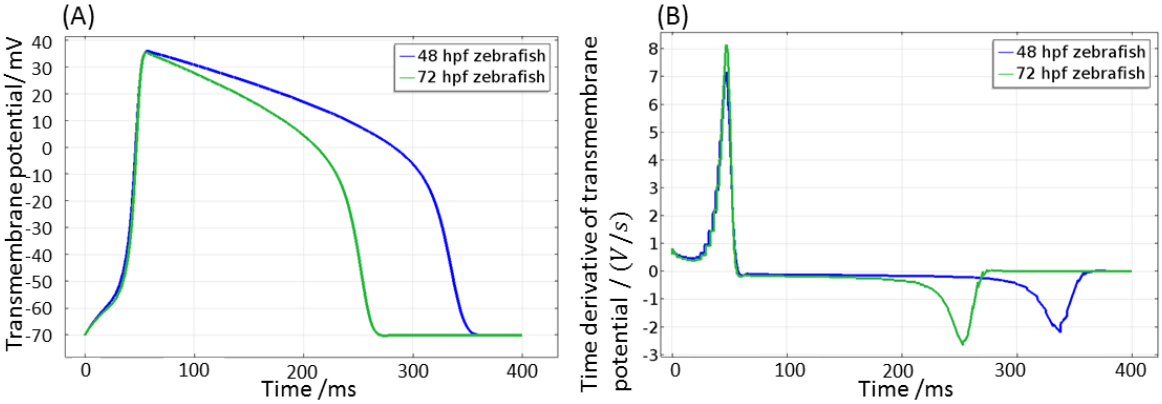

Figure 4.15: (A) APs of the single larval zebrafish myocyte model of 48 hpf zebrafish and 72 hpf zebrafish. (B) The time derivatives of transmembrane potential versus time produced by the single larval zebrafish myocyte model of 48 hpf zebrafish and 72 hpf zebrafish.

Table 4.4: The key AP parameters produced by the single myocyte model of 48 hpf zebrafish and 72 hpf zebrafish comparing with experimental results of 48 hpf and 72 hpf zebrafish found in the literature.

	Resting potential/ mV	MUV/(V/s)	Maximum down stroke velocity/(V/s)	AP amplitude/ mV	APD at 80% repolarization / ms
Single myocyte model for 48 hpf zebrafish	-70	7.1	-2.1	106	300
Experimental results of 48 hpf zebrafish	-66[11], -70[5], -78.5[56]	6[5],7.15[56]	-1.69[56]	91.9[11],104[5], 117[56]	231[11], 272[5], 350[56]
Single myocyte model for 72 hpf zebrafish	-70	8.1	-2.5	116	220
Experimental results of 72 hpf zebrafish	No data	7.5-9[57]	No data	No data	220[57]

4.2 Single human myocyte model

4.2.1 Model geometry and electrical model

A micrograph of a human ventricular myocyte is shown in Figure 4.16 (A). It is typically about $99-108\ \mu m$ in length [126] and the cross section area is around $205.25-283.39\ \mu m^2$ [126]. In this model as shown in Figure 4.16 (B), the human ventricular myocyte was simplified as a block with $100\ \mu m$ in length and its cross section area is a square with edge lengths of $17.32\ \mu m$ which gives a cross section area of $300\ \mu m^2$. This myocyte was placed in the middle of the extracellular space in $200\ \mu m\ \times 18.17\ \mu m \times\ 18.17\ \mu m$. The cross section area of the extracellular space was chosen to replicate the measured extracellular volume fraction [99]. The extracellular volume fraction is defined as the percentage of the cross section area of the extracellular space in the overall spaces. The extracellular volume fraction of the model is 10% which is same as in [99].

The electrical model is the same as the zebrafish myocyte model and the electrical parameters such as the extracellular and intracellular conductivities were the same as well. The stimulation of the human ventricular myocyte is similar to the zebrafish myocyte model which is by injecting a stimulation current to the stimulated membrane of the myocyte as shown in Figure 4.16 (B).

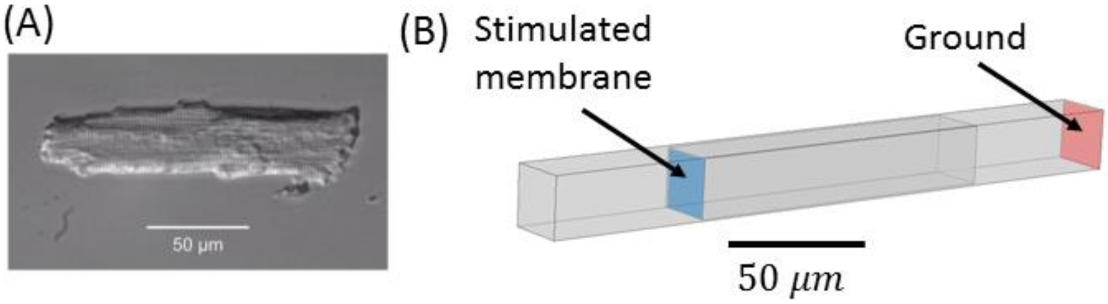

Figure 4.16: (A) The micrograph of a typical human ventricular myocyte from [127]. Scale bar: $50\ \mu m$; (B) Geometry of single human ventricular myocyte model. Scale bar: $50\ \mu m$. The stimulation current is applied to the myocyte membrane in blue. The ground boundary condition is applied to the extracellular space boundary in red.

4.2.2 Ionic current models

To compare the phenomenological model and the biophysical models, two ionic current models were applied to this human ventricular myocyte model. One is the FHN model same to the larval zebrafish myocyte model, the other is the Luo and Rudy model (LR model) [43].

4.2.2.1 FHN model

Firstly, the FHN model was applied to the single human myocyte model. The parameters in the FHN model were adjusted to match the measured APs as shown in Table 4.7 through similar optimisation process as the zebrafish myocyte model and the final parameters are shown in Table 4.5. The stimulation current was changed from the values used in the zebrafish myocyte model. This was because it is found that a bigger stimulation current was needed in the human myocyte model to have a similar effect of activating the APs as the zebrafish myocyte model. Therefore, the final time duration of the stimulation current used in this human model was changed to $10\ ms$ which is larger than $2\ ms$ in the zebrafish model. Three different maximum magnitudes of the stimulation current were used to activate the human myocyte as $50, 80\ and\ 150\ \mu A/cm^2$. The resulting APs of the human myocyte model using the FHN model using these three stimulation currents were shown in Figure 4.17 (A). The corresponding time derivatives of transmembrane potential were plotted against time in Figure 4.17 (B). It is shown that the larger stimulation currents are, the faster the myocytes were activated which is consistent with the modelling results of the zebrafish model. In addition, the MUVs increased with the increase of the stimulation currents. Except for the MUV, the key AP parameters such as the AP amplitude and APD are not affected by the stimulation current. The key AP parameters produced by model using the stimulation current at $80\ \mu A/cm^2$ were chosen to compare with the measured human APs in Table 4.7 along with the modelling results produced by the LR model described later.

Table 4.5: Parameters of the FHN model used in the single human ventricular myocyte

FHN model parameters	parameters
a	0.13
b	0
c1	0.19
c2	0.5
d	1
e	0.00035
A	0.1205
B	-0.08
k	1000

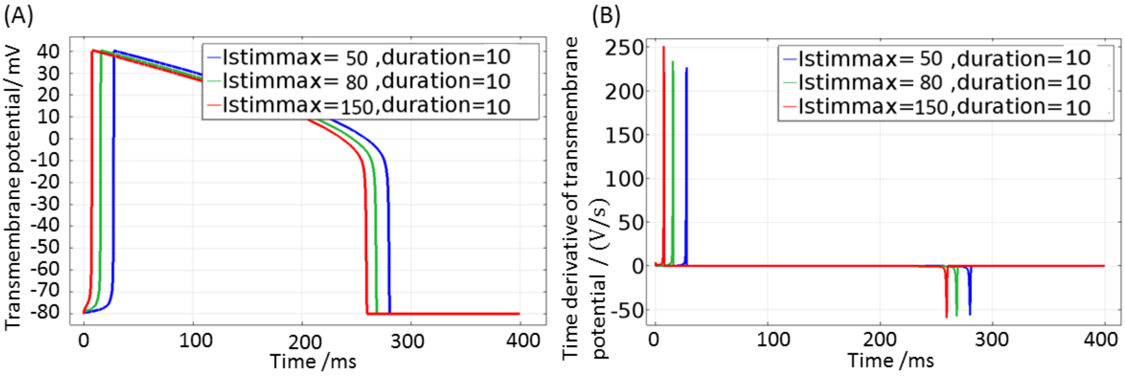

Figure 4.17: (A) APs of the single human myocyte model using the FHN model with various stimulation currents. (B) The time derivatives of transmembrane potential versus time of the single human myocyte model using the FHN model with various stimulation currents.

4.2.2.2 LR model

The LR model was then applied to the single human myocyte model. The LR model was chosen because it has been applied to a discrete human cardiac tissue model before [98]. Therefore, the modelling results can be directly compared with theirs. This LR model [43] has six ionic currents: a fast sodium current I_{Na}, a slow inward current I_{si}, a time-dependent potassium current I_K, a time-independent potassium current I_{K1}, a plateau potassium current I_{Kp} and a time-independent background current I_b. The ionic currents are determined by ionic gating variables. The gating variables are computed from a coupled system of eight nonlinear ordinary differential equations. Change of ionic currents changes the transmembrane potential which will also affect the ionic gating variables and the ionic currents. The differential equations are in the form:

$$\frac{dy}{dt} = \frac{y_\infty - y}{\tau_y} \tag{4.12}$$

where

$$\tau_y = \frac{1}{\alpha_y + \beta_y} \tag{4.13}$$

$$y_\infty = \frac{\alpha_y}{\alpha_y + \beta_y} \tag{4.14}$$

y is any gating variable, τ_y is the time constant of the gating variable, and y_∞ is the steady-state value of y. α_y and β_y are voltage-dependent rate constants. Note that α_y and β_y of the time-independent potassium current I_{K1} depend on the extracellular potassium concentration.

The sum of the six ionic currents is the total ionic current I_{ion} similar to the Hodgkin-Huxley model described in Chapter 2:

$$I_{ion} = I_{Na} + I_{si} + I_K + I_{K1} + I_{Kp} + I_b \tag{4.15}$$

Each ionic current is described below:

Fast sodium current:

$$I_{Na} = 23 \times m^3 \times h \times j \times (V - E_{Na}) \tag{4.16}$$

For $V \geq -40\ mV$

$$\alpha_h = \alpha_j = 0 \tag{4.17}$$

$$\beta_h = \frac{1}{0.13 \times [1 + \exp\left(\frac{V + 10.66}{-11.1}\right)]} \tag{4.18}$$

$$\beta_j = 0.3 \times \frac{\exp\left(-2.535 \times 10^{-7} V\right)}{1 + \exp[-0.1 \times (V + 32)]} \tag{4.19}$$

For $V < -40\ mV$

$$\alpha_h = 0.135 \times \exp\left(\frac{80 + V}{-6.8}\right) \tag{4.20}$$

$$\beta_h = 3.56 \times \exp(0.079V) + 3.1 \times 10^5 \times exp(0.35V) \tag{4.21}$$

$$\begin{aligned}\alpha_j = {} & [-1.2714 \times 10^5 \times \exp(0.2444V) \\ & - 3.474 \times 10^5 \times \exp(-0.0439V)] \\ & \times \frac{V + 37.78}{1 + \exp[0.311 \times (V + 79.23)]}\end{aligned} \tag{4.22}$$

$$\beta_j = 0.1212 \times \frac{\exp(-0.01052V)}{1 + \exp[-0.1378 \times (V + 40.14)]} \tag{4.23}$$

For all range of V

$$\alpha_m = 0.32 \times \frac{V + 47.13}{1 + \exp[-0.1 \times (V + 47.13)]} \tag{4.24}$$

$$\beta_m = 0.08 \times \exp\left(-\frac{V}{11}\right) \tag{4.25}$$

Slow inward current:

$$I_{si} = 0.09 \times d \times f \times (V - E_{si}) \tag{4.26}$$

$$E_{si} = 7.7 - 13.0287 \times \ln([Ca]_i) \tag{4.27}$$

$$\alpha_d = 0.095 \times \frac{\exp[-0.01 \times (V - 5)]}{1 + \exp[-0.072 \times (V - 5)]} \tag{4.28}$$

$$\beta_d = 0.07 \times \frac{\exp[-0.017 \times (V + 44)]}{1 + \exp[0.05 \times (V + 44)]} \tag{4.29}$$

$$\alpha_f = 0.012 \times \frac{\exp[-0.008(V + 28)]}{1 + \exp[0.15 \times (V + 28)]} \tag{4.30}$$

$$\beta_f = 0.0065 \times \frac{\exp[-0.02 \times (V + 30)]}{1 + \exp[-0.2 \times (V + 30)]} \tag{4.31}$$

Calcium uptake:

$$\frac{d([Ca]_i)}{dt} = -10^{-4} \times I_{si} + 0.07 \times (10^{-4} - [Ca]_i) \tag{4.32}$$

Time-dependent potassium current:

$$I_K = \overline{G_k} \times X \times X_i \times (V - E_K) \tag{4.33}$$

$$\overline{G_k} = 0.282 \times \sqrt{\frac{[K]_o}{5.4}} \tag{4.34}$$

For $V > -100mV$

$$X_i = 2.837 \times \frac{\{\exp[0.04 \times (V + 77)] - 1\}}{(V + 77) \times \exp[0.04 \times (V + 35)]} \tag{4.35}$$

For $V \leq -100mV$

$$X_i = 1 \tag{4.36}$$

$$\alpha_X = 0.0005 \times \frac{\exp[0.083 \times (V + 50)]}{1 + \exp[0.057 \times (V + 50)]} \tag{4.37}$$

$$\beta_X = 0.0013 \times \frac{\exp[-0.06 \times (V + 20)]}{1 + \exp[-0.04 \times (V + 20)]} \tag{4.38}$$

Time-independent potassium current:

$$I_{K1} = \overline{G_{k1}} \times K1_\infty \times (V - E_{K1}) \tag{4.39}$$

$$\overline{G_{k1}} = 0.6047 \times \sqrt{\frac{[K]_o}{5.4}} \tag{4.40}$$

$$\alpha_{K1} = \frac{1.02}{1 + \exp[0.2385 \times (V - E_{K1} - 59.215)]} \tag{4.41}$$

$$\beta_{K1} = \frac{0.49124 \times \exp[0.08032 \times (V - E_{K1} + 5.476)]}{1 + \exp[-0.5143 \times (V - E_{K1} + 4.753)]} + \frac{\exp[0.06175 \times (V - E_{K1} - 594.31)]}{1 + \exp[-0.5143 \times (V - E_{K1} + 4.753)]} \tag{4.42}$$

$$E_{K1} = 1 \times 10^3 \times \frac{RT}{F} \times \ln\left(\frac{[K]_o}{[K]_i}\right) \tag{4.43}$$

Plateau potassium current:

$$I_{Kp} = 0.0183 \times \mathrm{Kp} \times \left(\mathrm{V} - E_{Kp}\right) \tag{4.44}$$

$$E_{Kp} = E_{K1} \tag{4.45}$$

$$\mathrm{Kp} = \frac{1}{1 + \exp\left[\frac{7.488 - V}{5.98}\right]} \tag{4.46}$$

Background current:

$$I_b = 0.03921 \times (V + 59.87) \tag{4.47}$$

Total time-independent potassium current:

$$I_{K1(T)} = I_{K1} + I_{Kp} + I_b \tag{4.48}$$

All ionic currents are in $\mu A/cm^2$ and V is the transmembrane potential in mV. G_i is the maximum conductance of channel i (mS/cm^2). m, h, j are activation gate, fast inactivation gate, and slow inactivation gate of I_{Na}. $[A]_o$ and $[A]_i$ are extracellular and intracellular concentrations of ion A respectively (mM). d and f are activation gate and inactivation gate of I_{si}. X and X_i are activation gate and inactivation gate of I_K. $K1$ is the inactivation gate of I_{K1}. y_∞ is the steady-state value of activation (inactivation) gate y. α_y and β_y are opening and closing rate constants of gate y ($msec^{-1}$). τ_y is the time constant of gate y ($msec$). R is the universal gas constant equal to $8.314\ \mathrm{J/(K \cdot mol)}$. T is the temperature which is the human body temperature equal to $309\ K$. F is Faraday's constant equal to $9.649 \times 10^4\ C/mol \cdot$

From the standard settings, the intracellular and extracellular potassium concentrations $[K]_i$ and $[K]_o$ are $145\ mM$ and $5.4\ mM$ respectively. The initial intracellular calcium concentration $[Ca]_i$ is $2 \times 10^{-4}\ mM$. The maximum conductance of the sodium channel $\overline{G_{Na}}$ is $23\ mS/cm^2$ and the reversal potential of sodium E_{Na} is $54.4\ mV$. The reversal potential of sodium E_K is $-77\ mV$ and the maximum conductance of the potassium channel $\overline{G_K}$ is $0.282\ mS/cm^2$.

The initial values of the gating variables are from the values reported in [115] as shown in Table 4.6. The initial value of the transmembrane potential is $-85\ mV$.

Table 4.6: Initial values of the gate variables used in the LR model in the single human myocyte model from [115]

Gating variables	Initial value
m	0.00167
h	0.938
j	1
d	0.00298
f	1
x	0.00602

Similarly to the human myocyte model using the FHN model, the time duration of the stimulation current is $10\ ms$. Three different maximum magnitudes of the stimulation current were used to activate the myocyte as $50, 80\ and\ 150\ \mu A/cm^2$. The resulting APs of the human myocyte model based on the LR model using these three stimulation currents were shown in Figure 4.18 (A). The corresponding time derivatives of transmembrane potential were plotted against time in Figure 4.18 (B). As shown in Figure 4.18 (A), the AP activated by the stimulation current at $150\ \mu A/cm^2$ has a hump as $50\ mV$ in maximum which is higher than 38 mV produced by the model using a smaller stimulation current at $80\ \mu A/cm^2$ while the myocyte was not activated produced by the model using a much smaller stimulation current at $50\ \mu A/cm^2$. In addition, the APD at repolarisation 90% produced by this larger stimulation current at $150\ \mu A/cm^2$ was $360\ ms$ which is a little longer than the $380\ ms$ produced by the smaller stimulation current at $80\ \mu A/cm^2$. As shown in Figure 4.18 (B), the MUVs are also affected by different stimulation currents. Increasing stimulation current from $80\ \mu A/cm^2$ to $150\ \mu A/cm^2$ resulting in the MUVs increasing from $310\ V/s$ to $340\ V/s$. These results show that the stimulation current would affect the shape of AP and should be chosen wisely. The AP produced by the stimulation current at $80\,\mu A/cm^2$ in maximum is least affected by the stimulation current. Therefore, key AP parameters produce by this model were chosen to compare with the other APs later.

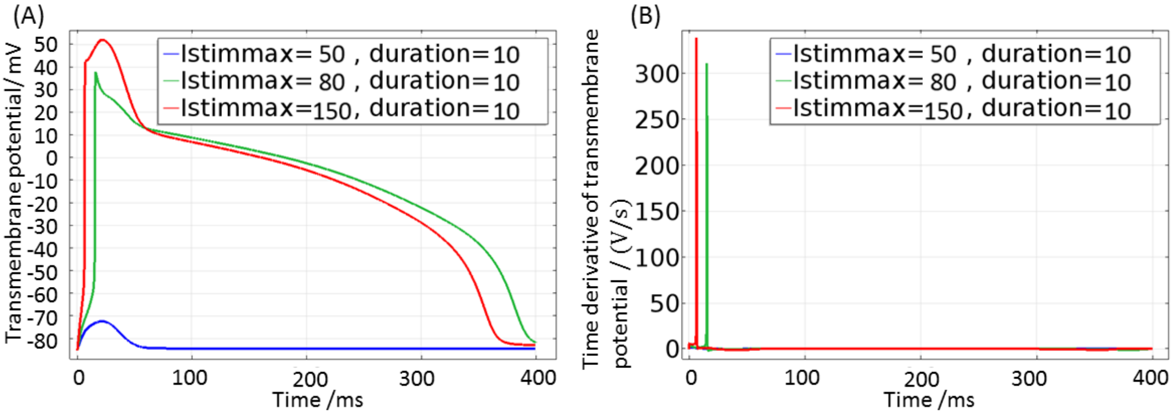

Figure 4.18: (A) APs of the single human myocyte model using the LR model with various stimulation currents. (B) The time derivative of transmembrane potential versus time of the single human myocyte model using LR model with various stimulation currents.

4.2.2.3 AP Comparison

The APs produced by the single human myocyte model using the FHN model and the LR model were plotted with the original AP produced by the LR model in [43] as shown in Figure 4.19. The AP produced by both human myocyte models used the same stimulation current of $80\,\mu A/cm^2$ in maximum. Their key AP parameters were compared with the model AP produced by the LR model in standard settings (extracellular potassium concentration $[K]_o = 5.4\,mM$) [43] and the measured human results in Table 4.7. It shows that the AP produced by the human myocyte model using the LR model is generally similar to the AP produced by the LR model [43]. As shown in Table 4.7, the APD produced by the human myocyte model using the LR model is about 4% longer than the APD produced by the LR model. In addition its MUV is about 23% smaller than that produced by the LR model. For comparison, the AP produced by the human myocyte model using the FHN model has a shorter APD and a smaller MUV which is still in the range of the measured human results. As shown in Figure 4.19, there is a notch after the peak of AP known as the phase 1 in both LR models but not in the FHN model.

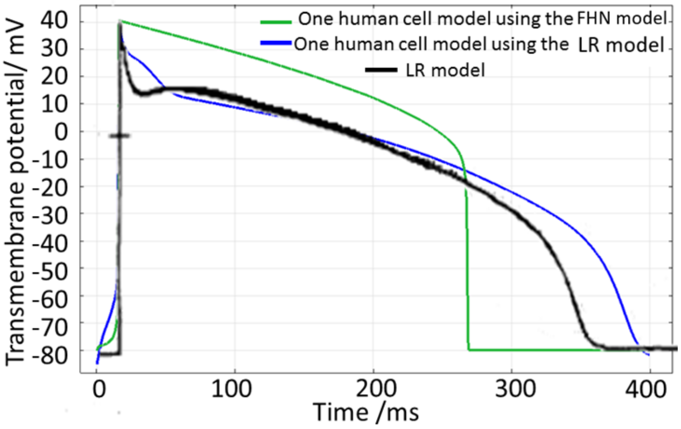

Figure 4.19: APs produced by the single human myocyte model using the FHN model and the LR model and the original AP produced by the LR model [43]. The original AP produced by the LR model were redrawn from [43] using the standard settings (extracellular potassium concentration $[K]_o = 5.4\,mM$).

Table 4.7: The key AP parameters produced by the single human myocyte model using the FHN model and the LR model using the same stimulation current at $80\,\mu A/cm^2$ in maximum comparing with the model AP produced by the LR model in standard settings (extracellular potassium concentration $[K]_o = 5.4\,mM$) and the measured human results.

	Resting potential/ mV	MUV/(V/s)	Maximum down stroke velocity/(V/s)	AP amplitude/ mV	APD at 90% repolarization /ms
Human myocyte model using the FHN model	-80	230	-60	120	267
Human myocyte model using the LR model	-85	310	-1.5	123	380
Modelling results produced by the LR model [43]	-84	400	No data	126	366
Measured human results in literature	-77[6]	100-150[128], 400[98], 246[99], 180[6], 446[129]	no data	125 [98], 100[6], 132[130]	197 [131], 270[132], 432 [129]

4.2.3 Applying finite element analysis

The finite element method was used to solve both human myocyte models with COMSOL. The models were solved from $0\ s$ to $400\ ms$ at $0.1\ ms$ time step to simulate one cardiac cycle. The mesh of the human cell is shown in Figure 4.20. There are 35360 elements in the cell mesh and its average element size is $1.87\ \mu m^3$.

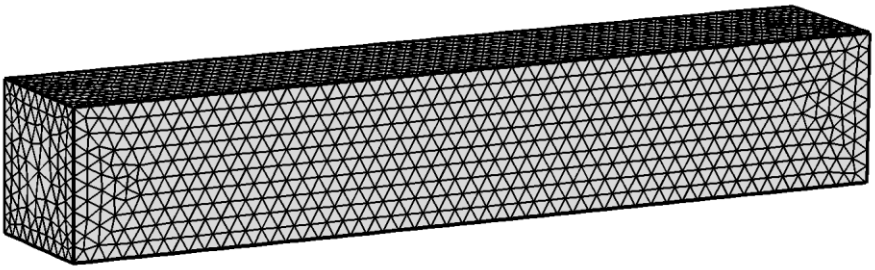

Figure 4.20: Meshes of the human cell

The single human ventricular myocyte model using the FHN model used the global standard unit system called the international system of units (SI) which is derived from the metric system. However for the human model using the LR model, the units are not the same standard unit system, as the units in the LR model are not standard such as the current in $\mu A/cm^2$ and transmembrane potential in mV. The unit of length in LR model is centimetre cm rather than metre m in the SI system. In order to apply the unit system in the LR model, the default model geometry created using the standard unit m was scaled up 100 times to be in cm. Therefore, the model geometries of both models are not in the size, due to the different unit systems. Both models were meshed using the pre-set physical-controlled mesh at fine level. The number of tetrahedral elements in the final mesh of both models were very close as shown in Table 4.8. However the number of degrees of freedom of the model using the LR model is 122887 which is about 2 times bigger than the model using the FHN model. As is mentioned in Chapter 3, the solution time and computational requirements are related to the number of degrees of freedom. The number of degrees of freedom is decided by the number of nodes in the meshed geometry and the number of dependent variables. The numbers of nodes in the meshed geometry in both models are about the same, but there are more dependent variables in the LR model (10 variables) than in the FHN model (4 variables). Therefore the number of degrees of freedom in the myocyte model using the LR model is larger. The larger number of degrees of freedom often leads to longer computation time. Both models were solved from $0\ s$ to $400\ ms$ at $0.1\ ms$ time step to simulate one cardiac cycle. The computation times for both models are shown in Table 4.8 which is the time taken with an Intel Core i5-4590 CPU @3.3GHz and 16 GB of RAM. As shown in Table 4.8, the computation time of model using the LR model is 2.5 hours which is 5 times longer than that of the model using the FHN model.

Table 4.8: Mesh and computation information of the single human ventricular myocyte models using the FHN model and the LR model

Model	Human myocyte model using the FHN model	Human myocyte model using the LR model
Tetrahedral elements	35360	35362
Number of degrees of freedom	122887	281858
Computation time/ hours	0.5	2.5

4.3 Summary

This chapter described the single ventricular myocyte model of both larval zebrafish and human which is the first step to develop a whole larval zebrafish heart model. Instead of using a continuum approach (bidomain model) as the previous larval zebrafish heart model [36], this model aims to simulate the cardiac electrical activities at microscopic level with the histological details of myocytes which is a more realistic approach: the discrete approach. This discrete approach has been previously used in several human cardiac tissue models [98-100]. As this is the first attempt to apply this discrete model to modelling the larval zebrafish heart, a human myocyte model was built for comparison.

First, the development of single ventricular myocyte model of larval zebrafish was described. The ionic current model, the FHN model were applied to this larval zebrafish myocyte model starting with using the previous parameters for ventricle in the previous larval zebrafish heart model [36]. In section 4.1.4, two stimulation methods to start an AP of the myocyte were investigated including applying a stimulation current to a boundary of the myocyte and setting the initial intracellular potential to a value above resting potential. It was found that both methods are able to start an AP if suitable currents or voltages are used. However the MUVs of the AP varied with different currents or voltages. Larger stimulation currents or voltages resulted in larger MUVs (Figure 4.4 and Figure 4.5). In order to investigate what changes the MUV, the time step of simulation and the measurement points were investigated. It is found that the time step would not affect the resultant MUV as long as the time step is the same or shorter than $0.1\ ms$ (Figure 4.6). In addition, the MUVs may be recorded wrongly if the measurement point is not chosen wisely. From Figure 4.7 (A), it is shown that at the stimulated boundary, the stimulation current injection causes sudden and fast changes of the transmembrane potential which then gives distorted MUV. It will not affect the resultant MUVs if the measurement point far from the stimulated boundary is chosen as shown in Figure 4.7. This measurement point was used to plot all model results in this chapter. In summary, both stimulation methods work very similarly and either of them can be used to activate the myocyte if a suitable measurement point is chosen.

The MUV is affected by the stimulation method which can vary from $540\ V/s$ to $800\ V/s$ produced by the single larval zebrafish myocyte model using the FHN parameters from [36]. However the lower range of the MUV is still hundreds times larger than the measured MUV ($6 - 9\ V/s$) found in literature as shown in Table 4.2. It is impossible to reduce the MUV by only reducing the stimulation current (low stimulation current and voltage can't activate the myocyte as shown in Figure 4.4 and Figure 4.5). Therefore, the stimulation method was fixed and parameters of the FHN model were adjusted in the single larval zebrafish myocyte model to resemble the realistic MUV. The stimulation current method was chosen to conduct the optimal process of the FHN parameters. Note that the setting of the stimulation current is not the only settings to start an AP. As it is shown in the strength-duration curve in Figure 4.3 that there are infinite combinations of the stimulation time duration and strength which can maintain the same effect on starting an AP. The final FHN parameters are applied to the same myocyte model later which is activated by setting the intracellular potential to a high value. Both models using different stimulation method produced similar APs.

The effects of parameters in the FHN model were studied with the aid of the previous study in [36]. It is found that:

(1) Reducing “c1” reduces the MUV and the APD.

(2) Reducing “e” increases the APD.

(3) Reducing “A” reduces the AP amplitude and “B” determines the resting potential.

It is interesting to find that reducing “e” after the MUV reduces by reducing “c1” makes the AP upstroke too much up to $70\ mV$ (Figure 4.10). Therefore the stimulation current needs to reduce to bring down the upstroke of the AP. A possible explanation to this is that the smaller upstroke velocity of the AP is, the smaller stimulation charges are needed to depolarisation the myocyte.

The final parameters of the FHN model and the resulting key AP parameters are shown in Table 4.3 and Table 4.4. Note that the parameters of the FHN model are not the only settings to achieve the APs of 48 hpf and 72 hpf zebrafish. As stated before, different stimulation methods would affect the MUV which would, therefore, lead to different parameters of the FHN model if the same AP needs to reproduce. If the stimulation method is fixed, the MUV can be adjusted by two parameters “c1” and “c2”. In here only “c1” was varied. However it is possible to achieve a similar AP by varying “c2” along with the other parameters of the FHN model.

The single human ventricular myocyte models were implemented by using two different types of ionic current models, the FHN model [42] and the LR model [43]. The FHN model is a phenomenological model and the LR model [43] is a biophysical model. It has been found that similar to the zebrafish myocyte model, increasing the stimulation current results in an increase of the MUVs in both models as shown in Figure 4.17 and Figure 4.18. Using the same stimulation current, both models were able to simulate the human ventricular AP as shown in Figure 4.19 and the key AP parameters were compared in Table 4.7. As shown in Figure 4.19, the AP produced by the human myocyte model based on the LR model is close to the original AP produced by the LR model with smaller differences in the APDs and the MUVs. The AP produced by the human myocyte model using the FHN model is different from the APs using the LR model including the absence of the notch after the peak known as the phase 1 during an AP, a shorter APD and a smaller MUV. The absence of the phase 1 is a limitation of a phenomenological model like the FHN model. As is shown in Chapter 3, the original AP produced by the FHN model also missed this level of details. The differences in APDs and MUVs can be fixed by varying the parameters in the FHN model. However the APDs and MUVs produced by the human myocyte model using the FHN model are in the ranges of these measured human APs found in the literature. Therefore the AP produced by the human myocyte model based on the FHN model is acceptable. It has also been found that as shown in Table 4.8, the LR model required a longer solution time and required more computational load than the FHN model which should be considered in the case that the computational power is limited.

As there is no available biophysical model of zebrafish heart can be found, only the phenomenological model like the FHN model can be used to replicate the measured AP of larval zebrafish. Therefore in order to validate the use of FHN model in the larval zebrafish model, the human myocyte model based on the FHN model was chosen to expand into a human cardiac tissue model in later section. If the expanded human cardiac tissue model using the FHN model can produce similar electrophysiological properties as the published discrete human cardiac tissue model [98], it can be validated that the use of the FHN model in the discrete larval zebrafish model is a reasonable choice.

5. CARDIAC FIBRE MODELS

The previous chapter described the single myocyte models of both larval zebrafish and human. Both models are able to simulate the APs resembling the measured APs found in the literature. In this chapter, the single myocyte models using the FHN model were expanded to a cardiac fibre which allows the AP propagation in a unidirectional direction to be simulated. Larval zebrafish ventricular fibre (LZVF) models were implemented for a 48 hpf zebrafish, referred as LZVF1 model and for a 72 hpf zebrafish referred as LZVF2 model. The single human ventricular cell model was expanded to a human ventricular fibre (HVF) model. The LZVF models simulate discontinuous cardiac propagation and reproduce the measured conduction velocities (CVs) in the 48 hpf and 72 hpf zebrafish ventricle by adjusting the gap junction resistivities. For comparison, the HVF model was built which reproduces the measured CVs in the human heart with all of the parameters determined by the published electrophysiological properties of human cardiac tissue. In order to validate the gap junction resistivity used in the LZVF model, the numbers of gap junctions channel per myocyte in all models were determined by the gap junction resistivity, the total gap junction area per myocyte and the individual gap junction channel conductance, and then compared with measured results found in the literature. This is followed by a convergence analysis of all three models. Then the effect of stimulation currents on the CVs and the maximum upstroke velocities (MUVs) were investigated. Finally, the effect of changing the extracellular space size on the CVs and extracellular potential were investigated and compared with similar results in other modelling works. A paper [133] was published by Physical biology based on the work in this chapter.

5.1 Model geometry

The model geometry of the LZVF model is shown in Figure 5.1 (A) and (B). This ventricular fibre is made up of 50 myocytes connected end to end. All myocytes are in the same size as the single larval zebrafish myocyte model, i.e. a cube in 10 μm length. Gap junctions are distributed on the membrane separating two neighbouring myocytes. This fibre is placed in the middle of an extracellular domain represented by a block 560 μm in length, 20 μm in width and depth. The human ventricular fibre (HVF) model has a similar geometry as shown in Figure 5.1 (C) and (D). The model human myocyte is same as the myocyte size in single human myocyte model and the extracellular domain size were based on the literature. The myocyte size and extracellular size of both zebrafish and human are compared with the literature when available as shown in Table 5.1.

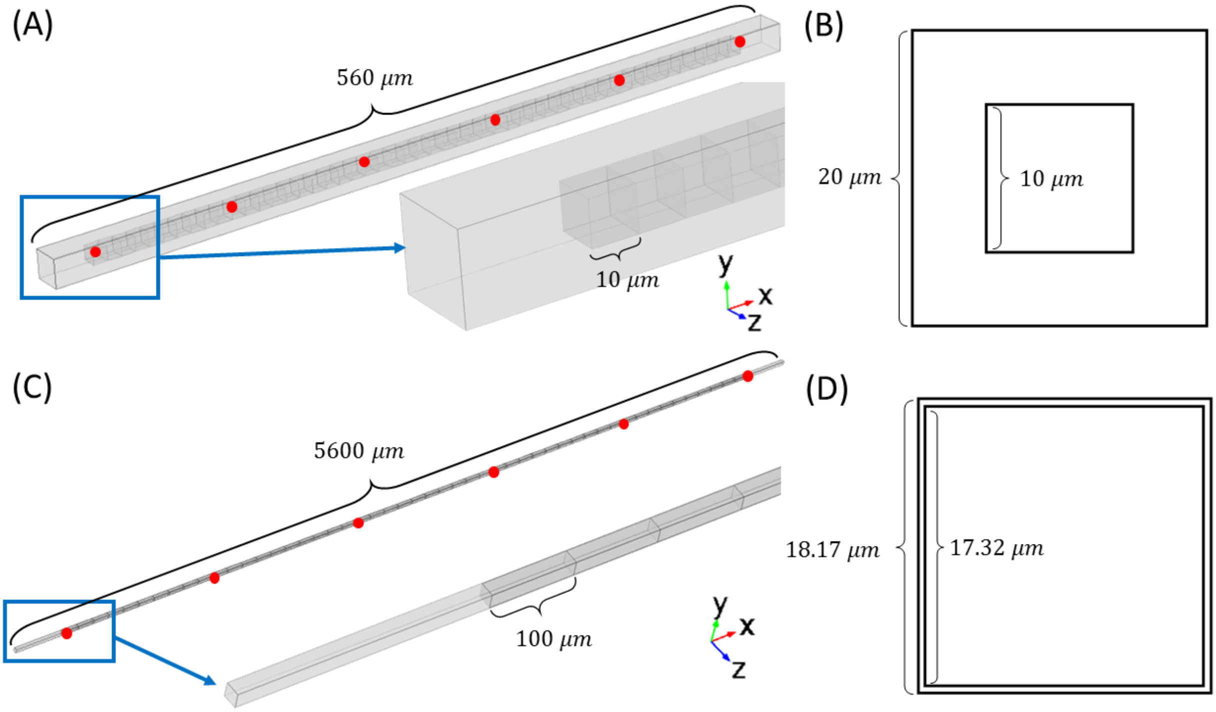

Figure 5.1: (A) Geometry of the LZVF model and a close-up view of a few myocytes; (B) cross-sectional view of the LZVF model; (C) Geometry of the HVF model and a close-up view of a few myocytes; (D) cross-sectional view of the HVF model. The red dots represent the points at which transmembrane potential was measured.

Table 5.1: Comparison of the model geometry of the LZVF and the HVF models with the literature (z for the LZVF model and h for the HVF model)

Model	LZVF	HVF	References
Myocyte length/ μm	10	100	z.[119]; h.99-108 [126]
Cross-sectional area of a myocyte $/\mu m^2$	100	300	z. 75-125 [119]; h. 205.25-283.39 [126]
Total gap junction area for a myocyte$/\mu m^2$	200	600	z. no data; h.420 [134]
Percentage of gap junction area in total membrane area $/\%$	33.3%	7.9%	z. no data; h. 5.2% [135]
Length of extracellular domain $/\mu m$	560	5600	z. no data; h. no data
Side length of extracellular domain $Dex\ /\mu m$	20	18.17	z. no data; h. no data
Percentage of extracellular space in total space $/\%$	77.7	18.9	z. no data; h. 20-25 [136]

5.2 Electrical model

The electrical models of the LZVF and the HVF model are very similar to the single myocyte models described in the previous chapter. Only the boundary conditions for the membranes connecting two neighbouring myocytes were added. These membranes were assumed to be uniformly distributed with gap junctions whose total conductance is G_{gap}. The gap junction area was assumed to consist of a resistance $\frac{1}{G_{gap}}$, in parallel with a capacitance C_m so that the transmembrane currents between two myocytes I_{12} and I_{21} depend on the differences of intracellular potentials of both myocytes where $\mathrm{I}_{12} = -\mathrm{I}_{21}$ as

$$\mathrm{I}_{12} = -\sigma_{\mathrm{i}}\nabla\mathrm{V}_{\mathrm{i}1} \cdot \boldsymbol{n} = C_m \frac{\partial(V_{i1} - V_{i2})}{\partial t} + G_{gap}(V_{i1} - V_{i2}) \tag{5.1}$$

$$\mathrm{I}_{21} = -\sigma_{\mathrm{i}}\nabla\mathrm{V}_{\mathrm{i}2} \cdot \boldsymbol{n} = -C_m \frac{\partial(V_{i1} - V_{i2})}{\partial t} - G_{gap}(V_{i1} - V_{i2}) \tag{5.2}$$

All physical equations used in the LZVF and the HVF models are summarised in Figure 5.2.

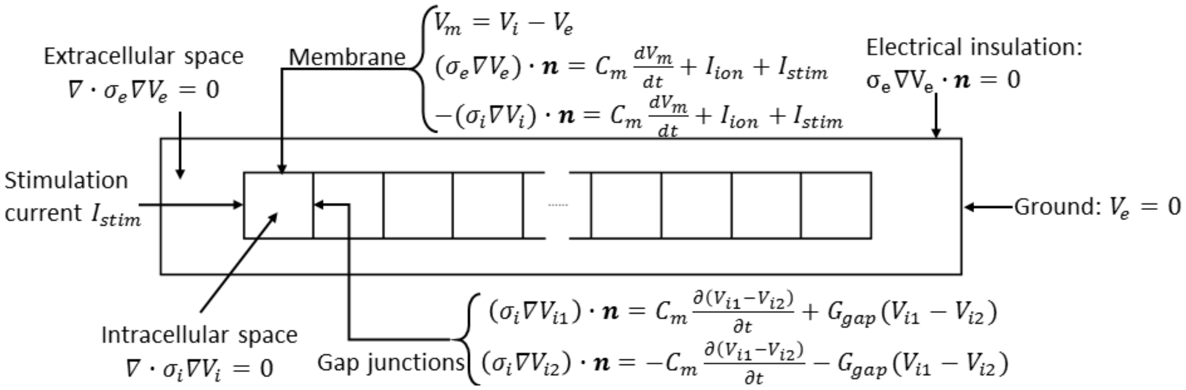

Figure 5.2: Overview of physical equations in the LZVF and the HVF models

The electrical parameters, used in these models, are shown in Table 5.2. Similar to the single larval zebrafish myocyte models, the conductivities and membrane capacitance for the human heart were applied to the LZVF models. The gap junction resistivities (=total gap junction resistance multiplied by the contact area between two myocytes) in the LZVF models were adjusted so that the CVs, obtained using the model, matched the measured CVs in the 48 and 72 hpf zebrafish ventricle, as shown in Table 5.2. For the HVF model, the gap junction resistivity used by Roberts et al [99], was chosen which is similar to that used by Stinstra et al [98]. The stimulation currents used in the LZVF and HVF models are larger than in the single myocyte models as the small stimulation currents in the single myocyte model cannot start an AP in the model fibre.

Table 5.2: Electrical parameters used in the LZVF and the HVF models (z for zebrafish, h for human and [a] is for the fitted values).

Model	HVF	LZVF1	LZVF2	References
Extracellular conductivity(mS/cm)	20	20	20	z and h. [121]
Intracellular conductivity(mS/cm)	4	4	4	z and h. [122]
Gap junction resistivity (Ωcm^2)	1.125	200[a]	110[a]	h. [99]
Membrane capacitance $(\mu F/cm^2)$	1	1	1	z and h. [123]
Maximum stimulation current density $I_{stimmax}$ $(\mu A/cm^2)$	300	50	50	z. no data; h. no data
Stimulation current duration $T_{stim}(ms)$	10	2	2	z. no data; h. no data

The same parameters of the FHN model used in the single myocyte model were used in the LZVF and the HVF models as shown in Table 5.3. Initial conditions for intracellular potential $\mathrm{V_i}$, extracellular potential $\mathrm{V_e}$, and recovery variable u are shown in Table 5.4 which is also same as the single myocyte models.

Table 5.3: Parameters of the FHN model used in the LZVF1, the LZVF2 and the HVF models

FN model parameters	Human	LZVF1	LZVF2
A	0.13	0.13	0.13
B	0	0	0
c1	0.19	0.007	0.0085
c2	0.5	0.5	0.5
D	1	1	1
E	0.00035	0.000013	0.0000225
A	0.1205	0.108	0.108
B	-0.08	-0.07	-0.07
K	1000	1000	1000

Table 5.4: Initial conditions in the LZVF and the HVF models

Initial conditions	Human	Zebrafish
$\mathrm{V_i}/mV$	-80	-70
$\mathrm{V_e}/mV$	0	0
u	0	0

The finite element method was used to solve the LZVF and the HVF models with COMSOL. The statistics of the tetrahedral elements in both models are shown in Table 5.5 along with the number of degrees of freedom. They were solved from $0\ ms$ to $400\ ms$ to simulate one cardiac cycle. The computation time was the time taken on a computer with an Intel Core i5-4590 CPU @3.3GHz and 16 GB of RAM. The finite element method was used to solve the LZVF and HVF models with COMSOL Multiphysics. Cross sections through the meshes of the LZVF and HVF models are shown in Figure 5.3. The mean mesh element volumes of the extracellular space, the intracellular space and total spaces for the LZVF and HVF model are shown in Figure 5.4 (A) and (C). The mean mesh element areas of the membrane, the gap junction area and extracellular boundaries (outer boundaries of the extracellular block) for the LZVF and HVF model are also shown in Figure 5.4 (B) and (D).

Table 5.5: Mesh and computation information using COMSOL

Model	HVF	LZVF1	LZVF2
Total tetrahedral elements	11018	443912	443912
Average tetrahedral elements in a myocyte	67	1875	1875
Number of degrees of freedom	56198	848420	848420
Computation time	10 mins	2.5 hrs	2.5 hrs

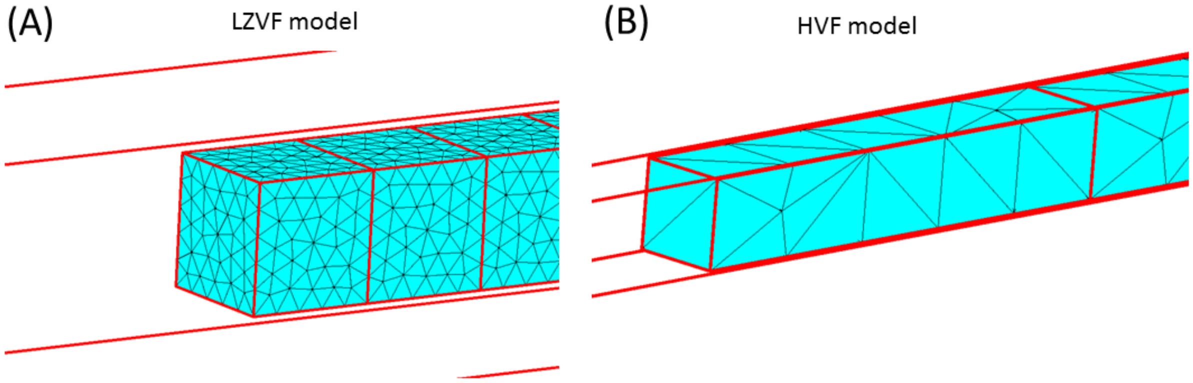

Figure 5.3: Oblique views of the meshes in (A) the LZVF model and (B) the HVF model. Note that only the elements which meet the surface can be seen. Each cell in the LZVF model contains an average of 1875 elements whilst each cell in the HVF model contains an average of 67 elements.

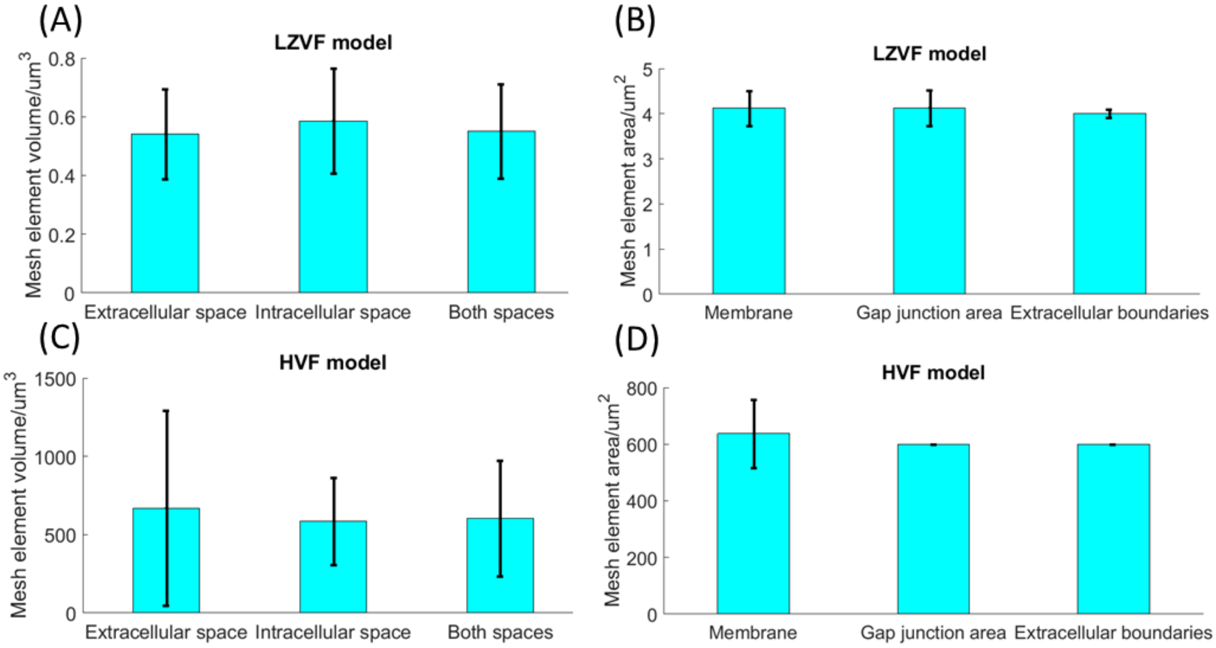

Figure 5.4: (A) Mean mesh element volumes of different regions in the LZVF model. (B) Mean mesh element areas of different regions in the LZVF model. (C) Mean mesh element volumes of different regions in the HVF model. (D) Mean mesh element areas of different regions in the HVF model. The error bars are the standard deviations of mesh element volume/area.

5.3 AP propagation

AP propagation in the LZVF and the HVF models was initiated at the first myocyte at the left end of the fibre by the stimulation current injection. In Figure 5.5, the transmembrane potentials were plotted as a function of time for 6 equally spaced points as marked in red in Figure 5.1 (A) and (C), in which the distance between two neighbouring points is 10 cell lengths. For all three models, the APs measured at the first point have a higher peak than the others which was probably caused by edge effects at the end of the fibre and the injection of stimulation current as described in Chapter 4. It may be observed that for the LZVF1 model, the time delays between the first point and the second point and between the fifth point and the sixth point were different to the time delays between the other neighbouring points (Figure 5.5 (A)). This difference in delay was probably also caused by edge effects at both ends of the fibre and the injection of stimulation current, however the other two models did not show similar effects (Figure 5.5 (B) and (C)). Overall, AP propagation in all models was generally stable except for the myocytes near the two ends of the fibre.

The distances of the myocytes in the fibre from the stimulated membrane were plotted against the activation times for the LZVF and the HVF models in Figure 5.6 and the 6 equally spaced points were marked. The activation time is defined as the time when its transmembrane potential reaches $0\ mV$.

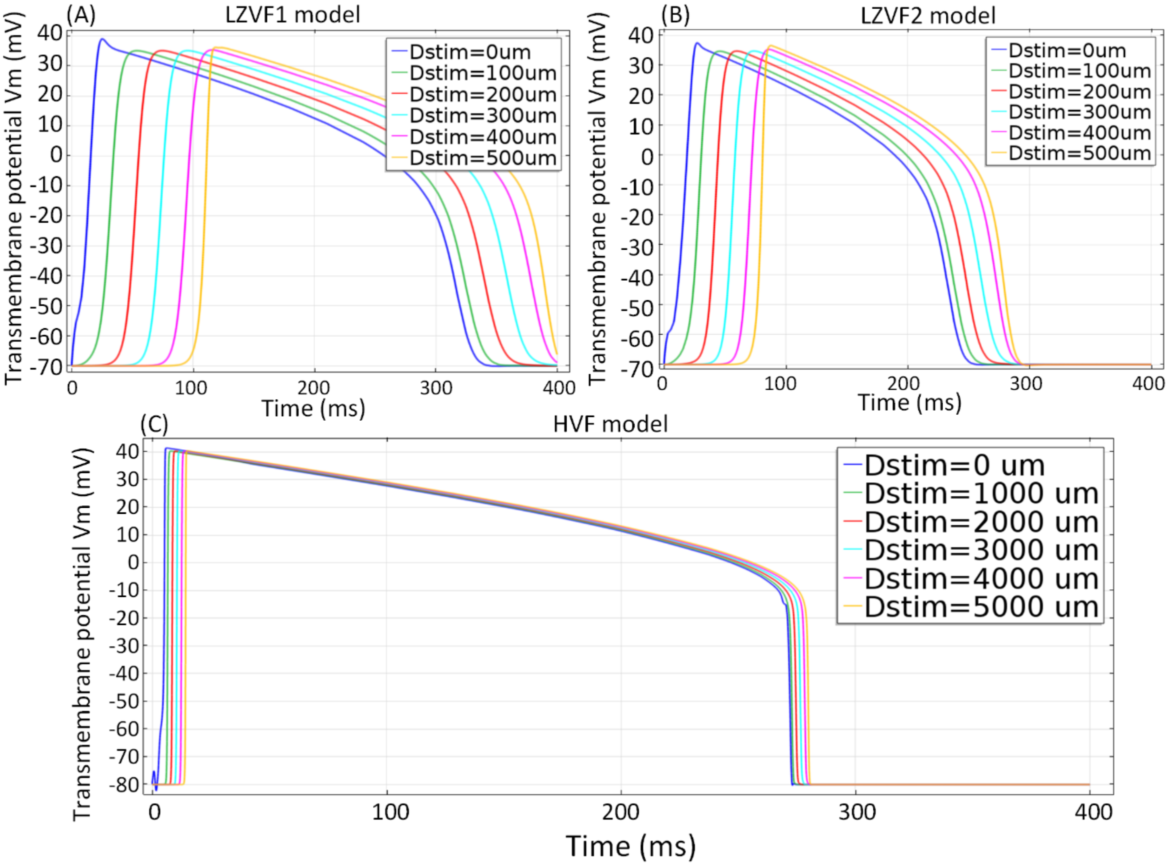

Figure 5.5: APs of 6 equally spaced points of which the distances from the stimulated membrane is $Dstim$ for (A) LZVF1 model, (B) LZVF2 model and (C) HVF model.

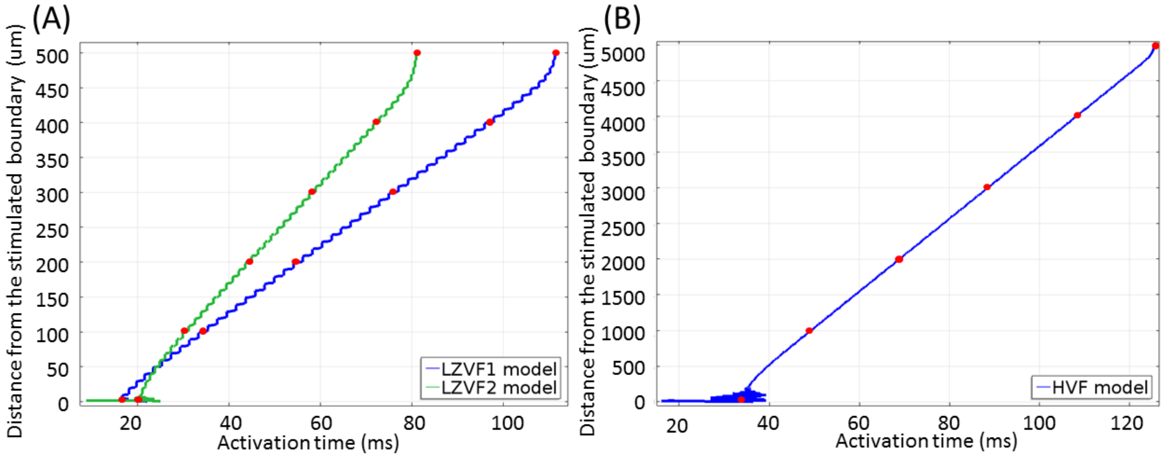

Figure 5.6: Distances from the stimulated membrane vs activation time for: (A) LZVF1 model (blue) and LZVF2 model (green); (B) HVF model.

The time derivatives of transmembrane potential (upstroke velocity) of all three models were plotted against time in Figure 5.7. It is shown that the upstroke velocities of the first and the last point in the model fibre are different from the other points in the middle which is also illustrated in Figure 5.8. As is shown in Figure 5.8, the MUVs of both ends of the fibre are larger than the middle section. These abnormal values are due to the edge effects and the stimulation current injection same as those found in [98]. In order to avoid the errors arising from the edge effects, only the points in the middle section of the fibre are used to compute the key AP parameters. The resulting key AP parameters are the average values of these 4 points shown in Table 5.6. As shown in Figure 5.7, the upstroke of AP for the HVF model is much faster than that for the LZVF model which is also reflected by the MUVs of $206\ V/s$ comparing with $6.67 - 8.05\ V/s$ for the LZVF model as shown in Table 5.6. The derivation of CVs in the LZVF and the HVF models also only used the results of the middle 4 points. These CVs are derived by applying first-order polynomial curve fitting to Figure 5.6 and the results are compared with the measured CVs in Table 5.6.

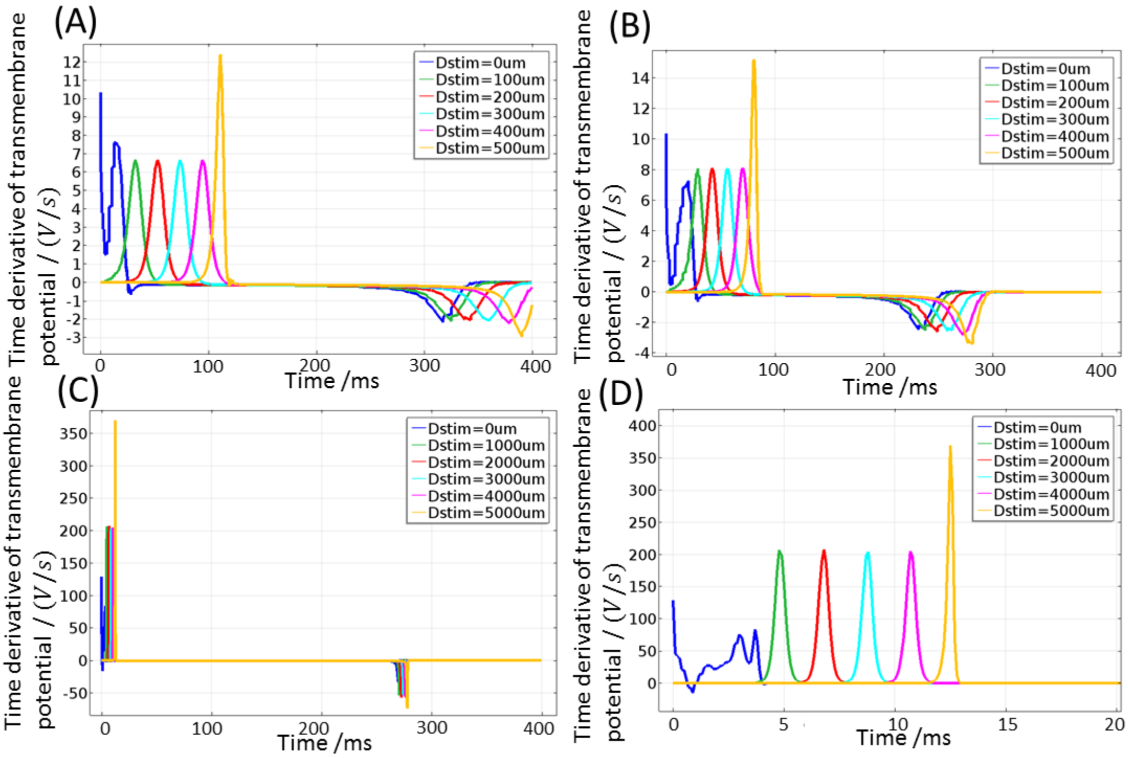

Figure 5.7: the time derivative of transmembrane potential vs time produced by (A) the LZVF1 model, (B) the LZVF2 model and (C) the HVF model. (D) close-up view of the first $20\ ms$ of (C).

Table 5.6: The key AP parameters produced by the LZVF and the HVF models compared with the measured APs in literature. In addition, the targeted experimental CV values are shown to compare to those achieved in the models

	Resting potential/ mV	Maximum upstroke velocity/(V/s)	Maximum down stroke velocity/(V/ s)	AP amplitude/ mV	APD /ms	CV/(um/ ms)
LZVF1 model	-70	6.67	-2.1	105.2	297	4.8
Measured values for 48 hpf zebrafish	-66[11], -70[5], -78.5[56]	6[5],7.15[56]	-1.69[56]	91.9[11],104[5], 117[56]	231[11], 272[5], 350[56]	4.8[78]
LZVF2 model	-70	8.05	-2.6	104.8	220	7.2
Measured values for 72 hpf zebrafish	No data	7.5-9[57]	No data	No data	220[57]	7.5[78],4-12 [57]
HVF model	-80	206	-54	120	198	510
Representative human values	-77[6]	100-150[128], 400[98], 246[99], 180[6], 446[129]	no data	100[6], 132[130]	197[131], 270[132], 432 [129]	500[128], 430[98], 494-568[99], 480[137],

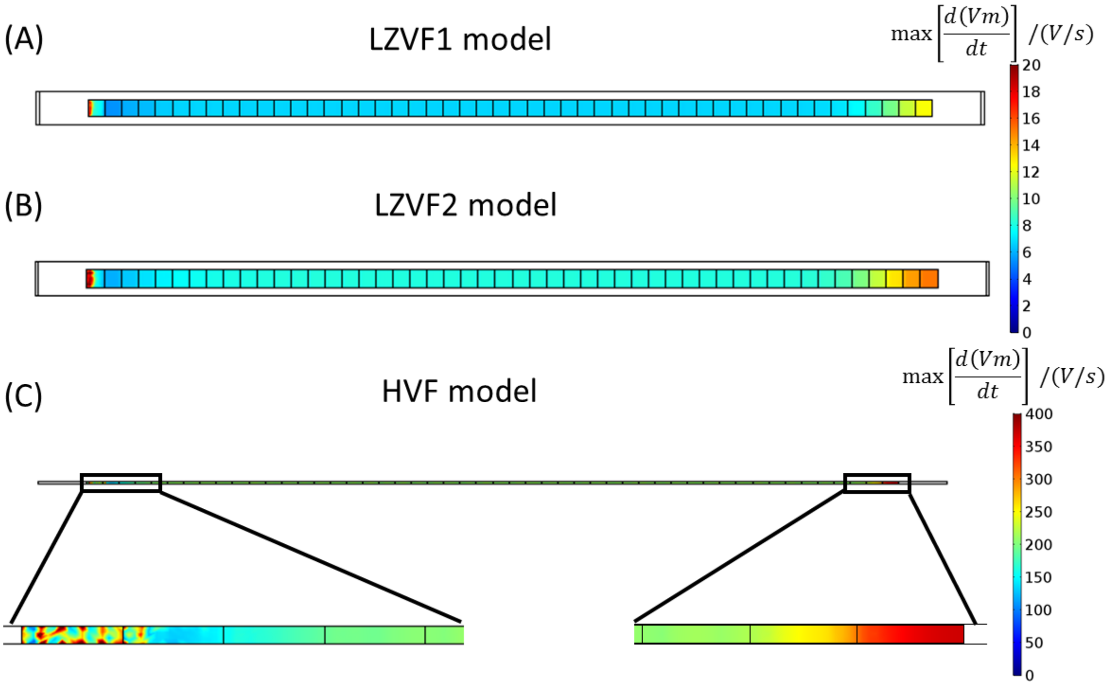

Figure 5.8: The maximum upstroke velocities of the whole fibre in (A) the LZVF1, (B) the LZVF2 and (C) the HVF models. The black boxes show the maximum upstroke velocities of both ends of the model human ventricular fibre.

In order to investigate the discontinuous nature of AP propagation in all models, the transmembrane potentials of the whole fibre at a time point during the upstroke period were plotted, as shown in Figure 5.9. Figure 5.9 also shows the transmembrane potential at the same time plotted against the distance from the stimulated membrane. As shown in Figure 5.9 (A) and (B), at time 60 ms approximately 18 myocytes in the LZVF1 model reached 40 mV (fully depolarised) whilst about 25 myocytes in the LZVF2 model reached this AP stage. In both LZVF models, there are about 16 myocytes in the transition from the polarized state to depolarized state. For comparison, about half myocytes in the HVF model fully depolarised at time 7 ms and there are about 3-4 myocytes in the transition. In this transition zone, the transmembrane potential varied discontinuously with the distance for the LZVF models which can be observed in the corresponding curves as small steps. The effect of discontinuous conduction is less pronounced for the HVF model and the smaller number of myocytes in the transition in HVF model is consistent with a larger upstroke velocity.

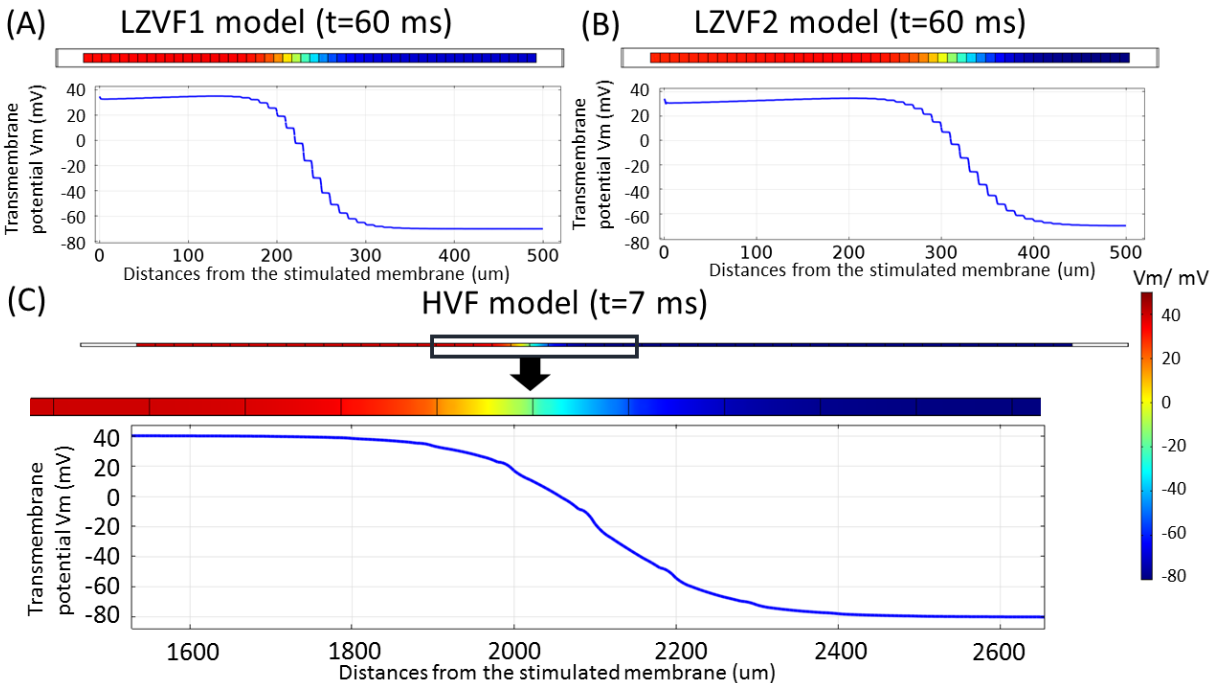

Figure 5.9: Transmembrane potential V_m in the (a) LZVF1 model, (b) LZVF2 model at time 60 ms during the upstroke period with corresponding transmembrane potential plotted against the distance from the stimulated membrane below; (c) Transmembrane potential V_m in the HVF model at time 7 ms during the upstroke period and a close-up view of 10 myocytes during the upstroke period with the corresponding V_m plotted against the distance from the stimulated membrane. Colour bar: from $-80\ mV$ (blue) to 50 mV (red).

5.4 Gap junction investigation

To investigate whether the gap junction resistivity used in the LZVF models was reasonable, the numbers of gap junction channels per myocyte for all models were estimated. Each gap junction channel is made up of two connexons (or hemichannels), each of which consists of six symmetrical integral membrane protein units called connexins. The individual gap junction channel resistance is determined by the types of connexins. Connexin40 (Cx40), connexin43 (Cx43), and connexin45 (Cx45) are three main connexins regulating the functionality of myocytes in the mammalian heart [55]. Connexin43 has been found in both the 48-100 hpf zebrafish and human ventricle, Connexin40 was found in 48-100 hpf zebrafish ventricle [55, 56] but not in the human ventricle although it is present in the atrium and no Cx 45 is found in either larval zebrafish or human ventricle. Since there is no available experimental data on the individual gap junction channel conductances in the zebrafish heart, it is assumed to be the values obtained experimentally in the human case and these are shown for the different connexins in Table 5.7.

In order to estimate the number of gap junction channels per myocyte, the gap junction resistivity from Table 5.7 was used together with the total gap junction area for a cell to determine the total resistance of gap junctions per myocyte. The individual gap junction channel conductances were used to derive the values shown in Table 5.7. Note that the total resistance of gap junctions per myocyte in the human case is consistent with the value obtained from the paper [99], which is to be expected as the HVF model used the same gap junction resistivity.

Table 5.7: Gap junction information in the LZVF and HVF models (z for zebrafish, h for human and h* are derived values from the literature by applying the same method as the model values)

	LZVF1 model	LZVF2 model	HVF model	Reference values from the literature for comparison
Types of connexins	Cx40, Cx43	Cx40, Cx43	Cx43	z,[56]; h,[55]
Range of individual gap junction channel conductance / pS	20-160	20-160	20-110	Cx40: 30,80,120[138], 150-160 [139]; Cx43: 20,40,70[140], 25 (rest),110 (open) [141]
Total resistance of gap junction channels per myocyte / Ω	1×10^8	5.5×10^7	3.75×10^5	z, no data; h*, 1×10^6 [142]; 1.3×10^6 [128]; 3.75×10^5 [99]; 1.7×10^6-2.12×10^6[143, 144]
Number of gap junction channels per myocyte obtained from total resistance and gap junction conductance.	31-250	57-455	$2.42 \times 10^4 - 1.33 \times 10^5$	z, no data; h, the order of 10^4 [145];h*, $9.09 \times 10^3 - 5 \times 10^4$ [142]; $7 \times 10^3 - 3.85 \times 10^4$ [128]; $2.42 \times 10^4 - 1.33 \times 10^5$ [99]

5.5 Convergence analysis

In order to validate the stability and reliability of the LZVF and the HVF models, a convergence analysis for different levels of mesh was conducted. For finer meshes, the geometry of the model was divided into more elements which should improve the accuracy of the results; in this case, the CVs. The convergence analysis is conducted in the following steps. First, plots similar to Figure 5.6, used to derive the CVs of LZVF and HVF models, were produced using different mesh levels (Figure 5.10 (A)-(C)). Second, the proportional differences of the CVs between the finest mesh and progressively coarser meshes were also plotted against the mesh levels (Figure 5.10 (D) and (E)). If the plots in Figure 5.10 (A)-(C) for different mesh levels tended to overlap with the increasing mesh level and the proportional difference of the CVs between the finest mesh and coarser meshes were less than 5% in Figure 5.10 (D) and (E), which means that the modelling results had converged. COMSOL has a number of default mesh levels, which were used in the modelling work. These are “extremely fine”, “extra fine”, “finer”, “fine”, “normal”, “coarse”, “coarser” and “extra coarse”. A mesh better than the “extremely fine” level was used for the LZVF models, called “better mesh” as there is a much smaller membrane area in the LZVF models than in HVF model.

The LZVF models in the paper were produced by meshing using the “better mesh” settings. Apart from results meshed at the “normal” level, almost all the others overlap except at the first point at the stimulated membrane (Figure 5.10 (A)) and their proportional differences of CVs are lower than 2% (Figure 5.10 (D)). These figures show that the model CVs with meshing at all levels had converged however the activation time for the first point at the stimulated membrane may vary a little for different meshes. As discussed in section 5.3, the results of the first and last points were probably influenced by edge effects or stimulation current injection. So the CVs produced by the LZVF1 model were obtained using the results for other 4 points.

Similarly, the results of meshing at the “better mesh” and “extremely fine” level for the LZVF2 model overlap (Figure 5.10 (B)) and the proportional differences of CVs were lower than 2% for mesh levels better than “fine” (Figure 5.10 (D)) which indicates they had converged.

The HVF model was produced by meshing at the “finer” level. The results obtained from the HVF model, meshed using “finer”, “normal” and “coarse levels” almost overlap except for the first point (Figure 5.10 (C)) which indicates convergence. Similarly to the LZVF models, the CV was derived using curves plotted without the first and last points. In addition, the proportional differences of CVs were lower than 1% for mesh levels better than “coarser” (Figure 5.10 (D)). Thus it can be concluded that the HVF model results were converged and the CV values are reliable.

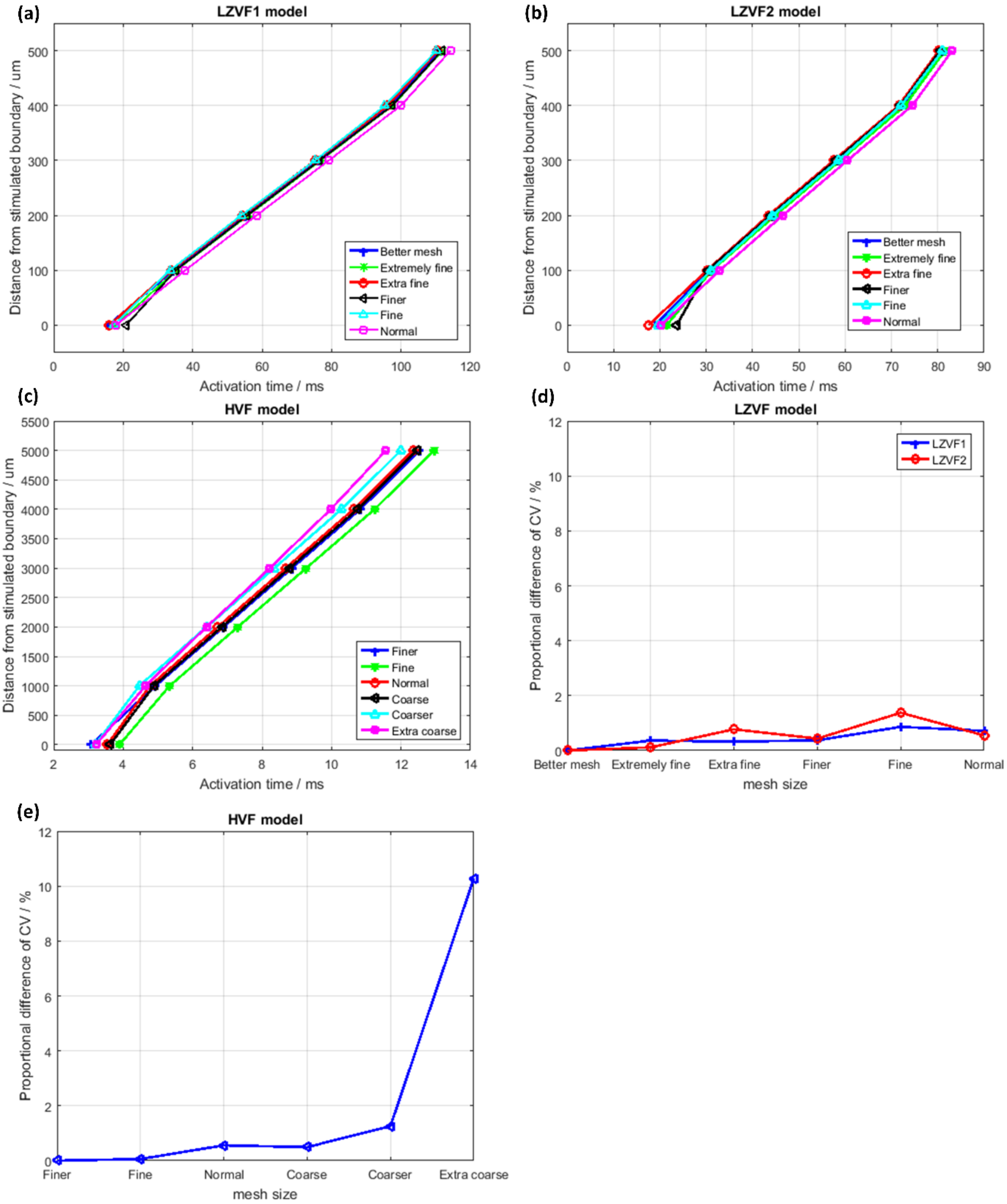

Figure 5.10: Convergence analysis: Distance of 6 equally spaced points, from the stimulated membrane plotted against time when the transmembrane potential reaches 0 mV in (A) LZVF1 model, (B) LZVF2 model, and (C) HVF model; the proportional differences of CV between the finest mesh results and each mesh results versus different mesh levels in (D) LZVF1 (blue) and LZVF2 (red) models, (E) HVF model.

5.6 Investigation of stimulation current

The stimulation current magnitude was investigated to ensure that the use of modelled AP did not introduce any anomalies. In the LZVF and the HVF models, an external stimulation current I_{stim} was applied to the left membrane of the first cell from the left end of the fibre to start the depolarization (Figure 5.2). Taking into account the area of the membrane, the total maximum stimulation current applied to the membrane was $50\ pA$ in the LZVF models and $9\ nA$ in the HVF model (Figure 5.11).

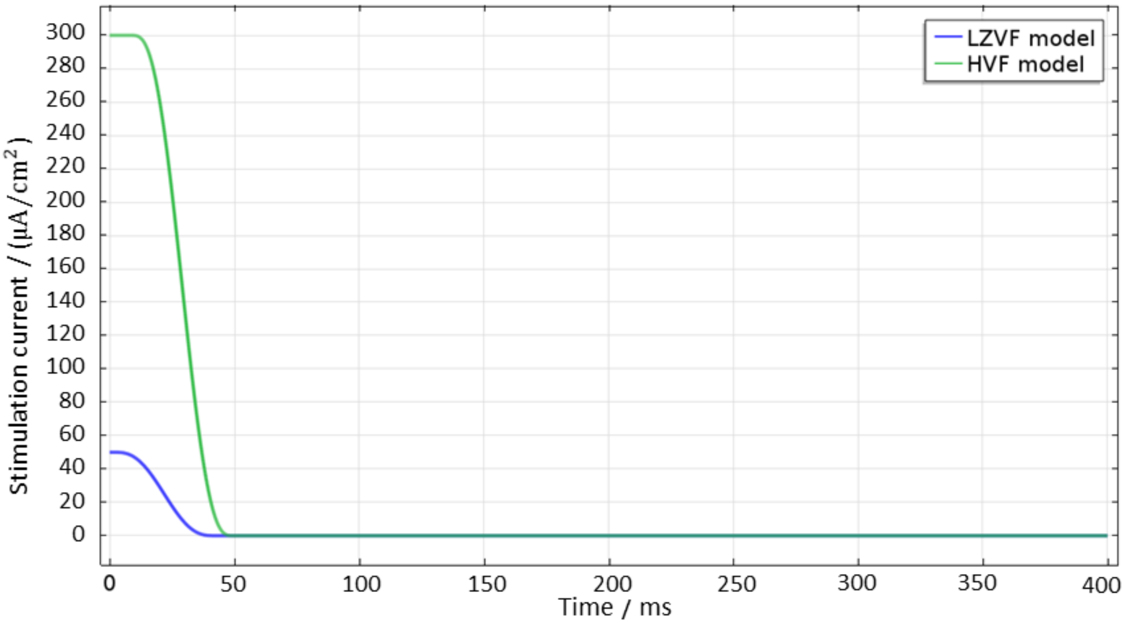

Figure 5.11: Stimulation current I_{stim} in the LZVF model (blue) and the HVF model (green).

As it is known that the stimulation current magnitude affects the time at which the first myocyte starts to depolarize, the relationship between the CV of AP propagation and stimulation current magnitude was investigated. The distances of the 6 equally spaced points from the stimulated membrane were plotted against time when the transmembrane potential reached $0\ mV$ for the LZVF1 model with varying the maximum stimulation current $I_{stimmax}$ at $50, 100, 150\ and\ 200\ \mu A/\ cm^2$ (Figure 5.12). This shows that variation of maximum stimulation current does not affect the slope of the curves (CV). Also, larger stimulation current magnitude results in faster depolarization of myocytes similar to the modelling results of single myocyte models in Chapter 4.

As is found in the previous chapter, the MUV is a sensitive parameter to the stimulation current in the single larval zebrafish myocyte model. Larger stimulation current results in larger MUV. Therefore, in order to investigate the effect of stimulation current on the MUV in the LZVF model, the stimulation currents in LZVF1 model were increased same as in Figure 5.12. The resulting MUV of the whole fibre were plotted in Figure 5.13. It shows that in the middle section of the fibre, the MUVs are unchanged in models with different stimulation currents. At the left end of the fibre, there is one myocyte showing the abnormal MUV with the maximum stimulation current at $100\,\mu A/\,cm^2$ whilst it increase to two myocytes with the maximum stimulation current at $150\,\mu A/\,cm^2$ and to three myocytes with maximum stimulation current at $200\,\mu A/\,cm^2$. The abnormal MUVs at the end of the fibre for all three models are very similar. This illustrates that the stimulation current only affects the first few myocytes where it is applied. The key AP parameters shown before were derived from the middle 4 points which are not affected by the stimulation current.

Note that the extremely fine mesh level was used in this section and following sections, to reduce computation time, as the modelling results were found to be sufficiently converged at this level (See section 5.5).

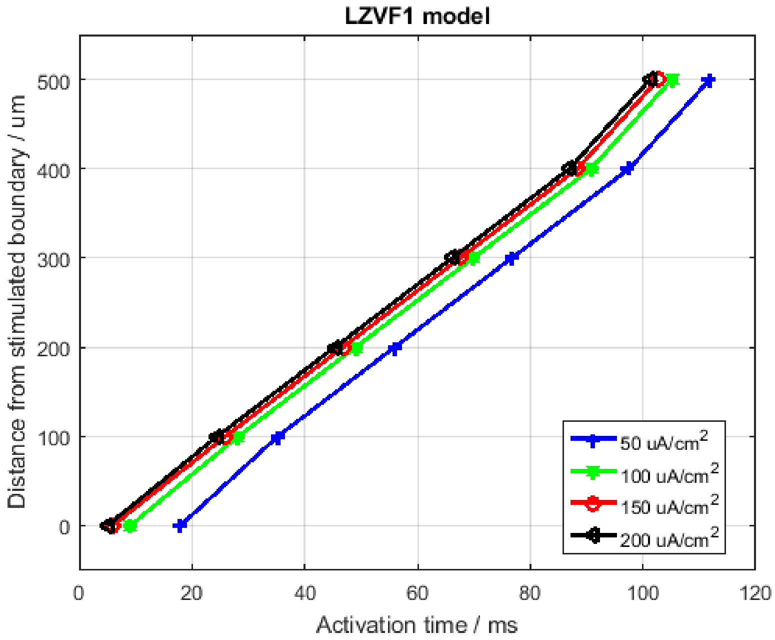

Figure 5.12: Stimulation current investigation: Distance of 6 equally spaced points from the stimulated membrane vs time when the transmembrane potential reaches 0 mV with a variation of the maximum stimulation current $I_{stimmax}$ at: 50 (blue), 100 (green), 150 (red), and 200 (black).

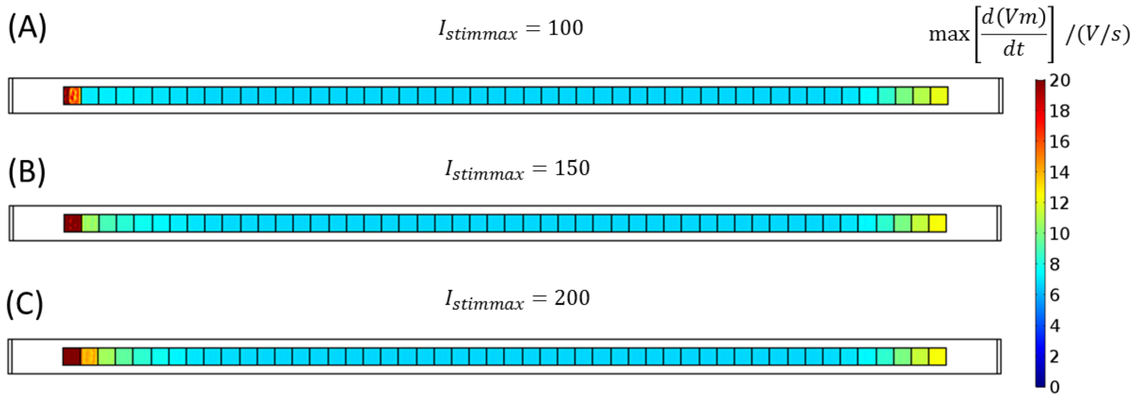

Figure 5.13: The MUVs of the whole fibre in LZVF1 model with a variation of the maximum stimulation current $I_{stimmax}$: (A) 100, (B) 150, and (C) 200. Scale bar: 0 V/s (blue) to 20 V/s (red).

5.7 Investigation of the extracellular space size

It has been found that the modelled CV reduces as the ratio of extracellular space to total space reduces [99]. According to the classical cable theory, this is reasonable as the decrease of extracellular space size results in increasing the extracellular resistance which reduces the CV of AP propagation. The effects of extracellular space size on AP propagation were investigated by varying the side length of the extracellular space Dex with the myocytes remaining in the middle of the model. (The Fine mesh level was used in these simulations, to reduce computation time, as the modelling results were converged at this level). The resulting extracellular potentials at the 6 equally spaced points were plotted as a function of time with different extracellular space size for the HVF model (Figure 5.14) and the LZVF1 model (Figure 5.16) The CVs for different values of Dex were also obtained using the same technique as described in section 5.3. The activation time for the 6 equally spaced points was plotted together with the distances to the stimulated membrane, for different extracellular space areas for both the HVF (Figure 5.15) and LZVF1 models (Figure 5.17). Note that the HVF model and LZVF model use $Dex = 18.17\ \mu m$ and $Dex = 20\ \mu m$ respectively. These results were summarised for the HVF model in Table 5.8 and for the LZVF1 model in Table 5.9. For the HVF model, as the extracellular space sizes increase, the CVs increase whilst the maximum absolute extracellular potentials reduce, which is similar to the results in [99] and the prediction of classical cable theory. In fact for extracellular area fractions similar to those used in [99], the extracellular potential is numerically very similar. However for the LZVF1 model (Table 5.9), although the extracellular potential did reduce, the CV did not vary with different extracellular space size. A possible explanation is that the small size of the myocytes in the LZVF model, together with the much larger gap junction resistance leading to a much larger intracellular resistance than in the HVF model makes the CV insensitive to the extracellular space size which is similar to the case described in section 2.2.2 in Chapter 2.

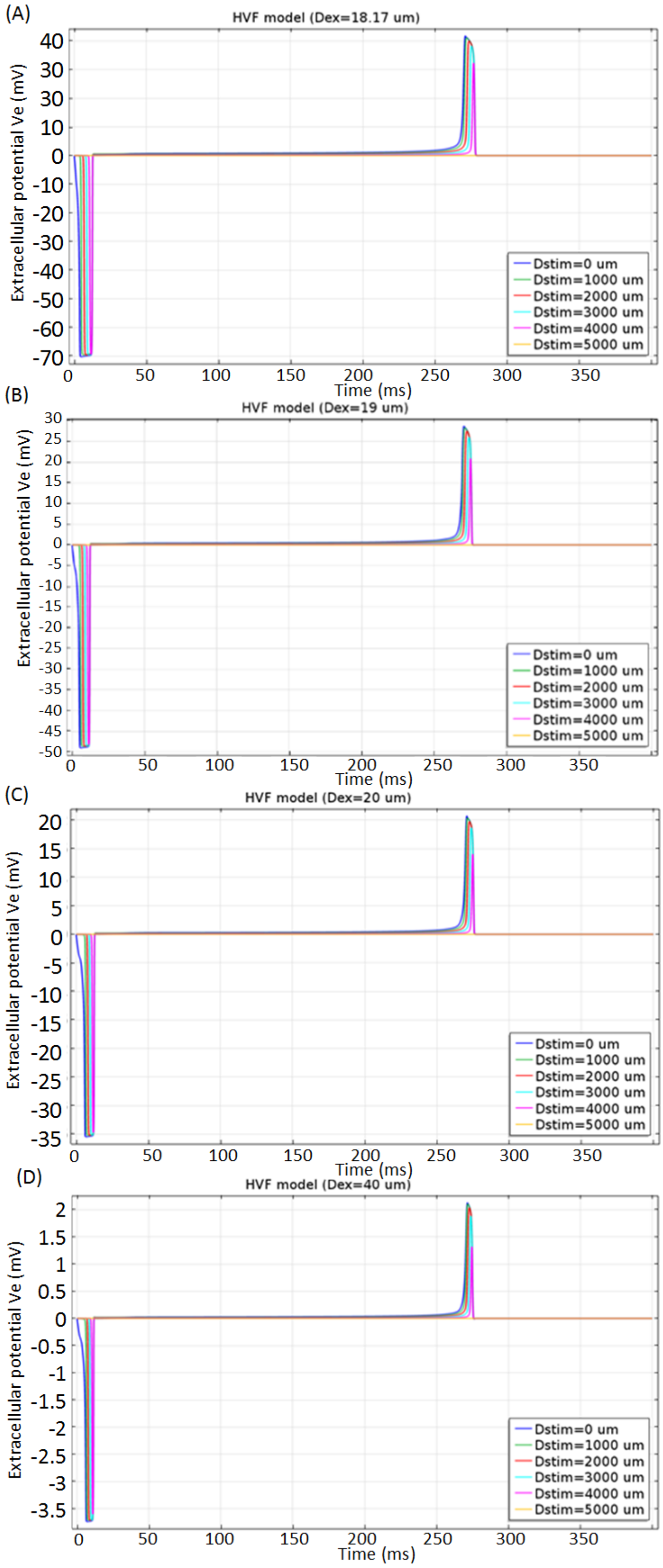

Figure 5.14: Extracellular potential V_e of the 6 equally spaced points versus time for the HVF model with various side lengths of cross-section area of extracellular spaces Dex equal to: (A) 18.17 μm; (B) 19 μm; (C) 20 μm; (D) 40 μm.

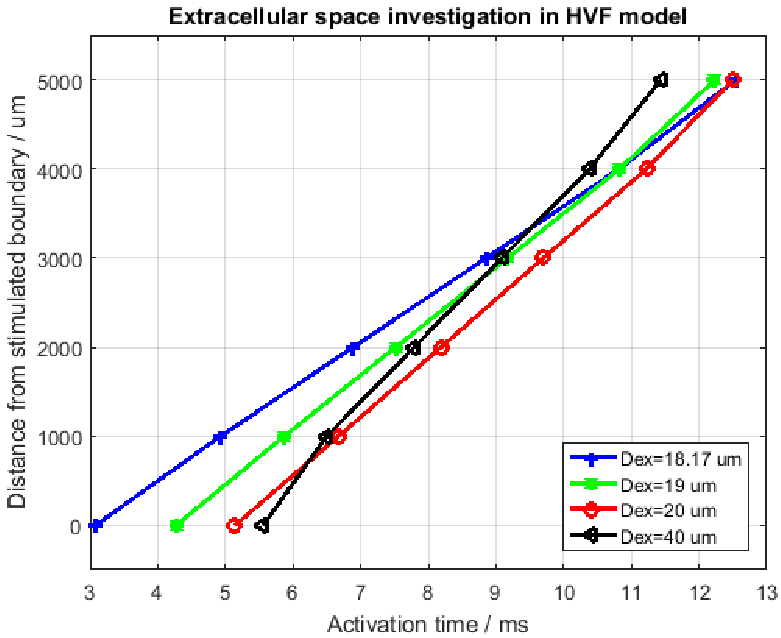

Figure 5.15: Distances of 6 equally spaced points, from the stimulated membrane versus time when the transmembrane potential reaches 0 mV in the HVF model with various side lengths of cross-section area of extracellular space: 18.17 μm (blue), 19μm (black), 20 μm (green) and 40 μm (red).

Table 5.8: Investigation of the effect of extracellular space size on CV and maximum absolute extracellular potential in the HVF model.

Side length of cross-section area in extracellular space Dex /μm	Cross section area of extracellular space/μm^2	Percentages of the cross-section area of extracellular space to the total cross-section area	CV/(um/ ms)	Maximum absolute extracellular potential V_e/ mV
18.17	330.15	9.09%	508.8	70
19	361	16.9%	604.9	48
20	400	25%	658.9	35
40	1600	81.25%	772.3	3.7

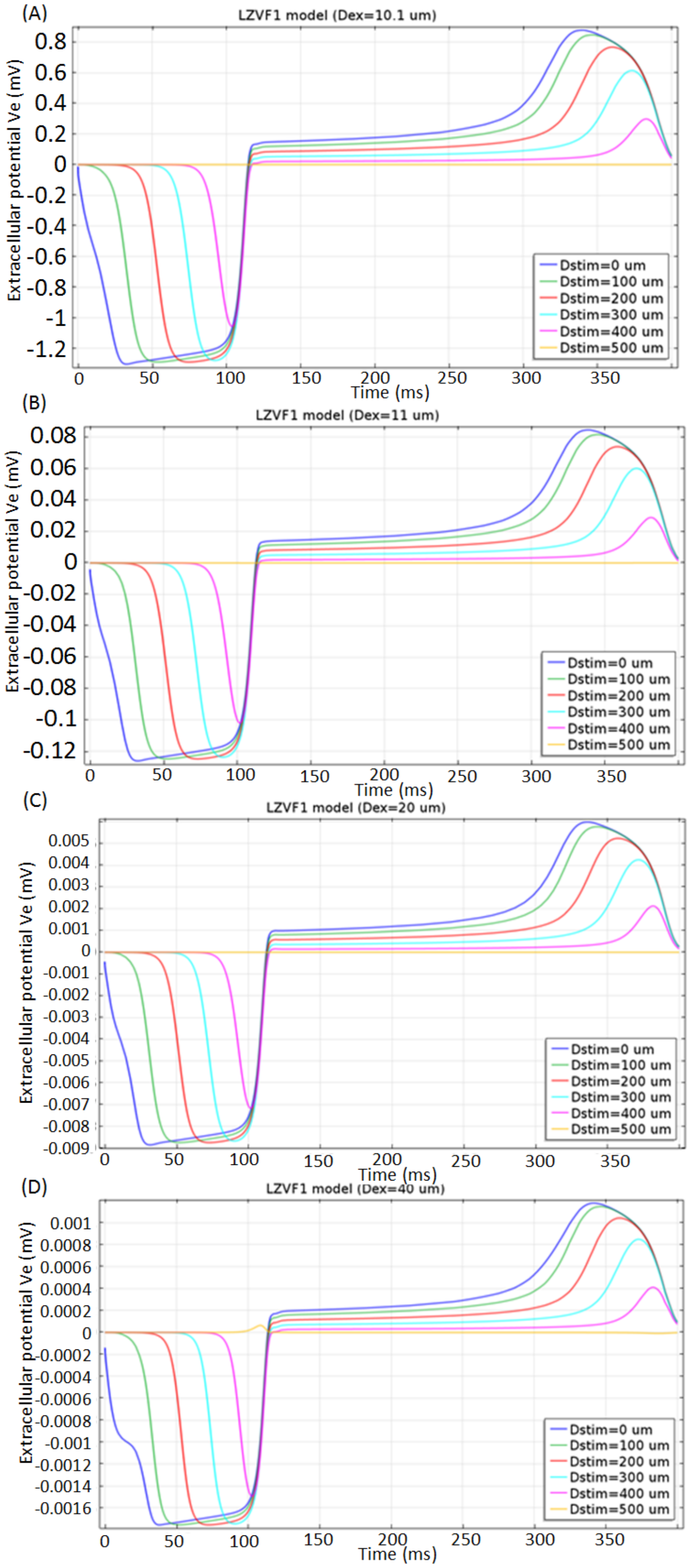

Figure 5.16: Extracellular potential V_e of the 6 equally spaced points versus time by the LZVF1 model with various side lengths of the cross-section area of extracellular spaces Dex: (A) 10.1 μm; (B) 10.2 μm; (C) 11 μm; (D) 40 μm.

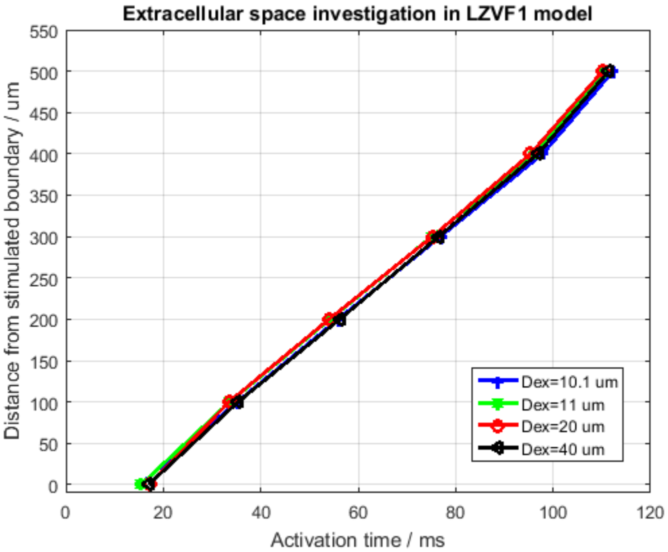

Figure 5.17: Distances of 6 equally spaced points from the stimulated membrane vs the time when the transmembrane potential reaches 0V in the LZVF1 model with various side lengths of cross-section area of extracellular space:18.17 μm (blue), 19 μm (green), 20 μm (red) and 40 μm (black).

Table 5.9: Investigation of effects of extracellular space size on CV and maximum absolute extracellular potential in the LZVF1 model.

Side length of cross-section area in extracellular space $Dex\ /\mu m$	Percentages of the cross-section area of extracellular space to the total cross-section area	$\mathrm{CV}/(um/ms)$	Maximum absolute extracellular potential V_e/mV
10.1	1.97%	4.8	1.3
11	17.36%	4.8	0.12
20	75%	4.8	0.009
40	93.75%	4.9	0.0017

5.8 Discussion

This chapter described the first discrete model of larval zebrafish cardiac tissue taking account of the cellular nature and the cell interconnectivity. This model successfully simulated discontinuous cardiac propagation and reproduced the measured CVs in the 48 hpf and 72 hpf zebrafish heart. For comparison, a discrete model of human ventricular fibre was built. All of the parameters in the HVF model were determined by the published electrophysiological properties of human cardiac tissue but for the LZVF model, the published parameters are used where they were available. The same extracellular and intracellular conductivities and membrane capacitance were used in LZVF model as in the human case. In the LZVF models, the gap junction resistivity was adjusted to give the CV values observed experimentally.

In order to validate the use of FHN model in the LZVF models, the HVF model was constructed. This shows that using the FHN model, the HVF model successfully simulates AP propagation and reproduces realistic CVs in human. In order to further explore the validity of this approach, the effect of varying the dimensions of the extracellular space upon the extracellular potentials and CVs as described in section 5.7 was investigated. It is shown that as the extracellular space increased from 9.09% to 25% of the total volume, the CVs increased by 29.5% (Table 5.8), This is consistent with the results of Roberts et al [99], who using the Luo and Rudy model to describe ionic currents, constructed a model with a similar geometry tours and found a 15% increase in CV for a change of extracellular volume from 10% to 25%. In both cases, the direction of change is to be expected from the classical cable theory. In addition, the magnitudes of the maximum extracellular potential, for these volume fractions, that emerge from the HVF model are very close to the value that they reported. It is also interesting to compare the width of the wavefront of activation as the upstroke progresses, shown in Figure 5.9 (C) with the results of Stintstra et al [98]. In both cases, the transmembrane potential changes gradually from a polarized state to the depolarized state over a length of about 3 myocytes. The plot of transmembrane potential versus distance along the membrane is also very similar. It can be concluded that the results obtained using this modelling approach, are consistent with similar and more sophisticated models which are based upon biophysical ion current models.

There have been a number of papers reporting discrete cellular models of human ventricular fibres [98, 99, 128]. Although compared to some of these, the HVF model has a simple geometry and used the FHN model to describe ionic currents, it successfully gave values of the CV in the fibre, consistent both with real tissue CVs and those obtained in the other discrete models, as is shown in Table 5.6. This is not surprising because the parameters of the FHN model were adjusted to give APs with parameters which agree well with those observed in real tissue. In particular, the CV is very sensitive to the AP upstroke velocity [48], and the parameters of the FHN model for the human case were chosen to obtain a MUV in the correct range. For the zebrafish case, the MUVs for the 48 hpf and 72 hpf cases are two orders of magnitude smaller than the human case and this can be seen in Table 5.6 In the adult zebrafish, the MUV is similar in magnitude to the human case and it has been suggested that the reason for the change from embryo to adult is caused by the differences in the expression of types of ion channels between embryonic and adult myocytes [6], as is also observed in the human case.

In the previous larval zebrafish heart model based on the bidomain model [36], although realistic MUVs were reproduced by adjusting the parameters of FHN model, it was not sufficient to explain the low CV observed experimentally. It was found that in order to obtain CVs comparable to those observed experimentally, scaled conductivities should be used. The value used was $1.55 \times 10^{-5} S/m$ which is about one hundred thousand times smaller than the measured conductivities of the human heart. This difference is significant when compared with bidomain models of human cardiac tissue. In the reported human cardiac tissue models based on bidomain model, the measured conductivities are within a factor of 10 of the model conductivities [38], which are averaged over the properties and geometry of the networks of myocytes and gap junctions between them. Whilst there is no available measured intracellular and extracellular conductivities of zebrafish cardiac tissue, it is unlikely that they would be of the same order of magnitude as $1.55 \times 10^{-5} S/m$. The discrepancy is most likely due to the role that the gap junctions play in the electrodynamics of the heart which were ignored in the previous work.

Discrete cardiac models are usually limited because of the increased geometrical complexity and the computational load compared to a bidomain model. Over the last ten years, the increase of computational speed, has made it feasible to model cardiac tissue using a discrete approach [100] and it has been applied to small volumes of human cardiac tissue such as a bundle of myocardium with 132 myocytes [98] and a cardiac fibre with 50 myocytes [99]. However, although up to 16000 human cardiac cells have been modelled successfully using the discrete approach [100], the human heart contains as many as 2×10^9 myocytes [146] and is still difficult to model.

The discrete nature of LZVF models has a clear effect on the conduction of electrical signals along the cardiac fibre. The transmembrane potential shows pronounced steps in the region where the myocytes transition from polarised to depolarised, as may be seen in Figure 5.9. The transmembrane potential varies little across an individual myocyte. In contrast the transmembrane potential varies smoothly with distance in the HVF model. This difference arises because the much higher gap junction resistivity in the LZVF case leads to weak electrical coupling between the myocytes, whereas in the HVF case the coupling is stronger. The transmembrane potential obtained using a bidomain model of a human ventricular fibre with the same geometry as the HVF model would be expected to vary in a similar smooth way with distance. The steps in the variation of transmembrane potential with distance for the LZVF models could not be reproduced by a bidomain model and illustrate the problems with the previous bidomain based whole heart zebrafish heart model.

The development of the LZVF model paves the way to a model of the entire larval zebrafish heart in the next step. This would allow cardiac propagation to be simulated in the whole heart level and hence the ECG could be predicted. By incorporating abnormal cellular structure such as disordered myocyte alignment and irregular behaviour or distribution of gap junctions, such models could be further used to assess the ECG of the diseased heart.

The gap junction resistivities required to obtain CVs comparable to those observed are $200\ \Omega \cdot cm^2$ and $110\ \Omega \cdot cm^2$ for the LZVF1 and the LZVF2 models respectively. These are much larger than the $1.125\ \Omega \cdot cm^2$ required for the HVF model. The resistances of the gap junction channels per myocyte are consequently larger, although the smaller cross-sectional area of the larval zebrafish myocytes ($100\ \mu m^2$) versus ($300\ \mu m^2$) is partly responsible for this. In Table 5.7, it shows the numbers of gap junction channels per myocyte which is derived from the total resistance of gap junction channels per myocyte. Due to the uncertainties in quantities such as the individual gap junction channel conductances and the simplified nature of the LZVF and the HVF models, these must be taken as order of magnitude estimates. On this basis, there is a good agreement between the numbers of gap junction channels per myocyte obtained from both zebrafish models, but these values are two to three orders of magnitude smaller than the number of gap junction channels per myocyte derived from the HVF model, which is consistent with the two orders of magnitude between the gap junction resistivities used in the models. The gap junction resistivity that is used in the HVF model is the same as that used in [99] and was chosen in order to compare the modelling results with those reported in that publication and a similar CV are obtained. Other larger reported values for the intercellular resistance associated with the gap junction channels, which come from adult mammalian hearts, are also shown in Table 5.7 and these result in a smaller number of gap junction channels, but the values are still much larger than those obtained from the LZVF models. However they are consistent with computer simulations which investigated the effect of varying gap junction channel numbers on the CV of mammalian ventricular muscle [145]. So the results are consistent with there being a lower density of gap junctions between cells in the larval zebrafish heart than in the adult mammalian heart.

5.9 Summary

Discrete models of larval zebrafish ventricular fibres based upon cube-shaped myocytes were described in this chapter which are comparable in size to those in the 48 and 72 hpf zebrafish hearts. These models use realistic intracellular and extracellular conductivities and incorporate gap junctions as ohmic resistances connecting the myocytes. The membrane capacitance is also realistic, but the phenomenological FHN model was chosen to represent ionic membrane currents because it can be modified to resemble zebrafish APs in different regions of the heart. The parameters of the FHN model, were adjusted to give APs which are consistent with published data. The key parameter of these ventricular fibre models is the gap junction resistivity, which is adjusted to obtain CVs in agreement with the published observations of activation propagation in the larval zebrafish hearts. In order to validate this approach, a similar model of a human ventricular fibre were constructed and found that the results agree well with similar models [99] and also with more sophisticated models [98] published elsewhere, based on the Luo and Rudy model [43]. Apart from the ionic current model, all of the electrical properties of the human model are the same as the published models including the gap junction resistivity. For the zebrafish models, it needs to use a gap junction resistivity which is two orders of magnitude higher than the human case, which is consistent with a lower density of gap junction channels. This is a one dimensional model with all of the gap junctions located at the interfaces between myocytes, which is a reasonable approach for mammalian cardiac tissue, but in the three-dimensional zebrafish embryo heart, gap junctions may be located laterally, allowing for propagation in more than one dimension. How this would affect the gap junction resistivities required for a discrete model would be described in the following chapters. As the ultimate aim of this project is the creation of such a three-dimensional model of a whole larval zebrafish heart and the work described here shows that such a model is feasible. The aim of such modelling work is to understand the electrical activity of the larval zebrafish heart in the normal state and in the diseased or genetically modified state. The methods applied here allow to consider situations where the density or distributions of gap junction channels are varied from the normal state and conditions where the geometry of the heart is affected. The use of the FHN model to represent ionic currents may not be a barrier addressing situations where particular ion channels are modified or absent. If the effect on the AP is known, then this approach is still applicable.

6. CARDIAC TISSUE MODELS

The ventricular fibre models in the previous chapter simulated the electrical propagation in a single, linear, direction. However, as introduced in Chapter 2, in the human cardiac tissue, the cardiac propagation is anisotropic. The anisotropic electrical propagation in heart is mainly determined by the cellular nature of the tissue, for example: cell morphology, extracellular spaces, and the number of gap junctions (GJs) and their spatial distribution. In order to investigate how these factors influence cardiac propagation in the larval zebrafish heart, the larval zebrafish ventricular fibre (LZVF) model introduced in Chapter 5 was expanded to cell array models to simulate the electrical propagation in a two-dimensional space. As introduced in Chapter 2, GJs in the zebrafish heart are not only in the intercalated discs, but also in other regions like the lateral walls of the fibres [64]. However the specific distribution of GJs in larval zebrafish cardiac tissue is still unclear. Therefore, in the cell array models for larval zebrafish described later, the distribution of the GJs was simulated in two ways. First, the cells were simplified as cubic blocks which are same to the myocytes in the LZVF model. The GJs were distributed uniformly in the interior boundaries as in the LZVF model. Second, the cells were simulated as polygonal cells which allow to include more extracellular spaces between cells. The GJs are only distributed in the boundaries connected two cells. The effects of factors on conduction velocity (CV) were investigated here using the cubic cell array model including the stimulation current, extracellular space size, cell number and effective GJs conductance. Then the cardiac propagation in the polygonal cell array model was investigated and compared with the cubic cell array model. Finally, two cell cylinder models resembling the tube-like heart in a 24 hpf zebrafish introduced in Chapter 2 were described based on the cubic cells and the polygonal cells which simulated three-dimensional propagation.

6.1 Modelling cardiac propagation in 2 dimensions

6.1.1 Model geometry

Model geometries were constructed using COMSOL. The first model is the cubic cell array model. As with the LZVF1 model, cubic cells are tightly packed in a 2D cell array including 225 cells as shown in Figure 6.1 (C). The length L of the cubic cell is $12.5\ \mu m$ to replicate the ventricular myocytes in 52-72 hpf zebrafish heart [46, 147]. These myocytes are larger than the myocytes in 48 hpf zebrafish which has been simulated in the previous chapter. The larger myocyte size is chosen to simulate here because the whole heart model described in the next Chapter is for 72 hpf zebrafish heart.

However as shown in Figure 6.1 (A), typical histological human cardiac tissue also has extracellular spaces between cells rather than only tightly packed cells. The AP propagation from cell to cell is not only through the GJs, but also through the extracellular spaces. Thus a more realistic cell array model is developed to incorporate these extracellular spaces as the second cell array model: the polygonal cell array model. In this model, 15 times 15 polygonal cells with $12.5\ \mu m$ in length similar to the first cell array model were constructed. The extracellular spaces at four corners of the polygonal cells are called internal extracellular spaces for convenience below. The length of these spaces at each corner is $\frac{L}{4}$ as shown in Figure 6.1 (B).

Both cell array models were placed in the middle of a block representing the external extracellular space with $220\ \mu m$ in height and width and $50\ \mu m$ in depth as shown in Figure 6.3 (C) and (D).

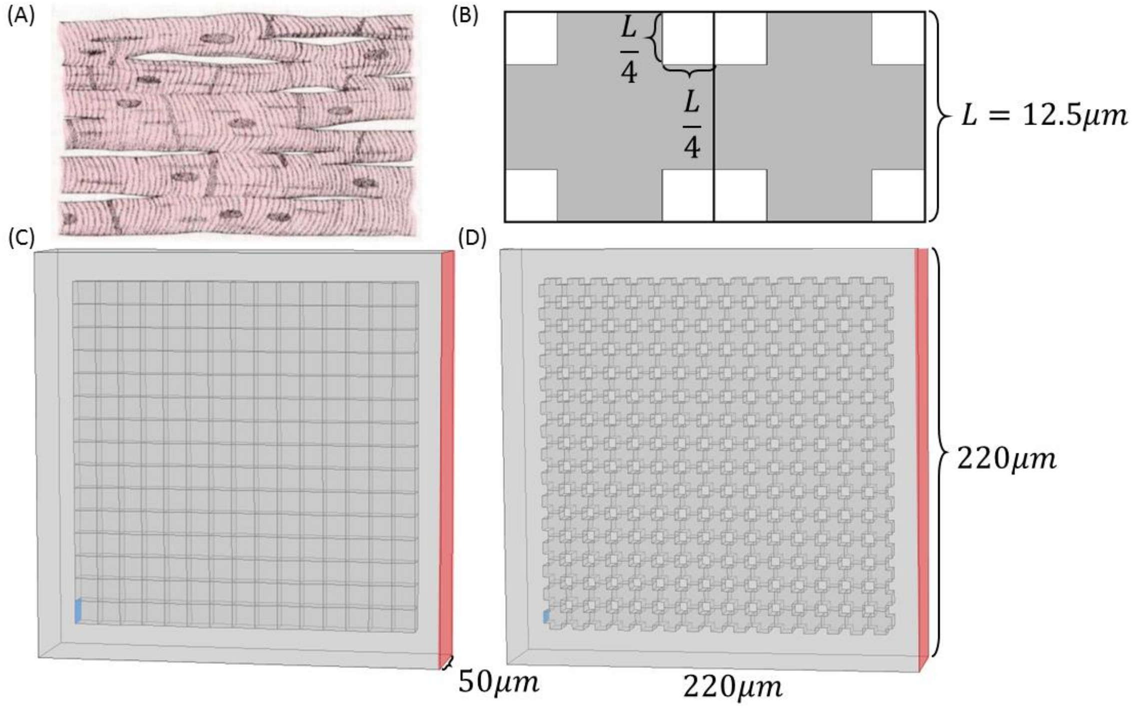

Figure 6.1: (A) Histological human cardiac tissue from [148]; (B) Cubic cells in black outlines and polygonal cells filled in grey; (C) Cubic cell array model geometry; (D) polygonal cell array model geometry; The stimulation currents were applied to the left boundary of cell at left bottom corner marked in the blue and the ground conditions were applied to a boundary on the extracellular block at the opposite side of the stimulated cell marked in red.

6.1.2 Cubic cell array model

The electrical model and parameters used in the cubic cell array model were same to the LZVF1 model except for the stimulation current. As shown in Figure 6.1 (A), the stimulation current and the ground condition were applied to the boundaries in blue and red respectively.

Preliminary tests on the magnitude of the stimulation current were conducted and found that the same stimulation current magnitude ($50\,\mu A/cm^2$) as used in the LZVF models in Chapter 5 cannot activate the cells in this cell array model. Therefore it was increased and the effects of the different stimulation currents on the AP shapes and the maximum upstroke velocity (MUVs) were investigated. As shown in Figure 6.2 (A), the APs produced by the models using stimulation currents at $200\,\mu A/cm^2$ and $400\,\mu A/cm^2$ are not in the realistic shapes of AP as there are long time delays between the depolarization and before reaching the maximum potentials. In addition, their MUVs as shown in Figure 6.2 (B) and (C) shows distortions at the area near the stimulated cell. In comparison, a larger stimulation current at $800\ \mu A/cm^2$ leads to a normal AP and no distortions on the MUV. Therefore this stimulation current at $800\ \mu A/cm^2$ was chosen. As shown in Figure 6.2 (D), the MUVs varied across the cell array. The four cells near the stimulated boundaries have extremely large MUV which is caused by the stimulation current injection. In the middle section of the cell array, the MUV is about $6-8\ V/s$ which is comparable to $6.67\ V/s$ produced by the LZVF1 model. It is gradually increased to about $13\ V/s$ near the top-right corner which is the farthest region from the stimulated cell. This result is very similar to the LZVF models that the MUVs at both ends of the fibre are larger than in the middle section.

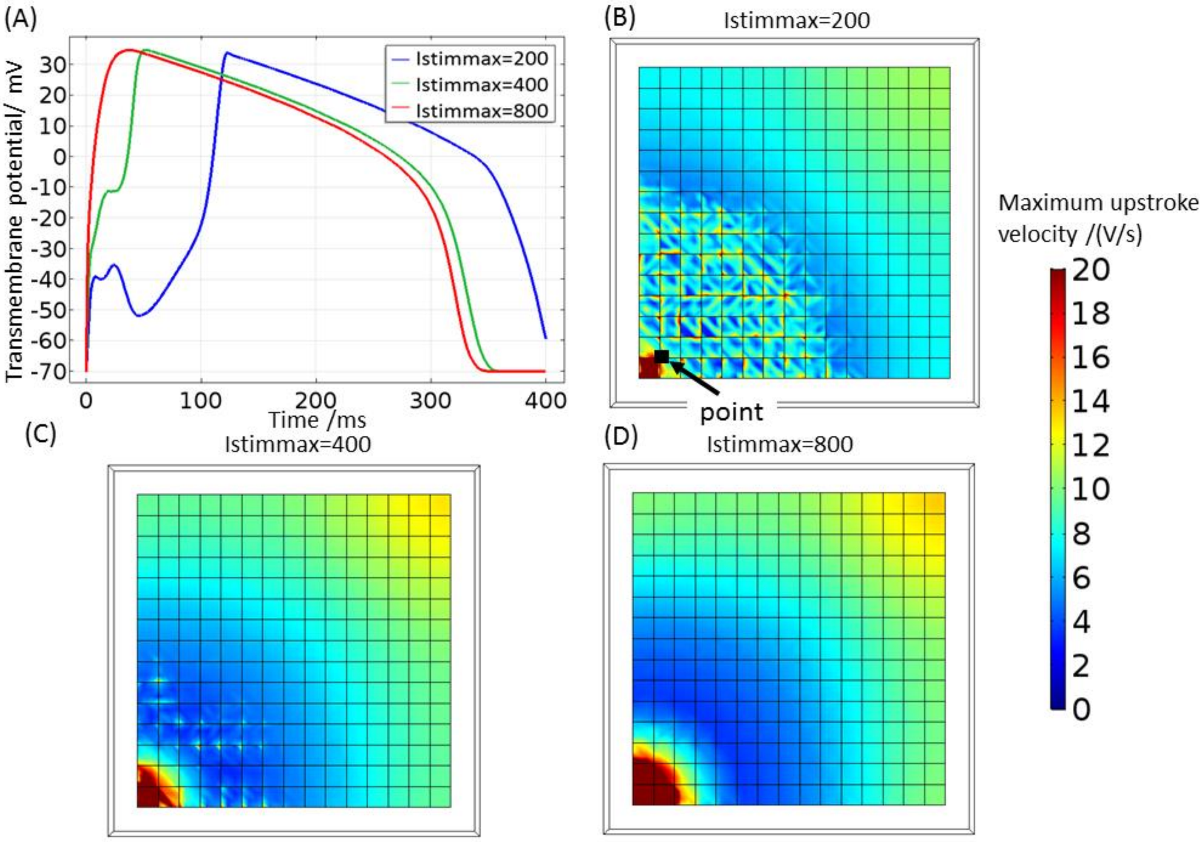

Figure 6.2: (A) APs measured at the point marked in black in (B) produced by the cubic cell array model using various stimulation currents of 200, 400 and $800\ \mu A/cm^2$; MUVs produced by the cubic cell array model using various stimulation currents of (B) 200, (C) 400 and (D) $800\ \mu A/cm^2$.

A plane intersecting the middle of the cell array model was chosen to plot the activation time in Figure 6.3 (A). Same as in the LZVF model, the activation time was defined as the time when the intracellular potential reaches $0\ mV$. As shown in Figure 6.3 (A), the activation times were dependent on the distance from the stimulated cell. The pattern of activation time is symmetric diagonally and the cell at the top-right corner is the last activated cell. The distances from the stimulated membrane along the diagonal line marked in black in Figure 6.3 (A) were plotted against the activation times as shown in Figure 6.3 (B). Small steps indicate the difference of activation times between the neighbouring cells. Despite these small steps, it is also shown that the plots are not linear but curved especially at both ends due to the edge effects. Therefore, 3 different sections were chosen to derive the CVs by applying the first order polynomial curve fitting. As shown in Figure 6.3 (B), 5 data points representing the 5 cells in these sections were marked in different colours and their activation times and distances were used in the curve fitting to derive the CVs labelled in Figure 6.3 (B). The derived CVs increase from $2.84\ um/ms$ near the stimulated cell (section 1) to $9.73\ um/ms$ in the middle section (section 2). The maximum CV is $29.86\ um/ms$ at the top-right corner of the cell array model (section 3).

Different from the LZVF models described in Chapter 5, the depolarization wave front in the cell array is convex. For the cells in the middle of the cell array, they are directly connected to three cells comparing with only one cell in the LZVF models. The charges carried by the depolarizing currents are not only used to activate these cells but also transport to the surrounding non-activated cells. For the cell at the top-right corner, there is no more non-activated cell after it. Therefore, all charges arriving at the top-right corner are used to activate the cells which result in a much faster activation and a larger CV. Overall, the CV in the middle section (section 2) is least affected by the stimulation currents and the edge effects than the other CVs.

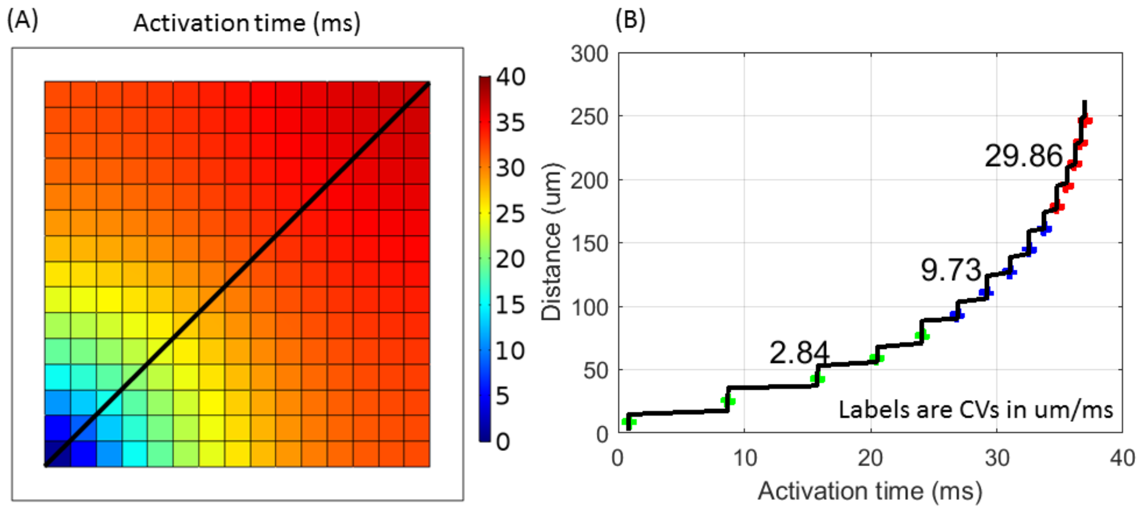

Figure 6.3: (A) Activation time map of the cubic cell array model and (B) Distances from the stimulated membrane along the black diagonal line shown in (A) versus activation time labelled with CVs for section 1 (green points), section 2 (blue points) and section 3 (red points).

However it should be noted that the edge effects would be less obvious in a larger cell array including more cells. The cell numbers in the cell array model were increased in order to test this. As shown in Figure 6.4, the maximum CV is $26.11\ um/ms$ at the top-right corner of the 45*45 cell array model which is smaller than $27.26\ um/ms$ in 25*25 cell array model and $29.86\ um/ms$ in the 15*15 cell array model shown in Figure 6.3. The plots become more linear with the increase of cell number and only show a small curved section at the ends. This feature is also similar to the LZVF model as shown in Figure 5.6.

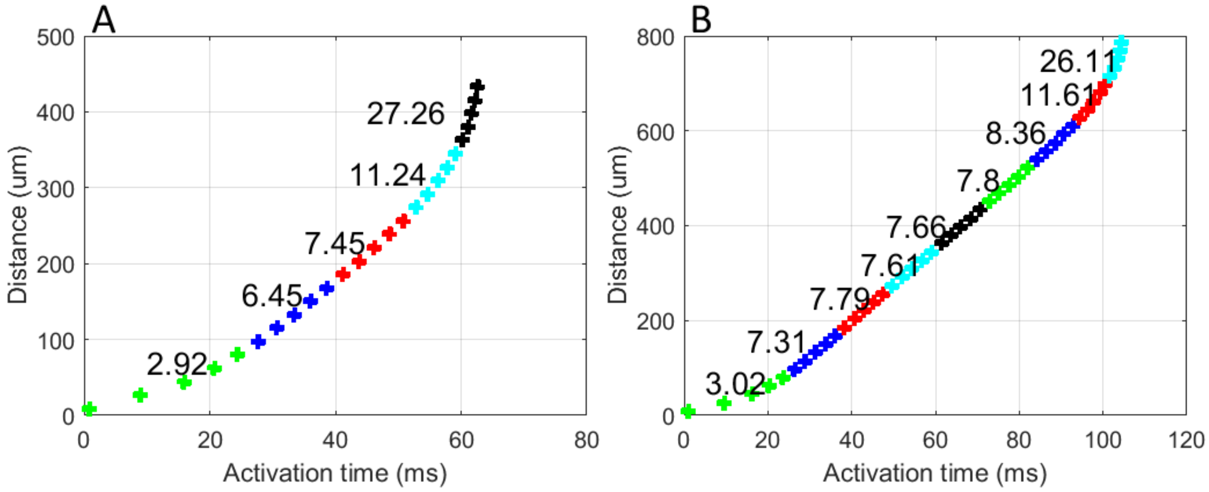

Figure 6.4: Distances from the stimulated membrane versus activation time labelled with CVs for sections in different colours (each section includes 5 cell points) with a larger cell array model having: (A) 25*25 cells and (B) 45*45 cells.

6.1.3 Investigation of factors that affected the conduction velocity

In the cubic cell array model, three factors were investigated: the stimulation current, extracellular space size, and effective GJ conductance. The CVs of all three sections in the cubic cell array model were plotted against the three factors in Figure 6.5.

It has been found in the LZVF1 model that varying the magnitude of the stimulation current would not affect the CV in the fibre. As shown in Figure 6.5 (A), except for the CVs produced by the stimulation current at 400 $\mu A/cm^2$ the other CVs produced by models using larger stimulation currents are very similar ranging within 1 um/ms. As shown in Figure 6.2 (A) and (C), the stimulation current at 400 $\mu A/cm^2$ resulted in a distorted AP and a distorted MUV which is not a reliable result. For the other stimulation currents, the variation of CVs is not significant which is consistent with the modelling results produced by the LZVF1 model.

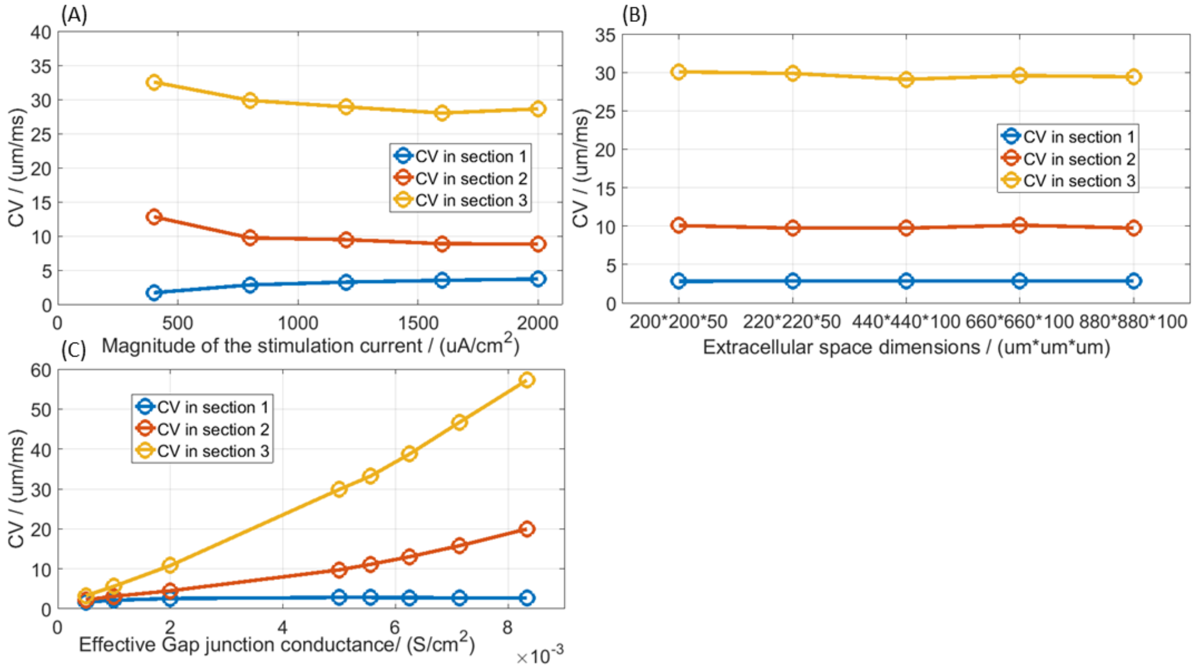

Figure 6.5: CVs of three sections in the cubic cell array model shown in Figure 6.3 (B) versus: (A) the magnitude of the stimulation current, (B) extracellular spaces dimensions, (C) effective GJ conductance.

The extracellular space size has been investigated in LZVF1 model and it was found that this factor does not affect the CV. In order to find whether it is still the same in the cell array model, the extracellular space sizes were varied by changing the dimensions of its length, width and depth and are plotted in Figure 6.5 (B). It is shown that as the extracellular space sizes varied, the CVs for all three sections showed little variation, which is also consistent with the modelling results produced by the LZVF1 model.

The same effective GJ resistivity used in the LZVF1 model ($200\ \Omega \cdot \mathrm{cm}^2$) was applied to the cell array models. The effective GJ conductance is the reciprocal of the effective GJ resistance which is $5 \times 10^{-3}\ \mathrm{S/cm}^2$. This effective GJ conductances in the cubic cell array were varied from $5 \times 10^{-4}\ \mathrm{S/cm}^2$ until $8.3 \times 10^{-3}\ \mathrm{S/cm}^2$ and were plotted against the CVs of section 2 in Figure 6.5 (C). It can be seen that with the increase of the GJ conductance, all CVs of the three sections increased starting at a low increase rate and gradually to be a high increase rate. As the GJ conductance increases, it results in decreasing the intercellular conduction delay which leads to the increase of the CV. This modelling result is consistent with modelling results reported in [145, 149].

Similar to the method used in Chapter 5, the numbers of GJ channels per myocyte in the cubic cell array model were derived from the effective GJ resistivity, GJ area per myocyte and individual GJ channel conductance. As shown in Table 6.1 using the same GJ resistivity at $200\ \Omega\text{cm}^2$ as in the LZVF1 model, the number of GJ channels per myocyte in the cubic cell array model is about 3 times larger than in the LZVF1 model. It results in a larger CV as $9.73\ \mu m/ms$ comparing with $4.8\ \mu m/ms$ in the LZVF1 model shown in Chapter 5. A larger GJ resistivity at $500\ \Omega\text{cm}^2$ in the cubic cell array model leads to a similar CV as in the LZVF1 model and the resulting number of GJ channels per myocyte is very close to the LZVF1 model.

Table 6.1: Varying gap junction resistivities in the cubic cell array model

Effective gap junction resistivity/ (Ωcm^2)	Effective gap junction conductance / $(\times 10^{-3}\ S/cm^2)$	gap junction area per myocyte / (μm^2)	Number of gap junction channels per myocyte	CVs of section 2 / $(\mu m/ms)$
2000	0.5	292	9-73	2.26
1000	1	292	18-146	3.12
500	2	292	37-292	4.5
200	5	292	91-730	9.73
180	5.6	292	101-810	11.12

6.1.4 Polygonal cell array model

The electrical model and all parameters used in the polygonal cell array model were the same as the cubic cell array model, including the stimulation current.

The activation time map was plotted as shown in Figure 6.6 (A) by using the same method as in the cubic cell array model. Apart from the cells near to the stimulated cell, the pattern of the activation time map was similar to the cubic cell array model in Figure 6.3 (A). Because the diagonal line of the polygonal cell array model also crosses the extracellular spaces which do not have intracellular potentials, no diagonal line of activation time as in Figure 6.3 (B) was plotted. Only the activation times of cells on the diagonal line were plotted as data points as shown in Figure 6.6 (B). Similar to the cubic cell array model, the CVs increase from section 1 ($2.3\ um/ms$) to section 2 ($3.82\ um/ms$) and then to section 3 ($8.97\ um/ms$). The CV of section 1 is similar to $2.84\ um/ms$ produced by the cubic cell array model. However the CVs of section 2 and 3 are about 2-3 times smaller than those CVs produced by the cubic cell array model.

The reduction of the CVs in polygonal array model can be explained by two factors. First, comparing with the cubic cell array model, the polygonal cell array model has a larger extracellular space and a smaller intracellular space. The conductivity of the extracellular space is $20\ mS/cm$ which is larger than the conductivity of the intracellular space ($4\ mS/cm$). Therefore, the CVs reduce.

Second, apart from the size change of the intracellular and extracellular spaces, the internal extracellular spaces in the polygonal cell array model increased the membrane area which is controlled by the FHN ionic current model and also reduced the GJ area, comparing with the cubic cell array model. As it is found from the cubic cell array model that increasing the GJ conductance increases the CV (Figure 6.5 (C)). With the same effective GJ conductance as in the cubic cell array model, the reduction of the GJ area in the polygonal cell array model results in reducing the total GJ conductance which is also responsible for the decrease of CVs.

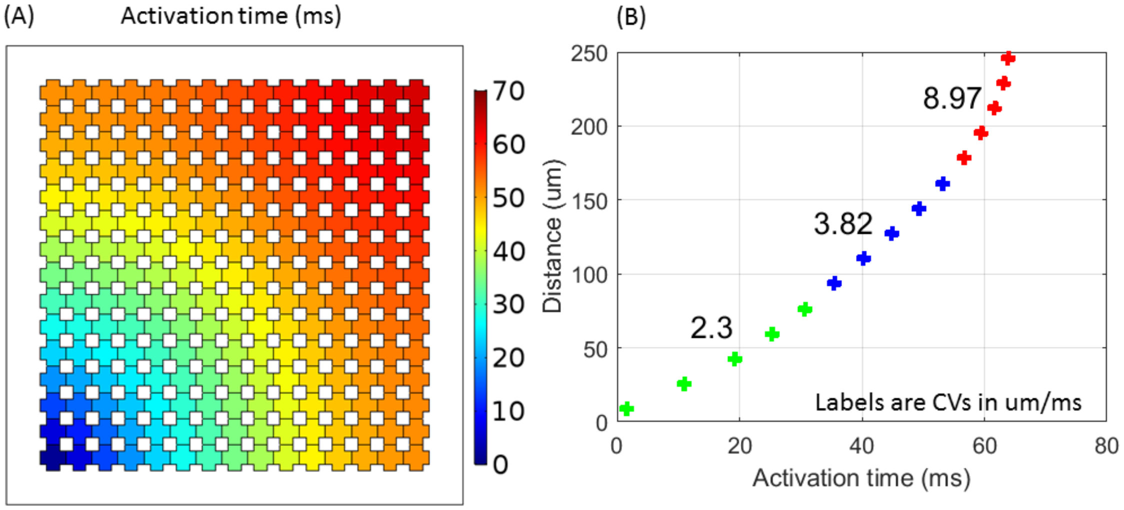

Figure 6.6: (A) Activation time map and (B) Distances from the stimulated membrane along the diagonal line versus activation times of cells on the line labelled with the CVs for section 1 (green points), section 2 (blue points) and section 3 (red points) similar to Figure 6.3 (B).

6.1.5 Cubic cell array to polygonal cell array

In order to investigate how the changes of the internal extracellular spaces affect the CVs, the internal extracellular space sizes were reduced gradually by reducing the length $\frac{L}{4}$ as shown in Figure 6.1 (B) to $\frac{L}{6}$, $\frac{L}{8}$ and $\frac{L}{12}$. The internal extracellular space information of these three polygonal cell array models and the cubic cell array model were summarized along with the resulting CVs of section 2 in Table 6.2.

Table 6.2: Varying the internal extracellular spaces in the polygonal cell array model compared with the cubic cell array model

	Internal extracellular space volume per cell / μm^3	Internal extracellular volume percentage /%	GP surface area percentage/ %	CV of the section 2 / (um/ms)
Cubic cell array	0	0	66.67	9.73
polygonal cell array 1 $(\frac{L}{12})$	54.25	2.78	55.56	6.38
polygonal cell array 2 $(\frac{L}{8})$	122.07	6.25	50	5.43
polygonal cell array 3 $(\frac{L}{6})$	217.01	11.11	44.44	4.85
polygonal cell array 4 $(\frac{L}{4})$	488.28	25	33.33	3.82

The CV maps of polygonal cell array models were plotted in Figure 6.7 (A-C) and the CVs of section 2 were plotted against the internal extracellular volume percentages in Figure 6.7 (D). It is shown that the CV reduces with the increase of the internal extracellular volume percentages. As the increase of the internal extracellular volume percentage is associated with the decrease of the total GJ conductance per cell. The GJ conductance in the polygonal cell array model was investigated in the next section with fixed model geometry as in Figure 6.1 (D).

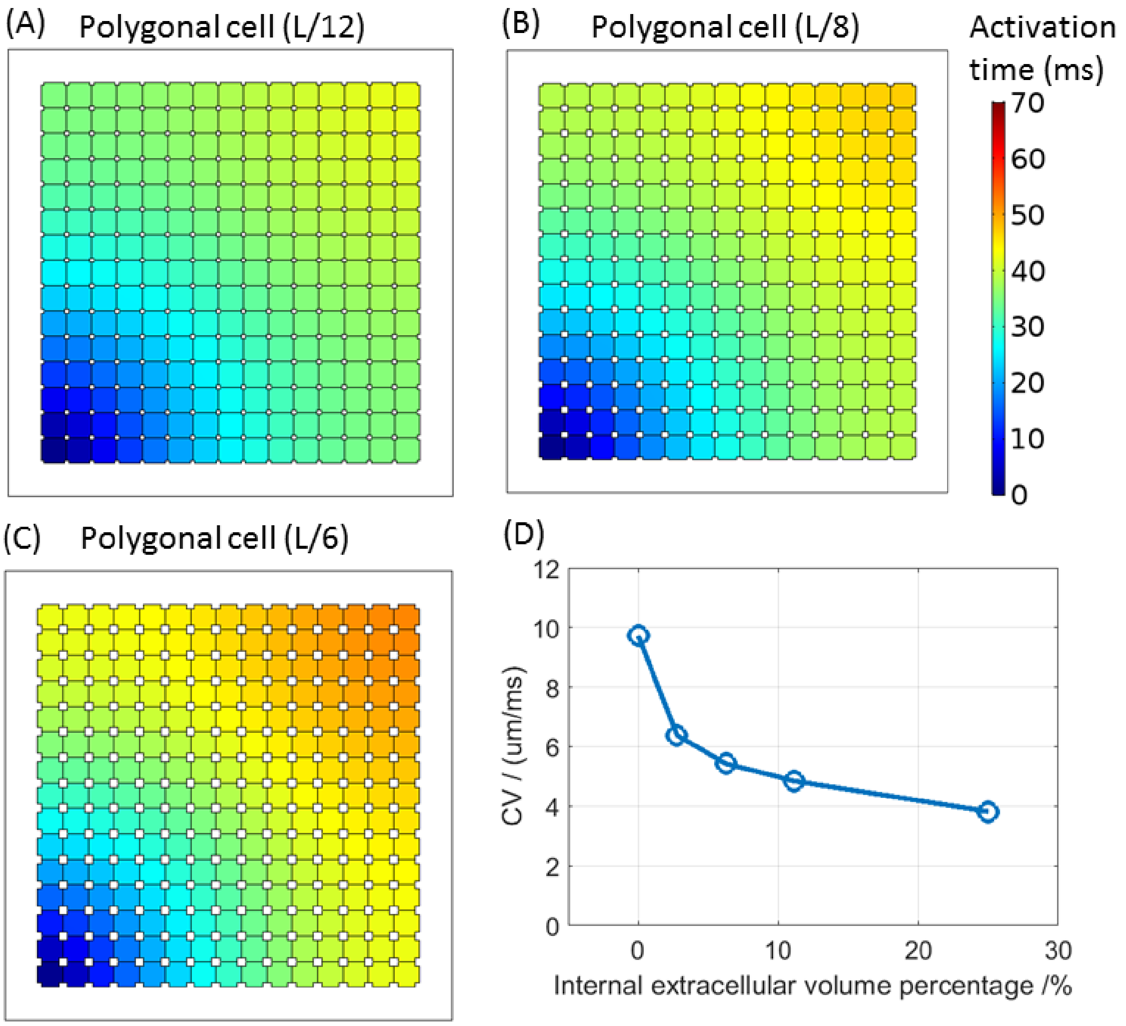

Figure 6.7: Activation time maps of (A) polygonal cell array 1 ($\frac{L}{12}$), (B) polygonal cell array 2 ($\frac{L}{8}$), (C) polygonal cell array 3 ($\frac{L}{6}$); (D) CVs of the section 2 in the cubic and polygonal cell array models versus the internal extracellular volume percentages as shown in Table 6.2.

6.1.6 Varying the gap junction conductance

The polygonal cell array model has smaller CVs when compared with the cubic cell array model as shown in Figure 6.3 (B) and Figure 6.6 (B), which is probably due to the smaller GJ conductance. Therefore the GJ conductance in the polygonal cell array model was increased in order to achieve the same CV as in the cubic cell array model. The number of GJ channels per cell was derived from the GJ area per cell, and the effective GJ conductance using the same method used in Chapter 5 as shown in Table 6.3. The CVs of section 2 are also shown in this table and were plotted against the effective GJ conductance in Figure 6.8.

As shown in Table 6.3, with the same effective GJ conductance of $0.005\ \mathrm{S/cm^2}$, the CV of section 2 in the polygonal cell array was around half of the CV in the cubic cell array. The results are consistent with the derived number of GJ channels per cell in the polygonal cell array model being half of that in the cubic cell array model. Then the effective GJ conductance of the polygonal cell array model was increased to $0.01\ \mathrm{S/cm^2}$ as the derived number of GJ channel per cell was also increased to be the same as the cubic cell array model. The resulting CV of section 2 was $5.48\ um/ms$ which is still smaller than it in the cubic cell array model. Therefore the effective GJ conductance was increased more to $0.0168\ S/cm^2$ resulting in the CV to be $10.39\ um/ms$ which is more close to the $9.73\ um/ms$ in the cubic cell array. The derived number of GJ channel per cell, based on $0.0168\ S/cm^2$ gap junction conductance, was about one and a half times larger than in the cubic cell array. These modelling results imply that the CV is not only affected by the GJ conductance but also other factors such as the increase of the membrane between extracellular and intracellular spaces and the volume changes of extracellular spaces.

Overall, adding the internal extracellular spaces in the cell array model results in the reduction of CVs. Even if the effective GJ conductance in the polygonal cell array model increases to match the number of GJ channels per cell in the cubic cell array, the resulting CV is still smaller than that in the cubic cell array.

Table 6.3: GJ information and CVs of section 2 in cubic and polygonal cell array models

Geometry type	Effective gap junction resistance /(Ωcm^2)	Effective gap junction conductance / (S/cm^2)	Gap junction area per cell / (μm^2)	Number of gap junction channels per myocyte	CVs of section 2 / ($\mu m/ms$)
Cubic cell array	200	0.005	292	91-730	9.73
Polygonal cell array	200	0.005	146	46-365	3.82
Polygonal cell array 1	100	0.01	146	91-730	5.48
Polygonal cell array 2	80	0.0125	146	114-913	6.97
Polygonal cell array 3	70	0.0143	146	130-1043	8.12
Polygonal cell array 4	60	0.0168	146	152-1217	10.39

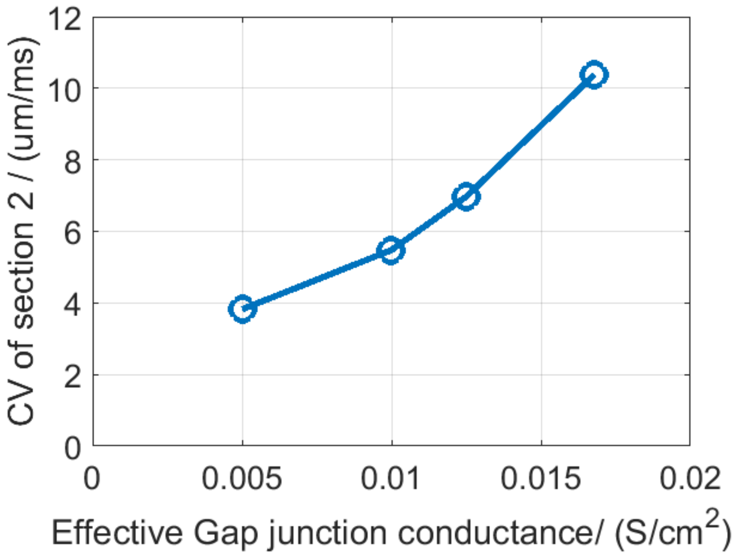

Figure 6.8: CVs of section 2 in the polygonal cell array models versus various effective GJ conductance.

6.2 Modelling the cardiac propagation in 3 dimensions

The cardiac propagation in the real larval zebrafish heart is not only limited to 2D but also in three dimensions (3D) based on the anatomy of the heart [46]. As introduced in Chapter 2, on the early stage of zebrafish development, during 27-36 hpf, zebrafish have a simple tube-like heart and the cardiac propagation in the heart is linear and unidirectional from the sinus venous where the pacemaker activity at the SA node started [56]. Instead of directly modelling the complex larval zebrafish heart with two chambers, this tube-like heart, appearing in the 24 hpf zebrafish, was simulated to investigate the cardiac propagation in 3D.

6.2.1 Model geometry

The image of the tube-like heart in 24 hpf zebrafish is from [56] as shown in Figure 6.9 (A). The model heart was simplified as a cell cylinder including 225 cells which is the same as the cell array models in the last section. The first cell cylinder has no internal extracellular spaces as shown in Figure 6.9 (B). Fifteen cells are tightly packed in a cell ring and fifteen such cell rings are stacked together to form a cylinder. The size of the cells are chosen to be similar to the cell array with the length L as 12.5 µm. This model was titled: the cubic cell cylinder model. The second polygonal cell cylinder model has the same cell number as in the cubic cell cylinder model but includes the internal extracellular spaces as shown in Figure 6.9 (C). For each cell, the four corners are partitioned by a block with cross section area of $\frac{\mathrm{L}}{4} \times \frac{\mathrm{L}}{4}$ as shown in Figure 6.9 (D). Both cell cylinder models are placed in the middle of a block representing the external extracellular space with height of 375 µm and, width and depth of 150 µm as shown in Figure 6.9 (B) and (C).

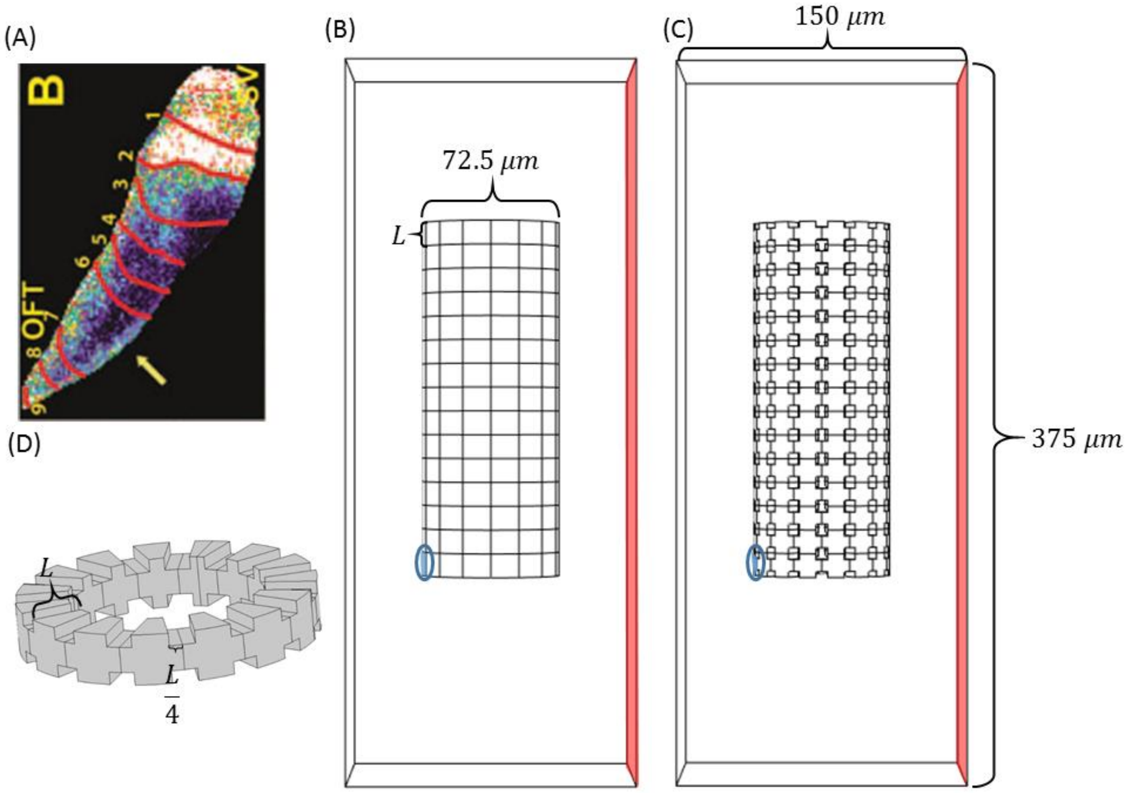

Figure 6.9: (A) Image of 24 hpf zebrafish heart from [56]; Model geometry for (B) cubic cell cylinder and (C) polygonal cell cylinder; (D) a cell ring in the polygonal cell cylinder including 15 cells; The stimulation current is applied to a surface boundary of a cell at the bottom cell ring marked in the blue circle and the ground condition is applied to a boundary on the extracellular block at the opposite side of the stimulated cell marked in red.

6.2.2 AP propagation

Same electrical model as the cell array models was used in the cell cylinder models including the stimulation current. The location of the stimulation current and ground condition applied are illustrated in Figure 6.9 (B) and (C).

The activation time maps for both cubic and polygonal cell cylinder models were shown in Figure 6.10. It shows that the activation in the polygonal cell cylinder is slower than the activation in the cubic cell cylinder. The maximum activation time occurs at the top cell ring in both models. The maximum activation time is about 30 ms in the cubic cell cylinder which is smaller than about 37 ms in the cubic cell array as shown in Figure 6.3. The maximum activation time is about $50\,ms$ in the polygonal cell cylinder which is smaller than about $65\,ms$ in the polygonal cell array as shown in Figure 6.6.

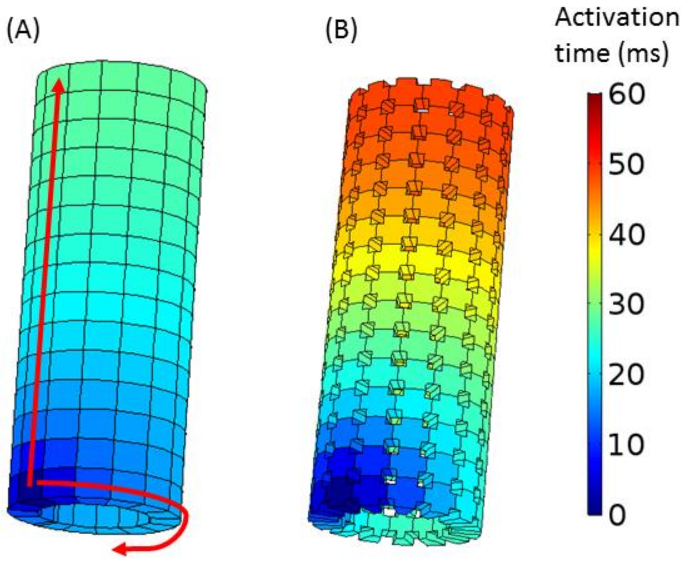

Figure 6.10: Activation time maps of (A) cubic cell cylinder model and (B) polygonal cell cylinder model. The cells on red arrow lines were used to plot Figure 6.11 for the cardiac propagation in longitudinal and transverse directions

The distances from the stimulated membrane along the longitudinal and transverse lines for both cell cylinder models were plotted against the activation times of cells on the lines as shown in Figure 6.11 which are used to derive the CVs. The longitudinal and transverse lines were marked with red arrows in Figure 6.10 (A). The longitudinal line starts from the stimulated cell including 15 cells and the transverse line starts from the stimulated cell including 8 cells. There are only 8 cells used in deriving the transverse CVs because the AP propagation is bidirectional within the cell ring. The last activated cell in this cell ring is the 8th cell from the stimulated cell. Similar to the cell array model, the CVs were derived for the cells in different sections showing in different colours. There are three sections for the longitudinal CVs where each section has five cells. There are also three sections for the transverse CVs where each section has three cells. Because there are only 8 cells in the transverse line, the CV of the middle section is using the data points in black circle as shown in Figure 6.11 which are also used in deriving the CVs of the other sections.

As shown in Figure 6.11 similar to the cubic cell array model, the CVs increase from the section near the stimulated cell and reach the maximum at the furthest section from the stimulated cell. The CVs of different sections in longitudinal direction in the cubic cell cylinder model in Figure 6.11 (A) and (B) are similar to the CVs derived in the cubic cell array model as shown in Figure 6.3 (B). The CVs in polygonal cell cylinders in Figure 6.11 (C) and (D) are also similar to the CVs derived in the polygonal cell array model as shown in Figure 6.6 (B). Overall, the modelling results of the cell cylinder model are similar to the cell array models.

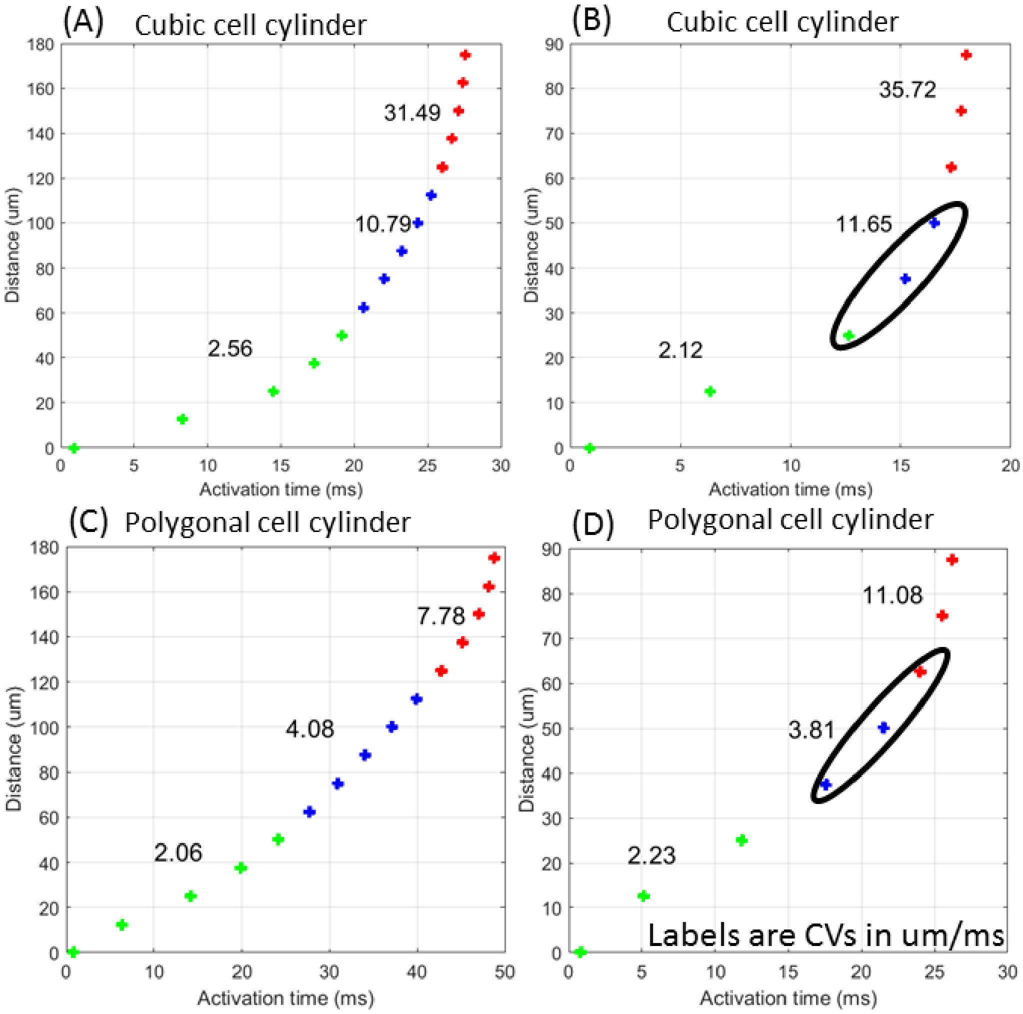

Figure 6.11: Distances from the stimulated membrane along the longitudinal line vs activation times of cells on the line labelled with CVs for section 1 (green points), section 2 (blue points) and section 3 (red points) for (A) cubic cell cylinder model and (C) polygonal cell cylinder model. Distances from the stimulated membrane along the transverse line vs activation times of cells on the line labelled with CVs for section 1 (green points), section 2 (black circle) and section 3 (red points) for (B) cubic cell cylinder model and (D) polygonal cell cylinder model

6.2.3 Varying the gap junction conductance

Similar to the procedure in Section 6.1.6, the GJ conductances in the polygonal cell cylinder models were varied to get same CVs in the cubic cell cylinder models. Similar effective GJ conductance in the polygonal cell array models was applied to the polygonal cell cylinder models. The number of GJ channels per myocyte in the cell cylinder models were derived from the effective GJ conductance and GJ area per myocyte. The GJ information and CVs of section 2 along the longitudinal line were listed in Table 6.4. With the same number of GJ channel per cell in the polygonal cell cylinder 1 model based on $100\ \Omega \cdot cm^2$ effective GJ resistance, the resulting CV of section 2 is 6.7 $\mu m/ms$ which is smaller than in the cubic cell cylinder model. Decreasing the effective GJ resistance to $60\ \Omega \cdot cm^2$ in polygonal cell cylinder model resulted in the closest CV of $11.62\ um/ms$ to $10.79\ \mu m/ms$ in the cubic cell cylinder model. The derived number of GJ channels per myocyte was about 50% larger than the cubic cell cylinder model. This modelling result is similar to the results produced by the cell array models.

Table 6.4: Gap junction information and CVs of section 2 in longitudinal line in cubic and polygonal cell cylinder models

Geometry type	Effective gap junction resistance /($\Omega \mathrm{cm}^2$)	Effective gap junction conductance / ($\mathrm{S/cm}^2$)	gap junction area per myocyte / ($\mu\mathrm{m}^2$)	Number of gap junction channels per myocyte	CVs of section 2 / ($\mu\mathrm{m/ms}$)
Cubic cell cylinder	200	0.005	303	95-758	10.79
Polygonal cell cylinder	200	0.005	160	48-380	4.08
Polygonal cell cylinder 1	100	0.010	160	95-760	6.7
Polygonal cell cylinder 2	80	0.0125	160	119-950	8.23
Polygonal cell cylinder 3	70	0.0143	160	136-1086	9.52
Polygonal cell cylinder 4	60	0.0168	160	158-1267	11.62

6.2.4 Mesh convergence analysis

In order to validate the stability and reliability of the cell array and cell cylinder models, mesh convergence analysis was conducted using the similar method as in Chapter 5. CV of section 2 in all model were chosen to test in here. The meshing parameters were varied from the fine level to the coarser level. Similar to the mesh convergence analysis in Chapter 5, when the proportional difference of the CVs from the CVs at the best meshing level is less than 5%, the results are considered as converged results.

The maximum CVs were plotted against the mesh levels for the cell array models in Figure 6.12 (A) and (C) and cell cylinder models in Figure 6.12 (E) and (G). The proportional differences of the CVs between the finest meshing results and each mesh results were also plotted against the mesh levels for the four models in Figure 6.12 (B) (D) (F) (H).

The proportional differences of CVs in the cubic cell array model are less than 1% for all meshing levels as shown in Figure 6.12 (B). Thus all mesh levels are safe to use. The coarser level mesh was used to produce the results in order to optimise computation time.

The proportional differences of CVs in the polygonal cell array model for all levels are less than 5% as shown in Figure 6.12 (D). Thus all mesh levels are safe to use. Coarser level mesh was used in the model.

The proportional differences of CVs in cubic cell cylinder models are less than 4% for all mesh level as shown in Figure 6.12 (F). Thus all mesh levels are safe to use. The normal level mesh was used in the cubic cell cylinder model.

All proportional differences of CVs in polygonal cell cylinder models are less than 1% as shown in Figure 6.12 (H). Thus all mesh levels are safe to use. The coarser level mesh was used in the polygonal cell cylinder model.

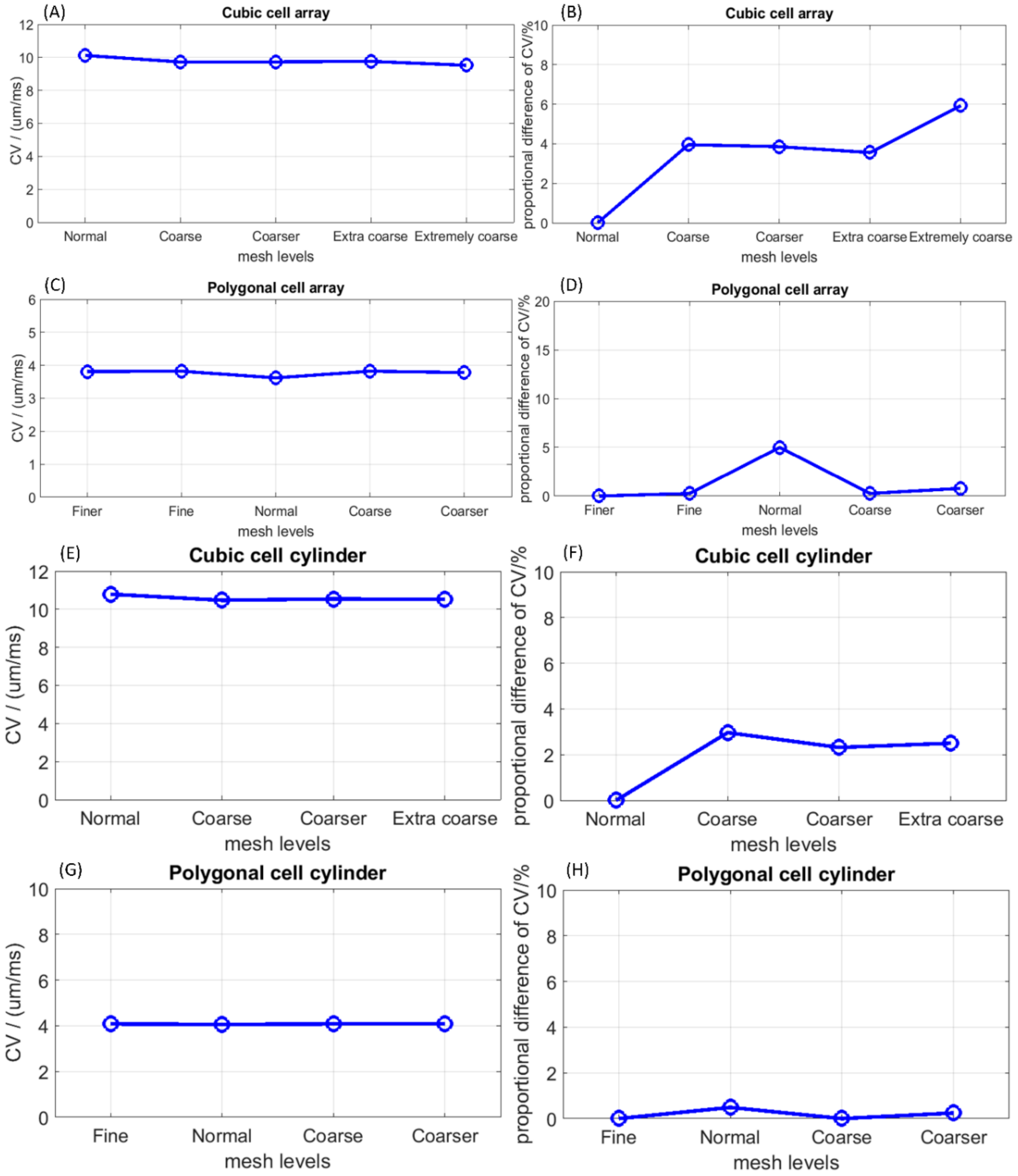

Figure 6.12: CVs versus the mesh levels in (A) cubic cell array model, (C) polygonal cell array model and in (E) cubic and (G) polygonal cell cylinder models; Proportional difference of CV versus the mesh levels in (B) cubic cell array model, (D) polygonal cell array model and in (F) cubic and (H) polygonal cell cylinder models

6.3 Summary

This chapter presents cardiac tissue models for larval zebrafish heart that simulated the cardiac propagation in 2D and 3D. A sheet of cardiac tissue in the larval zebrafish heart was modelled as a cell array model using the simplified cubic cells as in the LZVF1 model. In order to incorporate the real historical cellular structure of human cardiac tissue, extracellular spaces were added between cardiac cells as the polygonal cell array model. In order to understand the 2D cardiac propagation, three factors in the cubic cell array model were varied to investigate their effects on the CVs. The effective GJ conductance was found to have a major influence on the CV. As the distribution of internal extracellular space in the larval zebrafish cardiac tissue is unknown, the internal extracellular space sizes in the polygonal cell array model were varied to investigate its effects on the CV. It has been found that the CV reduces with the increase of the internal extracellular volume percentages. After that, with the internal extracellular space size fixed, the effective GJ conductance in the polygonal cell array model was adjusted in order to achieve the same CV in cubic cell array model.

Next, the 2D propagation in the cell array models were expanded to 3D. A cell cylinder model resembling the tube-like heart in 24 hpf zebrafish was developed based on the cubic cells in the cubic cell array model. Then this cubic cell cylinder model was modified to be a polygonal cell cylinder model to include the internal extracellular spaces.

Unlike the 1D unidirectional cardiac propagation in the LZVF models described in Chapter 5, the propagation in the cardiac tissue models in this chapter is multidirectional which is highly depended on the cardiac tissue shape. In the cell array models, the cardiac propagation was symmetrical in both the longitudinal and transverse directions. The CVs increased in both directions with the increase of the distance from the stimulated cell. The cells on the top and right edges of the cell array reach the maximum CVs.

In the cell cylinder models, the AP propagation includes the bidirectional propagation in the cell ring and the upward propagation along the longitudinal line. Because each cell ring is symmetrical and also a closed loop, the propagation in both directions in the cell ring was the same which resulted in very similar activation times in all cells in the same cell ring, except for the cell ring including the stimulated cell. The CVs increased along the longitudinal line with the increase of the distances from the stimulated cell and the maximum CVs were achieved on the top cell ring.

The CVs in the cell cylinder models in different sections are comparable to the CVs in the cell array models. It reveals that although there are fewer edges in the cell cylinder models, the difference of the CVs between them is not significant.

Adding internal extracellular spaces in both cell array and cell cylinder models reduces the CV. With the increase of the internal extracellular spaces, the GJ area reduced thus the number of GJ channel reduced. In order to produce the same CV as in the cubic cell array models, the effective GJ conductance in the polygonal cell array model was increased. It is found that the effective GJ conductance which derived the same number of GJ channels as in the cubic cell models cannot produce the same CV as in the cubic cell models. The effective GJ conductance needed to increase more to achieve the same CVs.

7. WHOLE HEART MODEL

This chapter introduces a larval zebrafish whole heart model. As introduced in Chapter 2, the shape of the larval zebrafish heart changes during the development stages. Unlike the tube-like heart at 24 hpf modelled in Chapter 6, the larval zebrafish heart at 72 hpf has developed the atrioventricular (AV) band separating the two chambers, the atrium and ventricle. The larval zebrafish during this stage is widely used in *in vivo* experiments due to the heart being fully developed and the embryos being transparent. Many experiments have been conducted on the fish during this stage, for example AP recording [57], ECG recording [150] and optical mappings to study the cardiac conduction [46]. The larval zebrafish heart model introduced here is aiming to replicate these experimental results and then to help with the understanding of the electrophysiological properties of larval zebrafish heart at the cellular level. This chapter starts with the development of this heart model. This model was undertaken using a different discrete approach comparing with a previous 72 hpf zebrafish heart model based on the bidomain model [36]. The modelling results including the AP, activation times of different regions in the heart and ECGs which were compared with experimental results found in the literature. In the ECG section, it has been found that the model ECG did not replicate the recordings very well. It was assumed this is due to a low pass filter used in the experiments. Therefore, the model ECGs were filtered using the same filter and compared with the recordings. After that, the gap junction resistances used in this model were investigated, following with the mesh convergence analysis. At last, in order to replicate the measured activation time map in [57], bulbus arteriosus was added in the heart model.

7.1 Model geometry

The model geometry of the 72 hpf zebrafish heart model was developed in COMSOL. The model heart is made up of two hollow ellipsoids representing the atrium and ventricle, connected to each other by a hollow cylinder representing the atrioventricular (AV) band. The shapes of the atrium, ventricle and AV band were based on a published 72 hpf zebrafish heart model [36] (Figure 7.1). Their dimensions along with the outflow and inflow tracts shapes are consistent with several published images of the 72 hpf zebrafish heart [51, 151, 152].

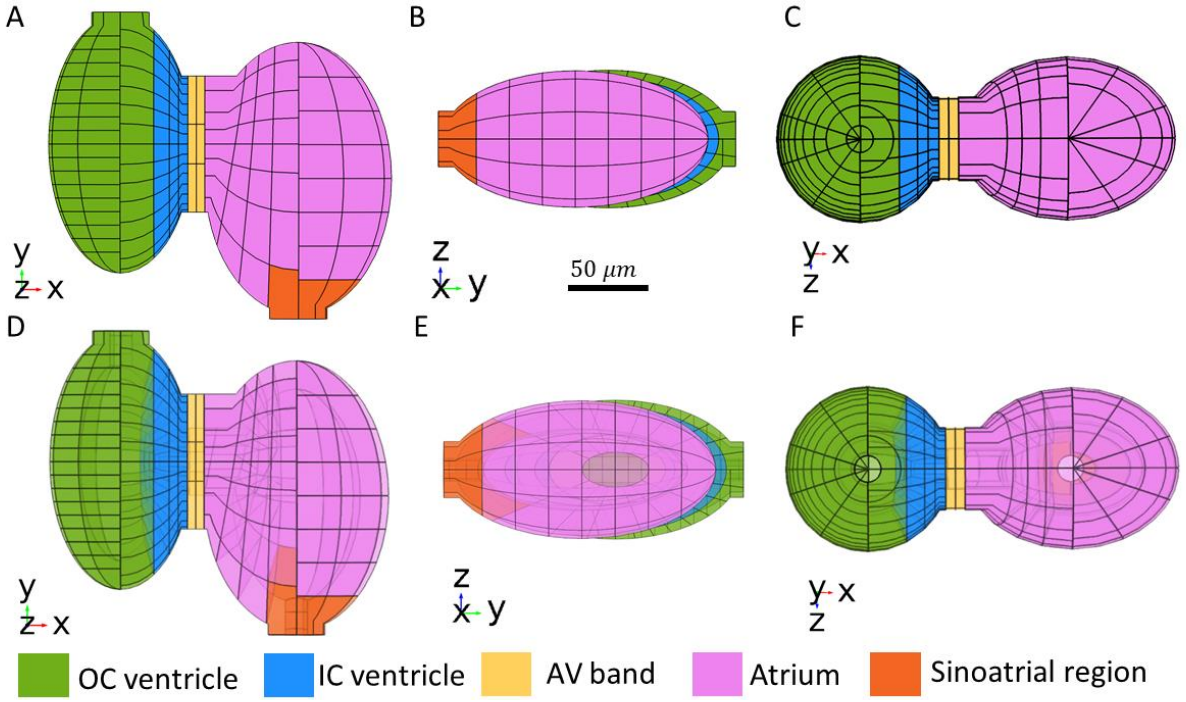

Figure 7.1: Geometry of the 72 hpf zebrafish heart model at: (A) front view, (B) side view, (C) vertical view; (D), (E), and (F) are transparent graphs of (A), (B) and (C) respectively.

The cross-sectional area of model ventricle is $1.02 \times 10^4 \mu m^2$ which is comparable to the measured ventricle diastolic area as $1.15 \times 10^4 \mu m^2$ in [81] and as $9 \times 10^3 \mu m^2$ in [153]. The model ventricle volume is $5.8 \times 10^5 \mu m^3$ comparing with the measured diastolic volume as $5.5 \times 10^5 \mu m^3$ in [154]. The cross-sectional area of model atrium is $1.39 \times 10^4 \mu m^2$ comparing with the measured atrium area as $1.2 \times 10^4 \mu m^2$ in [51]. The thickness of the model myocardial wall is 17 μm and the myocardial volume is $9.4 \times 10^5 \mu m^3$ which is comparable to the measured value of $9 \times 10^5 \mu m^3$ [82].

The geometry and arrangement of myocytes in the model heart is shown in Figure 7.1. The model heart was divided into a number of regions with different sizes and shapes of myocytes as shown. The irregular shapes and sizes of the cardiomyocytes in the larval zebrafish heart have been reported and shown in microscopy images as shown in Figure 7.2.

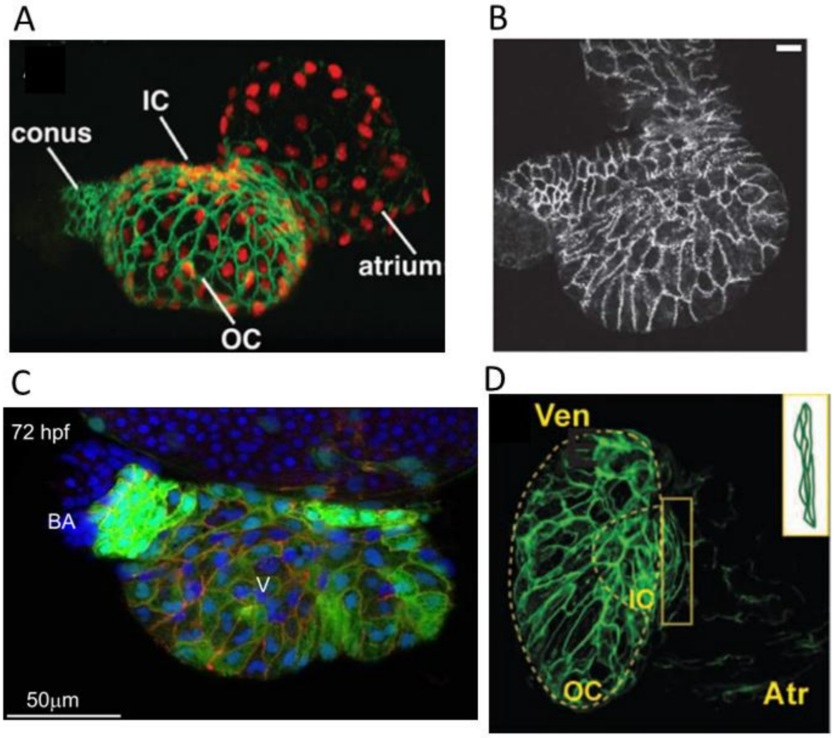

Figure 7.2: Microscopy images of zebrafish heart with myocytes' shapes: (A) 48 hpf zebrafish heart with nucleus stained in red and cell membranes stained in green. IC: inner curvature. OC: outer curvature. [39]; (B) 72 hpf zebrafish ventricle with cell membranes stained with anti-β-catenin [57]; (C) 72 hpf zebrafish ventricle with the membrane stained in green and red. BA: Bulbus arteriosus. V: ventricle [81]. (D) 48 hpf zebrafish heart with cell membranes stained in green. The yellow box shows the AV cardiomyocytes [56].

However based on these two-dimensional images, the complex cardiac tissue structure is difficult to simulate because of its uncertainty in 3 dimensions. Even if this complex cardiac tissue structure is modelled, it would require a tremendous number of mesh elements which would increase the computational load significantly. In this model, the cardiomyocytes were constructed by partitioning the whole heart geometry with surfaces or cones based on the cellular structure of different regions in the heart described in the literature, where it is available. It has been reported that the average surface area per myocyte in the outer curvature (OC) ventricle is larger than the inner curvature (IC) ventricle in the 48 hpf and 60 hpf zebrafish [56] [119]. In addition, the IC myocytes are more round (larger circularity) than the OC myocytes. In comparison, the myocytes in the AV band are more elongated and their orientation is orthogonal to the OC ventricular myocytes as shown in Figure 7.2 (D) [81]. In order to replicate these features of the larval zebrafish heart, the model ventricle was partitioned based on different rules to be two regions: the inner curvature (IC) and outer curvature (OC) ventricle. The AV band was partitioned to result in long and thin myocytes as shown in Figure 7.1. It was suggested that these ring-like orientation of cardiomyocytes are responsible for the AV conduction delays [155]. There is not much published data on the atrial cellular structure in larval zebrafish around 72 hpf. However, high-resolution images using confocal and two-photon microscopy of a 52 hpf zebrafish atrium was found in [46] and based on this, the model atrium is partitioned to give similar myocyte surface area. It has also been reported in this same paper that less than 10 cells are the sinoatrial region in the heart where the APs start. Thus in the model, at a similar position in the atrium, 7 myocytes are chosen to be the sinoatrial region to start the activation of the whole heart. The final cellular structure of the model is compared to the literature in Figure 7.3. As limited information has been found for 72 hpf zebrafish, the reported structures of the larval zebrafish heart in similar developing stages has also been compared including 48 hpf [56], 52 hpf [147], 54 hpf [82], 60 hpf [119], and 72 hpf [39]. The average surface area and circularity per myocyte in different regions in the model heart are compared to the literature along with myocyte number as shown in Figure 7.3. The circularity of the myocytes was calculated by:

$$C = \frac{4\pi S}{L^2} \tag{7.1}$$

Where S is the surface area and L is the perimeter of the surface area. The areas and perimeters are only for the outer surface of the model heart comparing with the results based on images in the literature.

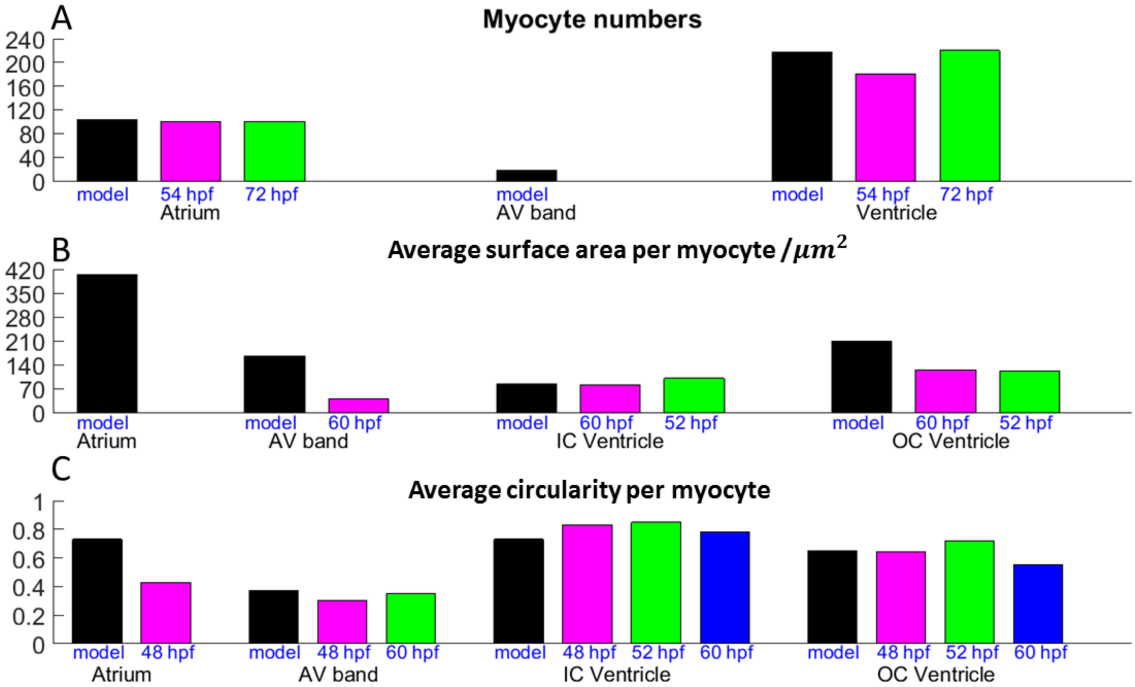

Figure 7.3: Cellular information of different regions in the model larval zebrafish heart (black) comparing with the literature for larval zebrafish heart in different developing stages (coloured) including (A) myocyte number, (B) average surface area per myocyte, (C) average circularity per myocyte.

Note that the model heart is about 1.7 times larger than the heart geometry in the previous published 72 hpf larval zebrafish heart model [36]. As the heart is beating regularly with varying size and shape while the ECGs are recorded, the previous model heart geometry reproduced the heart at the mid-point in a cardiac cycle. However a fixed heart is usually used in the electrophysiological experiments to eliminate the errors caused by the mechanical movements [46, 57]. It means that the heart is in the diastolic state which is the maximum volume of a cardiac cycle. In order to replicate the real size of the larval zebrafish heart used in the experiments, the model heart geometry was scaled up along with the model zebrafish body.

The current geometry of zebrafish body is based on the model zebrafish body reported in [36] which was constructed using a 3D modelling package, Blender (Blender Foundation), based on the available images of 72 hpf zebrafish. In the current model, the original geometry of fish body was imported from Blender to COMSOL and scaled up about 2 times to resemble the reported dimensions of 72 hpf zebrafish body in [156, 157]. The final model geometry of the 72 hpf zebrafish body is shown in different view angles in Figure 7.4 (B) and (D) which are comparable to the microphotographs found in [157] shown in Figure 7.4 (A) and (C).

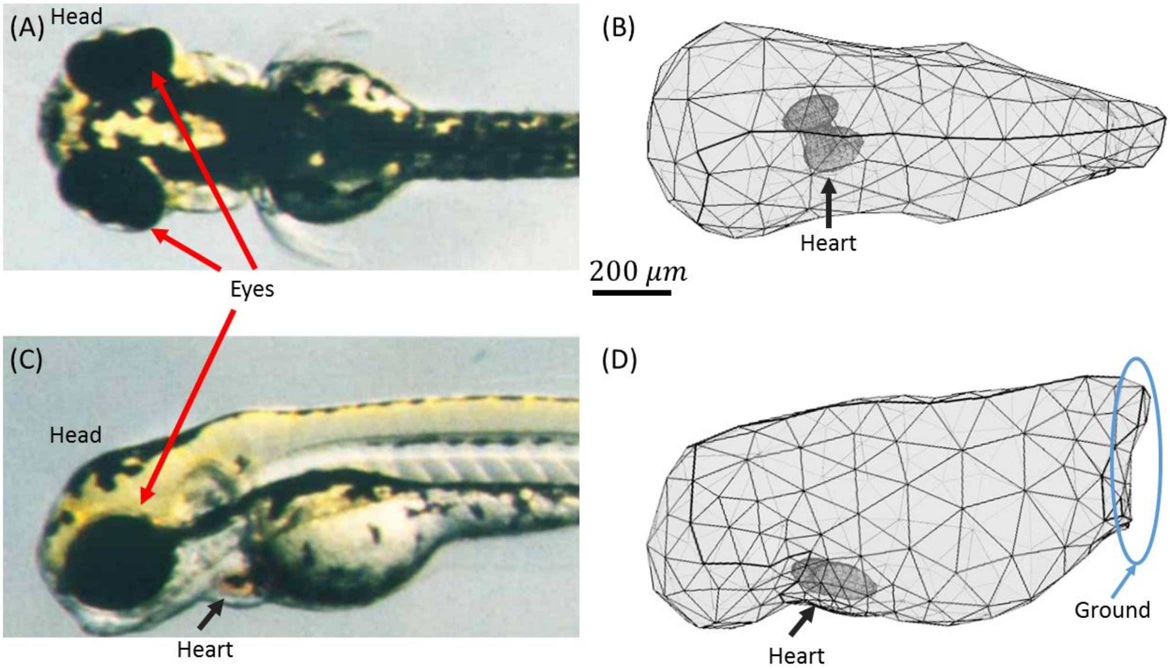

Figure 7.4: Microphotographs of a 72 hpf zebrafish body in (A) dorsal view and (C) left-side view[157]. Model geometry of the whole 72 hpf zebrafish body with heart in (B) left-side view and (D) dorsal view. Scale bar is 200 μm for all images. The ground condition is applied to the boundary in the blue circle.

7.2 Model settings

The electrical model applied here is a discrete approach which is similar to the larval zebrafish models in the previous chapters. The physical equations of this electrical model are summarized in Figure 7.5. This heart model was activated differently from the models described in the previous chapters. This model heart was stimulated by setting the initial intracellular potential of the cells in the sinoatrial regions to $-20\ mV$, which is higher than the resting potential. As discussed in Chapter 4, both applying stimulation currents and setting the potentials higher can start the activation. However applying stimulation currents resulted in distortions in the stimulated cells as shown in LZVF models in Chapter 5. Therefore, the simulation method was changed to set the initial intracellular potential higher in this model. The ground boundary condition is applied to the boundary at the end of the fish body near the tail as shown in Figure 7.4.

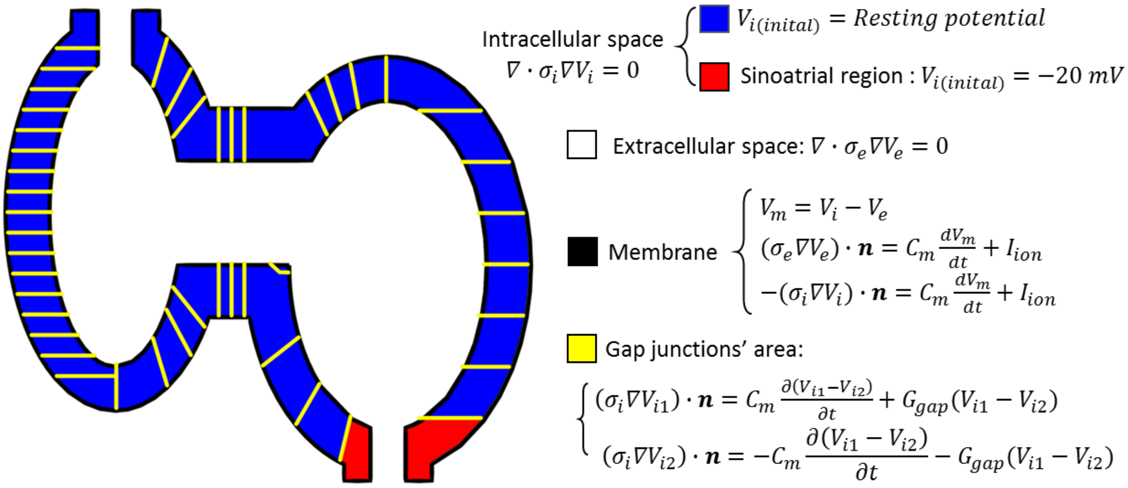

Figure 7.5: Electrical equations applied to different regions in the zebrafish heart model including the intracellular space consisting of the sinoatrial region (red) and the other non-self-excitatory regions (blue), the extracellular space (white), membrane (black) and the gap junctions' area (yellow).

The electrical parameters applied to the model are listed in Table 7.1. The intracellular and extracellular conductivities and membrane capacitance are the same as in the models described in Chapter 4, 5 and 6. The model gap junction resistivities of different heart regions were adjusted to fit a published isochronal activation map [57] because no measured gap junction resistance of the zebrafish heart can be found.

Table 7.1: Electrical parameters used in the 72 hpf zebrafish heart models

Regions	Fish body	Atrium and Sinoatrial region	AV band	IC Ventricle	OC ventricle
Conductivity/ (S/m)	2	0.4	0.4	0.4	0.4
Gap junctions resistivity / $\Omega \cdot m^2$	N/A	0.35	0.23	0.13	0.2
Membrane capacitance/ (F/m^2)	N/A	0.01	0.01	0.01	0.01

The ionic current model used here is the Rogers-McCulloch version of Fitzhugh-Nagumo model [42] which is similar to the previous models described in Chapter 4, 5 and 6. The parameters of this model were adjusted to resemble the measured AP of a 48 hpf zebrafish [56] as closely as possible as shown in Figure 7.7 and Figure 7.8. The measured AP of a 48 hpf zebrafish was chosen because no AP measurements of all regions in a 72 hpf zebrafish heart can be found by the time of writing. (A comparison of ventricular APs in 48 hpf and 72 hpf zebrafish heart can be found in Chapter 5.) The parameters used in the LZVF1 model are the primary parameters used for the adjustments to resemble APs in different regions in the heart. The final parameters are given in Table 7.2 compared with the parameters used in the LZVF1 model. The initial conditions of the model parameters were listed in Table 7.3. The initial values of intracellular potentials were chosen to equal to the resting potential of the different regions in the larval zebrafish heart [56] and the initial values of the extracellular potential are 0 mV as the ground potential.

Table 7.2: Parameters of the ionic current model used for the different regions of the larval zebrafish heart compared with the parameters used in the LZVF1 model

FN model parameters	Atrium and sinoatrial region	AV band	Ventricle	LZVF1
a	0.13	0.13	0.13	0.13
b	0	0	0	0
c1	0.012	0.003	0.006	0.007
c2	0.5	0.5	0.5	0.5
d	1	1	1	1
e	0.00006	0.000012	0.0000095	0.000013
A	0.1	0.09	0.12	0.108
B	-0.053	-0.0585	-0.075	-0.07
k	1000	1000	1000	1000

Table 7.3: Initial conditions in the zebrafish heart model

Initial conditions	Atrium and sinoatrial region	AV band	Ventricle
$\mathrm{V_i}/mV$	-53	-58.5	-75
$\mathrm{V_e}/mV$	0	0	0
u	0	0	0

The finite element method was applied to solve this zebrafish heart model with COMSOL. A finer mesh (smaller mesh size) was applied to the AV band domains than the mesh in other heart domains due to its complex cellular structure (dense gap junction area) (Figure 7.6 (A)). The model fish body was meshed at a coarser level than the heart. The final mesh of the model included the fish body of 93851 tetrahedral elements and the heart of 167901 tetrahedral elements with 839,114 degrees of freedom. The average element size of meshes in the heart is 5.7 μm^3. A close-up view of the mesh refinement in the heart is shown in Figure 7.6 (B). It shows that there are very small gaps between two points/boundaries which result in smaller elements in these regions to capture this detail. These small gaps are because during the geometry development, the left half and right half of the model ventricle/atrium has been partitioned separately. At the edges where both half of the model ventricle/atrium meet, it shows these small gaps. The model is solved from $0\,ms$ to $500\,ms$ at the time step of $1\,ms$ to simulate one cardiac cycle. This took 3 hours to compute on a computer with an Intel Core i5-4590 CPU @3.3GHz and 16 GB of RAM.

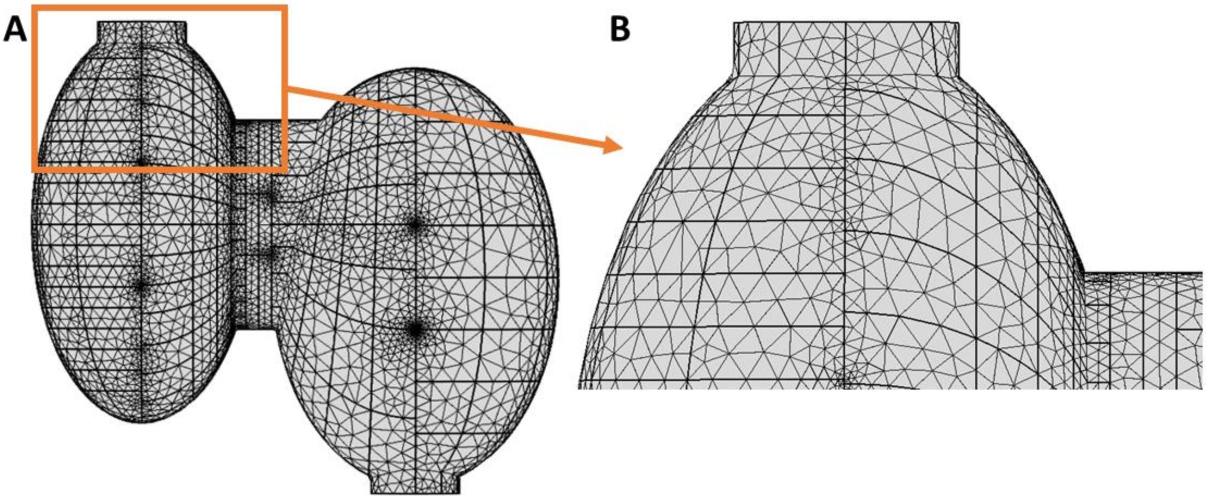

Figure 7.6: (A) Meshes of the model larval zebrafish heart; (B) close-up view of mesh elements in the model heart.

7.3 AP comparison

The model APs in different heart regions were compared with the recorded APs of a 48 hpf zebrafish in [56]. It has been found that in each region of the model heart, the AP characteristics such as the upstroke velocity varied if the APs were measured at different points. In Figure 7.7, the model APs measured at three different points in atrium, AV band and ventricle, were plotted. The locations of these measurement points are shown in Figure 7.7 (D) in the same colours as the line colours of the APs in Figure 7.7 (A), (B) and (C). The model APs measured in the atrium and ventricle replicate the recorded APs in terms of APD, APA and the upstroke velocity as shown in Figure 7.7 (A) and (C). For the AV band as shown in Figure 7.7 (D), the model AP measured near atrium has a much faster repolarisation which resembles the atrium AP and the model AP measured near the ventricle has a longer plateau phase which resembles the ventricle AP. It implies the APs at the transition area of two regions are determined by both regions. As the AV band is very small and contains fewer myocytes than the ventricle and atrium, the APs of the AV band were affected more by the atrium and ventricle rather than by the parameters used in the ionic current model (Table 7.2).

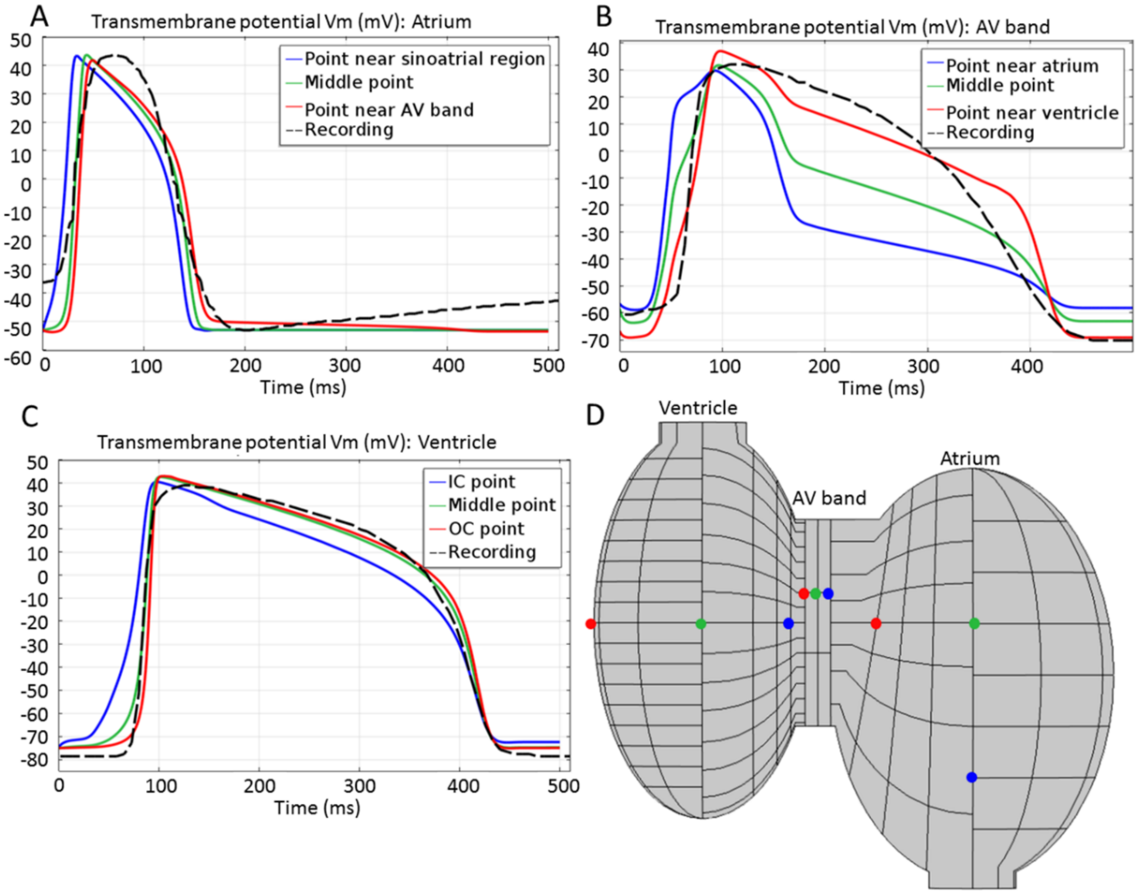

Figure 7.7: Model APs measured at the points shown in (D) in (A) atrium; (B) AV band and (C) ventricle. The lines of the model APs in (A), (B) and (C) are measured at the points that have the same colours. The recorded APs are from [56].

The average model AP characteristics measured at the atrium, the AV band and the ventricle were compared with the recorded values in Figure 7.8. Five random points in each region were chosen to calculate the average values. Noting that the 5 points did not include the points connecting two regions as their APs were affected by both regions. As shown in Figure 7.8 (A), the model AP amplitudes from the three regions are comparable to the recorded values with the differences less than 2 mV. The averaged model APDs in Figure 7.8 (B) replicated the recorded values with the differences of 17.34 ms in atrium, 24.7 ms in AV band and 5 ms in ventricle. The model maximum upstroke velocities (MUVs) of the five points in

Figure 7.8 (C) vary significantly in the ventricle and the atrium, however the final average model MUVs are comparable to the recorded values. The model MUV at the AV band is 3.46 V/s which is smaller than the recorded value (4.81 V/s). The MUP were also plotted on the whole surface of the heart as shown in Figure 7.9. It shows that MUVs are generally uniform except for the area near the sinoatrial region which were affected by the higher intracellular potential applied as stimulation. Similar to the MUV, the model maximum downstroke velocities of the five points varied significantly in the ventricle and atrium as shown in Figure 7.8 (D). However, the average model maximum downstroke velocities in all three regions are similar to the recorded values.

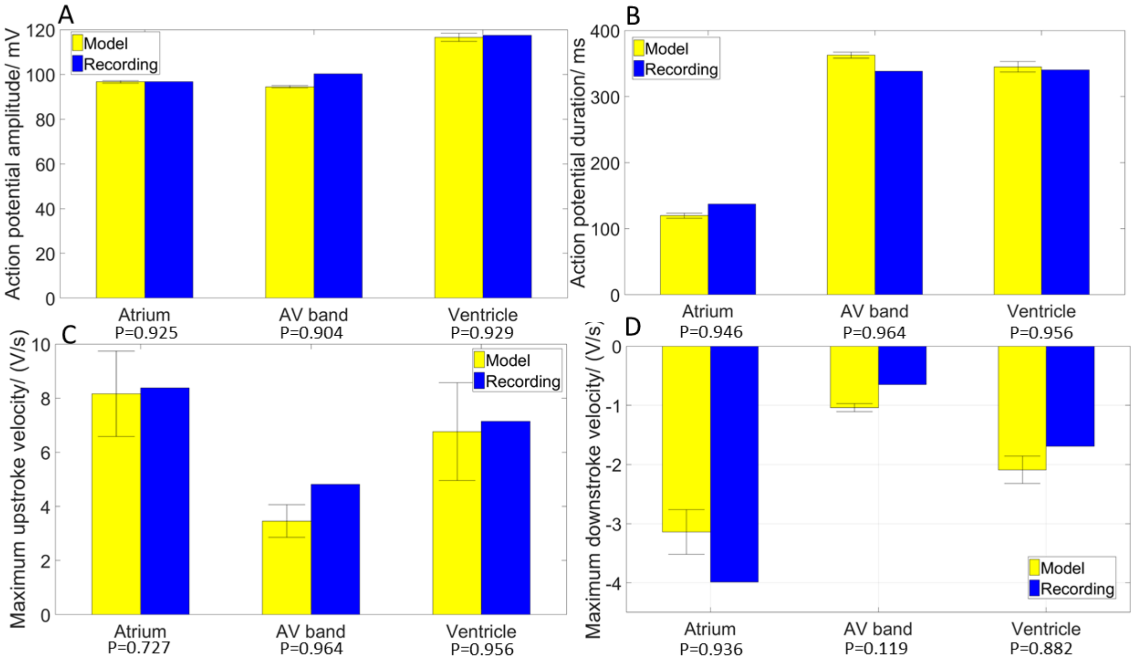

Figure 7.8: Average model AP characteristics comparing with the recorded AP characteristics including (A) action potential amplitude, (B) APD, (C) MUV and (D) maximum downstroke velocity. (n=5) student's t test: Error bars: s.e.m.

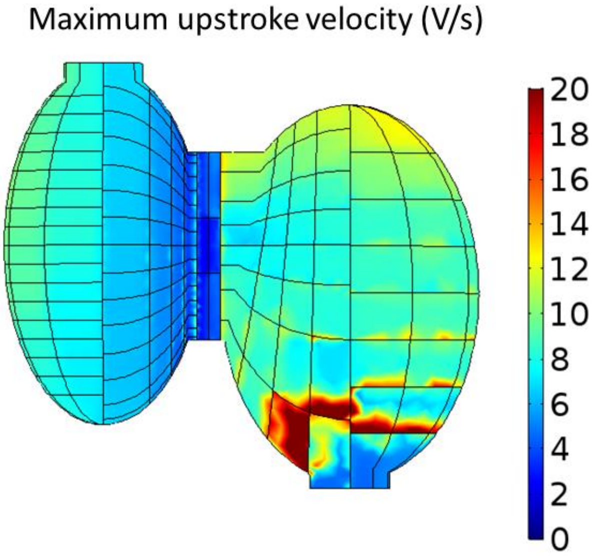

Figure 7.9: Maximum upstroke velocity of the 72 hpf zebrafish heart model

7.4 AP propagation

AP propagation in the model zebrafish heart starts at the sinoatrial region and then propagates to the atrium, the AV band and finally the ventricle. Figure 7.10 shows the transmembrane potential of the model heart at several time points for different stages in a complete cardiac cycle.

In order to trace the progress of activation through the heart at a time point in the cycle, an approximate centreline of the heart was defined by the boundaries on the surface of the heart as shown in blue in Figure 7.11 (B). At time $62\,ms$ as in Figure 7.10 (B), during the depolarisation of the heart, the transmembrane potential of this centreline was plotted against the distance along this line starting from the sinoatrial region in Figure 7.11 (A). The distances along the line of serval points on the boundaries marked in black are shown in Figure 7.11 (B). As shown in Figure 7.11, at the boundaries in the AV band and ventricle, steps can be observed which indicates the transmembrane potential differences between the neighbour myocytes as observed in the LZVF model in Chapter 5.

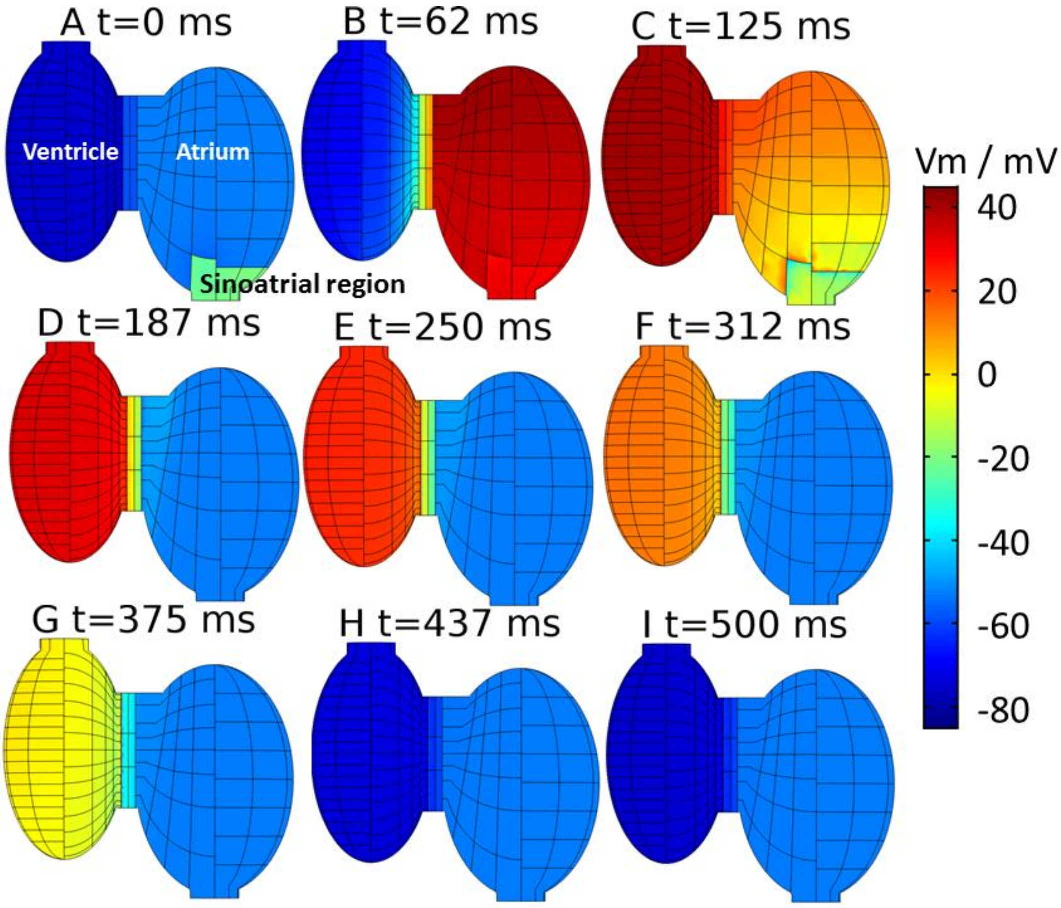

Figure 7.10: Temporal sequences of the transmembrane potential Vm at different stages. Time 0 ms: the start of atrial depolarisation. (A)activation started at sinoatrial region; (B) atrium depolarisation; (C) atrium repolarisation and ventricle depolarisation; (D) the end of atrium repolarisation and plateau stage of ventricle; (E)-(H) ventricle depolarisation.

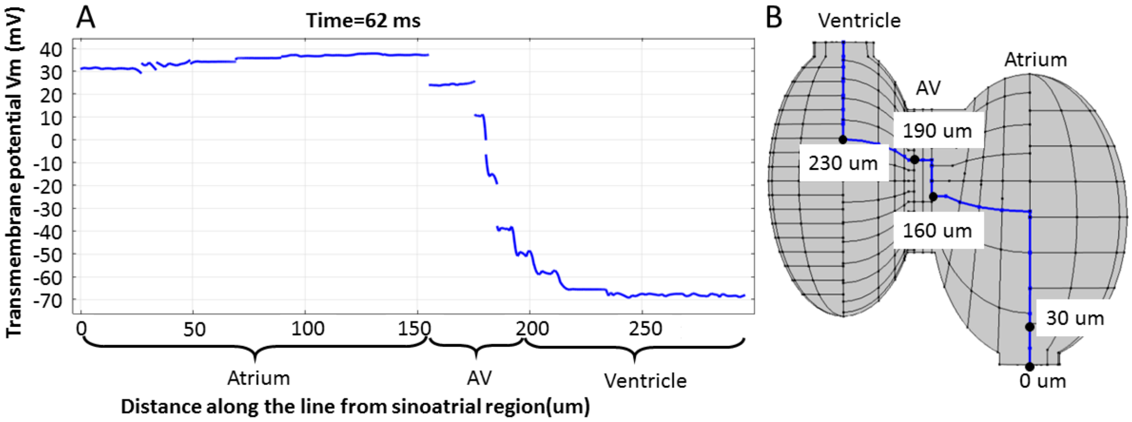

Figure 7.11: (A) Transmembrane potential Vm at time 62 ms during depolarisation vs the distance along the line starting from the sinoatrial region on heart surface as shown in blue in (B). (B) The approximate centreline on the heart with several points marked in black with distances.

The depolarisation of the model heart was then studied. As explained before, the gap junction resistivities of different heart regions were adjusted to match a published isochronal map of the activation times measured from a 72 hpf zebrafish heart [57]. The model activation time map is compared with the published map in Figure 7.12. Similar to the zebrafish models in the previous chapters, the activation time is defined as the time when the transmembrane potential reaches 0 mV during the rising phase of the AP. It may be observed that the entire myocyte area is not activated at the same time, particularly near the sinoatrial region. Therefore, the averaged activation time of the whole surface area of a myocyte was taken. The activation times of several myocytes were labelled in Figure 7.12 as an indication of the rate of progress of activation across the heart, in order to calculate the activation time delays in different heart regions later in Table 7.4.

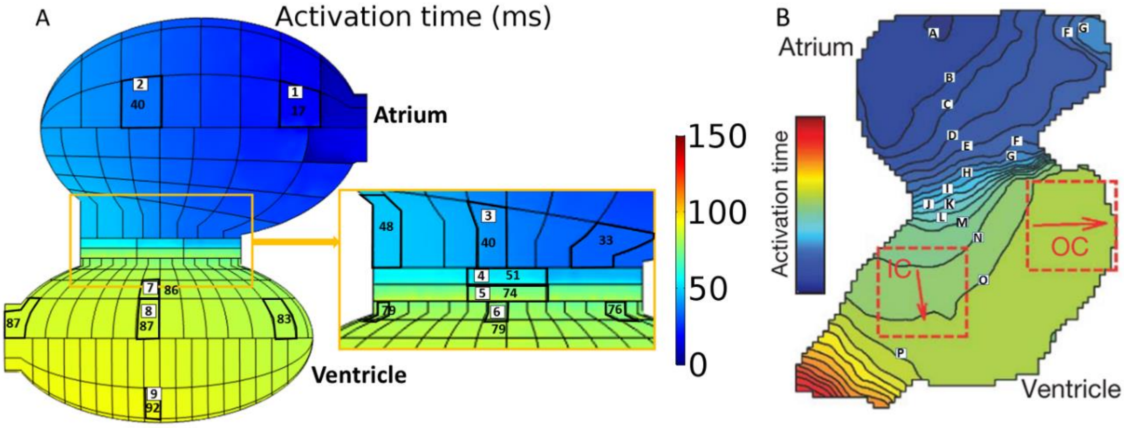

Figure 7.12: Activation time maps of the model heart (A) and the real heart [57] (B). In (A), the AV band (yellow box) is enlarged in the right. Several myocytes are labelled with their activation times. In (B), isochronal lines represent the activation times at 5 ms interval from [57]. These isochronal lines are labelled from “A” near the sinoatrial region where the activation starts to “P” at the end of ventricle where the latest activation happens.

As shown in Figure 7.12 (B), the isochronal lines are not uniform in each region. For example, in the atrium, the isochronal lines (activation time) in the area near the AV band (from F to H) are much denser than the isochronal lines in the chamber (From A to F), which implies a lower conduction velocity (CV) in the area near the AV band. Similar to the real heart, the model heart also shows a similar pattern of the activation times, for example there is an evident activation time delay between myocyte 3 and 4 in the transition area from the atrium to the AV band as 11 ms in Figure 7.12 (A) comparing with 10 ms from the isochronal line F to H in Figure 7.12 (B). The activation time delay in the model ventricle is 13 ms from myocyte 6 to 9 which is comparable to 10 ms in the reference map from the isochronal line M to P.

The activation time of the heart was plotted against the distance along the approximate centre line shown in Figure 7.11 (B), starting from the sinoatrial region in Figure 7.13. The activation time increases from the sinoatrial region to ventricle as indicated in the activation time maps in Figure 7.12. The activation time of each myocyte is not completely uniform but with small steps. These can be seen between 50 μm and 90 μm in atrium and between 190 μm and 230 μm in ventricle, which illustrate the activation time differences of neighbouring myocytes caused by the gap junctions. These steps can only be observed if the boundaries between the cells are perpendicular to the direction of the activation wave propagation. A large time delay of activation occurs between 170 μm to 190 μm which is in the AV band according to the Figure 7.11 (B). It agrees with the activation map in Figure 7.12 that the activation time delay in AV band is large.

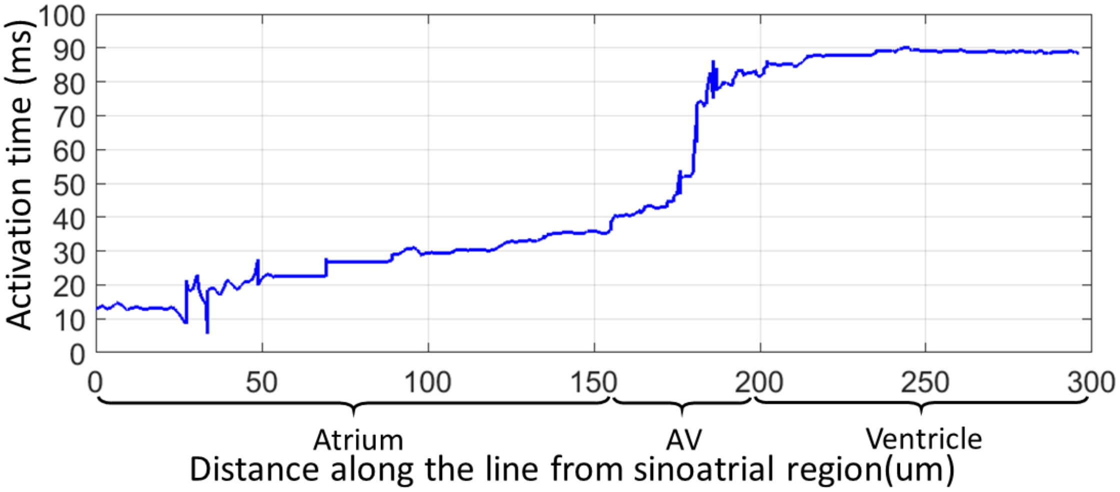

Figure 7.13: Activation time versus the distance along the line starting from the sinoatrial region on heart surface as shown in Figure 7.11 (B).

CVs in different heart regions produced by the model are compared with the reported CVs in [57] and CVs extracted from the measured activation time map as shown in Figure 7.12 (B). The heart was divided into four main regions (the sinoatrial region, the atrium, the AV band and the ventricle) and two transition areas (Atrium to AV band and AV band to ventricle). Then the activation time intervals in different regions were compared along with the CVs in Table 7.4. From Figure 7.12 (B), the CVs are estimated using the activation times of different regions and the spacing of the isochronal lines. In the model, based on the propagation wave direction, the myocytes labelled in Figure 7.12 (A) are used to derive the activation time intervals and CVs. The total model time interval from the atrium to the ventricle is $75\ ms$ (Myocyte 1 to 9) which is same to the measured values at $75\ ms$ (A to P). The other modelling results are also comparable to the values obtained from Figure 7.12 (B) as shown in Table 7.4.

Table 7.4: Comparison of activation time intervals and conduction velocities in different regions of heart between the model and values obtained from Figure 7.12 (B).

Regions	Model measurement	Model time interval (ms)	CV/ ($\mu m/ms$)	Real measurement from Figure 7.12 (B)	Real time interval (ms) from Figure 7.12 (B)	CV/ ($\mu m/ms$)
Atrium 1	Myocyte 1 to 2	23	3.46	B to E	15	0.6-6
Atrium 2	Myocyte 1 to 3	23	3.83	A to F	25	2-3.2
Transition from Atrium to AV band	Myocyte 3 to 4	11	1.69	F to H	10	0.5-1
AV band	Myocyte 4 to 5	23	0.22	H to L	25	0.2-0.4
Transition from AV band to ventricle	Myocyte 5 to 6	5	2.16	L to M	5	0.2-0.8
Ventricle	Myocyte 6 to 9	13	4.59	M to P	10	3.13-6.67
IC Ventricle	Myocyte 6 to 7	6	2.81	Reported data	N/A	4
OC ventricle	Myocyte 8 to 9	5	7.68	Reported data	N/A	12

7.5 ECG comparison

In Figure 7.14, the model ECGs were compared with the recorded ECGs from a 72 hpf zebrafish [36]. Like the human ECGs, the zebrafish ECGs show three main features: P wave, R wave and T wave (Figure 7.14). The P wave, R wave and T wave represent the atrial depolarisation, ventricular depolarisation and ventricular repolarisation respectively.

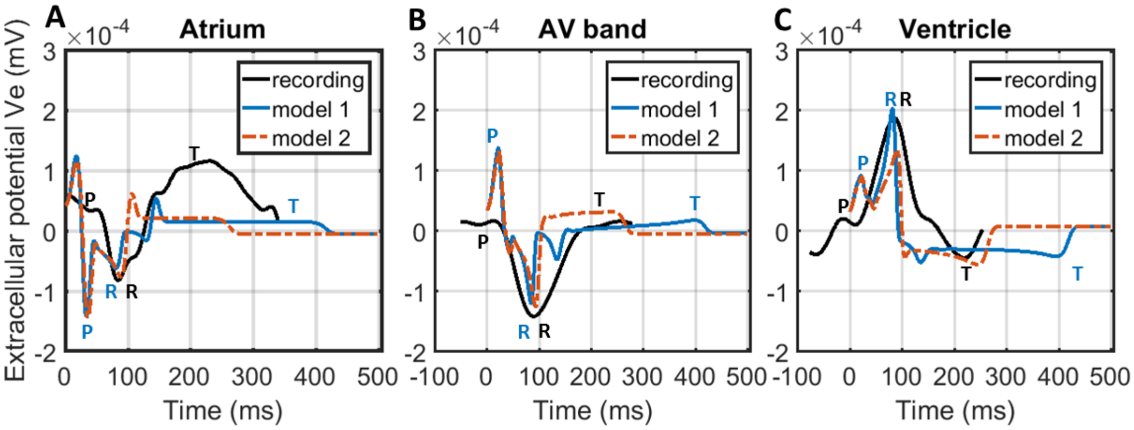

Figure 7.14: Model ECGs measured near (A) atrium, (B) AV band and (C) ventricle comparing with the recorded ECGs from [36]. Model 1 has an APD same to the reference [56] (Figure 7.8). Model 2 has a reduced APD (Figure 7.16) to fit with the QT length in the recorded ECGs.

The model ECGs are measured at three points on the surface of the fish body close to the three heart regions (atrium, AV band and ventricle), similar to the recoded ECGs. The positions of these points are chosen to be close to the electrodes' positions in the real recordings as shown in Figure 7.15 (D). The positions where the ECGs are recorded affect the morphology of the ECGs significantly in two aspects: the polarity and the magnitude of the peaks of the P, R, and T waves. The polarity of peaks of the P, R and T waves are determined by how the depolarisation wave or repolarisation wave propagates through the heart. In general, when the depolarisation wave propagates towards the recording point, it produces an upward peak in the ECG, while when it propagates away from the point, it produces a downward peak. On the contrary, a repolarisation wave propagating towards the recording point produces a downward peak in the ECG, whilst if it propagates away from the point, it produces an upward peak. The model ECGs measured near the atrium, the AV band and the ventricle were analysed using this rule to determine the location of the P wave, the R wave, and the T wave as shown in Figure 7.15. Taking the atrial ECG as an example as shown in Figure 7.15 (A), the ECG is measured at point “a” shown in Figure 7.15 (D) near the zebrafish atrium. The depolarisation wave starts at the sinoatrial region and travels towards the point “a” before about $30\ ms$ as the atrial AP1 (Blue) is in upstroke period, while the atrial AP2 has not started to upstroke. Therefore an upward peak is observed. From about $30\ ms$ to $50\ ms$, the atrial depolarisation wave gradually moves from the point “a” which gives a downward peak in the ECG known as the P wave. Similarly, the ventricular depolarisation starts at about $50\ ms$ and ends at about $100\ ms$ which is observed as a downward peak in the ECG known as the R wave. The atrial repolarisation wave first propagates to the recording point “a” then propagates away which is shown in the atrial ECG as firstly a downward peak and then an upward peak during $100\ ms$ to $170\ ms$. After a plateau phase of the ventricular AP, the rapid repolarisation wave in the ventricle propagates away from the point “a” starting at about $300\ ms$ and stops at about $450\ ms$ which is shown in the ECG as an upward peak known as the T wave. The ECGs of the other two regions were analysed using the same method and the results were marked in Figure 7.15 (B) and (C). Note that the locations of the peaks in the ECGs situated above or below zero volts are not of interest, as explained in [36].

In summary, the model atrial ECG has downward P and R waves and an upward T wave. The model AV band’s ECG has an upward P wave, a downward R wave and an upward T wave. The model ventricular ECG has upward P and R waves, and a downward T wave. These ECG characteristics agree with the recorded ECGs as shown in Figure 7.14.

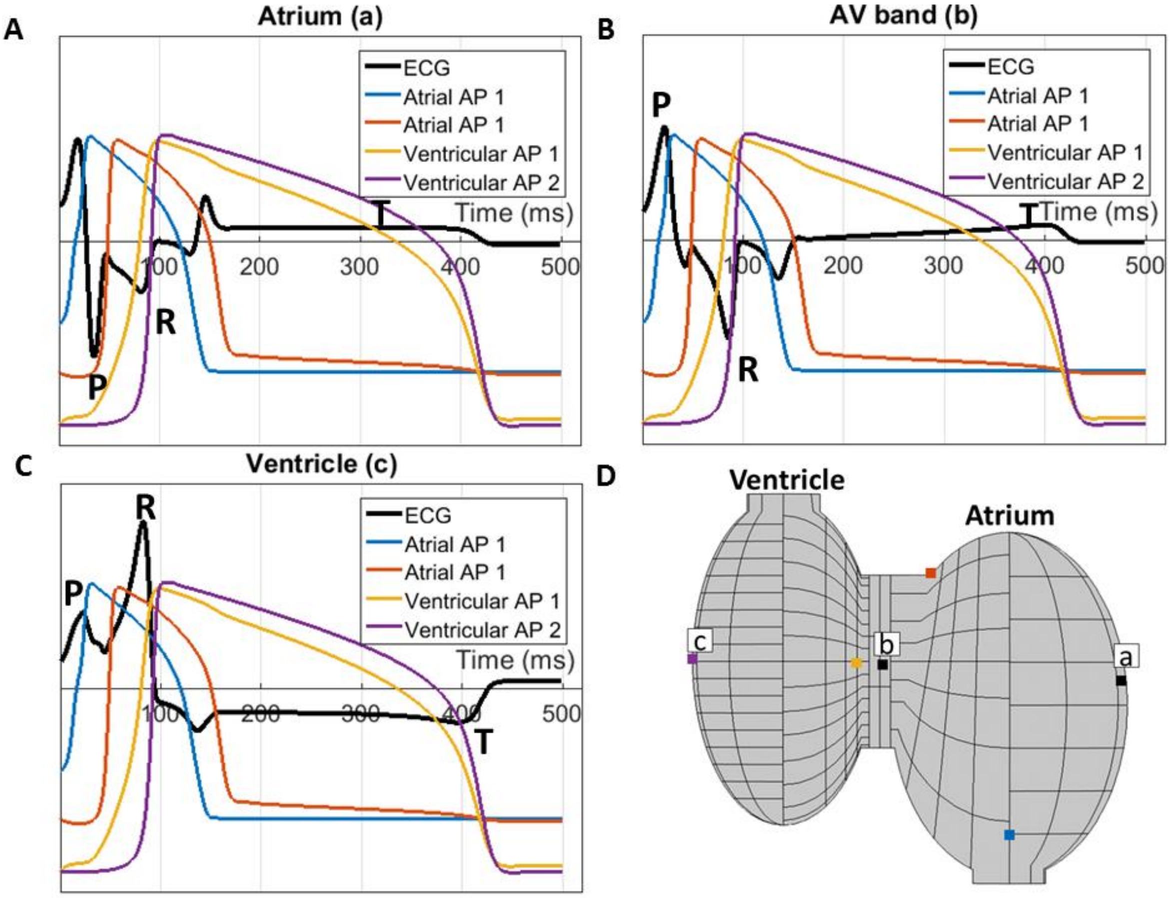

Figure 7.15: ECGs produced by the model 1 measured on the surface of the fish body near: (A) the atrium at point “a”, (B) the AV band at point “b” and (C) the ventricle at point “c” along with the APs measured from the points at the start and end of atrial and ventricular activations shown in (D). The lines of the model APs in (A), (B) and (C) are measured at the points that have the same colours.

To quantitatively compare the model ECGs with the recorded ECGs in [36], several characteristics commonly used in the assessment of the ECGs are measured as shown in Table 7.5. The P, R and T widths are the times from the start of P wave, R wave and T wave to their ends. PR interval is the time from the start of P wave to the start of the R wave which reflects the activation time in AV band. QT interval is the time from the start of the R wave to the end of the T wave which reflects the ventricular depolarisation and repolarisation. Based on the activation times of each region, three time points on the ECGs were selected for each waves as the start time, the peak time and the stop time. Note that in human ECGs, the PR interval is measured from the time of the start of the P wave to the time of the start of the Q wave and the

QT interval is measured from the time of the start of Q wave to the time of the end of the T wave. The Q wave in human ECGs is caused by the depolarisation and repolarisation of the septum. However, the larval zebrafish heart does not have septum, so there is no Q wave in zebrafish ECGs. Therefore the measurement of PR intervals and QT intervals in the model ECGs used the start time of the R wave.

As the absolute magnitude of the voltage in the recorded ECGs is unknown due to the amplification used in the measurements, the recorded ECGs were scaled in Figure 7.14 to be in the similar scale as the model ECGs in the range of $1 \times 10^{-4}\ mV$.

As shown in Figure 7.14 the ECGs produced by model 1 has a longer QT interval than the recorded ECGs. Model 1 is based on the AP measurement in [56] which was conducted on a 48 hpf zebrafish at room temperature (around $28℃$) while the ECGs reported in [36] was recorded at a higher temperature of $28℃$. It has been found that higher temperature reduces the APD in zebrafish without changing the shape of the APs [158]. Therefore, model 2 was developed by changing the parameters of the ionic current model (Table 7.2) to simulate the APs with a shorter APD. The APs produced by the model 2 were compared to the model 1 as shown in Figure 7.16. Both model ECG parameters were compared with the recorded ECGs in Table 7.5.

The two model ECGs resemble the recorded ECG to different extents. The P width measured at the ventricle produced by model 2 ($36\ ms$) replicates the recorded ECGs ($40\ ms$) the best while the second-best P width is measured at ventricle produced by the model 1 ($32\ ms$). For the R width, the best model ECG measured near the atrium by the model 2 ($50\ ms$) comparing with the recorded ECGs ($91\ ms$) while the second-best R width is also measured near the atrium by the model 1 ($49\ ms$). Similarly with the R width, the best model T width is also measured near the atrium by the model 1 ($151\ ms$) comparing with the recorded ECGs

($147\ ms$) while the second-best T width is measured near atrium by the model 2 ($153\ ms$). The model PR interval best replicates the recorded results (55 ms) measured near the ventricle by the model 2 at 46 ms while the second-best model PR interval is 43 ms measured near the ventricle by the model 1. The best and second-best model QT intervals resembling the recorded results are both produced by the model 2 measured near AV band (241 ms) and the ventricle (243 ms) comparing with the recorded results as 244 ms and 232 ms.

Table 7.5: Comparison of the ECG characteristics between the model and recorded results.

Region	Source	P width (ms)	R width (ms)	T width (ms)	PR (ms)	QT (ms)
Atrium	Recording	27	91	147	27	250
	Model 1	21	49	151	21	402
	Model 2	22	50	153	22	240
AV band	Recording	25	157	34	69	244
	Model 1	41	51	164	49	404
	Model 2	44	57	147	53	241
Ventricle	Recording	40	117	76	55	232
	Model 1	32	57	151	43	408
	Model 2	36	30	100	46	243

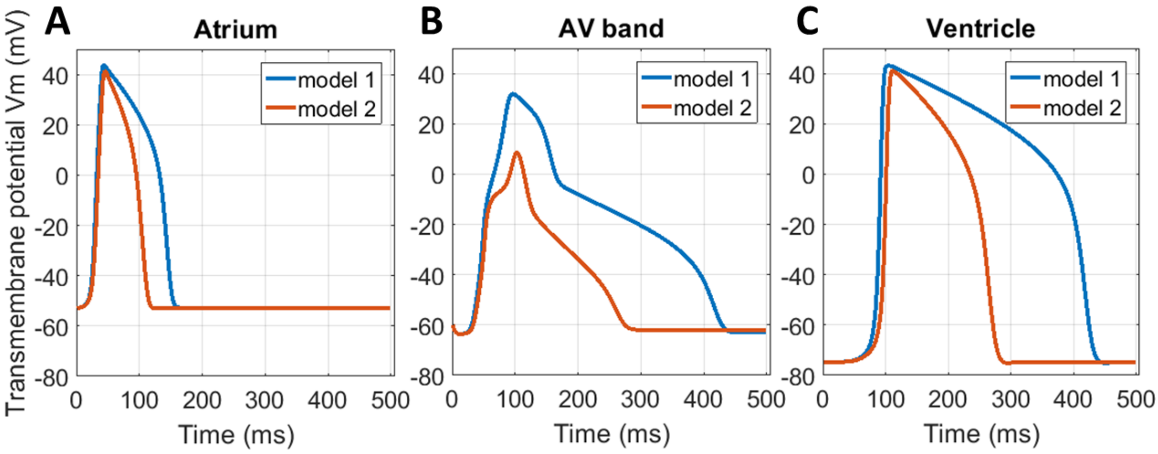

Figure 7.16: APs comparison between the model 1 and the model 2 in (A) atrium, (B) AV band and (C) ventricle. The measured points of the APs are the middle points (green) in the regions in Figure 7.7 (D).

7.5.1 Filtered ECGs

In the ECG recording procedures, the raw ECG signals go through a band pass filter to remove artefacts such as noises with frequency higher than 10 Hz and baseline wander (<0.1

Hz) [36]. However as can be seen in the model ECGs in Figure 7.14, there are higher frequency oscillations whose frequencies may be larger than the cut off frequency (10 Hz) of the filter used in the recording. Therefore in order to compare the model ECGs with the recorded ECGs more efficiently, the model ECGs are filtered by the same band pass filter used in the recordings using a MATLAB script.

The band pass filter is a 3rd order Butterworth filter and its magnitude and phase responses were plotted in Figure 7.17 (A). This filter will introduce a phase lag that is proportional to the frequency of the input ECGs. Thus the group delay of the filter, which is the time delay between the filtered and input signals, is plotted against time in Figure 7.17 (B). This is determined by the sampling rate of the filter which is 1000 Hz. The group delay for signals between 0.1 Hz and 10 Hz is about 1-2 samples which leads to $1 - 2\ ms$ time delay between the input ECGs and the filtered ECGs.

The model 2 ECGs were chosen to filter because they resemble the recorded ECGs better than the model 1 ECGs. In Figure 7.18 the original model ECGs, filtered model ECGs and recorded ECGs were plotted against time for the atrium, AV band and ventricle. It is shown that some details of the original model ECGs have been removed by the filtering process. For example the downward P peak is missing in the filtered atrial ECG. The downward peaks which occurred between the P and R waves in the AV band and ventricular ECGs were also filtered out. However, these filtered ECGs resemble the recorded ECGs better than the originals in terms of the overall trends. The same ECG characteristics shown in Table 7.5 were measured for filtered ECGs and compared with the original model ECGs and the recorded ECGs in Table 7.6. Unlike the method used in the original model ECGs, the time points of the P, R and T waves were selected based only on the visible peaks in the ECGs. Note the downward P wave in the filtered atrial ECG is missing, so the P wave is selected as the first upward peak.

The most outstanding difference between the filtered and the original model ECGs is the R width. All three filtered ECGs have a larger R width than the original ECGs for example at the atrium ($90\,ms$ versus $50\,ms$), at the AV band ($113\,ms$ versus $57\,ms$) and at the ventricle ($100\,ms$ versus $30\,ms$) which are more comparable to the recorded values of $91\,ms$ at the atrium, $157\,ms$ at the AV band and $117\,ms$ at the ventricle. The T widths measured in the filtered ECGs at the AV band ($67\,ms$) and the ventricle ($84\,ms$) resemble the recorded ECGs ($34\,ms$ and $76\,ms$) better than the original ECGs of $147\,ms$ at the AV band and $100\,ms$ at the ventricle. For the P width, PR width and QT interval, the filtered and the original ECGs do not show a large difference and they resemble the recorded ECGs to different extents.

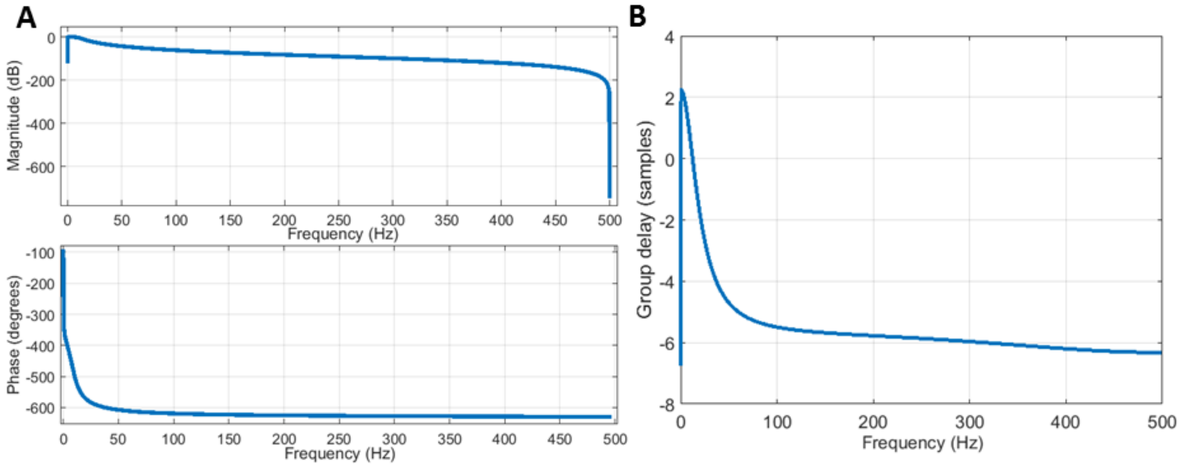

Figure 7.17: (A) Magnitude and phase responses and (B) of the band pass filter used in recording procedure and in the model.

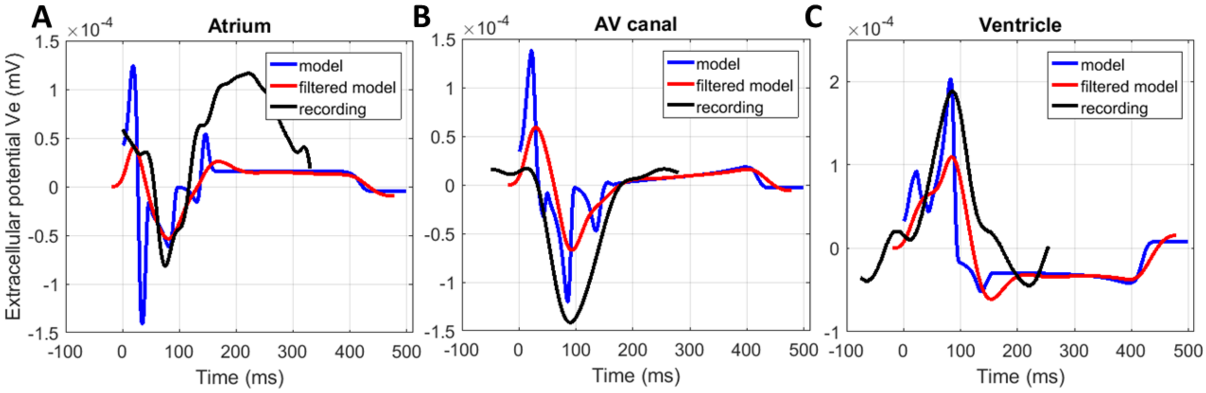

Figure 7.18: Filtered Model 2 ECGs measured near (A) atrium, (B) AV band and (C) ventricle comparing with the original model ECGs and recorded ECGs from [36].

Table 7.6: Comparison of the ECG characteristics between the original model 2, the filtered model 2 and the recorded results.

Region	Source	P width (ms)	R width (ms)	T width (ms)	PR (ms)	QT (ms)
Atrium	Recording	27	91	147	27	250
	Model 2	22	50	153	22	240
	Filtered Model 2	28	90	161	28	251
AV band	Recording	25	157	34	69	244
	Model 2	44	57	147	53	241
	Filtered Model 2	36	113	67	36	240
Ventricle	Recording	40	117	76	55	232
	Model 2	36	30	100	46	243
	Filtered Model 2	40	100	84	40	226

7.6 Gap junction resistivity

The fitted gap junction resistivities used in different heart regions in the model were investigated in this section using the similar method as used in Chapter 5 and 6. As is introduced in Chapter 2, it has been reported that Connexin 43 was observed in larval zebrafish heart at 48 hpf and also in 100 hpf while Connexin 40 was detected weakly in 48 hpf zebrafish and strongly in 100 hpf [56]. Because measured individual gap junction channel resistances for the zebrafish heart has not been found in the literature, the measured gap junction channel resistance based on humans consisting of the same connexins is assumed to be the gap junction channel resistance of the zebrafish as shown in Table 7.7.

The average gap junction resistance per myocyte in different regions of heart can be derived from the gap junction resistivity, the total gap junction area and the total number of myocytes. The total gap junction areas of each region were measured as shown in Table 7.7. For simplicity, the gap junction area connected two regions was included in the region which is near to the sinoatrial region, for example the gap junction area of the atrium and sinoatrial region includes the transition gap junction area connected the atrium and the AV band. Then this average gap junction resistance per myocyte in different heart regions and the individual gap junction channel conductance was used to derive the average number of gap junction channels per myocyte. The estimated average numbers of gap junction channels per myocyte in all heart regions are shown in Table 7.7. It is shown that there are more gap junction channels per myocyte in the model ventricle than in the model atrium or the model AV band. The estimated gap junction channel number per myocyte in AV band is the smallest which ranges from 11 to 89.

Table 7.7: Gap junction resistance investigation in 72 hpf zebrafish heart model

	Atrium and sinoatrial region	AV band	IC Ventricle	OC Ventricle	Reference
Types of connexins	Cx40, Cx43	Cx40, Cx43	Cx40, Cx43	Cx40, Cx43	
A range of individual gap junction channel conductance/pS	20-160	20-160	20-160	20-160	Cx40: 30,80,120[138], 150-160 [139]; ; Cx43: 20,40,70 30,60,90 110 [141, 159]
Gap junction resistivity / $\Omega \cdot m^2$	0.35	0.23	0.13	0.2	
Gap junction area/μm^2	64800	4920	30900	53800	
Average number of gap junction channels per myocyte	11-89	11-89	15-124	14-110	

7.7 Mesh convergence analysis

A mesh convergence analysis is conducted to validate the reliability of the modelling results of this zebrafish heart model using the method as in Chapter 5 and 6. A series of mesh levels are applied to the zebrafish heart models to see the variations of the modelling results. A finer mesh means that the geometry has been divided into more elements which increase the accuracy of the results. The final mesh level used in this model is the finer level.

The activation times of each region in the zebrafish heart is an important parameter coordinating the shapes of the ECGs. Therefore, several simulations were conducted by only varying the levels of meshes. In each model, four activation time intervals were measured including the activation time intervals from atrium to ventricle, within ventricle, within AV band and within atrium. In Figure 7.19 (A), these four activation time intervals were plotted against different mesh levels. Then the proportional differences between each result with the result produced by the model with the finest mesh level were plotted against the mesh levels in Figure 7.19 (B). It can be found that the proportional differences of all activation time intervals are decreasing with the increase of the mesh levels. From mesh level at normal to finer, all proportional differences are less than 6%. It can be concluded that this finer mesh level used in the zebrafish heart model is sufficient and the modelling results produced by this model are reliable.

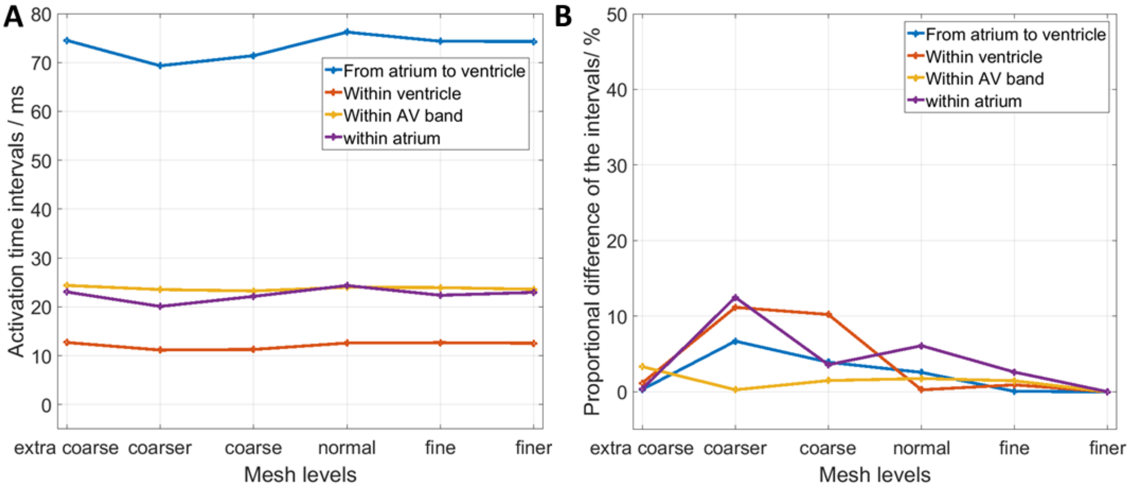

Figure 7.19: Mesh convergence analysis of the zebrafish heart model: (A) Four activation time intervals vs the mesh levels of the models. (B) The proportional difference of the same four activation time intervals between each result with the result produced by the model with the finer mesh level vs the mesh levels of the models.

7.8 Bulbus arteriosus

Bulbus arteriosus is the outflow tract which is extended from the ventricle as described in Chapter 2. In the larval zebrafish stage before 4 weeks post-fertilization, the bulbus arteriosus has the same characteristics as the myocardium and then it gradually transformed to smooth muscle [52]. As shown in Figure 7.12 (B) from the paper [57], the measured activation map has a region activated later than the ventricle which is probably the bulbus arteriosus. Therefore the heart model was amended in this section to include the bulbus arteriosus in 72 hpf zebrafish heart. An extra cylinder tube of length $34\ \mu m$ was added at the previous outflow tract which is in the similar length as shown in the paper [57]. Then it was partitioned into 18 myocytes with the cellular surface area at about $200\ \mu m^{2}$. The gap junction resistivity of this new region was set to $1.5\ \Omega \cdot m^{2}$ to achieve the measured activation times as shown in Figure 7.12 (B). The resulting activation time map was plotted in Figure 7.20. The total activation time delay produeced by this model, from the atrium to the bulbus arteriosus, is $123\ ms$ which is similar to $125\ ms$ in the measured activation time map. Based on the same method as in section 7.6, the average number of gap junction channels per myocyte in the model bulbus arteriosus is 1-9 which can be derived from its gap junction resistivity and gap junction area.

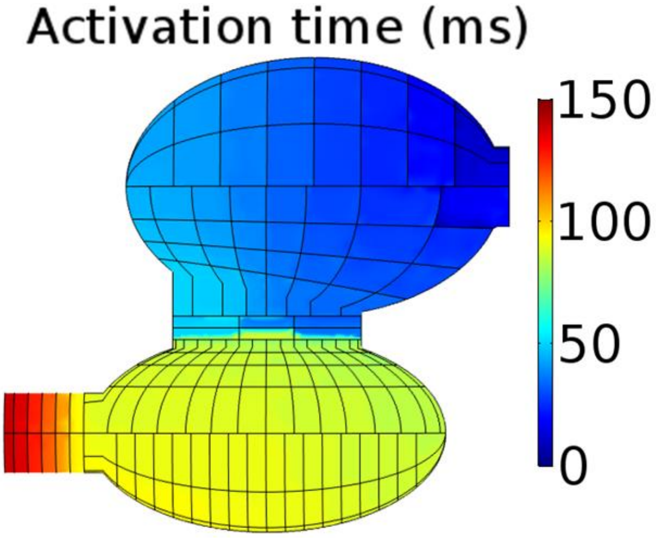

Figure 7.20: Activation time map of zebrafish heart model with bulbus arteriosus.

7.9 Summary

This chapter described a 72 hpf zebrafish heart model which resembles the electrical cardiac activities in a real 72 hpf zebrafish heart. Using the adjusted gap junction resisitivities of different heart regions, the 72 hpf zebrafish heart model reproduces many key features of cardiac propagation such as the activation times and the CVs which are comparable to measured results found in the literature. In addition, the ECGs were simulated and compared with the recorded ECGs. It has been found that the model ECGs based on the measured APs of a 48 hpf zebrafish resemble the general outlines of the recorded ECGs however the model QT intervals are much longer than the recorded ECGs. This finding is similar to the previous published larval zebrafish heart model based on the bidomain model [36]. It was explained in the previous model that the longer QT intervals are because of the different temperatures applied to the AP measurements and the ECG measurements. Therefore the APs in the heart model were adjusted similarly as the previous heart model and the resultant ECGs (Model 2) have shorter QT intervals as shown in Table 7.5 which are more comparable to the recorded ECGs. As shown in Figure 7.14, compared with the recorded ECGs, there are more peaks shown in the model ECGs such as the peak after the R peak which represents the atrial repolarisation. These peaks are high frequency signals. As the recorded ECGs were filtered by a low pass filter in order to remove noise [36], similar high frequency signals as the model ECGs could be removed as well. Therefore, same low pass filter used in the recorded ECGs were applied to filter the model ECGs. It was found that the filtered model ECGs do not have the peaks with high frequency such as the peak representing the atrial repolarisation (Figure 7.18) which resembles the recorded ECGs better than the unfiltered ones. In general, the average numbers of gap junction channels per myocyte in different heart regions derived from the adjusted gap junction resisitivities and gap junction area range from 10s to 100s which are a little smaller than the larval zebrafish ventricular fibre (LZVF) model in Chapter 5 and the cell array model in Chapter 6. It suggests that a lower density of gap junctions between cells in the heart model than in the LZVF model as the gap junctions are distributed in a larger area in the heart model, for example, the average gap junction area per myocyte in ventricle in the heart model is $389\ \mu m^2$ compared with $100\ \mu m^2$ in the LZVF model.

8. APPLICATION AND EXTENSION OF THE HEART MODEL

The larval zebrafish heart model described in the previous chapter simulated action potential (AP) propagation and electrocardiogram (ECG) in a 72 hpf zebrafish heart in a normal, healthy state. The ultimate goal of modelling the larval zebrafish heart is to provide a platform to study cardiac electrophysiology which would then potentially benefit the diagnosis and treatment of cardiovascular diseases. Therefore in the first section of this chapter, a modification of this larval zebrafish heart model, is described which simulates a common cardiac disorder: gap junction remodelling. It has been found that gap junction remodelling plays a role in cardiac conditions such as cardiac ischaemia [44] and congestive heart failure [45]. In the second section of this chapter, a 52 hpf zebrafish heart model is discussed, developed from the 72 hpf zebrafish heart model. It allows to further validate the heart model by reproducing the measured results including the activation time and CVs reported in [46].

8.1 Gap junction remodelling

Gap junction remodelling could be structural remodelling such as disturbances in the distribution of gap junctions or alterations in the number or the type of connexin(s) expressed [160]. These alternations of gap junctions in the heart result in abnormal electrical couplings between cardiomyocytes, potentially leading to pathophysiologic conductions and to many forms of heart diseases. In recent years, the role of gap junction remodelling in cardiac diseases has been studied experimentally. With the development of transgenic animals, the expression of specific types of connexins can be modified in order to generate animal models with specific connexins knocked out. Recently, a large number of these animal models have been developed which exhibited various electrophysiological abnormalities that can be revealed in their recorded ECGs. By comparing these ECGs with the control group, abnormal P, QRS and T waves can be identified which illustrate the abnormal conductions in different regions in the heart.

Many physiological studies of connexin knockout in animal models have been conducted and show that the loss of connexins in the heart has a significant effect on cardiac conduction and then potentially contributes to cardiac diseases as described in Chapter 2. For example, knockout of connexin43 (Cx43) in mouse hearts resulted in the reduction of ventricular CV up to about 50% and dramatically increased susceptibility to inducible ventricular arrhythmias and even sudden arrhythmic death [68-70]. Connexin40 (Cx40) knock-out mice exhibited slow atrial and ventricular conduction and the atrium-derived abnormalities in cardiac rhythm which implies the possibilities of causing cardiac arrhythmogenesis [71].

An issue with the knock-out studies is that a specific type of connexin is totally or partially removed regardless of the region of the heart. For example, Cx40 and Cx43 have been found expressed in both atrium and ventricle in the human and mouse hearts [161]. Knocking out either of them affects the cardiac conduction in both atrium and ventricle. Therefore the effect of losing connexins in a specific region such as the atrium cannot be studied. This knock-out strategy is also not applicable to some disease conditions where connexins in a specific region are lost. For example a reduction of Cx43 has been found in the left ventricles of transplant patients with end-stage congestive heart failure [162].

In order to investigate the effect of gap junction remodelling on different regions in the heart, the gap junction resistivities in the atrium, atrioventricular (AV) band and ventricle in the larval zebrafish heart model were varied separately. Several simulations for different gap junction resistivities were conducted and for each case, two typical modelling results were shown in the following sections.

8.1.1 Varying atrial gap junction resistivities

In this section, the atrial gap junction resistivity, Ra, in the model was doubled to $0.7\ \Omega \cdot m^2$ from the original $0.35\ \Omega \cdot m^2$and then tripled to $1.05\ \Omega \cdot m^2$ with all the other settings unchanged. The resulting activation maps and ECGs are compared with the original model result (model 1) in Figure 8.1 and the main ECG characteristics of them are compared in Table 8.1. The resulting average number of gap junction channels per myocyte are calculated using the modified atrial gap junction resistivities shown in Table 8.2. The increase of the atrial gap junction resistivity results in the reduction of gap junction channels in the atrium which resembles the partial loss of connexins.

As shown in Figure 8.1 (A), (B) and (C), in all three models, the atrial area near the sinoatrial region activated at a similar time, however the area near AV band activated at different times. The activation time of the myocytes at the AV band connected to the atrium in the model 1 is about $50\ ms$ comparing with about $75\ ms$ in the $Ra = 0.7$ model and about $100\ ms$ in the $Ra = 1.05$ model. Because the geometries of all three models are same which means the distances of activation waves travelled are same as well, the doubled and tripled atrial gap junction resistivities resulted in about 50% and 100% reduction of the CVs in the atrium when compared with the model 1. As described in Chapter 2, the PR interval represents the time from the start of atrial depolarisation to the start of ventricular depolarisation including the AV band depolarisation time. As shown in Table 8.1, the PR intervals measured near atrium are 35% longer in the $Ra = 0.7$ model and 110% in the $Ra = 1.05$ model than in the model 1 which were similar to the increasing rates of the activation time intervals from the atrium to the ventricle. The P widths representing the atrial depolarisation measured near atrium are 29%

longer in the $Ra = 0.7$ model and 52% longer in the $Ra = 1.05$ model than in the model 1. As shown in Figure 8.1 (D), (E) and (F), the PR intervals and the P widths of the ECGs measured near the atrium showed the most significant increase with the increase of atrial gap junction resistivities comparing with the other ECGs. This is reasonable as the atrial ECGs were measured at the nearest point to atrium which captured the variation of atrial cardiac propagation most clearly.

As shown in Figure 8.1 (E) and (F), compared with the model 1, prolonged R widths are observed in both large Ra models from the ECGs measured near AV band and ventricle. The R widths of the AV band ECGs are about 8% longer in the $Ra = 0.7$ model and 20% in the $Ra = 1.05$ model than in the model 1 while the R widths of ventricular ECG are 5% longer in the $Ra = 0.7$ model and 25% in the $Ra = 1.05$ model than in the model 1. Although the R wave indicates the ventricular depolarisation, this prolongation of the R width cannot be explained by the prolongation of activation time delay in ventricle. As is shown in Figure 8.1 (E) and (F), downward peaks are shown in the model 1 ECGs at about time $150\ ms$ which indicates the atrial repolarisation that was explained in the previous chapter. These prolonged R waves last until about $150\ ms$ and as the R wave is also a downward peak, it is very likely being added with this downward peak representing the atrial repolarisation. Therefore, longer R widths were observed. This can also be verified by the activation maps where the activation time intervals within ventricle are the same in all three models at about $10\ ms$.

The QT intervals measured in the ventricle are 1% longer in the $Ra = 0.7$ model and 5% longer in $Ra = 1.05$ model than in the model 1 while the other QT intervals measured near atrium and AV band are very similar. The small increase of the QT interval is only observed in the ventricular ECG because the ECG measured near the ventricle deflects the cardiac propagation of ventricle mostly than the ECGs measured elsewhere. These prolonged QT intervals are due to the prolonged T widths as shown in Table 8.1. According to the activation time maps in Figure 8.1 (A), (B) and (C), the last activation times of ventricle are about $120\ ms$ in the $Ra = 0.7$ model and about $140\ ms$ in the $Ra = 1.05$ model comparing with $72\ ms$ in the model 1. Therefore, the T waves produced by the larger Ra models finished later which resulted in longer T widths and QT intervals.

In all ECGs, the magnitude of the P peaks and R peaks in both larger Ra models are smaller than in the model 1 while the magnitude of the T peaks are about the same in all models.

In summary, the increase of atrial gap junction resistivity in the larval zebrafish heart model simulated the partial loss of connexins in the atrium. This results in a significant increase of the P width and the PR interval and a small increase of the R width, the T width and the QT interval in the ECGs.

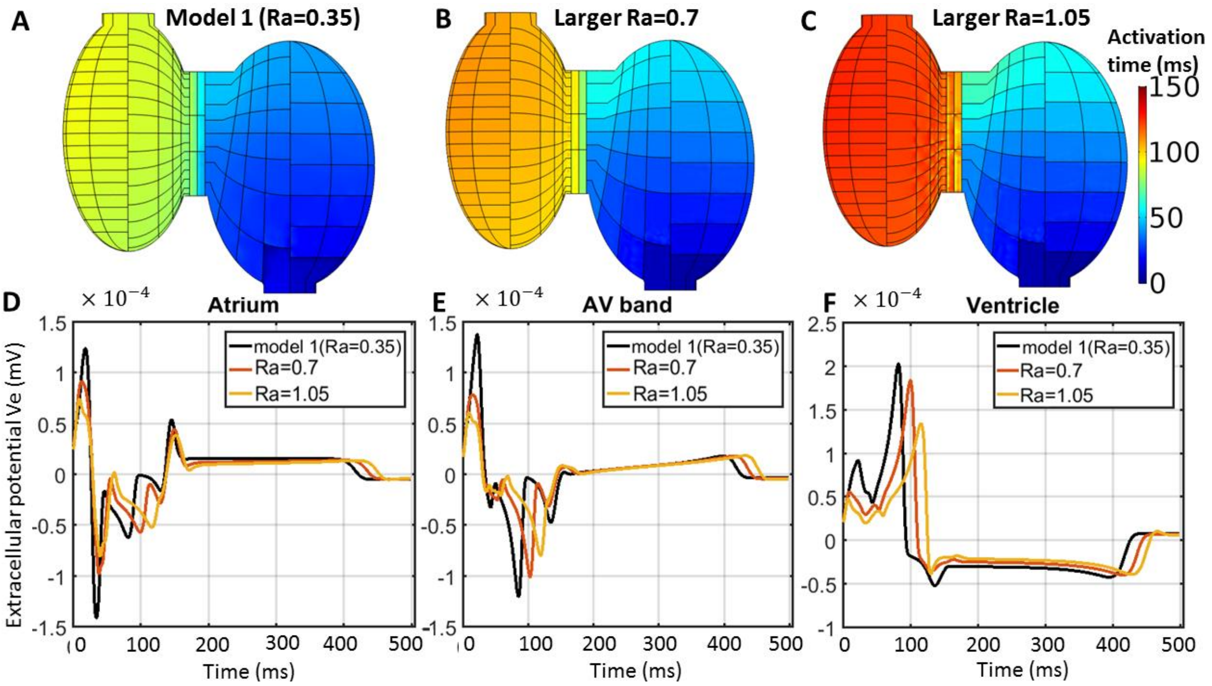

Figure 8.1: Activation time maps of models with the atrial gap junction resistivities at (A) $0.35\ \Omega \cdot m^2$, (B) $0.7\ \Omega \cdot m^2$and (C) $1.05\ \Omega \cdot m^2$. The ECGs for these three models measured at (D) atrium, (E) AV band and (F) ventricle were plotted.

Table 8.1: ECG characteristics comparison between the model 1 and two models using larger atrial gap junction resistivities Ra as shown in Figure 8.1(D-F).

Region	Source	P width (ms)	R width (ms)	T width (ms)	PR (ms)	QT (ms)
Atrium	Model 1	21	49	151	21	402
	$Ra = 0.7$	27	49	164	36	400
	$Ra = 1.05$	32	55	177	44	404
AV band	Model 1	41	51	164	49	404
	$Ra = 0.7$	34	55	164	59	404
	$Ra = 1.05$	35	61	171	68	405
Ventricle	Model 1	32	57	151	43	408
	$Ra = 0.7$	32	60	165	53	411
	$Ra = 1.05$	31	71	185	59	427

Table 8.2: Gap junction information of the larger Ra models comparing with the model

Atrium	Model 1	$Ra = 0.7$	$Ra = 1.05$
Gap junction resistivity / $\Omega \cdot m^2$	0.35	0.7	1.05
Gap junction area/μm^2	64800	64800	64800
Average number of gap junction channels per myocyte	15-89	6-45	4-30

8.1.2 Varying AV band gap junction resistivities

In this section, the gap junction resistivities in the AV band, Rav, in the larval zebrafish heart model were increased to 0.46 $\Omega \cdot m^2$ and 0.8 $\Omega \cdot m^2$ from 0.23 $\Omega \cdot m^2$ in the model 1. The resulting activation time maps and ECGs are shown in Figure 8.2 and their main ECG characteristics are compared in Table 8.3. The gap junction information of the larger Rav models are compared with the model 1 in Table 8.4. As shown in Figure 8.2 (A) and (B), the activation time in the AV band produced by the $Rav = 0.46$ model is about 50 ms which is much longer than 23 ms in the model 1. As the gap junction resistivity in the AV band in the $Rav = 0.46$ model was doubled comparing with the model 1, the derived average number of gap junction channels per myocyte in the $Rav = 0.46$ model reduces to 6-45 comparing with 11-89 in model 1 (Table 8.4). This explains the longer activation time delay in the AV band in the $Rav = 0.46$ model. This feature is also reflected in the ECG measured near atrium as shown in Figure 8.2 (D) which exhibits a 41% increase of the R width, a 24% increase of the PR interval and a 5.2% increase of the QT interval as shown in Table 8.3. As shown in Figure 8.2 (D), (E) and (F), the R peaks in the $Rav = 0.46$ model are at about $110\,ms$ comparing with about $90\,ms$ in the model 1 which is consistent with the time difference of activation time delays in AV band in both models ($50\,ms$ versus $23\,ms$).

Increasing the gap junction resistivities in the model AV band to $0.8\ \Omega \cdot m^2$ resulted in an interesting result. Although the average number of gap junction channels per myocyte in AV band in the $Rav = 0.8$ model is 3-26 as shown in Table 8.4, the AP propagation was terminated in the AV band as shown in Figure 8.2 (C). It is also illustrated in the ventricular ECG as shown in Figure 8.2 (F) that there is no R or T peak produced by the $Rav = 0.8$ model. In the atrial and AV band ECGs in Figure 8.2 (D) and (E), there are still downward peaks after the P wave produced by the $Rav = 0.8$ model which are later than the R peak produced by the model 1. However these downward peaks are not the R waves but represent the atrial repolarisation as explained in the previous chapter. These downward peaks in the $Rav = 0.8$ model occurred at the same time at about $140\,ms$ as the downward peaks representing the atrial repolarisation produced by the model 1 as shown in Figure 8.2 (D) and (E). At the same time at $140\,ms$, there are also downward peaks produced by all three models in ventricular ECGs shown in Figure 8.2 (F) representing the atrial repolarisation as well.

The ECGs produced by the large Rav models exhibit the AV block which a typical heart block disorder caused by abnormal atrioventricular conduction, as described in Chapter 2. It has been reported that mice hearts with a reduced number of gap junctions (Connexin 40) exhibit AV block which detected via the recorded ECGs exhibiting a prolonged P wave, PR interval, QRS complex and QT interval [163]. The ECGs produced by the $Rav = 0.46$ model resembles the first-degree AV block in human ECGs [37]. The ECGs with no R waves produced by the $Rav = 0.8$ model resemble human ECGs missing the QRS complex which is the second degree AV block known as Wenkebach phenomenon [37].

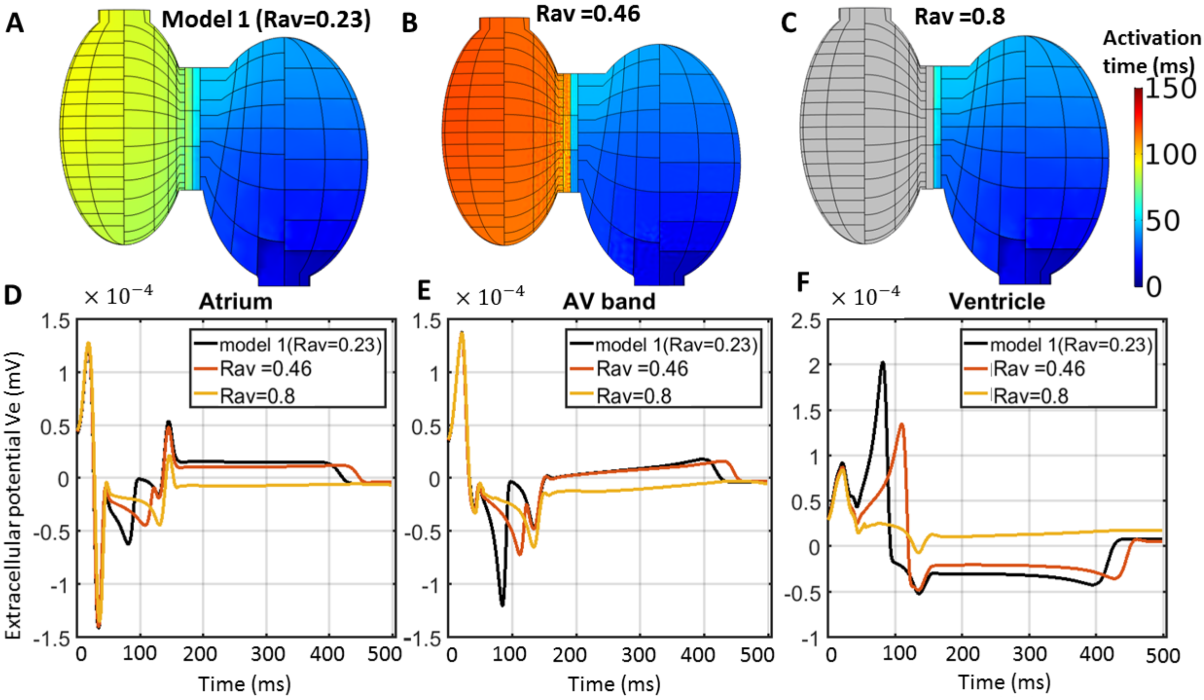

Figure 8.2: Activation time maps of models with the AV band gap junction resistivities at (A) $0.23\ \Omega \cdot m^2$, (B) $0.46\ \Omega \cdot m^2$ and (C) $0.8\ \Omega \cdot m^2$. The ECGs for these three models measured at (D) atrium, (E) AV band and (F) ventricle were plotted.

Table 8.3: ECG characteristics comparison between the model 1 and two models using larger AV gap junction resistivities Rav as shown in Figure 8.2 (D-F).

Region	Source	P width (ms)	R width (ms)	T width (ms)	PR (ms)	QT (ms)
Atrium	Model 1	21	49	151	21	402
	$Rav = 0.46$	19	69	176	26	423
	$Rav = 0.8$	20	-	-	-	-
AV band	Model 1	41	51	164	49	404
	$Rav = 0.46$	40	69	177	53	421
	$Rav = 0.8$	40	-	-	-	-
Ventricle	Model 1	32	57	151	43	408
	$Rav = 0.46$	32	83	189	42	447
	$Rav = 0.8$	32	-	-	-	-

Table 8.4: Gap junction information of the larger Rav models comparing with the model 1

AV band	Model 1	Rav=0.46	Rav=0.8
Gap junction resistivity / $\Omega \cdot m^2$	0.23	0.46	0.8
Gap junction area/μm^2	4920	4920	4920
Average number of gap junction channels per myocyte	11-89	6-45	3-26

8.1.3 Varying ventricular gap junction resistivities

In this section, the ventricular gap junction resistivities, $Rven$, in the larval zebrafish heart model were varied. Model 1 has an IC ventricular gap junction resistivity of $0.13\ \Omega \cdot m^2$ and an OC ventricular gap junction resistivity of $0.2\ \Omega \cdot m^2$. Different IC and OC ventricular gap junction resistivities in the model 1 resulted in different CVs in the IC and OC ventricle which replicates the measured results reported by [57] as shown in the previous chapter.

From preliminary trials, it was found that a doubled or a tripled ventricular gap junction resistivities do not have a big effect on the activation time in the model ventricle. Therefore ventricular gap junction resistivities as large as $0.8\ and\ 2\ \Omega \cdot m^2$ were chosen to report here. For simplicity, both IC and OC ventricular gap junction resistivities were set to same values in both cases.

The activation time maps and ECGs for these models are shown in Figure 8.3. It is interesting to see that the start times of ventricular activation are about $60\ ms$ in both larger $Rven$ models which are earlier than the $75\ ms$ in the model 1. It is possible that as the larger ventricular resistivity in the larger $Rven$ models impedes charge carried by the depolarisation wave from reaching the ventricle quickly. Instead, these charges remained in the AV band and the transition area from the AV band to ventricle which causes an earlier activation in these myocytes. The latest activation time of myocyte in ventricle activation is at about $110\ ms$ in the $Rven = 0.8$ model and about $140\ ms$ in the $Rven = 2$ model which are later than $90\ ms$ observed in the model 1. Therefore, the activation time intervals in the ventricle are $50\ ms$ in the $Rven = 0.8$ model and $80\ ms$ in the $Rven = 2$ model which are larger than about $15\ ms$ in the model 1.

As shown in Figure 8.3, the atrial activation was very similar in all three models as shown in the activation time maps which were also reflected in the ECGs as very similar P waves. As shown in Table 8.5, the R widths in the ECGs measured at all three positions are longer in the larger $Rven$ models than in model 1. For example, the R width in the ECG measured near ventricle is 16% longer in the $Rven = 0.8$ model and 56 % longer in the $Rven = 2$ model than the model 1. In addition, the R peaks in all ECGs produced by the larger $Rven$ models also occurred later than the model 1. It is consistent with the longer total activation time intervals in the ventricle in the larger $Rven$ models as stated above. The QT intervals produced by the larger $Rven$ models in all ECGs are longer than in the model 1 as well, as shown in Table 8.5. For example, in the ventricular ECGs, the QT intervals are 6% longer in the $Rven = 0.8$ model longer and 11% longer in $Rven = 2$ model than in the model 1. The PR intervals in the larger $Rven$ models are prolonged in atrial and AV ECGs comparing with model 1. The PR interval reflects the activation time delay caused by the AV band. However from the activation maps in Figure 8.3 (A-B), the activation time intervals in the AV band are smaller in the larger $Rven$ models than in the model 1 which is in contrast with the fact that a longer PR interval in the atrial and AV band ECGs found in the larger $Rven$ models. However in the ventricular ECGs, the PR intervals in all three models are the same. These modelling results illustrate that errors could be brought in due to the placements of recorded electrodes.

As shown in Table 8.6, although the average number of gap junction channels per myocyte in the $Rven = 2$ model is as small as 1-8 in IC ventricle and 1-11 in the OC ventricle, the ventricle still activated but requires a longer time. Similarly, the atrium still activated with the average number of gap junction channels per myocyte as 4-30 in Table 8.2. However as shown in Table 8.4, the activation in the AV band terminated with an average number of gap junction channels per myocyte of 3-26. This implies that different regions in the heart could be affected by the reduction of gap junction number in different degrees. Compared with the atrium and ventricle in the larval zebrafish heart, the AV band in the larval zebrafish heart is more vulnerable to exhibit cardiac block when the number of gap junctions is reduced. As described in the previous chapter, there are fewer myocytes in the AV band and these myocytes are much thinner and longer than those in the atrium and ventricle which possibly contributes to this vulnerability to cardiac blocks.

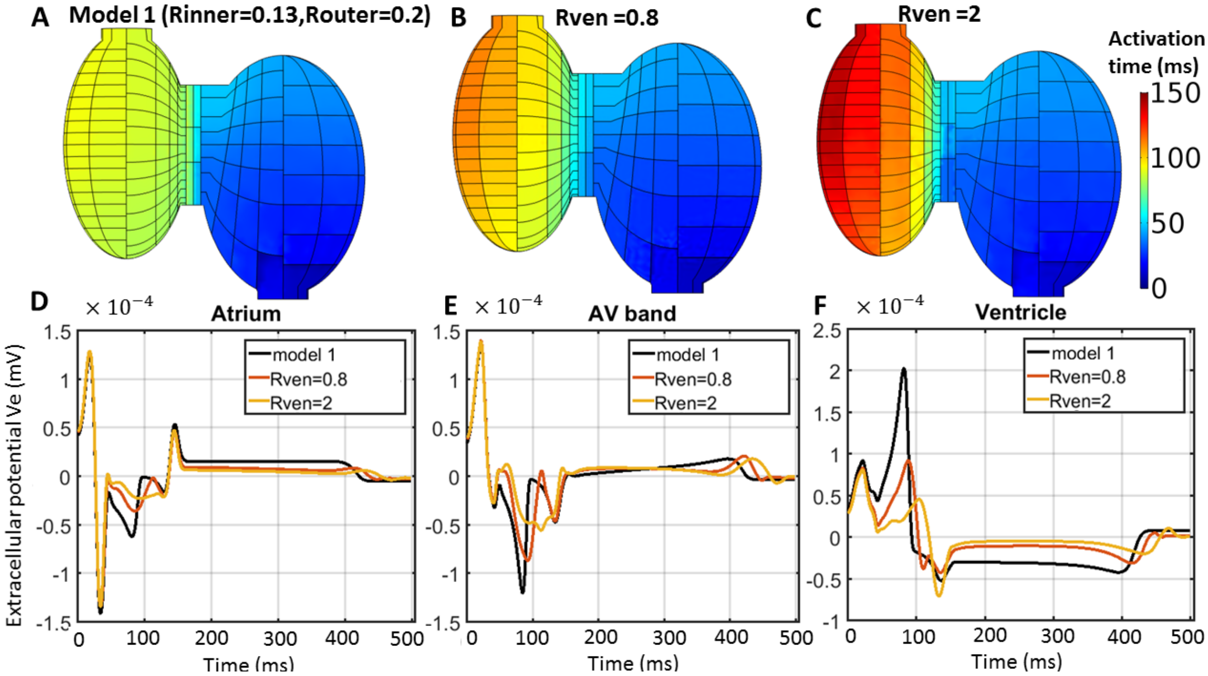

Figure 8.3: Activation time maps of (A) the model 1 with inner ventricular gap junction resistivity at $0.13\ \Omega \cdot m^2$ and outer ventricular gap junction resistivity at $0.2\ \Omega \cdot m^2$ and the larger $Rven$ models with both inner and outer ventricular gap junction resistivities at (B) $0.8\ \Omega \cdot m^2$ and (C) $2\ \Omega \cdot m^2$. The ECGs for these three models measured at (D) atrium, (E) AV band and (F) ventricle were plotted.

Table 8.5: ECG characteristics comparison between the model 1 and two models using larger ventricular gap junction resistivities $Rven$ as shown in Figure 8.3 (D-F).

Region	Source	P width (ms)	R width (ms)	T width (ms)	PR (ms)	QT (ms)
Atrium	Model 1	21	49	151	21	402
	$Rven = 0.8$	19	60	125	26	423
	$Rven = 2$	19	58	110	36	432
AV band	Model 1	41	51	164	49	404
	$Rven = 0.8$	41	56	111	56	421
	$Rven = 2$	40	67	112	61	435
Ventricle	Model 1	32	57	151	43	408
	$Rven = 0.8$	34	67	175	43	432
	Rven=2	35	89	195	43	454

Table 8.6: Gap junction information of the larger $Rven$ models comparing with the model 1

Ventricle	Model 1		$Rven = 0.8$		$Rven = 2$	
	IC Ventricle	OC Ventricle	IC Ventricle	OC Ventricle	IC Ventricle	OC Ventricle
Gap junction resistivity / $\Omega \cdot m^2$	0.13	0.2	0.8	0.8	2	2
Gap junction area/ μm^2	30900	53800	30900	53800	30900	53800
Average number of gap junction channels per myocyte	15-124	14-110	3-20	3-28	1-8	1-11

8.2 52 hours post fertilisation zebrafish model

8.2.1 Model settings

A 52 hpf zebrafish heart model was developed based on the model geometry of 72 hpf zebrafish heart The overall size and shape of the heart were unchanged in the 52 hpf heart model as shown in Figure 8.4 (A), because it has been shown that the dimensions and shape of the zebrafish heart chamber did not change too much from 52 hpf to 72 hpf [81, 153]. This model geometry is comparable to the images of 52 hpf zebrafish in [46].

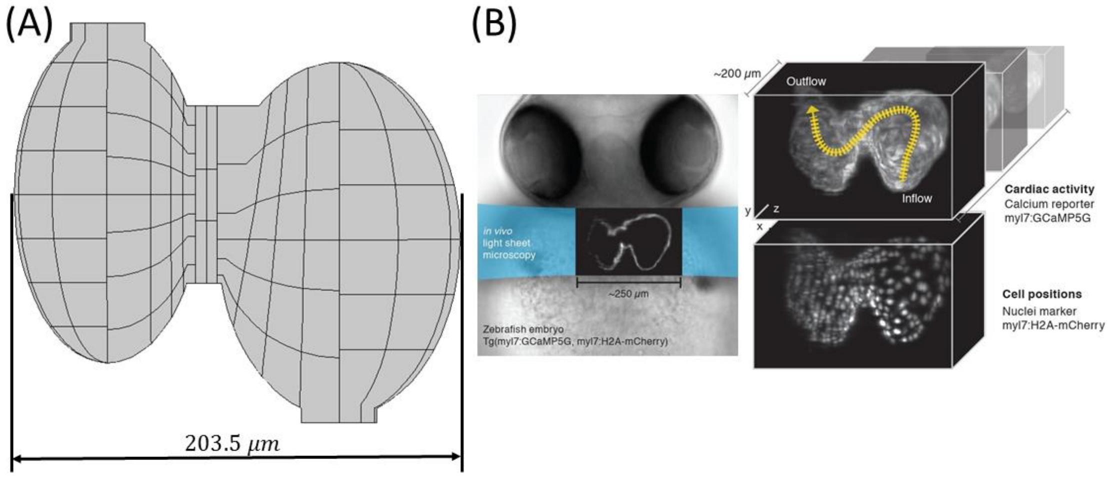

Figure 8.4: (A) heart geometry of 52 hpf zebrafish heart model; (B) Images of 52 hpf zebrafish heart with fluorescent markers expressed in myocardial cells report calcium transient activity and cell positions in [46].

Comparing with the 72 hpf zebrafish heart, there are fewer myocytes in the 52 hpf zebrafish as shown in Table 8.7. In addition, the average surface areas per myocyte in the 52 hpf zebrafish heart are larger than in the 72 hpf zebrafish heart. Thus the model heart geometry was partitioned into myocytes based on the cellular structure of the 52 hpf zebrafish heart where available. If there is no measured data for 52 hpf zebrafish, 48 hpf or 60 hpf zebrafish data was used instead.

The resulting model cellular information in the 52 hpf zebrafish heart model are compared with the 72 hpf zebrafish model and also compared with the literature for zebrafish in different stages from 48 hpf to 72 hpf in Table 8.7. The total myocyte number in the 52 hpf zebrafish heart model is 192 which is the same as 192 in 52 hpf zebrafish reported in [46] and is close to 200 observed the 48 hpf zebrafish [39].

Table 8.7: Geometrical comparison of the 72 hpf and 52 hpf zebrafish heart model with the literature (some of them were estimated from images).

	Region	Myocyte number	Average surface area per myocyte /μm^2	Average circularity per myocyte
72 hpf zebrafish model	Atrium	104	405	0.73
	AV band	12	165	0.27
	ventricle	218	152 (83.5 (IC) and 207.5 (OC))	0.73 (IC)-0.65 (OC)
52 hpf zebrafish model	Atrium	78	540	0.73
	AV band	12	165	0.27
	ventricle	104	319 (163 (IC) and 452 (OC)	0.73 (IC)-0.65 (OC)
Real 48 hpf zebrafish	Atrium	80 [39]	-	-
	AV band	-	-	0.3 [56]
	ventricle	120 [39]	380 [81]	0.83 (IC)-0.64 (OC) [56]
Real 52 hpf zebrafish	Atrium	75 [46]	500-700 (estimated from images in [46])	-
	AV band	-	-	-
	ventricle	117 [46]	200-400 (estimated from images in [46])	0.75 (IC)-0.5 (OC) [57]
Real 60 hpf zebrafish	Atrium	-	-	-
	AV band	-	40 [119]	0.35 [119]
	ventricle	-	80 (IC)-120 (OC) [119]	0.75 (IC)-0.55 (OC) [119]
Real 72 hpf zebrafish	Atrium	100 [39]	-	-
	AV band	-	-	-
	ventricle	220 [39]	500 [81], 4(IC)-7 (OC) [57]	0.75 (IC)-0.5 (OC) [57]

The electrical equations applied to the 52 hpf zebrafish heart model are the same as the 72 hpf zebrafish heart model except for the gap junction resistivities in different regions of the heart. The gap junction resisitivities were adjusted in order to replicate the measured activation times in a 52 hpf zebrafish heart [46] as shown in Figure 8.5. The final gap junction resistivities used in the 52 hpf zebrafish heart model were compared with the 72 hpf zebrafish heart model together with the total gap junction area of each region and the resulting average number of gap junction channels per myocyte as shown in Table 8.8. The average numbers of gap junction channels per myocyte in the 52 hpf zebrafish heart model in different regions are about 3 to 10 times smaller than the 72 hpf zebrafish heart model which implies the increase of gap junctions in larval zebrafish heart during the development stages from 48 hpf to 72 hpf.

Table 8.8: Gap junction information of the 52 hpf zebrafish model comparing with the 72 hpf zebrafish heart model

		Atrium and sinoatrial region	AV band	IC Ventricle	OC Ventricle
72 hpf zebrafish	Gap junction resistivity / $\Omega \cdot m^2$	0.35	0.23	0.13	0.2
	Total gap junction area/ μm^2	64800	4920	30900	53800
	Average number of gap junction channels per myocyte	11-89	11-89	15-124	14-110
52 hpf zebrafish	Gap junction resistivity / $\Omega \cdot m^2$	4	1	1.5	1.5
	Total gap junction area/ μm^2	58200	4920	23200	31400
	Average number of gap junction channels per myocyte	1-9	3-20	2-16	2-19

8.2.2 Modelling results

8.2.2.1 Activation time

The 52 hpf zebrafish heart model aims to replicate the measured results of a 52 hpf zebrafish heart found in [46]. The measured activation time map of the 52 hpf zebrafish heart is shown in Figure 8.5 (B). The total measured activation time delay is about $220\ ms$ which is much longer than about $75\ ms$ in 72 hpf zebrafish heart as described in the previous chapter. The activation times of the approximated centreline produced by the model are shown in Figure 8.5 (A) compared with the published activation times on the centreline of the heart as shown in Figure 8.5 (B). In general, the model activation time of the centreline is comparable to the published line. For example, the total activation time interval from atrium to ventricle is $190\,ms$ which is about the same as the $190\,ms$ in the published line. In addition, the model activation time line for the atrium section (a distance less than $180\,um$) has a smaller slope than that of the AV band and ventricle section which resembles Figure 8.5 (C). A major difference is that the model line shows steps from myocyte to myocyte but the published line is a continuous line. These small steps in the model line indicate the discontinuous cardiac propagation at cellular level. However the published line was a fitted line based on activation times of each myocyte. Another difference is that the maximum measured activation time of the ventricle in the measured line is in the middle of the ventricle section as shown in Figure 8.5 (C) while the model activation time in ventricle is constant from distance along the line of $250\,um$. This is because the model line only show the activation times of cells along the line while the published line is an averaged line of all the dots (cells) at the same distance as shown in Figure 8.5 (C). Therefore in the published line, cells at the OC ventricle were also included, which activated later than the cells on the boundaries of the approximate centre line shown in Figure 8.5 (B).

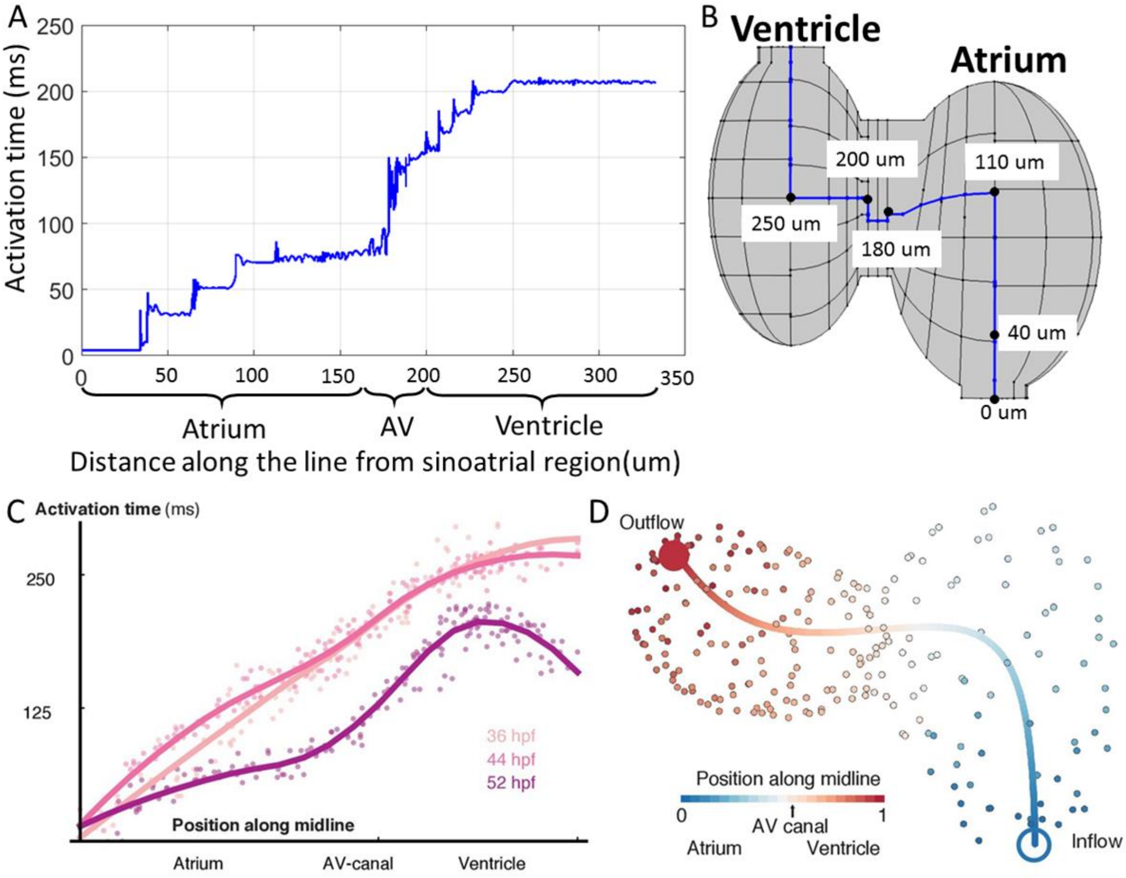

Figure 8.5: (A) Activation time of the boundaries on the approximated centreline versus the distance along the line from the sinoatrial region in the 52 hpf zebrafish heart model. (B) Boundaries on the approximated centreline in the 52 hpf zebrafish heart model are shown in blue. (C) The distribution of activation times along the centerline in the real 36, 44, and 52 hpf zebrafish hearts in [46]. Dots indicate activation time of each cell and the smooth regression profiles are solid lines. (D) The centreline of the 52 hpf zebrafish heart in [46].

8.2.2.2 Cell-based activation time map

The published activation time map in [46] is shown in Figure 8.6 (B). Instead of plotting activation time for every point on the surface of the zebrafish heart as in the activation time map of 72 hpf zebrafish heart as in the previous chapter, the activation time of each individual cell in this activation time map were measured based on the time-point of 10% calcium transient over one cardiac cycle and only plotted at the positions of their nucleus. In order to replicate this activation time map, the activation times of all myocytes in the model heart were calculated as the average activation time over the myocyte surface. The activation time was defined as the time point when the transmembrane potential reaches $0\,mV$ for the first time. Then these activation times ($tact$) minus the minimum activation time ($min(tact)$) were plotted at the corresponding centroids of the myocytes in the model heart. The resulting activation time map of the 52 hpf zebrafish heart model is shown in Figure 8.6 (A). Both activation time maps look alike given that the ventricle was twisted in a different angle as shown in Figure 8.6 (B). However as shown in Figure 8.6, there are about 16 cells in red near the sinoatrial region of the model heart compared with about 7 cells in the published map. This means that there are more myocytes activated at an earlier time which were probably caused by a large stimulation. Similar to the 72 hpf zebrafish heart model, the start of activation was triggered by a higher intracellular potential of cells in the sinoatrial region than the resting potential. Therefore modifications to the stimulation method are required and will be discussed in section 8.2.3.

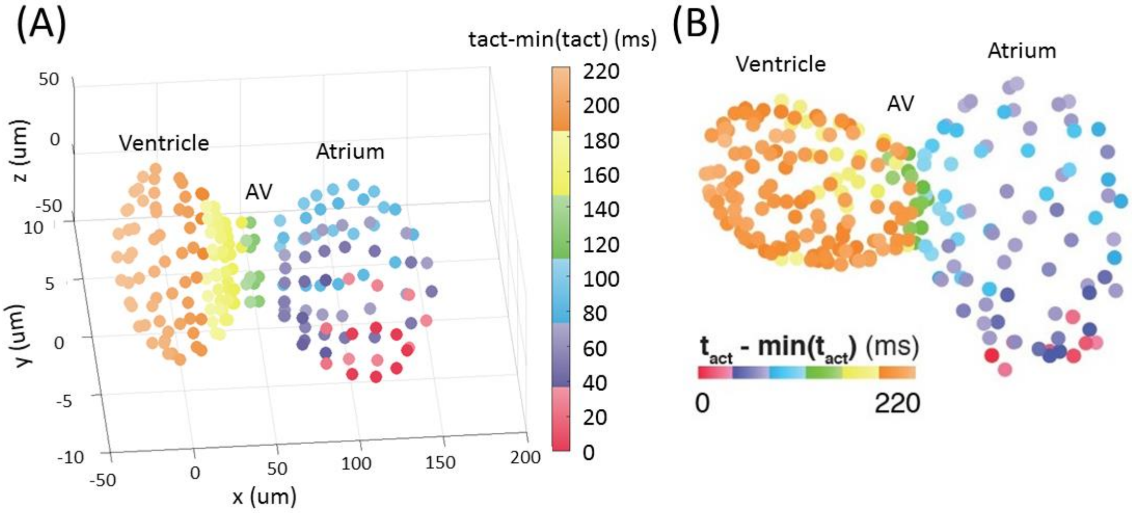

Figure 8.6: (A) Activation time map of the 52 hpf zebrafish heart model. The activation time is defined as the time when the transmembrane potential reaches 0 mV during the rising phase of its AP. (B) measured activation time of calcium transient in 52 hpf zebrafish heart [46]. The activation time t_{act} is based on the time-point of 10% calcium transient amplitude in every individual cell. Colour bar in (A) was generated based on the RGB values in order to resemble (B).

8.2.2.3 Cell-based conduction velocity map

The CV map produced in [46] and corresponding statistics are shown in Figure 8.7 (A) and (B). The methods used to plot the conduction speed map are described in [46] and was based on the average local cell-to-cell CV. At each cell’s position, the (harmonic) mean of the distance travelled by the activation per time was computed over all paths from the cell to its neighbours:

$$cs_i = n(\sum\nolimits_j \frac{dt(i,j)}{d(i,j)})^{-1} \tag{8.1}$$

for all neighbours j of the cell i with $dt(i,j)$ being the temporal difference in activation time and $d(i,j)$ the 3D Euclidean distance between nucleus of the cell i and the cell j.

The same method of plotting the CV map in [46] was attempted for the 52 hpf zebrafish heart model. However because the modelling data provided by COMSOL are limited, some compromises were made. For example, the 3D Euclidean distance between cells cannot be measured in the same way. Therefore, the distance between cells used the absolute distance between their centroids. In addition, the neighbours of each cell cannot be automatically recognized. Therefore, as a typical cell in the heart model is connected to about 8 cells, as shown in Figure 8.8, and the coordinates of their centroids are known, the neighbours of each cell were found by computing the distances between any two cells and finding the nearest 8 cells for each cell. Based on this 8 neighbours' method, the model CV map was computed and plotted in Figure 8.7 (C). All cells are linked to the 8 neighbours via grey wires as shown in Figure 8.7 (C).

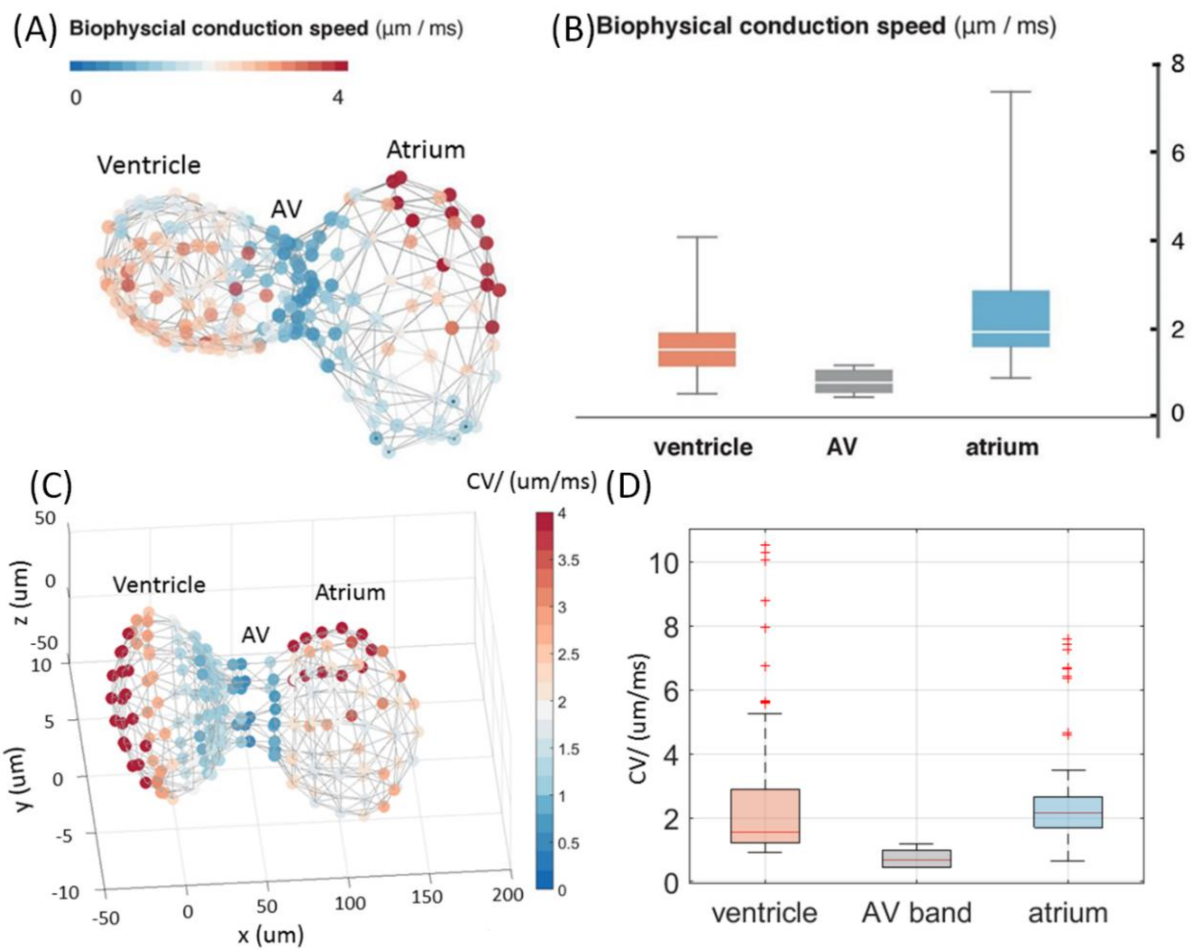

Figure 8.7: (A) CV map based on the visualized 3D networks of the 52 hpf zebrafish heart in [46]. (B) Descriptive statistics of CVs of the 52 hpf zebrafish heart in [46] in regions corresponding to atrium (blue), AC band (grey), and ventricle (orange). (The number “8” was added manually) (C) CV map of the 52 hpf zebrafish heart model based on the 8 neighbours’ method. (D) Box plot of CVs produced by model in regions corresponding to atrium (blue), AC band (grey), and ventricle (orange).

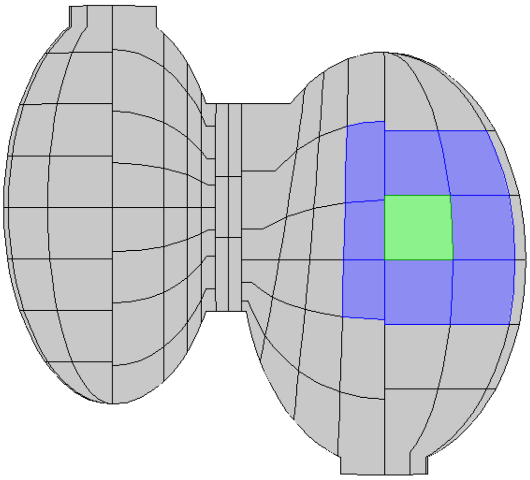

Figure 8.8: A typical example of 8 neighbour cells in blue of the cell in green in 52 hpf zebrafish heart model.

The corresponding statistics of CV map for the model were plotted in Figure 8.7 (D). The method used to plot the corresponding statistics of CV map in [46] as shown in Figure 8.7 (B) were not described in the paper [46]. However, this plot looks like a boxplot. A typical boxplot displays the distribution of data based on five values: the "minimum", first quartile (Q1), median, third quartile (Q3) and the "maximum" as shown in Figure 8.9. The median is the middle value of the dataset which is 50th percentile of the data. The first quartile (25th percentile) and third quartile (75th percentile) are the middle numbers between the smallest/highest values and the median of the dataset. Note that the smallest or the highest values are not the "minimum" or the "maximum". The data in the 25th to the 75th percentile are in the interquartile range (IQR). The whiskers are the extended lines from the box which shows the data within $1.5 \times IQR$ range of the first quartile and the third quartile. The "maximum" and the "minimum" are $Q3 + 1.5 \times IQR$ and $Q1 - 1.5 \times IQR$. The outliners are data points out of the range between the "maximum" and the "minimum". Typically, the outliners are not considered in the whiskers and usually plotted separately as dots or using the `'+'` symbol in MATLAB as shown in Figure 8.7 (D).

As shown in Figure 8.7 (B) and (D), the median CV in model ventricle (1.5 $\mu m/ms$) are the same as the measured value (1.5 $\mu m/ms$). However the top edge of the box indicating the third quartile (Q3) of the data is 2.8 $\mu m/ms$ which is higher than the reference (1.8 $\mu m/ms$). In addition, as shown in Figure 8.7 (C) the model ventricle had more cells in red at the OC ventricle which indicates a higher CV at the OC ventricle area than in the published map as shown in Figure 8.7 (A). It shows that the CVs for ventricle produced by the model were larger than in the published map, therefore further modifications were needed. In order to replicate the published results, the gap junction resistivity in model ventricle would need to increase to reduce the CVs in ventricle especially for the OC ventricle region.

The boxplot for the AV band produced by the model had a median at about 0.6 $\mu m/ms$ with the top and bottom edges of box at about 1 $\mu m/ms$ and 0.5 $\mu m/ms$ which was very close to the published result. The upper edge of the whisker for the AV band produced by the model was about 1.1 $\mu m/ms$ which was also similar (1.3 $\mu m/ms$). The lower edge of the whisker for the AV band produced by the model is not visible because it overlaps with the bottom edge of the box. However it is still comparable to the lower edge of the whisker in the published plot at about 0.5 $\mu m/ms$.

The boxplot for the atrium produced by the model had a median at about 1.7 $\mu m/ms$ comparing with about 1.8 $\mu m/ms$ in the published plot. The top and bottom edges of the box for the model atrium were about 0.9 $\mu m/ms$ and 2.5 $\mu m/ms$ comparing with 1.5 $\mu m/ms$ and 2.8 $\mu m/ms$ in the published map. The upper edge of the whisker for atrium produced by the model was about 5 $\mu m/ms$ which was smaller than 7.5 $\mu m/ms$ in the published map. The lower edge of the whisker for atrium produced by the model is about 0.3 $\mu m/ms$ which was also smaller than 0.7 $\mu m/ms$ in the published plot. However as the meaning of the whisker of the published boxplot was uncertain, it could stand for the largest and smallest CVs. If the whisker in published plot are the largest and smallest CVs, then the model resembles it better as the largest CV in model atrium was 8 $\mu m/ms$.

In summary, for the atrium and AV band, both the CV map and the boxplot produced by the model were similar to the published results. No modification is needed to be made for the model atrium and AV band.

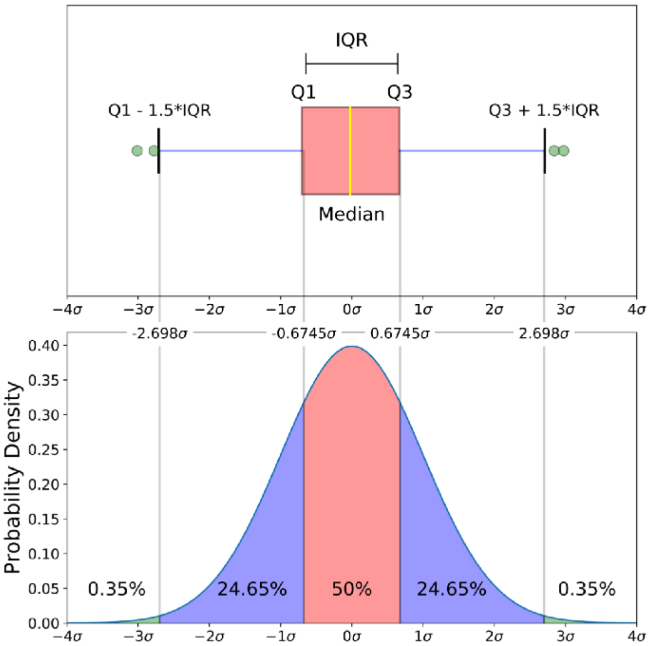

Figure 8.9: Boxplot and the corresponding probability density function of a normal $N(0,1\sigma^2)$ population from [164].

8.2.3 Modified 52 hpf zebrafish heart model

As shown in the previous section, two modifications were needed. The first was the stimulation method of the heart. As shown in Figure 8.6, cells near the sinoatrial region of the model heart were activated more quickly than in the published map. A smaller stimulation was needed to slow down the activation of these cells. Therefore, a new boundary condition of the stimulation was applied to the modified model. Instead of using a high intracellular potential in all cells in the sinoatrial region, a stimulation current was applied to the membranes of these cells as shown in Figure 8.10. The stimulation current was plotted against time as shown in Figure 8.10 (B).

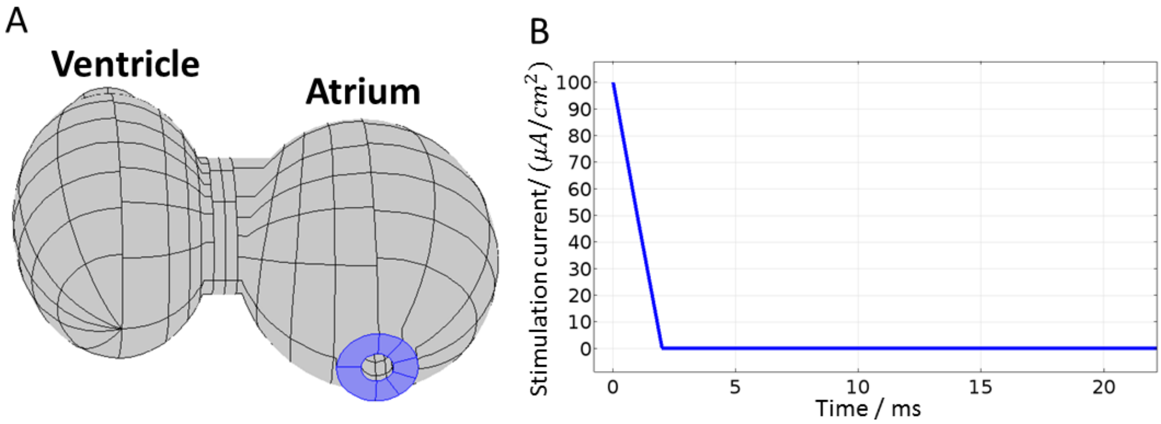

Figure 8.10: (A) Boundaries in the sinoatrial region in 52 hpf zebrafish heart model in blue where stimulation current was applied. (B) Stimulation current versus time.

The second modification was the gap junction resistivity of the model ventricle. As shown in Figure 8.7, the CV in the model ventricle was higher than the published result. Therefore the gap junction resistivities of model ventricle were increased to reduce the CV in the model ventricle. The adjusted gap junction resistivities in the modified 52 hpf zebrafish heart model were compared with the original model and 72 hpf zebrafish heart model along with the resulting average number of gap junction channels per myocyte in Table 8.9. As is shown, in the modified model, the gap junction resisitivity in the OC ventricle is 2 times larger than in the IC ventricle which is similar as in the 72 hpf zebrafish heart model.

Table 8.9: Gap junction information of the modified 52 hpf zebrafish heart model comparing with the previous 52 hpf zebrafish heart model and 72 hpf zebrafish heart model

Model		Atrium and sinoatrial region	AV band	IC Ventricle	OC Ventricle
52 hpf zebrafish	Gap junction resistivity / $\Omega \cdot m^2$	4	1	1.5	1.5
	Total gap junction area/ μm^2	58200	4920	23200	31400
	Average number of gap junction channels per myocyte	1-9	3-20	2-16	2-19
Modified 52 hpf zebrafish	Gap junction resistivity / $\Omega \cdot m^2$	4	1	2	4
	Total gap junction area/ μm^2	58200	4920	23200	31400
	Average number of gap junction channels per myocyte	1-9	3-20	2-12	1-7
72 hpf zebrafish	Gap junction resistivity / $\Omega \cdot m^2$	0.35	0.23	0.13	0.2
	Total gap junction area/ μm^2	64800	4920	30900	53800
	Average number of gap junction channels per myocyte	11-89	11-89	15-124	14-110

8.2.3.1 Modelling results

The activation time map, CV map and boxplot of CVs in different regions produced by the modified 52 hpf zebrafish heart model are shown in Figure 8.11 and Figure 8.12. The activation time map produced by the modified model has 4 cells in red which is closer to the 7 cells in red in the published map than the 16 cells in red in the original map. The model ventricle region in the CV map produced by the modified model has fewer points in red compared with the CV map produced by the original model in Figure 8.7 (C) and resembles the published CV map as shown in Figure 8.12 (A) better as well. The boxplot for ventricle produced by the modified model also resembled the published boxplot better than the original model as shown in Figure 8.12 (B) and (D).

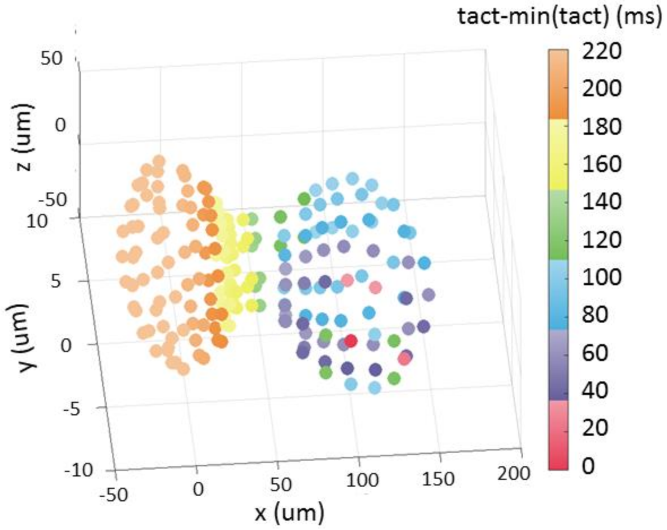

Figure 8.11: Activation time map of the modified 52 hpf zebrafish heart model

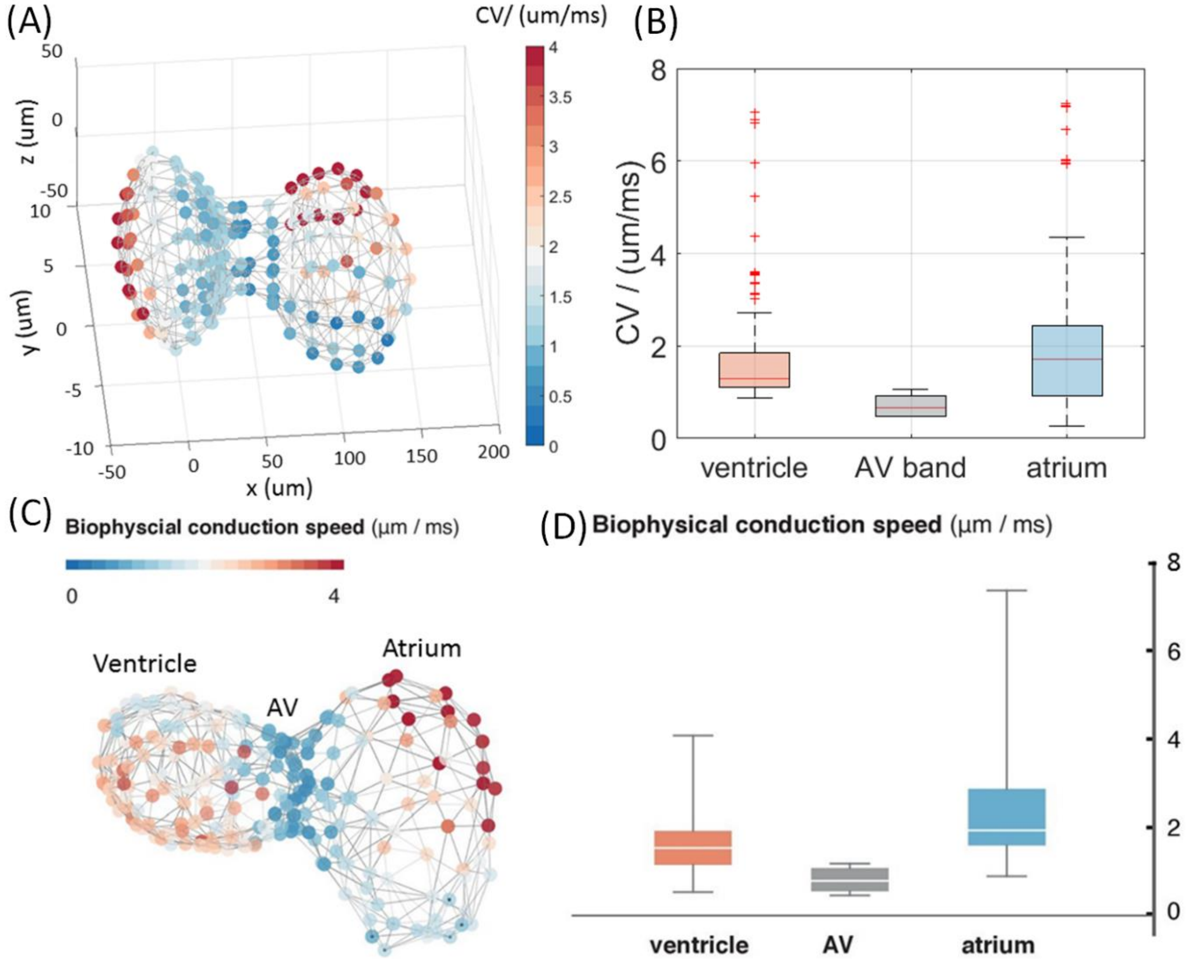

Figure 8.12: (A) CV map of the modified 52 hpf zebrafish heart model based on 8 neighbours' method. (B) Box plot of CVs produced by model in regions corresponding to atrium (blue), AC band (grey), and ventricle (orange). (C) CV map based on the visualized 3D networks of the 52 hpf zebrafish heart in [46]. (D) Descriptive statistics of CVs in [46] in regions corresponding to atrium (blue), AC band (grey), and ventricle (orange). (The number "8" was added manually)

8.2.3.2 Improvements to the cell-based conduction velocity map

In order to compute similar CV map as the published CV map in [46], the 8 neighbours' method was developed to find the neighbours of each cell in the model heart. The 8 neighbours' method is based on finding the nearest 8 cells of the target cell by comparing the distances of all cells to the target cell and extracting the 8 cells with the 8 smallest distances. However the 8 cells with the smallest distances to the target cell are not always the "real" neighbours. For example as shown in Figure 8.13 (A), the green cell is the target cell and the 8 cells in blue are the 8 neighbours found by the 8 neighbours' method. However, the actual 8 neighbours are the cells in blue in Figure 8.13 (B) which are the cells in contact with the target cell. Moreover, some cells in the model heart do not have 8 neighbours such as the cells in the sinoatrial regions or near the apex of the ventricle. Therefore, a new method was developed which is to find cells that are in contact with the target cell (i.e. sharing the same interior boundaries). A cell is typically connected with 4 cells as shown in Figure 8.14, therefore this method is called 4 neighbours' method.

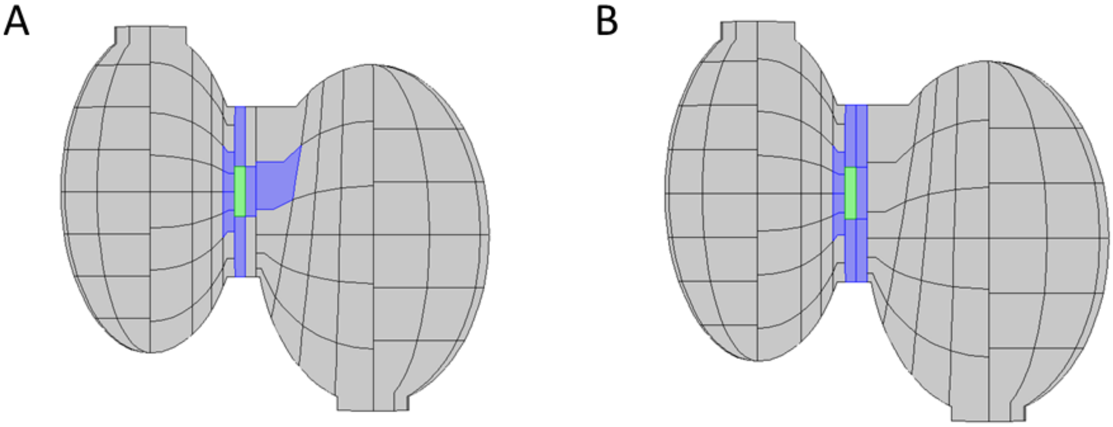

Figure 8.13: (A) 8 neighbours (blue) of the target cell (green) in 52 hpf zebrafish heart model found by the 8 neighbours' method; (B) the actual 8 neighbours (blue) of the target cell (green).

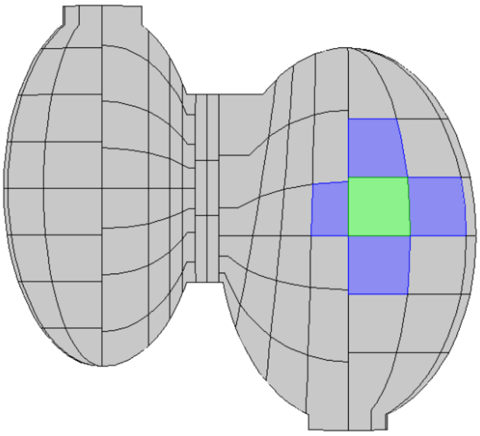

Figure 8.14:A typical example of 4 neighbours (blue) of the target cell (green) in the 52 hpf zebrafish heart model.

The CV map and the boxplot of CVs in different regions of the heart based on the 4 neighbours' method are shown in Figure 8.15 (A) and (B). All cells are only connected to 4 neighbours via grey wires rather than 8 neighbours, so the wires are less dense than the plots in Figure 8.12. The CV map based on the 4 neighbours' method as shown in Figure 8.15 (A) is very similar to the results based on the 8 neighbours' method in Figure 8.12 (A). Both maps showed high CVs (around 4 $\mu m/ms$) in the apex of the atrium and the OC ventricle and also small CVs in the AV band (around 1 $\mu m/ms$). In the published map as shown in Figure 8.15 (C), similar high CVs appeared in the apex of atrium and also similar small CVs appeared in the AV band. The CVs in different regions of the heart can also be compared using the boxplots as shown in Figure 8.15 (B). Compared with boxplots based on the 8 neighbours' method Figure 8.12 (B), the median CVs for all three regions based on the 4 neighbours method varies little within the range of 0.1 $\mu m/ms$. The largest CV in atrium is 8.1 $\mu m/ms$ which are slightly bigger than 7.3 $\mu m/ms$ in atrium based on the 8 neighbours' method. In summary, the CVs based on both methods are very similar and resembled the published plots to a good extent (Figure 8.15).

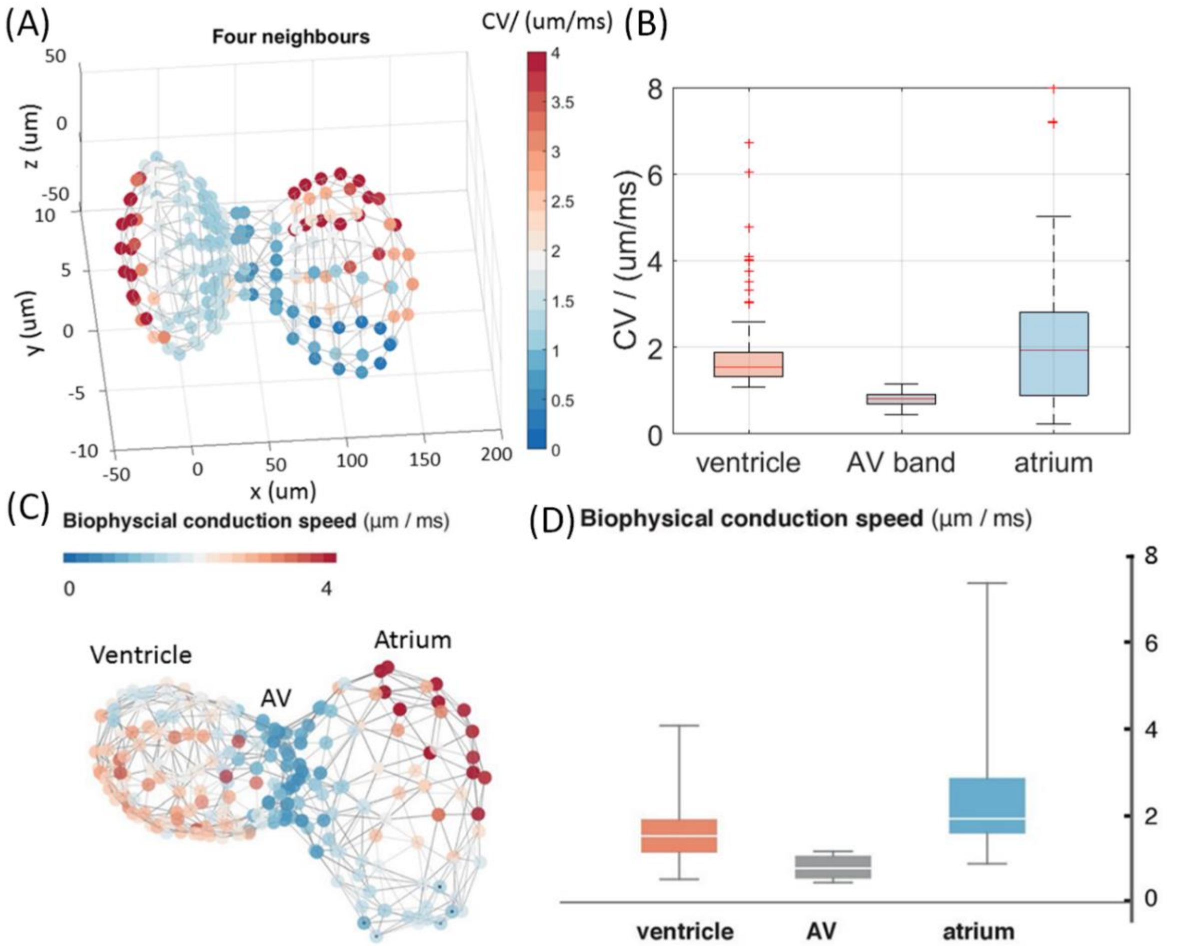

Figure 8.15: (A) CV map of the modified 52 hpf zebrafish heart model based on the 4 neighbours' method. (B) Box plot of CVs produced by model in regions corresponding to atrium (blue), AC band (grey), and ventricle (orange). (C) CV map based on the visualized 3D networks of the 52 hpf zebrafish heart in [46]. (D) Descriptive statistics of CVs in [46] in regions corresponding to atrium (blue), AC band (grey), and ventricle (orange). (The number "8" was added manually)

8.3 Summary

This chapter described an application and an extension of the larval zebrafish heart model described in Chapter 7. Firstly, the larval zebrafish heart model is modified to simulate the gap junction remodelling by varying the gap junction resistivities in different regions of the heart. These models simulated the partial loss of gap junctions in the atrium, or the AV band or the ventricle and exhibited similar ECG features as found in literature such as prolonged P waves, PR intervals, and QT intervals. In section 8.1.2, the variation of AV band gap junction resisitvities resulted in ECGs exhibiting different degrees of AV block including the first-degree AV block and second-degree AV block which is also a common cardiac condition occurred in humans [37]. This application illustrates the potential of this larval zebrafish heart model to study the disease-related alterations at cellular level such as the gap junction remodelling on the whole heart level which allows direct comparison with the resultant ECGs.

Secondly, the zebrafish heart model in Chapter 7 was extended to be a 52 hpf zebrafish heart model in order to reproduce the cardiac propagation in a 52 hpf zebrafish reported in [46]. Compared with the 72 hpf zebrafish heart, there are fewer myocytes in the 52 hpf zebrafish heart. However the size and shape of the heart at both stages are very similar. Therefore, the geometry of the 72 hpf model heart has been modified to include fewer myocytes. In addition, the gap junction resistivities in the 52 hpf zebrafish heart model were adjusted to replicate the longer activation time delay at $220\ ms$ comparing with $75\ ms$ in a 72 hpf zebrafish heart. The 52 hpf zebrafish heart model reproduced the cell-based activation time map and CV maps shown in [46] to a good extent. Two different methods of computing the CVs of each cell in the heart has been developed known as the 8 neighbours' method and the 4 neighbours' method. It has been found both methods result in similar CV maps and boxplot of CVs that resembled the measured CV map in [46]. This extension of the larval zebrafish heart model illustrates the feasibility of this model to simulate larval zebrafish heart in different development stages. It also paves the way to simulate other animal hearts with more complicated structure and more myocytes.

9. CONCLUSION AND FUTURE WORK

In this thesis, a series of multiscale models of larval zebrafish heart were described beginning with a single cell model which was then expanded to cardiac tissue models such as a ventricular fibre and cell arrays and finally a whole heart model. Cardiac propagation at multiple levels in the larval zebrafish heart has been simulated. The electrical equations used in these larval zebrafish models are similar. Realistic cell sizes have been simulated with an electrically active membrane separating the intracellular and extracellular spaces. Both spaces are filled with and surrounded by electrically passive conducting fluid. In the multicellular models cells are connected by gap junctions modelled by passive electrical resistances. The electrical activity of the active membranes was described by a Fitzhugh-Nagumo (FHN) type model which was able to reproduce the main AP parameters reported in the literature. In a previous published larval zebrafish heart model using the bidomain model [36], unphysical and unbiological conductivity values had to be used order to replicate the realistic features of cardiac propagation. The models described here solved this problem using a discrete approach. Rather than treating the heart as a continuum as in the biodomain model, this discrete approach incorporates the cellular structures and model the effects of gap junctions separately.

The most significant achievement is that the larval zebrafish heart model introduced here is the first cell level model of the whole heart of any vertebrate. This model has been used to reproduce the published results of three techniques which have been applied to the zebrafish embryo heart including the measurements of the electrocardiogram [150]. activation maps [57] and conduction velocity maps [46]. Whilst the model ECGs reproduced many of the features of experimentally observed ECGs, they contained additional high frequency components. After filtering using the same filter as used in the recorded ECGs, the resemblance was much better.

The key parameter of these larval zebrafish models is the gap junction resistivity, which is adjusted to obtain CVs in agreement with the published observations. This approach of using the adjusted gap junction resistivities has been compared to a similar model of a human ventricular fibre (HVF) as introduced in Chapter 5 which used a measured gap junction resistivity. Using the average gap junction area per myocyte and the derived number of gap junction channels per myocyte, the density of gap junction channels on the gap junction area can be derived and is shown in Table 9.1 for all of the different models. As is shown, the density of gap junction channels of the HVF model is much larger than the larval zebrafish ventricular fibre model number 1 (LZVF1). This is consistent with the fact that the human CV is also much larger than the larval zebrafish CV. For the zebrafish models, although the CVs produced are the same, the density of gap junction channels for the ventricle in the 72 hpf zebrafish heart model is about 10 times smaller than the LZVF1 model whilst for the cubic cell array model described in Chapter 6, it is about 3 times smaller than the LZVF1 model. This suggests that a high density of gap junction channels is required in the LZVF model where the cardiac propagation is in one dimensional (along the chain) whilst a lower density of gap junctions are required by the cubic cell array model or the heart model where cardiac propagation is in two or more dimensions. For the 48 hpf zebrafish heart model, an even lower density of gap junction channels than the 72 hpf zebrafish heart model is required to give 3 times smaller CVs than in the 72 hpf heart model.

Table 9.1: Gap junction information comparison between different models in Chapter 5-8

Model	Average gap junction area per myocyte/ μm^2	Number of gap junction channels per myocyte	Density of gap junction channels per unit area /$(number/\mu m^2)$	CV/ $(\mu m/ms)$
HVF	300	2.42×10^4-1.33×10^5	80.7-443.3	510
LZVF1	100	31-250	0.31-2.5	4.8
Cubic cell array	292	37-292	0.125-1	4.5
Polygonal cell array	146	46-365	0.32-2.5	3.82
Ventricle in 72 hpf zebrafish heart	389	14-110	0.035-0.284	4.6
Ventricle in 48 hpf zebrafish heart	525	2-12	0.0038-0.023	1.5

In Chapter 8, it has been demonstrated that the larval zebrafish heart model has potential applications in simulating cardiac diseases or conditions. Benefiting from the discrete approach used in this model, cardiac conditions associated with abnormal cellular structure can be simulated. In this thesis, the potential for the discrete model to study cardiac disorders through simulating the gap junction remodelling has been demonstrated. It has been found that by adjusting the gap junctions resistivities, a common cardiac condition: AV block, can be simulated where the model ECGs were qualitatively comparable to experimental results in mice [163]. Using this larval zebrafish heart model, it is possible to simulate other cardiac conditions caused either by genetic modification or drug treatments which are associated with abnormal cellular structure in the future.

9.1 Future work

The work described in this thesis could be built upon in a number of different directions, which can be grouped as follows: the refinements of the current models in section 9.1.1 and 9.1.2 and the extensions of the current models in section 9.1.3.

9.1.1 Geometrical refinement

The model geometry of the larval zebrafish heart described in Chapter 7 is based on images from the literature and a previous published larval zebrafish heart geometry [36]. This model geometry does not accurately correspond to the exact shape of the real heart because of a number of technical issues. For example, it is difficult to image the larval zebrafish heart from a ventral or lateral view because of the transparency of larval zebrafish. In addition, errors can be introduced when the geometry is constructed based on 2-dimensional images viewed from different angles. In order to construct more realistic heart geometry, images at cellular resolution are needed which can be possibly produced by more advanced imaging techniques such as optical projection tomography (OPT) and high-speed selective plane illumination microscopy (SPIM) [165].

The other geometrical feature of the larval zebrafish heart that could possibly affect the accuracy of the modelling results is its multilayer structure of the heart wall at 3-5 dpf. There are three layers which are the endocardium, myocardium and epicardium as shown in Figure 9.1 (A). As shown in Figure 9.1 (B), at 48 hpf, cardiac jelly separates the endocardial and myocardial layers and its thickness reduces gradually. By 96 hpf, cardiac jelly remains in the atrium and disappears in the ventricle. It may be seen that in Figure 9.1 (B), some regions of the myocardium in 72 hpf zebrafish ventricle have two layers of cells. However, the current larval zebrafish heart model only simulated the myocardium with one cell layer at a constant thickness. A more realistic model geometry would include this multilayer structure. For the 72 hpf zebrafish heart, a thicker ventricular myocardium than the atrial myocardium would mean more electrical activity in the ventricle than in the atrium which possibly affects the resultant ECGs. In addition, as shown in Figure 9.1 (B), trabeculae form at 60 hpf which have not been modelled in the current larval zebrafish heart model, which could possibly affect its accuracy.

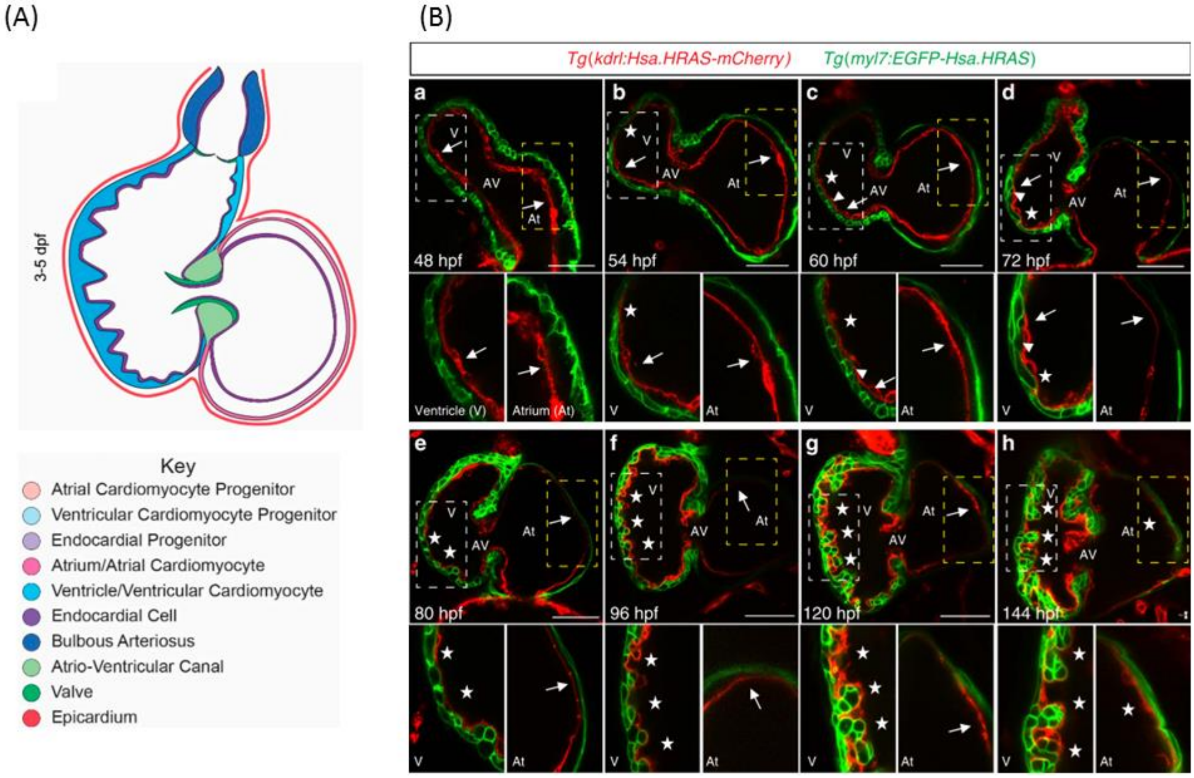

Figure 9.1: (A) cross-sectional view of the larval zebrafish heart at 3-5 dpf from [80] (B) heart in developing larval zebrafish heart from [79] with the endocardial and myocardial membranes labelled in red and green, respectively. Arrowheads show the trabecular cardiomyocytes.

The myocytes in the larval zebrafish heart model reported here were divided by straight surfaces without any extracellular spaces between the myocytes. Although no description of the extracellular spaces between cells in the larval zebrafish has been found in the literature, there are papers for human cardiac tissue showing the existence of these extracellular spaces, as described in Chapter 2. In the future, with the enrichment of this information in larval zebrafish heart, the current model heart geometry could be modified accordingly. Preliminary work for this have been conducted as described in Chapter 6. As shown in Table 9.1, it is interesting to note that the density of gap junction channels in the polygonal cell array model is same to the density in the LZVF1 model which is larger than in the cubic cell array model. It implies that adding extracellular spaces between cells would result in the increase of density of gap junction channels however the number of gap junction channels per myocyte is similar to models including no extracellular spaces between cells (cubic cell array model).

9.1.2 Ionic current model

The ionic current model used in the current heart model is the FHN model which is a phenomenological model which only reproduced the overall shape of AP. A more realistic model would be a biophysical model based on individual ionic channels on the cell membrane such as the Luo and Rudy model [43]. However currently most biophysical models are designed for human or mammalian model animals and there is no biophysical model for the zebrafish heart. As it has been found that most fundamental ionic currents found in human are also present in zebrafish, it may be possible to modify a current human biophysical model for the zebrafish case. However, there are differences. For example, there is no fast phase 1 repolarization in the APs of either the larval or adult zebrafish heart due to the absence of the transient outward current I_{to} [6]. In addition, a T-type Ca^{2+}current, which is present in atrium and ventricle in both larval and adult zebrafish is only present in the heart of mammalian embryos [11].

9.1.3 Electromechanical model

It would be possible to develop an electromechanical model of the larval zebrafish heart based on the current electrical larval zebrafish heart model. COMSOL is a multiphysics modelling platform which allows the coupling of different systems. The movement of the heart can be simulated using the deformed mesh interface and, fluid-structure interaction would constrain the simulated movement of the structural wall and fluid flow. An example of heart movements associated with computational fluid dynamics (CFD) in a 48 hpf zebrafish heart carried out by other workers is shown in Figure 9.2. Several experimental results of blood flow patterns and hemodynamic stress have been published for larval zebrafish and could be used to validate the mechanical aspects of the model [166]. Coupling the electrical and mechanical dynamics of a heart model would provide a new diagnostic tool for understanding the experiments carried out with this model animal.

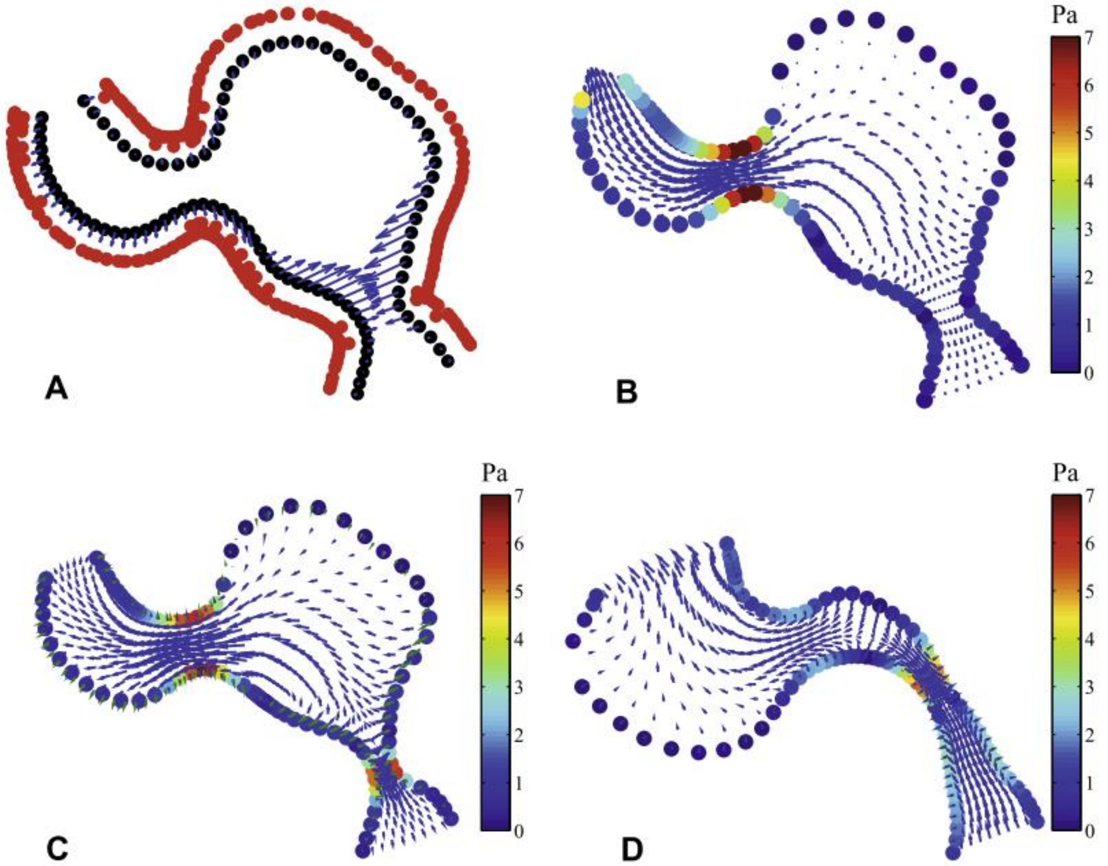

Figure 9.2: (A) Computational set-up of modelling the mechanical and hydrodynamics in a 48 hpf zebrafish heart for a given time point: red points, source points; black points, collocation points (wall points); vectors, velocity boundary conditions. (B–D) Computed instantaneous velocity field (vectors) and wall shear stress (colour coded) at three different time points during the atrial contraction.[167]

10. APPENDIX

Publication list

Published: Qian, S. and E. Tarte (2019). "Finite element modelling of discontinuous action potential propagation in larval zebrafish and human cardiac tissue." Physical biology 17(1): 016001.

In preparation: "Cell-based larval zebrafish heart model and its application to simulate AV block": based on the content in Chapter 7 and Chapter 8.

11. BIBLIOGRAPHY

[1] Wang H, Naghavi M, Allen C, Barber R, Carter A, Casey D, et al. Global, regional, and national life expectancy, all-cause mortality, and cause-specific mortality for 249 causes of death, 1980–2015: a systematic analysis for the Global Burden of Disease Study 2015. The Lancet. 2016;388(10053):1459-544.

[2] Vornanen M, Hassinen M. Zebrafish heart as a model for human cardiac electrophysiology. Channels. 2016;10(2):101-10.

[3] King JA, Garelick TS, Brevard ME, Chen W, Messenger TL, Duong TQ, et al. Procedure for minimizing stress for fMRI studies in conscious rats. J Neurosci Methods. 2005;148(2):154-60.

[4] Barrionuevo WR, Burggren WW. O2 consumption and heart rate in developing zebrafish (Danio rerio): influence of temperature and ambient O2. Am J Physiol. 1999;276(2 Pt 2):R505-13.

[5] Arnaout R, Ferrer T, Huisken J, Spitzer K, Stainier DY, Tristani-Firouzi M, et al. Zebrafish model for human long QT syndrome. Proc Natl Acad Sci U S A. 2007;104(27):11316-21.

[6] Nemtsas P, Wettwer E, Christ T, Weidinger G, Ravens U. Adult zebrafish heart as a model for human heart? An electrophysiological study. Journal of molecular and cellular cardiology. 2010;48(1):161-71.

[7] Wythe JD, Jurynec MJ, Urness LD, Jones CA, Sabeh MK, Werdich AA, et al. Hadp1, a newly identified pleckstrin homology domain protein, is required for cardiac contractility in zebrafish. Disease models & mechanisms. 2011;4(5):607-21.

[8] Koumi S, Backer CL, Arentzen CE. Characterization of inwardly rectifying K+ channel in human cardiac myocytes. Alterations in channel behavior in myocytes isolated from patients with idiopathic dilated cardiomyopathy. Circulation. 1995;92(2):164-74.

[9] Milan DJ, Jones IL, Ellinor PT, MacRae CA. In vivo recording of adult zebrafish electrocardiogram and assessment of drug-induced QT prolongation. Am J Physiol Heart Circ Physiol. 2006;291(1):H269-73.

[10] Wehrens XH, Kirchhoff S, Doevendans PA. Mouse electrocardiography: an interval of thirty years. Cardiovasc Res. 2000;45(1):231-7.

[11] Alday A, Alonso H, Gallego M, Urrutia J, Letamendia A, Callol C, et al. Ionic channels underlying the ventricular action potential in zebrafish embryo. Pharmacol Res. 2014;84:26-31.

[12] Sanhueza D, Montoya A, Sierralta J, Kukuljan M. Expression of voltage-activated calcium channels in the early zebrafish embryo. Zygote. 2009;17(2):131-5.

[13] Langheinrich U, Vacun G, Wagner T. Zebrafish embryos express an orthologue of HERG and are sensitive toward a range of QT-prolonging drugs inducing severe arrhythmia. Toxicol Appl Pharmacol. 2003;193(3):370-82.

[14] Howe K, Clark MD, Torroja CF, Torrance J, Berthelot C, Muffato M, et al. The zebrafish reference genome sequence and its relationship to the human genome. Nature. 2013;496(7446):498-503.

[15] Dooley K, Zon LI. Zebrafish: a model system for the study of human disease. Curr Opin Genet Dev. 2000;10(3):252-6.

[16] Leong I, Skinner J, Shelling A, Love D. Zebrafish as a model for long QT syndrome: the evidence and the means of manipulating zebrafish gene expression. Acta physiologica. 2010;199(3):257-76.

[17] Asnani A, Peterson RT. The zebrafish as a tool to identify novel therapies for human cardiovascular disease. Disease models & mechanisms. 2014;7(7):763-7.

[18] Peal DS, Mills RW, Lynch SN, Mosley JM, Lim E, Ellinor PT, et al. Novel chemical suppressors of long QT syndrome identified by an in vivo functional screen. Circulation. 2011;123(1):23-30.

[19] Driever W, Solnica-Krezel L, Schier AF, Neuhauss SC, Malicki J, Stemple DL, et al. A genetic screen for mutations affecting embryogenesis in zebrafish. Development. 1996;123(1):37-46.

[20] Xu X, Meiler SE, Zhong TP, Mohideen M, Crossley DA, Burggren WW, et al. Cardiomyopathy in zebrafish due to mutation in an alternatively spliced exon of titin. Nature genetics. 2002;30(2):205-9.

[21] Lieschke GJ, Currie PD. Animal models of human disease: zebrafish swim into view. Nat Rev Genet. 2007;8(5):353-67.

[22] Milan DJ, Peterson TA, Ruskin JN, Peterson RT, MacRae CA. Drugs that induce repolarization abnormalities cause bradycardia in zebrafish. Circulation. 2003;107(10):1355-8.

[23] Baker K, Warren KS, Yellen G, Fishman MC. Defective "pacemaker" current (Ih) in a zebrafish mutant with a slow heart rate. Proc Natl Acad Sci U S A. 1997;94(9):4554-9.

[24] Verkerk AO, Remme CA. Zebrafish: a novel research tool for cardiac (patho)electrophysiology and ion channel disorders. Front Physiol. 2012;3:255.

[25] Dhillon SS, Dóró É, Magyary I, Egginton S, Sík A, Müller F. Optimisation of embryonic and larval ECG measurement in zebrafish for quantifying the effect of QT prolonging drugs. PloS one. 2013;8(4):e60552.

[26] Dhillon SS. Validation of the biological responses of reference drugs in the zebrafish embryo by electrocardiographic analysis and by novel phenotyping tools: University of Birmingham; 2015.

[27] Liu CC, Li L, Lam YW, Siu CW, Cheng SH. Improvement of surface ECG recording in adult zebrafish reveals that the value of this model exceeds our expectation. Scientific reports. 2016;6:25073.

[28] Zakaria ZZ, Benslimane FM, Nasrallah GK, Shurbaji S, Younes NN, Mraiche F, et al. Using zebrafish for investigating the molecular mechanisms of drug-induced cardiotoxicity. Biomed Res Int. 2018;2018.

[29] Zon LI, Peterson RT. In vivo drug discovery in the zebrafish. Nat Rev Drug Discov. 2005;4(1):35-44.

[30] Gierten J, Pylatiuk C, Hammouda OT, Schock C, Stegmaier J, Wittbrodt J, et al. Automated high-throughput heart rate measurement in medaka and zebrafish embryos under physiological conditions. bioRxiv. 2019:548594.

[31] Martin WK, Tennant AH, Conolly RB, Prince K, Stevens JS, DeMarini DM, et al. High-Throughput Video Processing of Heart Rate Responses in Multiple Wild-type Embryonic Zebrafish per Imaging Field. Scientific reports. 2019;9(1):145.

[32] Nygren A, Fiset C, Firek L, Clark JW, Lindblad DS, Clark RB, et al. Mathematical model of an adult human atrial cell: the role of K+ currents in repolarization. Circ Res. 1998;82(1):63-81.

[33] ten Tusscher KH, Noble D, Noble PJ, Panfilov AV. A model for human ventricular tissue. Am J Physiol Heart Circ Physiol. 2004;286(4):H1573-89.

[34] Harrild D, Henriquez C. A computer model of normal conduction in the human atria. Circ Res. 2000;87(7):E25-36.

[35] Sovilj S, Magjarevic R, Lovell NH, Dokos S. A simplified 3D model of whole heart electrical activity and 12-lead ECG generation. Comput Math Methods Med. 2013;2013:134208.

[36] Crowcombe J, Dhillon SS, Hurst RM, Egginton S, Muller F, Sik A, et al. 3D Finite Element Electrical Model of Larval Zebrafish ECG Signals. PLoS One. 2016;11(11):e0165655.

[37] Malmmivuo J, Plonsey R. Bioelectromagnetism. Oxford University Press, New York; 1995.

[38] Johnston BM. Six Conductivity Values to Use in the Bidomain Model of Cardiac Tissue. IEEE Trans Biomed Eng. 2016;63(7):1525-31.

[39] Grimes AC, Erwin KN, Stadt HA, Hunter GL, Gefroh HA, Tsai H-J, et al. PCB126 exposure disrupts zebrafish ventricular and branchial but not early neural crest development. Toxicological sciences. 2008;106(1):193-205.

[40] Spach MS, Miller WT, 3rd, Geselowitz DB, Barr RC, Kootsey JM, Johnson EA. The discontinuous nature of propagation in normal canine cardiac muscle. Evidence for recurrent discontinuities of intracellular resistance that affect the membrane currents. Circ Res. 1981;48(1):39-54.

[41] Keener J, Sneyd J. Mathematical physiology: I: cellular physiology: Springer Science & Business Media; 2010.

[42] Rogers JM, McCulloch AD. A collocation--Galerkin finite element model of cardiac action potential propagation. IEEE Trans Biomed Eng. 1994;41(8):743-57.

[43] Luo C-h, Rudy Y. A model of the ventricular cardiac action potential. Depolarization, repolarization, and their interaction. Circulation research. 1991;68(6):1501-26.

[44] Severs NJ, Bruce AF, Dupont E, Rothery S. Remodelling of gap junctions and connexin expression in diseased myocardium. Cardiovascular research. 2008;80(1):9-19.

[45] Bruce AF, Rothery S, Dupont E, Severs NJ. Gap junction remodelling in human heart failure is associated with increased interaction of connexin43 with ZO-1. Cardiovascular research. 2007;77(4):757-65.

[46] Weber M, Scherf N, Meyer AM, Panakova D, Kohl P, Huisken J. Cell-accurate optical mapping across the entire developing heart. Elife. 2017;6:e28307.

[47] Hodgkin AL, Huxley AF. A quantitative description of membrane current and its application to conduction and excitation in nerve. J Physiol. 1952;117(4):500-44.

[48] Buchanan Jr JW, Saito T, Gettes LS. The effects of antiarrhythmic drugs, stimulation frequency, and potassium-induced resting membrane potential changes on conduction velocity and dV/dtmax in guinea pig myocardium. Circulation research. 1985;56(5):696-703.

[49] Santana LF, Cheng EP, Lederer WJ. How does the shape of the cardiac action potential control calcium signaling and contraction in the heart? Journal of molecular and cellular cardiology. 2010;49(6):901.

[50] Boron WF, Boulpaep EL. Medical Physiology E-Book: Elsevier Health Sciences; 2016.

[51] Felker A, Prummel KD, Merks AM, Mickoleit M, Brombacher EC, Huisken J, et al. Continuous addition of progenitors forms the cardiac ventricle in zebrafish. Nat Commun. 2018;9(1):2001.

[52] Hu N, Sedmera D, Yost HJ, Clark EB. Structure and function of the developing zebrafish heart. The Anatomical Record: An Official Publication of the American Association of Anatomists. 2000;260(2):148-57.

[53] Kumar NM, Gilula NB, editors. Molecular biology and genetics of gap junction channels. Seminars in cell biology; 1992: Elsevier.

[54] Meşe G, Richard G, White TW. Gap junctions: basic structure and function. Journal of Investigative Dermatology. 2007;127(11):2516-24.

[55] Gros DB, Jongsma HJ. Connexins in mammalian heart function. Bioessays. 1996;18(9):719-30.

[56] Chi NC, Shaw RM, Jungblut B, Huisken J, Ferrer T, Arnaout R, et al. Genetic and physiologic dissection of the vertebrate cardiac conduction system. PLoS Biol. 2008;6(5):e109.

[57] Panáková D, Werdich AA, MacRae CA. Wnt11 patterns a myocardial electrical gradient via regulation of the L-type Ca2+ channel. Nature. 2010;466(7308):874.

[58] Christie TL, Mui R, White TW, Valdimarsson G. Molecular cloning, functional analysis, and RNA expression analysis of connexin45.6: a zebrafish cardiovascular connexin. Am J Physiol Heart Circ Physiol. 2004;286(5):H1623-32.

[59] Essner J, Laing J, Beyer E, Johnson R, Hackett Jr P. Expression of Zebrafish connexin43. 4 in the Notochord and Tail Bud of Wild-Type and Mutantno tailEmbryos. Developmental biology. 1996;177(2):449-62.

[60] Peters NS, Severs NJ, Rothery SM, Lincoln C, Yacoub MH, Green CR. Spatiotemporal relation between gap junctions and fascia adherens junctions during postnatal development of human ventricular myocardium. Circulation. 1994;90(2):713-25.

[61] Valderrabano M. Influence of anisotropic conduction properties in the propagation of the cardiac action potential. Progress in Biophysics & Molecular Biology. 2007;94(1-2):144-68.

[62] Kléber AG, Rudy Y. Basic mechanisms of cardiac impulse propagation and associated arrhythmias. Physiological reviews. 2004;84(2):431-88.

[63] Maesen B, Zeemering S, Afonso C, Eckstein J, Burton RA, van Hunnik A, et al. Rearrangement of atrial bundle architecture and consequent changes in anisotropy of conduction constitute the 3-dimensional substrate for atrial fibrillation. Circ Arrhythm Electrophysiol. 2013;6(5):967-75.

[64] Cobb JL. Gap junctions in the heart of teleost fish. Cell Tissue Res. 1974;154(1):131-4.

[65] Guyton Arthur C, Hall Jhon E. Textbook of medical physiology. Prism Books Pvt Limited; 1996.

[66] Koeppen BM, Stanton BA. Berne and levy physiology e-book: Elsevier Health Sciences; 2017.

[67] Chi NC, Shaw RM, Jungblut B, Huisken J, Ferrer T, Arnaout R, et al. Genetic and physiologic dissection of the vertebrate cardiac conduction system. PLoS biology. 2008;6(5):e109.

[68] Danik SB, Liu F, Zhang J, Suk HJ, Morley GE, Fishman GI, et al. Modulation of cardiac gap junction expression and arrhythmic susceptibility. Circ Res. 2004;95(10):1035-41.

[69] Gutstein DE, Morley GE, Tamaddon H, Vaidya D, Schneider MD, Chen J, et al. Conduction slowing and sudden arrhythmic death in mice with cardiac-restricted inactivation of connexin43. Circ Res. 2001;88(3):333-9.

[70] Kostin S, Rieger M, Dammer S, Hein S, Richter M, Klövekorn W-P, et al. Gap junction remodeling and altered connexin43 expression in the failing human heart. Cardiac Cell Biology: Springer; 2003. p. 135-44.

[71] Kirchhoff S, Nelles E, Hagendorff A, Kruger O, Traub O, Willecke K. Reduced cardiac conduction velocity and predisposition to arrhythmias in connexin40-deficient mice. Curr Biol. 1998;8(5):299-302.

[72] Peters NS, Coromilas J, Severs NJ, Wit AL. Disturbed connexin43 gap junction distribution correlates with the location of reentrant circuits in the epicardial border zone

of healing canine infarcts that cause ventricular tachycardia. Circulation. 1997;95(4):988-96.

[73] Matsushita T, Oyamada M, Fujimoto K, Yasuda Y, Masuda S, Wada Y, et al. Remodeling of cell-cell and cell–extracellular matrix interactions at the border zone of rat myocardial infarcts. Circulation research. 1999;85(11):1046-55.

[74] Severs NJ, Coppen SR, Dupont E, Yeh HI, Ko YS, Matsushita T. Gap junction alterations in human cardiac disease. Cardiovasc Res. 2004;62(2):368-77.

[75] Sabeh MK, Kekhia H, MacRae CA. Optical mapping in the developing zebrafish heart. Pediatric cardiology. 2012;33(6):916-22.

[76] Glickman NS, Yelon D, editors. Cardiac development in zebrafish: coordination of form and function. Seminars in cell & developmental biology; 2002: Elsevier.

[77] Auman HJ, Coleman H, Riley HE, Olale F, Tsai H-J, Yelon D. Functional modulation of cardiac form through regionally confined cell shape changes. PLoS biology. 2007;5(3):e53.

[78] Werdich AA, Brzezinski A, Jeyaraj D, Sabeh MK, Ficker E, Wan X, et al. The zebrafish as a novel animal model to study the molecular mechanisms of mechano-electrical feedback in the heart. Prog Biophys Mol Bio. 2012;110(2):154-65.

[79] Rasouli SJ, Stainier DY. Regulation of cardiomyocyte behavior in zebrafish trabeculation by Neuregulin 2a signaling. Nature communications. 2017;8:15281.

[80] Brown DR, Samsa LA, Qian L, Liu J. Advances in the study of heart development and disease using zebrafish. Journal of cardiovascular development and disease. 2016;3(2):13.

[81] Matrone G, Wilson KS, Mullins JJ, Tucker CS, Denvir MA. Temporal cohesion of the structural, functional and molecular characteristics of the developing zebrafish heart. Differentiation. 2015;89(5):117-27.

[82] Dietrich AC, Lombardo VA, Veerkamp J, Priller F, Abdelilah-Seyfried S. Blood flow and Bmp signaling control endocardial chamber morphogenesis. Dev Cell. 2014;30(4):367-77.

[83] Khonsary SA. Guyton and Hall: textbook of medical physiology. Surgical neurology international. 2017;8.

[84] Douglas G, Nicol F, Robertson C. Macleod's Clinical Examination E-Book: With STUDENT CONSULT Online Access: Elsevier Health Sciences; 2013.

[85] Mulroney S, Myers A. Netter's Essential Physiology E-Book: Elsevier Health Sciences; 2015.

[86] Lines G, Buist M, Grottum P, Pullan A, Sundnes J, Tveito A. Mathematical models and numerical methods for the forward problem in cardiac electrophysiology. Computing and Visualization in Science. 2003;5(4):215-39.

[87] Plonsey R, Heppner DB. Considerations of quasi-stationarity in electrophysiological systems. Bull Math Biophys. 1967;29(4):657-64.

[88] Tirziu D, Giordano FJ, Simons M. Cell communications in the heart. Circulation. 2010;122(9):928-37.

[89] Clayton RH, Bernus O, Cherry EM, Dierckx H, Fenton FH, Mirabella L, et al. Models of cardiac tissue electrophysiology: progress, challenges and open questions. Prog Biophys Mol Biol. 2011;104(1-3):22-48.

[90] Henriquez CS. Simulating the electrical behavior of cardiac tissue using the bidomain model. Critical reviews in biomedical engineering. 1993;21(1):1-77.

[91] Roth BJ, Wikswo J. Electrical stimulation of cardiac tissue: a bidomain model with active membrane properties. IEEE Transactions on Biomedical Engineering. 1994;41(3):232-40.

[92] Sovilj S, Magjarević R, Lovell NH, Dokos S. A simplified 3D model of whole heart electrical activity and 12-lead ECG generation. Computational and mathematical methods in medicine. 2013;2013.

[93] Rohr S. Role of gap junctions in the propagation of the cardiac action potential. Cardiovascular research. 2004;62(2):309-22.

[94] Frank J, Langer G. The myocardial interstitium: its structure and its role in ionic exchange. The Journal of cell biology. 1974;60(3):586-601.

[95] Diaz PJ, Rudy Y, Plonsey R. Intercalated discs as a cause for discontinuous propagation in cardiac muscle: A theoretical simulation. Annals of biomedical engineering. 1983;11(3):177-89.

[96] Henriquez C, Plonsey R. Effect of resistive discontinuities on waveshape and velocity in a single cardiac fibre. Medical and Biological Engineering and Computing. 1987;25(4):428-38.

[97] Leon L, Roberge F. Directional characteristics of action potential propagation in cardiac muscle. A model study. Circulation research. 1991;69(2):378-95.

[98] Stinstra J, MacLeod R, Henriquez C. Incorporating histology into a 3D microscopic computer model of myocardium to study propagation at a cellular level. Annals of biomedical engineering. 2010;38(4):1399-414.

[99] Roberts SF, Stinstra JG, Henriquez CS. Effect of nonuniform interstitial space properties on impulse propagation: a discrete multidomain model. Biophys J. 2008;95(8):3724-37.

[100] Tveito A, Jæger KH, Kuchta M, Mardal K-A, Rognes ME. A Cell-Based Framework for Numerical Modeling of Electrical Conduction in Cardiac Tissue. Front Phys. 2017;5:48.

[101] Jæger KH, Edwards AG, McCulloch A, Tveito A. Properties of cardiac conduction in a cell-based computational model. PLoS computational biology. 2019;15(5):e1007042.

[102] Moe GK, Rheinboldt WC, Abildskov JA. A Computer Model of Atrial Fibrillation. Am Heart J. 1964;67(2):200-20.

[103] Atienza FA, Carrión JR, Alberola AG, Álvarez JLR, Muñoz JJS, Sánchez JM, et al. A probabilistic model of cardiac electrical activity based on a cellular automata system. Revista Española de Cardiología (English Edition). 2005;58(1):41-7.

[104] Barbosa CRH. Simulation of a plane wavefront propagating in cardiac tissue using a cellular automata model. Physics in medicine and biology. 2003;48(24):4151.

[105] Leon LJ, Horáček BM. Computer model of excitation and recovery in the anisotropic myocardium: I. Rectangular and cubic arrays of excitable elements. Journal of electrocardiology. 1991;24(1):1-15.

[106] Siregar P, Sinteff J, Julen N, Le Beux P. An interactive 3D anisotropic cellular automata model of the heart. Computers and Biomedical Research. 1998;31(5):323-47.

[107] Wei D, Okazaki O, Harumi K, Harasawa E, Hosaka H. Comparative simulation of excitation and body surface electrocardiogram with isotropic and anisotropic computer heart models. IEEE Transactions on biomedical engineering. 1995;42(4):343-57.

[108] Henzinger TA. The theory of hybrid automata. Verification of Digital and Hybrid Systems: Springer; 2000. p. 265-92.

[109] Ye P, Entcheva E, Grosu R, Smolka SA, editors. Efficient modeling of excitable cells using hybrid automata. Proc of CMSB; 2005.

[110] Noble D, Garny A, Noble PJ. How the Hodgkin–Huxley equations inspired the cardiac physiome project. The Journal of physiology. 2012;590(11):2613-28.

[111] Noble D, Varghese A, Kohl P, Noble P. Improved guinea-pig ventricular cell model incorporating a diadic space, IKr and IKs, and length-and tension-dependent processes. The Canadian journal of cardiology. 1998;14(1):123-34.

[112] Grandi E, Pasqualini FS, Bers DM. A novel computational model of the human ventricular action potential and Ca transient. J Mol Cell Cardiol. 2010;48(1):112-21.

[113] Fitzhugh R. Impulses and Physiological States in Theoretical Models of Nerve Membrane. Biophys J. 1961;1(6):445-66.

[114] Dokos S, Cloherty SL, Lovell NH, editors. Computational model of atrial electrical activation and propagation. Engineering in Medicine and Biology Society, 2007 EMBS 2007 29th Annual International Conference of the IEEE; 2007: IEEE.

[115] Pullan AJ, Cheng LK, Buist ML. Mathematically modelling the electrical activity of the heart: from cell to body surface and back again: World Scientific Publishing Company; 2005.

[116] Miller CE, Henriquez CS. Finite element analysis of bioelectric phenomena. Crit Rev Biomed Eng. 1990;18(3):207-33.

[117] Zienkiewicz OC, Taylor RL, Zhu JZ. The finite element method: its basis and fundamentals: Elsevier; 2005.

[118] Rovitto M. Electro-migration reliability issue in interconnects for three-dimensional integration technologies: Dissertation. http://www. iue. tuwien. ac. at/phd/rovitto; 2016.

[119] Chi NC, Bussen M, Brand-Arzamendi K, Ding C, Olgin JE, Shaw RM, et al. Cardiac conduction is required to preserve cardiac chamber morphology. Proceedings of the National Academy of Sciences. 2010;107(33):14662-7.

[120] Lin YF, Swinburne I, Yelon D. Multiple influences of blood flow on cardiomyocyte hypertrophy in the embryonic zebrafish heart. Dev Biol. 2012;362(2):242-53.

[121] Baumann SB, Wozny DR, Kelly SK, Meno FM. The electrical conductivity of human cerebrospinal fluid at body temperature. IEEE Transactions on Biomedical Engineering. 1997;44(3):220-3.

[122] Chapman RA, Fry CH. An analysis of the cable properties of frog ventricular myocardium. J Physiol. 1978;283(1):263-82.

[123] Satoh H, Delbridge LM, Blatter LA, Bers DM. Surface:volume relationship in cardiac myocytes studied with confocal microscopy and membrane capacitance measurements: species-dependence and developmental effects. Biophys J. 1996;70(3):1494-504.

[124] Crowcombe JE. Larval zebrafish electrocardiography electrodynmaic modelling and sensor design: University of Birmingham; 2017.

[125] Boinagrov D, Loudin J, Palanker D. Strength–duration relationship for extracellular neural stimulation: numerical and analytical models. Journal of neurophysiology. 2010;104(4):2236-48.

[126] Olivetti G, Cigola E, Maestri R, Corradi D, Lagrasta C, Gambert SR, et al. Aging, cardiac hypertrophy and ischemic cardiomyopathy do not affect the proportion of mononucleated and multinucleated myocytes in the human heart. Journal of molecular and cellular cardiology. 1996;28(7):1463-77.

[127] Meijer van Putten RM, Mengarelli I, Guan K, Zegers JG, van Ginneken AC, Verkerk AO, et al. Ion channelopathies in human induced pluripotent stem cell derived cardiomyocytes: a dynamic clamp study with virtual IK1. Frontiers in physiology. 2015;6:7.

[128] Spach MS, Heidlage JF, Dolber PC, Barr RC. Electrophysiological effects of remodeling cardiac gap junctions and cell size: experimental and model studies of normal cardiac growth. Circulation research. 2000;86(3):302-11.

[129] Pereon Y, Demolombe S, Baro I, Drouin E, Charpentier F, Escande D. Differential expression of KvLQT1 isoforms across the human ventricular wall. Am J Physiol Heart Circ Physiol. 2000;278(6):H1908-15.

[130] Li G-R, Feng J, Yue L, Carrier M. Transmural heterogeneity of action potentials andI to1 in myocytes isolated from the human right ventricle. American Journal of Physiology-Heart and Circulatory Physiology. 1998;275(2):H369-H77.

[131] Koller ML, Maier SK, Gelzer AR, Bauer WR, Meesmann M, Gilmour RF, Jr. Altered dynamics of action potential restitution and alternans in humans with structural heart disease. Circulation. 2005;112(11):1542-8.

[132] Bueno-Orovio A, Hanson BM, Gill JS, Taggart P, Rodriguez B. In vivo human left-to-right ventricular differences in rate adaptation transiently increase pro-arrhythmic risk following rate acceleration. PLoS One. 2012;7(12):e52234.

[133] Qian S, Tarte E. Finite element modelling of discontinuous action potential propagation in larval zebrafish and human cardiac tissue. Physical biology. 2019;17(1):016001.

[134] Gourdie RG, Green CR, Severs NJ. Gap junction distribution in adult mammalian myocardium revealed by an anti-peptide antibody and laser scanning confocal microscopy. J Cell Sci. 1991;99 (Pt 1)(1):41-55.

[135] Hoyt RH, Cohen ML, Saffitz JE. Distribution and three-dimensional structure of intercellular junctions in canine myocardium. Circ Res. 1989;64(3):563-74.

[136] Frank JS, Langer GA. The myocardial interstitium: its structure and its role in ionic exchange. J Cell Biol. 1974;60(3):586-601.

[137] Clerc L. Directional differences of impulse spread in trabecular muscle from mammalian heart. J Physiol. 1976;255(2):335-46.

[138] van Veen AA, van Rijen HV, Opthof T. Cardiac gap junction channels: modulation of expression and channel properties. Cardiovasc Res. 2001;51(2):217-29.

[139] Kanno S, Saffitz JE. The role of myocardial gap junctions in electrical conduction and arrhythmogenesis. Cardiovasc Pathol. 2001;10(4):169-77.

[140] Kwak BR, Saez JC, Wilders R, Chanson M, Fishman GI, Hertzberg EL, et al. Effects of cGMP-dependent phosphorylation on rat and human connexin43 gap junction channels. Pflugers Arch. 1995;430(5):770-8.

[141] Bukauskas FF, Bukauskiene A, Bennett MV, Verselis VK. Gating properties of gap junction channels assembled from connexin43 and connexin43 fused with green fluorescent protein. Biophys J. 2001;81(1):137-52.

[142] Stinstra JG, Hopenfeld B, MacLeod RS. On the passive cardiac conductivity. Annals of biomedical engineering. 2005;33(12):1743-51.

[143] Metzger P, Weingart R. Electric current flow in cell pairs isolated from adult rat hearts. J Physiol. 1985;366(1):177-95.

[144] Weingart R. Electrical properties of the nexal membrane studied in rat ventricular cell pairs. J Physiol. 1986;370(1):267-84.

[145] Cole WC, Picone JB, Sperelakis N. Gap junction uncoupling and discontinuous propagation in the heart. A comparison of experimental data with computer simulations. Biophys J. 1988;53(5):809-18.

[146] Adler C, Costabel U. Cell number in human heart in atrophy, hypertrophy, and under the influence of cytostatics. Recent advances in studies on cardiac structure and metabolism. 1974;6:343-55.

[147] Auman HJ, Coleman H, Riley HE, Olale F, Tsai HJ, Yelon D. Functional modulation of cardiac form through regionally confined cell shape changes. Plos Biology. 2007;5(3):604-15.

[148] Guyton AC. Textbook of medical physiology. Academic Medicine. 1961;36(5):556.

[149] Shaw RM, Rudy Y. Ionic mechanisms of propagation in cardiac tissue. Roles of the sodium and L-type calcium currents during reduced excitability and decreased gap junction coupling. Circ Res. 1997;81(5):727-41.

[150] Dhillon SS, Doro E, Magyary I, Egginton S, Sik A, Muller F. Optimisation of embryonic and larval ECG measurement in zebrafish for quantifying the effect of QT prolonging drugs. PLoS One. 2013;8(4):e60552.

[151] Samsa LA, Givens C, Tzima E, Stainier DY, Qian L, Liu J. Cardiac contraction activates endocardial Notch signaling to modulate chamber maturation in zebrafish. Development. 2015;142(23):4080-91.

[152] Guerra A, Germano RF, Stone O, Arnaout R, Guenther S, Ahuja S, et al. Distinct myocardial lineages break atrial symmetry during cardiogenesis in zebrafish. Elife. 2018;7:e32833.

[153] Sedletcaia A, Evans T. Heart Chamber Size in Zebrafish Is Regulated Redundantly by Duplicated tbx2 Genes. Developmental Dynamics. 2011;240(6):1548-57.

[154] Lee J, Fei P, Packard RRS, Kang H, Xu H, Baek KI, et al. 4-Dimensional light-sheet microscopy to elucidate shear stress modulation of cardiac trabeculation. The Journal of clinical investigation. 2016;126(5):1679-90.

[155] Moorman AF, de Jong F, Denyn MM, Lamers WH. Development of the cardiac conduction system. Circ Res. 1998;82(6):629-44.

[156] Zoupa M, Machera K. Zebrafish as an Alternative Vertebrate Model for Investigating Developmental Toxicity—The Triadimefon Example. International journal of molecular sciences. 2017;18(4):817.

[157] Kimmel CB, Ballard WW, Kimmel SR, Ullmann B, Schilling TF. Stages of embryonic development of the zebrafish. Dev Dyn. 1995;203(3):253-310.

[158] Lin E, Ribeiro A, Ding W, Hove-Madsen L, Sarunic MV, Beg MF, et al. Optical mapping of the electrical activity of isolated adult zebrafish hearts: acute effects of temperature. Am J Physiol Regul Integr Comp Physiol. 2014;306(11):R823-36.

[159] Kwak BR, Hermans MM, De Jonge HR, Lohmann SM, Jongsma HJ, Chanson M. Differential regulation of distinct types of gap junction channels by similar phosphorylating conditions. Mol Biol Cell. 1995;6(12):1707-19.

[160] Severs NJ, Dupont E, Coppen SR, Halliday D, Inett E, Baylis D, et al. Remodelling of gap junctions and connexin expression in heart disease. Biochim Biophys Acta. 2004;1662(1-2):138-48.

[161] van der Velden HM, Jongsma HJ. Cardiac gap junctions and connexins: their role in atrial fibrillation and potential as therapeutic targets. Cardiovascular research. 2002;54(2):270-9.

[162] Dupont E, Matsushita T, Kaba RA, Vozzi C, Coppen SR, Khan N, et al. Altered connexin expression in human congestive heart failure. J Mol Cell Cardiol. 2001;33(2):359-71.

[163] Simon AM, Goodenough DA, Paul DL. Mice lacking connexin40 have cardiac conduction abnormalities characteristic of atrioventricular block and bundle branch block. Current Biology. 1998;8(5):295-8.

[164] Galarnyk M. Understanding Boxplots. Retrieved from https://towardsdatascience.com/understanding-boxplots-5e2df7bcbd51. Sep,2018.

[165] Mickoleit M, Schmid B, Weber M, Fahrbach FO, Hombach S, Reischauer S, et al. High-resolution reconstruction of the beating zebrafish heart. Nat Methods. 2014;11(9):919-22.

[166] Yalcin HC, Amindari A, Butcher JT, Althani A, Yacoub M. Heart function and hemodynamic analysis for zebrafish embryos. Dev Dyn. 2017;246(11):868-80.

[167] Boselli F, Vermot J. Live imaging and modeling for shear stress quantification in the embryonic zebrafish heart. Methods. 2016;94:129-34.